JETP Letters, Vol. 80, No. 6, 2004, pp. 371–376. From Pis'ma v Zhurnal Éksperimental'noĭ i Teoreticheskoĭ Fiziki, Vol. 80, No. 6, 2004, pp. 423–428.

Evolution of High-Mass Diffraction from the Light Quark Valence Component of the Pomeron¶

N. N. Nikolaev[1, 2], W. Schäfer[1], B. G. Zakharov[2], and V. R. Zoller[3]

[1] *IKP (Theorie), Institut für Kernphysik, D-52428, Jülich, Germany*

[2] *Landau Institute for Theoretical Physics, Moscow, 117940 Russia*

[3] *Institute for Theoretical and Experimental Physics, Moscow, 117218 Russia*

Received August 11, 2004

We analyze the contribution from excitation of the $(q\bar{q})(f\bar{f})$, $(q\bar{q})g_1\ldots g_n(f\bar{f})$ Fock states of a photon to high-mass diffraction in DIS. We show that the large-Q^2 behavior of this contribution can be described by DLLA evolution from the nonperturbative $f\bar{f}$ valence state of the pomeron. Although of higher order in pQCD, the new contribution to high-mass diffraction is comparable to that from the excitation of the $q\bar{q}g$ Fock state of the photon. © *2004 MAIK "Nauka/Interperiodica".*

PACS numbers: 12.38.-t

In this communication, we report a direct evaluation of high-mass diffractive deep inelastic scattering (DIS) from excitation of the $(q\bar{q})(f\bar{f})$ Fock states of a photon (Fig. 1), where q and f are light quarks. The interest in this problem can be formulated as follows.

On the one hand, within perturbative QCD (pQCD) diffractive DIS, $\gamma^* p \longrightarrow X + p'$, can be described as quasielastic scattering and excitation of multiparton Fock states X of the incident photon of virtuality Q^2 [1, 2]. As such, it is a manifestly nonlinear (quadratic) functional of the dipole cross section for the multiparton states, $X = q\bar{q}, q\bar{q}g, \ldots$. For the forward case, $t = 0$, where t is the (p, p') momentum transfer squared,

$$\left.\frac{d\sigma^D}{dt}\right|_{t=0} = \frac{1}{16\pi}[\langle q\bar{q}|\sigma^2|q\bar{q}\rangle + \langle q\bar{q}g|\sigma_3^2 - \sigma^2|q\bar{q}g\rangle + \ldots], \quad (1)$$

where σ and σ_3 stand for the dipole cross section for the Fock states $|q\bar{q}\rangle$ and $|q\bar{q}g\rangle$, respectively, interacting with the proton target and evaluated at the starting point of the small-x evolution, $x_{\mathbf{IP}} = x_0$. On the other hand, motivated by the triple-reggeon approach to diffraction excitation [3], one would like to reinterpret a high-mass diffractive DIS as an inclusive DIS off the pomeron,

$$(Q^2 + M^2)\left.\frac{d\sigma^D}{dtdM^2}\right|_{t=0} = \langle q\bar{q}|\sigma^{\mathbf{IP}}(x_{\mathbf{IP}}, \beta, \mathbf{r})|q\bar{q}\rangle. \quad (2)$$

If possible at all, such a color dipole representation will only be meaningful if the effect of higher Fock states of the photon can consistently be reabsorbed into the small-β evolution of $\sigma^{\mathbf{IP}}(x_{\mathbf{IP}}, \beta, \mathbf{r})$ [2, 4]. Here, $\beta = Q^2/(M^2 + Q^2)$, where M is the mass of the diffractive system, is the Bjorken variable for DIS off the pomeron, $x_{\mathbf{IP}} = x/\beta$ is the rapidity gap variable—the fraction of the proton's lightcone momentum carried by the exchanged pomeron—and $x = Q^2/2m\nu$ is the standard Bjorken variable for DIS off the proton, and ν is the photon energy.

It is not clear a priori that nonlinear Eq. (1) can be cast in linear form (2). Furthermore, the expected val-

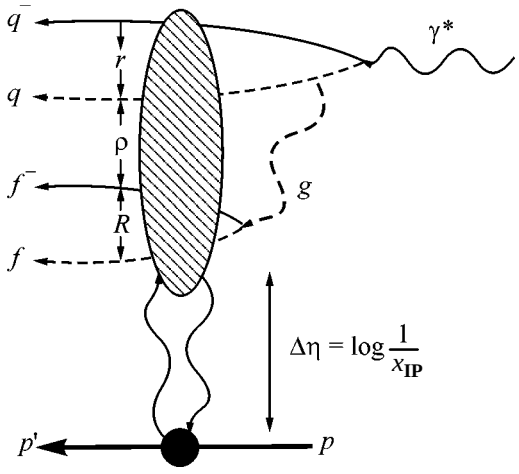

Fig. 1. The color dipole structure of diffractive excitation of perturbative $(q\bar{q})(f\bar{f})$ state of the photon with the rapidity gap $\Delta\eta$ from the proton. The contribution of other diagrams with radiation of the gluon and/or splitting $g \longrightarrow f\bar{f}$ after the interaction with the target vanishes to DLLA.

¶ This article was submitted by the authors in English.

ues of the square of the dipole cross section in (2) tend to be dominated by the contribution from large, nonperturbative, dipoles: $r \sim r_f = 1/m_f \sim 1$ fm for the excitation of $q\bar{q}$ states, which is the Born term for $\beta \sim 1$, and $\rho \sim R_c \sim 0.25$ fm for the Born term of high-mass, i.e., small-β, diffractive DIS: excitation of the $q\bar{q}g$ Fock states (for the determination of the propagation radius of perturbative gluons, R_c, from lattice QCD and elsewhere, see [5, 6]). Still, despite the manifestly nonperturbative Born term, resummation of double-leading-log approximation (DLLA)—strongly ordered energy and dipole size—contributions from $q\bar{q}g_1\ldots g_n$ excitation is possible and has been shown to correspond to the familiar DLLA evolution of the diffractive structure function [2]. Starting from [7], in phenomenological studies of diffractive DIS, it has become customary to apply the DGLAP evolution [8] to the whole diffractive structure function (SF),

$$f^{D(4)}(t=0, x_{\mathbf{IP}}, \beta, Q^2) = x_{\mathbf{IP}}F_2^{D(4)}(t=0, x_{\mathbf{IP}}, \beta, Q^2) = \frac{Q^2}{4\pi^2\alpha_{em}}(Q^2+M^2)\frac{d\sigma^D}{dtdM^2}\bigg|_{t=0} \quad (3)$$

(being differential in t, the so-defined diffractive SF is dimensionful, and $\sigma^{\mathbf{IP}}(x_{\mathbf{IP}}, \beta, \mathbf{r})$ has a dimension [mb]^2, but that does not affect its evolution properties; the t-integrated diffractive SF is dimensionless, but the modulation of the SF by the β-dependent diffraction slope [9] can spoil the evolution properties and, below, we focus on forward diffraction, $t = 0$). Although it has been argued that it is plausible [10] and the DGLAP evolution analyses have met with certain phenomenological success ([11–13] and references therein; for the review, see [14]), a direct demonstration of such a DGLAP evolution property of diffractive DIS is still missing.

The principal problem with extension of the analysis [2] to the contribution of the $(q\bar{q})(f\bar{f})$, $(q\bar{q})g_1\ldots g_n(f\bar{f})$ Fock states is that the $f\bar{f}$ dipoles have a large nonperturbative size, $R \sim r_f = 1/m_f \gg R_c$. The gross features of β-distribution in $\gamma^*p \longrightarrow (f\bar{f})p'$ are well understood: in close analogy to the valence structure function of the proton, it is peaked at $\beta \sim 1/2$, so that only finite masses, $M^2 \sim Q^2$, are excited [1, 15]. However, it is not obvious that this nonperturbative valence β-distribution defined by $\gamma^*p \longrightarrow (f\bar{f})p'$ will enter the evolution of the $q\bar{q}$ sea of the pomeron in precisely the same way as the valence quark density enters the evolution of the sea of nucleons. Here, we report a direct demonstration that such a pQCD evolution holds at least to the DLLA accuracy. Furthermore, we show that, although the $(q\bar{q})(f\bar{f})$ contribution is of higher order in the pQCD coupling α_S (see Fig. 1), it is enhanced by a potentially large numerical factor, $\propto[\sigma(r_f)/\sigma(R_c)]^2$, and, numerically, it is comparable to the leading-order $q\bar{q}g$ contribution. We report also a derivation of the inclusive spectrum of gluon jets from diffraction excitation of the $q\bar{q}g$ states of the photon, which clarifies the small-$\mathbf{r}^2$ scaling properties of $\sigma^{\mathbf{IP}}(x_{\mathbf{IP}}, \beta, \mathbf{r})$.

The further presentation is organized as follows. We start with a brief introduction into the color dipole description of small-β diffraction and demonstration of representation (2) for excitation of the $q\bar{q}g$ state. Then, we show how the DLLA contribution from $(q\bar{q})(f\bar{f})$ excitation to $f^{D(4)}(t=0, x_{\mathbf{IP}}, \beta, Q^2)$ can be cast in form (2) with $\sigma^{\mathbf{IP}}(x_{\mathbf{IP}}, \beta, \mathbf{r})$ evaluated for scattering of the $q\bar{q}$ dipole on the $f\bar{f}$ valence state of the pomeron. We present the DLLA evaluation of the small-β diffractive SF, compare our results with experimental data [12, 13], and conclude with a brief summary.

In the color dipole QCD approach to DIS [2, 4, 16], the two principal quantities are the dipole cross section, $\sigma(x, \mathbf{r})$, for interaction of the $q\bar{q}$ dipole $\mathbf{r}$ with the proton target, and the $q\bar{q}$ dipole size distribution in the projectile photon $e_q^2|\Psi_{\gamma^*}(Q^2, z, \mathbf{r})|^2$. In terms of $\sigma(x, \mathbf{r})$, the cross section of inclusive DIS has the form of an expectation value over the $q\bar{q}$ Fock state, $\sigma_{\gamma^*p}(x, Q^2) = \langle q\bar{q}|\sigma(x, \mathbf{r})|q\bar{q}\rangle$, the effect of higher-order perturbative Fock states, $q\bar{q}g_1\ldots g_n$, can be reabsorbed into the leading $\log(1/x)$ color dipole BFKL evolution of $\sigma(x, \mathbf{r})$. The relationship between the dipole cross section and the unintegrated gluon structure function $\mathcal{F}(x, \kappa^2) = \partial G(x, \kappa^2)/\partial\log\kappa^2$, reads

$$\sigma(x, \mathbf{r}) = \frac{4\pi\alpha_S(r^2)}{N_c} \times \int\frac{d^2\boldsymbol{\kappa}}{(\kappa^2+\mu_G^2)^2}[1-\exp(i\boldsymbol{\kappa}\mathbf{r})]\mathcal{F}(x, \kappa^2) \quad (4)$$
$$\approx \frac{\pi^2\alpha_S(r^2)}{N_c}r^2G\left(x, \frac{A}{r^2}\right),$$

where $R_c = 1/\mu_G$ is the Yukawa correlation radius for perturbative gluons, and, in the DLLA for small dipoles, $A \simeq 10$. Because of $\log Q^2$ scaling violations, $G(x, A/r^2)$ rises with the hard scale $A/\mathbf{r}^2$. To the lowest order in pQCD [16, 17],

$$\mathcal{F}(x, \boldsymbol{\kappa}^2) = \frac{G_F\alpha_S(\boldsymbol{\kappa}^2)}{\pi}N_cV_N(\boldsymbol{\kappa}), \quad (5)$$

where $N_cV_N(\boldsymbol{\kappa})$ can be regarded as the number of valence partons in the proton resolved by gluons at the scale $\boldsymbol{\kappa}^2$. Here, the vertex function $V_N(\boldsymbol{\kappa}) = 1 - G_2(\boldsymbol{\kappa}, -\boldsymbol{\kappa})$ and

the two-quark form-factor of the target nucleon, $G_2(\boldsymbol{\kappa}, -\boldsymbol{\kappa})$, vanishes for $\boldsymbol{\kappa}^2 \gtrsim R_N^{-2}$, where R_N is the radius of the nucleon.

The $q\bar{q}g$ contribution to (1) describes the first iteration of the $\log(1/\beta)$ evolution of diffractive DIS and can be separated into the radiative correction to the small-mass $q\bar{q}$ excitation and the Born term of the high-mass $q\bar{q}g$ excitation as follows. Let $\mathbf{r}$, $\boldsymbol{\rho}$, and $\boldsymbol{\rho} - \mathbf{r}$ be the $\bar{q}$–q, g–q, and g–$\bar{q}$ separations in the impact parameter (transverse size) plane. The $q\bar{q}g$ three-body interaction cross section equals [2]

$$\sigma_3(x, \mathbf{r}, \boldsymbol{\rho}) = \frac{C_A}{2C_F}[\sigma(x, \boldsymbol{\rho}) + \sigma(x, \boldsymbol{\rho} - \mathbf{r})] - \frac{1}{N_c^2 - 1}\sigma(x, \mathbf{r}). \quad (6)$$

For soft perturbative gluons carrying a small fraction of a photon's momentum, $z_g \ll 1$, and Yukawa infrared regularization, the wave function of the three-parton $q\bar{q}g$ state equals [2, 4]

$$\begin{aligned}|\Phi(\mathbf{r}, \boldsymbol{\rho}, z, z_g)|^2 &= \frac{e_q^2 C_F \alpha_S(r^2)}{\pi^2 z_g}\left|\Psi_{\gamma^*}(Q^2, z, \mathbf{r})\right|^2 \\ &\times \left|\mu_G K_1(\mu_G\rho)\frac{\boldsymbol{\rho}}{\rho} - \mu_G K_1(\mu_G|\boldsymbol{\rho} - \mathbf{r}|)\frac{\boldsymbol{\rho} - \mathbf{r}}{|\boldsymbol{\rho} - \mathbf{r}|}\right|^2 \\ &= \frac{e_q^2}{z_g}\left|\Psi_{\gamma^*}(Q^2, z, \mathbf{r})\right|^2 \mathcal{H}(\boldsymbol{\rho} - \mathbf{r}, \boldsymbol{\rho}) \\ &\simeq \frac{e_q^2 C_F \alpha_S(r^2)}{\pi^2 z_g}\left|\Psi_{\gamma^*}(Q^2, z, \mathbf{r})\right|^2 \frac{r^2}{\rho^4} F(\mu_G\rho),\end{aligned} \quad (7)$$

where $\mathcal{H}(\boldsymbol{\rho} - \mathbf{r}, \boldsymbol{\rho})$ is the kernel of the color dipole BFKL equation

$$\begin{aligned}\frac{\partial\sigma(x, \mathbf{r})}{\partial \log\frac{1}{x}} &= \mathcal{H} \otimes \sigma(x, \mathbf{r}) \\ &= \frac{2C_F}{C_A}\int d^2\boldsymbol{\rho}\mathcal{H}(\boldsymbol{\rho} - \mathbf{r}, \boldsymbol{\rho})[\sigma_3(x, \mathbf{r}, \boldsymbol{\rho}) - \sigma(x, \mathbf{r})] \quad (8) \\ &= \int d^2\boldsymbol{\rho}\mathcal{H}(\boldsymbol{\rho} - \mathbf{r}, \boldsymbol{\rho})[\sigma(x, \boldsymbol{\rho}) + \sigma(x, \boldsymbol{\rho} - \mathbf{r}) - \sigma(x, \mathbf{r})]\end{aligned}$$

and we also showed the DLLA approximation for $\mathbf{r}^2 \ll \boldsymbol{\rho}^2$. The form factor of the infrared cutoff, $F(z)$, satisfies $F(0) = 1$ and $F(z) \propto \exp(-2z)$ at $z > 1$ [2, 7].

Now notice that, in view of (7), the $q\bar{g}g$ contribution to (1) can be rearranged as

$$\mathcal{H}(\sigma_3^2 - \sigma^2) = 2\sigma\mathcal{H}(\sigma_3 - \sigma) + \mathcal{H}(\sigma_3 - \sigma)^2. \quad (9)$$

The first term in the right-hand side of (9) is the radiative correction to the small-mass $q\bar{q}$ excitation with the rapidity gap $x_{\mathbf{IP}} \sim x$, i.e., the contribution from the two-parton state to the total cross section of diffraction (1) must be calculated with the BFKL-evolved

$$\sigma(x_{\mathbf{IP}}, \mathbf{r}) = \sigma(x_0, \mathbf{r}) + \int_{x_{\mathbf{IP}}}^{x_0}\frac{dx'}{x'}\mathcal{H} \otimes \sigma(x', \mathbf{r}). \quad (10)$$

The second term in (9) is the Born term of the high-mass three-parton, $q\bar{q}g$, excitation with the rapidity gap $x_{\mathbf{IP}} = x_0$. In the high-mass regime $dz_g/z_g = dM^2/(M^2 + Q^2)$ and after undoing the z_g-integration, the DLLA three-parton cross section takes the form

$$\begin{aligned}(Q^2 + M^2)\left.\frac{d\sigma^D_{q\bar{q}g}}{dtdM^2}\right|_{t=0} &= \frac{1}{16\pi}\int dz d^2\mathbf{r} d^2\boldsymbol{\rho}\{z_g|\Phi(\mathbf{r}, \boldsymbol{\rho}, z, z_g)|^2\}_{z_g = 0} \\ &\times [\sigma_3(x_{\mathbf{IP}}, \mathbf{r}, \boldsymbol{\rho}) - \sigma(x_{\mathbf{IP}}, \mathbf{r})]^2 \quad (11) \\ &\simeq \frac{1}{16\pi}\int dz d^2\mathbf{r}\left|\Psi_{\gamma^*}(Q^2, z, \mathbf{r})\right|^2 \frac{\pi^2\alpha_S(r^2)}{N_c} r^2 \\ &\times \frac{C_A^2 N_c}{C_F}\int_{r^2} d^2\boldsymbol{\rho}\left[\frac{\sigma(x_{\mathbf{IP}}, \boldsymbol{\rho})}{\rho^2}\right]^2 F(\mu_G\rho).\end{aligned}$$

It gives a flat small-β behavior of $f^{D(4)}(t = 0, x_{\mathbf{IP}}, \beta, Q^2)$ with the strength controlled [2, 15] by nonperturbative large ρ, cut off from above at $\rho \sim R_c$ by the nonperturbative form factor $F(\mu_G\rho)$. The small-ρ integration can safely be extended to $\rho = 0$, so that (11) is of the desired color dipole form (2) and can be treated as DIS off the sea generated by perturbative splitting of gluons from the valence gg state of the pomeron. There is one caveat, though: the gluon density in the pomeron defined by Eq. (11),

$$G^{\mathbf{IP}}_{gg}(x_{\mathbf{IP}}, \beta) = \frac{C_A^2 N_c}{C_F}\int d^2\boldsymbol{\rho}\left[\frac{\sigma(x_{\mathbf{IP}}, \boldsymbol{\rho})}{\rho^2}\right]^2 F(\mu_G\rho), \quad (12)$$

is short of the collinear scaling violations present in (4).

The extension of the above analysis to the DLLA description of diffractive excitation of the high-mass $(q\bar{q})(f\bar{f})$ Fock state of the photon proceeds as follows. As we shall see a posteriori, the DLLA contribution comes from $\mathbf{r}^2 \ll \boldsymbol{\rho}^2 \ll \mathbf{R}^2$. First, we recall that the $q\bar{q}$ excitation is dominated by very asymmetric pairs, in which one of the final partons carries a very small fraction of the photons momentum, $z \sim m_q^2/Q^2 \ll 1$, so that, in the impact parameter space, the fast parton with $\bar{z} = 1 - z$ flies along the photon's trajectory, while the slower parton is at large transverse distance $r \sim 1/m_q$ from the parent photon [1]. Consequently, the fast par-

ton of the $f\bar{f}$ shall have the same impact parameter as the gluon radiated by the parent $q\bar{q}$ dipole. In view of the DLLA ordering, $\mathbf{r}^2 \ll \boldsymbol{\rho}^2 \ll \mathbf{R}^2$, the partons of the parent $q\bar{q}$ dipole and the fast parton of the radiative $f\bar{f}$ pair can be treated as the pointlike (anti)triplet color charge, and the $(q\bar{q})(f\bar{f})$ state interacts with the target nucleon as the $f\bar{f}$ dipole with the dipole cross section $\sigma(x_{\mathbf{IP}}, \mathbf{R})$. The distribution of $f\bar{f}$ color dipoles in the gluon of transverse momentum $\boldsymbol{\kappa}$ is identical to that in the photon subject to the substitutions $N_c\alpha_{em}e_f^2 \longrightarrow T_F\alpha_S(\boldsymbol{\kappa}^2)$ and $Q^2 \longrightarrow \boldsymbol{\kappa}^2$, so that the diffractive cross section of interest equals

$$(Q^2+M^2)\frac{d\sigma^D_{(q\bar{q})(f\bar{f})}}{dtdM^2}\bigg|_{t=0} = \frac{1}{16\pi} \times \int d^2\boldsymbol{\kappa}\frac{dg_{q\bar{q}}(Q^2,\boldsymbol{\kappa})}{d^2\boldsymbol{\kappa}}\frac{T_F\alpha_S(\boldsymbol{\kappa}^2)}{N_c\alpha_{em}e_f^2}\langle f\bar{f}|\sigma^2(x_{\mathbf{IP}},\mathbf{R})|f\bar{f}\rangle, \tag{13}$$

where the flux of gluons in the parent $q\bar{q}$ state is given by the momentum-space version of (7):

$$\frac{dg_{q\bar{q}}(Q^2,\boldsymbol{\kappa})}{d^2\boldsymbol{\kappa}} = \frac{1}{z_g}\int_0^1 dz_q\int d^2\mathbf{r}\left|\Psi_{\gamma^*}(Q^2,z_q,\mathbf{r})\right|^2 \times\frac{2e_q^2G_F\alpha_S(r^2)}{\pi^2}\frac{[1-\exp(i\boldsymbol{\kappa}\mathbf{r})]}{(\boldsymbol{\kappa}^2+\mu_G^2)^2}\boldsymbol{\kappa}^2. \tag{14}$$

Finally, note that

$$\frac{\boldsymbol{\kappa}^2}{4\pi^2\alpha_{em}}\frac{1}{16\pi e_f^2}\langle f\bar{f}|\sigma^2(x_{\mathbf{IP}},\mathbf{R})|f\bar{f}\rangle = \frac{\boldsymbol{\kappa}^2}{4\pi^2\alpha_{em}}\frac{d\sigma(\gamma^*(\boldsymbol{\kappa}^2)\longrightarrow f\bar{f})}{dt}\bigg|_{t=0} \tag{15}$$

$$= \frac{1}{e_f^2}\int_0^1\frac{d\beta}{\beta}f^{D(4)}_{f\bar{f}}(t=0,x_{\mathbf{IP}},\beta,\boldsymbol{\kappa}^2) = N^{\mathbf{IP}}_{f\bar{f}}(x_{\mathbf{IP}},\boldsymbol{\kappa}^2),$$

where $N^{\mathbf{IP}}_{f\bar{f}}(x_{\mathbf{IP}},\boldsymbol{\kappa}^2)$ can be reinterpreted as a number of charged valence partons, i.e., twice the number of $f\bar{f}$ dipoles, in the pomeron. Upon the substitution of (15) and (14) into (13), one readily recovers dipole representation (2), in which $\sigma^{\mathbf{IP}}(x_{\mathbf{IP}},\beta,\mathbf{r})$ is evaluated from Eq. (4), in which unintegrated gluon density (5) is substituted for by the unintegrated gluon density evolved from the $f\bar{f}$ state of the pomeron,

$$\mathcal{F}^{\mathbf{IP}}_{f\bar{f}}(\beta,\boldsymbol{\kappa}^2) = \frac{C_F\alpha_S(\boldsymbol{\kappa}^2)}{\pi}N^{\mathbf{IP}}_{f\bar{f}}(x_{\mathbf{IP}},\boldsymbol{\kappa}^2). \tag{16}$$

Furthermore, $N^{\mathbf{IP}}_{f\bar{f}}(x_{\mathbf{IP}},\boldsymbol{\kappa}^2)$ vanishes at $\boldsymbol{\kappa}^2 = 0$ and, according to [1, 16], flattens at $\boldsymbol{\kappa}^2 \gg m_f^2$, which, in comparison to (5), suggests a transverse size for the $f\bar{f}$ component of the pomeron $r_f \sim 1/m_f$. One can come to the same conclusion from the point that the dominant contribution to (14) comes from $f\bar{f}$ dipoles with $R \sim 1/m_f$.

The DLLA analysis of $q\bar{q}g_1\ldots g_n$ excitation developed in [2] can readily be extended to the higher, $(q\bar{q})g_1\ldots g_n(f\bar{f})$, states. The crucial point is that, to DLLA, the $f\bar{f}$ dipole is the largest one, so that the corresponding contribution to the diffractive cross section is still given by Eq. (13), where the DLLA evolution is reabsorbed into the flux of gluon g_n, which is the softest with respect to the photon. Viewed from the pomeron side, that amounts to the DLLA small-β evolution of $\sigma^{\mathbf{IP}}(x_{\mathbf{IP}},\beta,\mathbf{r})$ with the boundary condition defined by gluon density (16). As such, the emerging $\log^{n-1}(1/\beta)\log^n(1/\alpha_S(r^2))$ structure of DLLA expansion in the energy and collinear logarithms for diffractive SF from $(q\bar{q})g_1\ldots g_n(f\bar{f})$ excitation is identical to the DLLA structure of the proton SF. As shown in [2], DLLA expansion for diffractive SF from $(q\bar{q})g_1\ldots g_n$ excitation is of a marginally different structure, $\log^{n-1}(1/\beta)\log^{n-1}(1/\alpha_S(r^2))$. In addition, the two components of the diffractive structure function have a manifestly different $x_{\mathbf{IP}}$-dependence [7]: driven by $\sigma(x_{\mathbf{IP}},r_f)$ in (16) for the $q\bar{q}$, $(q\bar{q})(f\bar{f})$, $(q\bar{q})g_1\ldots g_n(f\bar{f})$ excitations and by $\sigma(x_{\mathbf{IP}},R_c)$ for the $(q\bar{q})g_1\ldots g_n$ excitations. This concludes the proof of DLLA small-β evolution at fixed $x_{\mathbf{IP}}$ of such a two-component diffractive structure function, $f^{D(4)}(t=0,x_{\mathbf{IP}},\beta,Q^2)$.

The absence of a scaling violation in (11) and (12) implies that, in contrast to (5), the corresponding unintegrated gluon density $\mathcal{F}^D_{gg}(\beta,\boldsymbol{\kappa}^2)$ vanishes for large $\boldsymbol{\kappa}^2$. A closely related observable is the transverse momentum, $\mathbf{p}$, spectrum of semihard diffractive gluons with $\mathbf{p}^2 \ll \mathbf{r}^{-2} \ll Q^2$ [18]. Since $\mathbf{p}$ is a variable conjugate to $\boldsymbol{\rho}$, upon the relevant Fourier transforms,

$$(Q^2+M^2)\frac{d\sigma^D(\gamma^*\longrightarrow gX)}{dtdM^2d^2\mathbf{p}}\bigg|_{t=0} = \frac{1}{16\pi(2\pi)^2}\int dzd^2\mathbf{r}C_F|\Psi_{\gamma^*}(z,\mathbf{r})|^2\frac{\alpha_S(r)}{\pi^2}$$

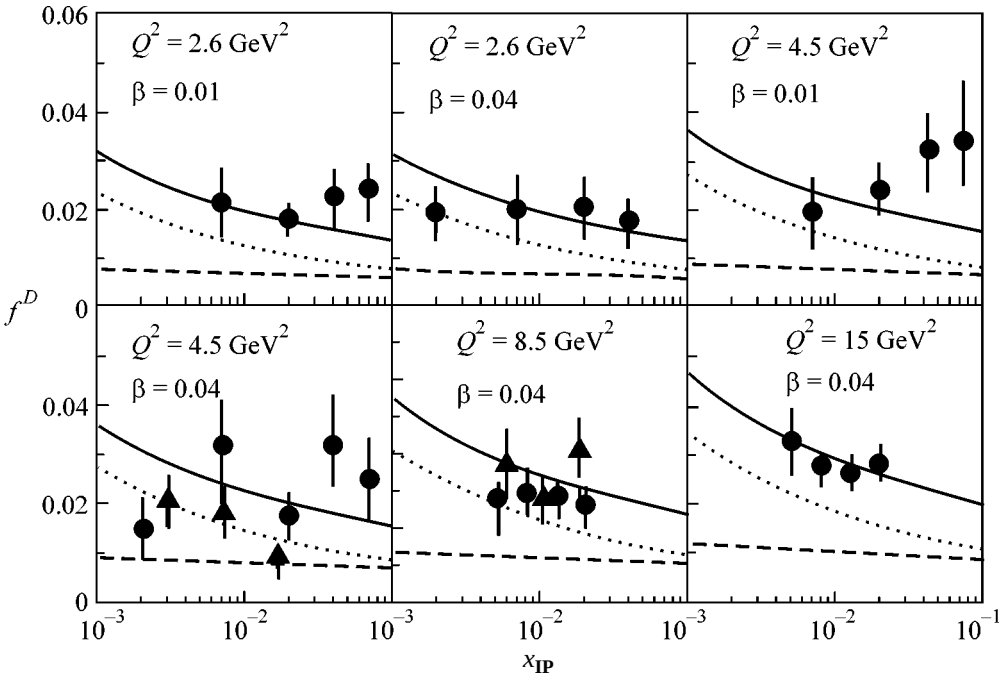

Fig. 2. The comparison with the experimental data on small-β, small-$x_{\mathbf{IP}}$ diffractive structure function ([12], full circles; [13], full triangles) of the theoretical evaluation of $f^{D(3)} = f^{D(3)}_{q\bar{q}g} + f^{D(3)}_{(q\bar{q})(f\bar{f})}$ shown by the solid line. The dotted line corresponds to $f^{D(3)}_{q\bar{q}g}$, and the dashed line represents $f^{D(3)}_{(q\bar{q})(f\bar{f})}$.

$$\times \left| \int d^2\boldsymbol{\rho} \exp(i\mathbf{p}\boldsymbol{\rho}) \left[\frac{\boldsymbol{\rho}}{\boldsymbol{\rho}^2} - \frac{\boldsymbol{\rho}-\mathbf{r}}{(\boldsymbol{\rho}-\mathbf{r})^2} \right] \times [\sigma_3(x_{\mathbf{IP}}, r, \boldsymbol{\rho}) - \sigma(x_{\mathbf{IP}}, \mathbf{r})] \right|^2 \tag{17}$$

$$= \int dz d^2\mathbf{r} |\Psi_{\gamma^*}(z, \mathbf{r})|^2 \frac{\pi\alpha_S(r^2)}{N_c} r^2 \times \frac{C_A^2}{4C_F N_c} \left[\frac{\alpha_S(\mathbf{p}^2) G(x_{\mathbf{IP}}, \mathbf{p}^2)}{\mathbf{p}^2} \right]^2.$$

Within the reinterpretation of diffraction as DIS of pomerons, the $\mathbf{p}$ has the meaning of intrinsic transverse momentum in the valence gg state of the pomeron. Indeed, spectrum (17) falls more steeply than the $1/\mathbf{p}^2$ spectrum of gluons from inclusive DIS off a nucleon.

The numerical results for high-mass, small-β diffraction depend on the input dipole cross section $\sigma(x, \mathbf{r})$. Here, we evaluate the lowest-order $q\bar{q}g$ and $(q\bar{q})(f\bar{f})$ contributions to diffractive DIS in a specific color dipole BFKL model [4, 19], which gives a good description of the proton SF data. The applicability domain of the small-β, small-$x_{\mathbf{IP}}$ formalism is $\beta, x_{\mathbf{IP}} < x_0 \ll 1$, the experience with inclusive DIS suggests $x_0 \sim 0.03$, although the theoretical curves in Fig. 2 are stretched up to $x_{\mathbf{IP}} = 0.1$. This small-β, small-$x_{\mathbf{IP}}$ domain is almost at the boundary of the HERA experiments, and the corresponding experimental data on the t-integrated diffractive structure function $f^{D(3)}(x_{\mathbf{IP}}, \beta, Q^2)$ from H1 ([12], circles) and ZEUS ([13], triangles) are shown in Fig. 2. We evaluate this structure function as

$$f^{D(3)}(x_{\mathbf{IP}}, \beta, Q^2) = \int dt\, f^{D(4)}(t, x_{\mathbf{IP}}, \beta, Q^2) \approx \frac{1}{B_{3\mathbf{IP}}} f^{D(4)}(t = 0, x_{\mathbf{IP}}, \beta, Q^2)$$

with the central value of the diffraction slope $B_{\mathbf{IP}} = B_D = 7.2 \pm 1.1^{+0.7}_{-0.9}$ GeV^{-2} as reported by ZEUS [20]. The apparent growth of the experimentally observed $f^{D(3)}(x_{\mathbf{IP}}, \beta, Q^2)$ toward large $x_{\mathbf{IP}} \sim 0.1$ is usually attributed to the nonvacuum admixture to the pomeron exchange. Two features of the theoretical results for small-β diffraction are noteworthy. First, the contributions from $q\bar{q}g$ and higher-order $(q\bar{q})(f\bar{f})$ states are of comparable magnitude because $R_c \ll r_f$ and the latter is enhanced $\propto [\sigma(x_{\mathbf{IP}}, r_f)/\sigma(x_{\mathbf{IP}}, R_c)]^2$. Second, because of the same inequality of the important dipole sizes, $R_c \ll r_f$, the $x_{\mathbf{IP}}$-dependence of the $q\bar{q}g$ excitation is steeper than that of the $(q\bar{q})(f\bar{f})$ excitation. This point has been made already in [7]: the numerically significant

contribution from the $(q\bar{q})(f\bar{f})$ excitation makes the overall $x_{\mathbf{IP}}$-dependence of $f^{D(3)}(x_{\mathbf{IP}}, \beta, Q^2)$ weaker than evaluated in [7] for pure $q\bar{q}g$ excitation. The solid curve in Fig. 2 is the combined contribution from the two mechanisms. It is in reasonable agreement with the HERA data.

To summarize, we reported the first explicit proof of the DLLA evolution property of the contribution to diffractive structure function from excitation of $(q\bar{q})(f\bar{f})$, $(q\bar{q})g_1\ldots g_n(f\bar{f})$ Fock states of the photon. We demonstrated that the corresponding diffractive SF can be cast in the color dipole representation. The boundary condition for DLLA small-β evolution is provided by the Born dipole cross section built perturbatively upon the valence $f\bar{f}$ state of the pomeron, as defined by the $\gamma^* p \longrightarrow (f\bar{f})p'$ excitation, in precisely the same manner as in inclusive DIS off the nucleon starting with the valence quark distribution. Compared to the $q\bar{q}g$ excitation, the $(q\bar{q})(f\bar{f})$ is of a higher order to pQCD. Still, the numerical evaluations confirm the expectation that the pQCD α_S suppression is compensated for by the larger dipoles in the $(q\bar{q})(f\bar{f})$ state compared to the $q\bar{q}g$ state of the photon.

This work has been partly supported by the INTAS (grant no. 00-00366) and the DFG (grant no. 436RUS17/72/03).

REFERENCES

1. N. N. Nikolaev and B. G. Zakharov, Z. Phys. C **53**, 331 (1992).
2. N. N. Nikolaev and B. G. Zakharov, Zh. Éksp. Teor. Fiz. **105**, 1117 (1994) [JETP **78**, 598 (1994)]; Z. Phys. C **64**, 631 (1994).
3. K. A. Ter-Martirosyan, Phys. Lett. B **44B**, 179 (1973); A. B. Kaidalov and K. A. Ter-Martirosyan, Nucl. Phys. B **75**, 471 (1974); G. Ingelman and P. E. Schlein, Phys. Lett. B **152B**, 256 (1985).
4. N. N. Nikolaev, B. G. Zakharov, and V. R. Zoller, JETP Lett. **59**, 6 (1994); Phys. Lett. B **328**, 486 (1994); Zh. Éksp. Teor. Fiz. **105**, 1498 (1994) [JETP **78**, 806 (1994)]; N. N. Nikolaev and B. G. Zakharov, Phys. Lett. B **327**, 149 (1994); Phys. Lett. B **327**, 157 (1994).
5. E. Meggiolaro, Phys. Lett. B **451**, 414 (1999).
6. J. H. Field, Phys. Rev. D **66**, 013013 (2002).
7. M. Genovese, N. N. Nikolaev, and B. G. Zakharov, Zh. Éksp. Teor. Fiz. **108**, 1141 (1995) [JETP **81**, 625 (1995)]; Phys. Lett. B **378**, 347 (1996); Phys. Lett. B **380**, 213 (1996).
8. V. N. Gribov and L. N. Lipatov, Yad. Fiz. **15**, 781 (1972) [Sov. J. Nucl. Phys. **15**, 438 (1972)]; Y. L. Dokshitzer, Zh. Éksp. Teor. Fiz. **73**, 1216 (1977) [Sov. Phys. JETP **46**, 641 (1977)]; G. Altarelli and G. Parisi, Nucl. Phys. B **126**, 298 (1977).
9. N. N. Nikolaev, A. V. Pronyaev, and B. G. Zakharov, JETP Lett. **68**, 634 (1998).
10. A. Berera and D. E. Soper, Phys. Rev. D **53**, 6162 (1996); J. C. Collins, Phys. Rev. D **57**, 3051 (1998); Phys. Rev. D **61**, 019902(E) (2000); M. Grazzini, L. Trentadue, and G. Veneziano, Nucl. Phys. B **519**, 394 (1998); L. Trentadue and G. Veneziano, Phys. Lett. B **323**, 201 (1994).
11. C. Royon, L. Schoeffel, J. Bartels, *et al.*, Phys. Rev. D **63**, 074004 (2001).
12. H1 Collab., *Measurements of the Diffractive Structure Function at HERA, submitted to XX International Symposium on Lepton and Photon Interactions* (Rome, 2001); Z. Phys. C **76**, 613 (1997).
13. J. Breitweg *et al.* (ZEUS Collab.), Eur. Phys. J. C **6**, 43 (1999).
14. A. Hebecker, Phys. Rep. **331**, 1 (2000).
15. M. Genovese, N. N. Nikolaev, and B. G. Zakharov, Phys. Lett. B **378**, 347 (1996); N. N. Nikolaev, A. V. Pronyaev, and B. G. Zakharov, Phys. Rev. D **59**, 091501 (1999).
16. N. N. Nikolaev and B. G. Zakharov, Z. Phys. C **49**, 607 (1991).
17. N. N. Nikolaev and B. G. Zakharov, Phys. Lett. B **332**, 177 (1994).
18. N. N. Nikolaev, *Monte Carlo Generators for HERA Physics* (Hamburg, 1998/1999), pp. 377–381; hep-ph/9905562.
19. N. N. Nikolaev, B. G. Zakharov, and V. R. Zoller, JETP Lett. **66**, 138 (1997); N. N. Nikolaev, J. Speth, and V. R. Zoller, Phys. Lett. B **473**, 157 (2000); JETP **93**, 957 (2001); V. R. Zoller, Phys. Lett. B **509**, 69 (2001).
20. J. Breitweg *et al.* (ZEUS Collab.), Eur. Phys. J. C **1**, 81 (1998).

JETP Letters, Vol. 80, No. 6, 2004, pp. 377–381. From Pis'ma v Zhurnal Éksperimental'noĭ i Teoreticheskoĭ Fiziki, Vol. 80, No. 6, 2004, pp. 429–433.

Study of 2β-Decay of ^{100}Mo and ^{82}Se Using the NEMO3 Detector¶

R. Arnold[1], C. Augier[2], J. Baker[3], A. Barabash[4, *], V. Brudanin[5], A. J. Caffrey[3], V. Egorov[5], J. L. Guyonnet[1], F. Hubert[14], Ph. Hubert[14], L. Jenner[6], C. Jollet[1], S. Jullian[2], A. Klimenko[5], O. Kochetov[5], S. Konovalov[4], V. Kovalenko[5], D. Lalanne[2], F. Leccia[14], I. Linck[1], C. Longuemare[7], G. Lutter[14], Ch. Marquet[14], F. Mauger[7], H. W. Nicholson[8], H. Ohsumi[9], F. Piquemal[14], J.-L. Reyss[10], R. Saakyan[6], X. Sarazin[2], F. Scheibling[1], Yu. Shitov[5], L. Simard[2], A. Smolnikov[5], I. Štekl[11], J. Suhonen[12], C. S. Sutton[8], G. Szklarz[2], V. Timkin[5], J. Thomas[6], V. Tretyak[5], V. Umatov[4], L. Vála[11], I. Vanyushin[4], S. Vasiliev[5], V. Vasilyev[4], V. Vorobel[13], and Ts. Vylov[5]

[1] *IReS, IN2P3-CNRS et Université Louis Pasteur, 67037 Strasbourg, France*
[2] *LAL, IN2P3-CNRS et Université Paris-Sud, 91405 Orsay, France*
[3] *INEEL, Idaho Falls, ID 83415, USA*
[4] *Institute of Theoretical and Experimental Physics, Moscow, 117218 Russia*
* *e-mail: Alexander.Barabash@itep.ru*
[5] *Joint Institute for Nuclear Research, Dubna, 141980 Russia*
[6] *University College London, London, United Kingdom*
[7] *LPC, IN2P3-CNRS et Université de Caen, 14032 Caen, France*
[8] *MHC, South Hadley, Massachusetts 01075, United States*
[9] *SAGA University, Saga, Saga 840-8502, Japan*
[10] *CFR, CNRS, 91190 Gif sur Yvette, France*
[11] *IEAP CTU, Prague, Czech Republic*
[12] *JYVÄSKYLÄ University, 40351 Jyväskylä, Finland*
[13] *Charles University, Prague, Czech Republic*
[14] *CENBG, IN2P3-CNRS et Université de Bordeaux, 33170 Gradignan, France*

Received August 2, 2004

Abstract—After analysis of 5797 h of data from the detector NEMO3, new limits on neutrinoless double beta decay of ^{100}Mo ($T_{1/2} > 3.1 \times 10^{23}$ y, 90% CL) and ^{82}Se ($T_{1/2} > 1.4 \times 10^{23}$ y, 90% CL) have been obtained. The corresponding limits on the effective majorana neutrino mass are: $\langle m_\nu \rangle < (0.8–1.2)$ eV and $\langle m_\nu \rangle < (1.5–3.1)$ eV, respectively. Also the limits on double-beta decay with Majoron emission are: $T_{1/2} > 1.4 \times 10^{22}$ y (90% CL) for ^{100}Mo and $T_{1/2} > 1.2 \times 10^{22}$ y (90% CL) for ^{82}Se. Corresponding bounds on the Majoron-neutrino coupling constant are $\langle g_{ee} \rangle < (0.5–0.9) \times 10^{-4}$ and $<(0.7–1.6) \times 10^{-4}$. Two-neutrino 2β-decay half-lives have been measured with a high accuracy, $T_{1/2}^{^{100}\mathrm{Mo}} = [7.68 \pm 0.02(\mathrm{stat}) \pm 0.54(\mathrm{syst})] \times 10^{18}$ y and $T_{1/2}^{^{82}\mathrm{Se}} = [10.3 \pm 0.3(\mathrm{stat}) \pm 0.7(\mathrm{syst})] \times 10^{19}$ y. © *2004 MAIK "Nauka/Interperiodica".*

PACS numbers: 14.80.Mz; 23.40.-s

Interest in neutrinoless double beta decay (2β0ν) has seen a significant rebirth in recent years after evidence for neutrino oscillations was obtained from the results of atmospheric [1] and solar [2–6] neutrino experiments (see, for example, the discussions in [7–9]).

This observation of oscillations was recently confirmed by the KamLAND experiment with reactor antineutrinos [10] and by the new SNO result [11]. These results are an impressive proof that neutrinos have a non-zero mass. However, the experiments studying neutrino oscillations are not sensitive to the nature of the neutrino mass (Dirac or Majorana?) and provide no information on the absolute scale of the neutrino masses, since such experiments are sensitive only to the difference, Δm^2. The detection and study of 2β0ν decay may clarify the following problems of neutrino physics (see discussions in [12–14]): (i) the neutrino's nature—is the neutrino a Dirac or a Majorana particle?; (ii) the absolute neutrino mass scale (a measurement or a limit on m_1); (iii) the type of neutrino mass hierarchy (normal, inverted, or quasidegenerate); and (iv) CP violation in the lepton sector (measurement of the Majorana CP-violating phases).

¶ This article was submitted by the authors in English.

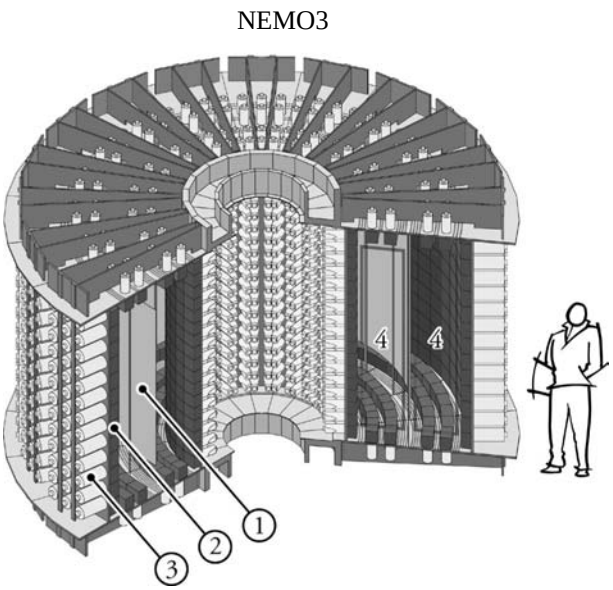

Fig. 1. The NEMO3 detector. 1—source foil; 2—plastic scintillator; 3—low radioactive PMT; 4—tracking chamber (6.180 octagonal Geiger cells).

The main goal of the NEMO3 experiment is to study neutrinoless double beta decay of different isotopes (^{100}Mo, ^{82}Se, etc.) with a sensitivity of up to ~10^{25} y, which corresponds to a sensitivity for the effective Majorana neutrino mass at the level of ~(0.1–0.3) eV [15]. The planned sensitivity for double beta decay with Majoron emission is ~10^{23} y (the sensitivity for the coupling constant of Majoron to neutrino $\langle g_{ee} \rangle$ is at the order of ~10^{-5}). In addition, one of the goals is a precise study of $2\beta2\nu$ decay for a number of nuclei (^{100}Mo, ^{82}Se, ^{116}Cd, ^{150}Nd, ^{130}Te, ^{96}Zr, and ^{48}Ca) with high statistics and to study all the major characteristics of the decay.

NEMO3 is a tracking detector, which in contrast to ^{76}Ge experiments [16, 17], detects not only the total energy deposition, but also other important parameters of the process. These include the energy of individual electrons, their angular distribution, the event vertex coordinates in the source plane, etc. This provides a unique opportunity to monitor and reject backgrounds. Since June of 2002, NEMO3 has been running in the Frejus Underground Laboratory (France), located at a depth of 4800 m.w.e.

The detector has a cylindrical shape and consists of 20 identical sectors (see Fig. 1). A thin (~30–60 mg/cm^2) source is placed in the center of the detector, which contains 2β-decaying nuclei and has a total area of 20 m^2 and a mass of about 10 kg. In particular, it includes 7.1 kg of enriched Mo (average enrichment is 98%; the total mass of ^{100}Mo is 6.914 kg) and 0.962 kg of Se (enrichment is 97%; the total mass of ^{82}Se is 0.932 kg). To investigate the external background, part of the source is made of very pure natural materials (TeO_2—0.767 kg and Cu—0.621 kg). The level of contamination of the source with radioactive impurities was obtained from measurements using low-background HPGe-detectors.

The basic detection principles of NEMO3 are the following. The energy of the electrons is measured with plastic scintillators coupled to PMTs (1940 individual counters), while the tracks are reconstructed from information obtained with drift Geiger cells (6180 cells). The tracking volume of the detector is filled with a mixture of ~95% He, 4% alcohol, 1% Ar, and 0.15% water at 20 mbar above atmospheric pressure. In addition, a magnetic field of 25 Gauss parallel to the detector's axis is created by a solenoid surrounding the detector. The magnetic field is used to identify electron–positron pairs to suppress the background associated with these events.

The main characteristics of the detector's performance are the following. The energy resolution of the scintillation counters lies in the interval of 14–17% (FWHM for 1 MeV electrons). The time resolution is 250 ps for an electron energy of 1 MeV. The reconstruction accuracy of a two-electron (2e) vertex is around 1 cm. The characteristics of the detector are studied in special calibration runs with radioactive sources. The energy calibration is carried out using ^{207}Bi with conversion electrons at energies 0.482 and 0.976 MeV, and ^{90}Sr with the end-point of the β spectrum at 2.283 MeV. The vertex reconstruction accuracy for $2e^-$ events was determined in measurements with ^{207}Bi. The time-of-flight properties were determined via measurements with ^{60}Co, in which two γ-quanta are emitted simultaneously, and ^{207}Bi, for which two electrons are emitted simultaneously, and neutron sources that provide high energy electrons crossing the detector.

The detector is surrounded by a passive shield made of 20 cm of steel, 30 cm of water contained in tanks covering the vertical exterior of the detector and wood and paraffin on the top and bottom. The level of radioactive impurities in the construction materials of the detector and the passive shield was tested with low-background HPGe detectors.

From June to December of 2002, a number of calibration and test measurements were carried out, as were the first data taken for double beta decay studies. Since February 14, 2003, the detector has been routinely taking double beta decay data. Calibrations with the radioactive sources are carried out every 1.5 months. Calorimeter stability is checked daily using a laser system between calibrations. A detailed description of the detector and its characteristics is presented in [18].

In this paper, we present the results for ^{100}Mo and ^{82}Se. Only part (5797 h of measurement) of the available data has been analyzed.

DOUBLE BETA DECAY OF ^{100}MO

2e-events with a common vertex at the source have been selected. For 2e-events, an electron was defined as a track between the source foil and a fired scintillation counter with the energy deposited being greater than 200 keV. The track curvature must be consistent with a negatively charged particle. The time-of-flight measurement should be consistent with the hypothesis of two electrons leaving the source from a common vertex simultaneously. In order to suppress the ^{214}Bi background, which is followed by a ^{214}Po α-decay, it is required that there be no delayed Geiger cell hits close to the event vertex or the electron track (within a delay of up to 700 μs). A typical 2e-event is shown in Fig. 2.

Figure 3 shows the 2β2ν energy spectrum for ^{100}Mo. The total number of useful events (after background subtraction) is ~141000. The signal-to-background ratio is 40/1, while it is 100/1 for energies above 1 MeV. This means that the background is negligible. The detection efficiencies, which included the selection cuts, were estimated by Monte Carlo (MC) simulations. This was done for two models of ^{100}Mo decay. The first one is the higher state dominance (HSD) mechanism, and the second is the single state dominance (SSD) mechanism (see [19]). For the SSD mechanism, it is assumed that the decay goes via the lowest 1^+ state of ^{100}Tc [20]. The detection efficiencies calculated by MC simulations were 5.68% for the SSD mechanism and 6.33% for the HSD mechanism. Correspondingly, the following results were obtained for the ^{100}Mo half-life:

$$T_{1/2} = [7.68 \pm 0.02(\text{stat}) \pm 0.54(\text{syst})] \times 10^{18} y \text{ (SSD)},$$

$$T_{1/2} = [8.57 \pm 0.02(\text{stat}) \pm 0.6(\text{syst})] \times 10^{18} y \text{ (HSD)}.$$

Preliminary analysis of the experimental single electron energy spectrum favors the SSD hypothesis. However, at the moment this question remains open and requires further studies. Both values are in agreement with the world mean value from other experiments: $(8 \pm 0.7) \times 10^{18}$ y [21, 22].

2β0ν-Decay

The energy range 2.65–3.2 MeV has been investigated. The information about the electron's energies and their angular distribution in 2e-events can be used to improve the selection of candidate events and, thus, improve the NEMO3 sensitivity [23]. Introducing a higher threshold of 900 keV for each electron, one gets 13 candidate events in this energy window. This is in agreement with our expectations from the background (18.8 events), coming mainly from ^{222}Rn (13 events), plus the 2β2ν contribution (5.8 events). The calculated 2β0ν efficiency is 8.2%. As a result, a limit has been set at $T_{1/2} > 3.1 \times 10^{23}$ y (90% CL), which is better than the best previous measurement ($T_{1/2} > 5.5 \times 10^{22}$ y [24]). Using the nuclear matrix elements (NMEs) from [25–27], the following range of limits on the neutrino mass has been derived: $\langle m_\nu \rangle < (0.8–1.2)$ eV. This range can be compared with that of the ^{76}Ge experiment [16] (using the same NMEs [25–27]), $\langle m_\nu \rangle < (0.33–0.84)$ eV.

For neutrinoless double beta decay caused by the right current admixture (λ term) in weak interactions, a 2.8–3.2 MeV energy window was used. An additional

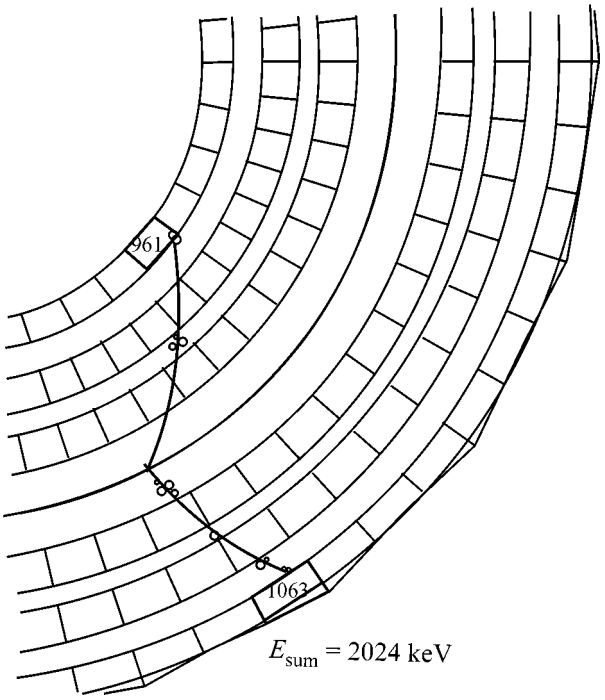

Fig. 2. A view of a reconstructed 2e-event in NEMO3. The sum energy of the electrons is 2024 keV; the energies of the electrons in the pair are 961 keV and 1063 keV.

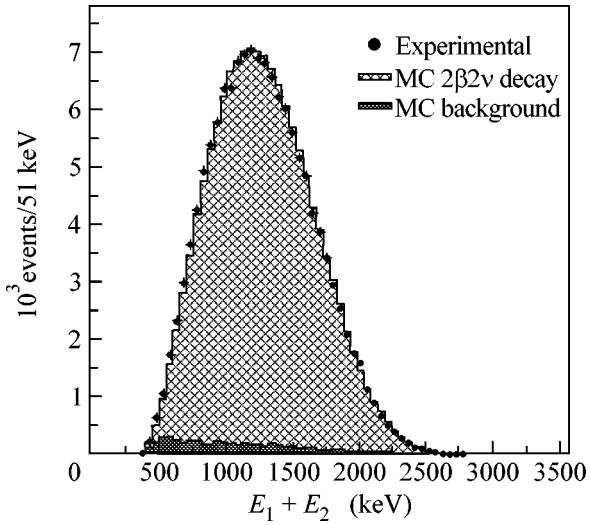

Fig. 3. 2β2ν spectrum of ^{100}Mo, background subtracted.

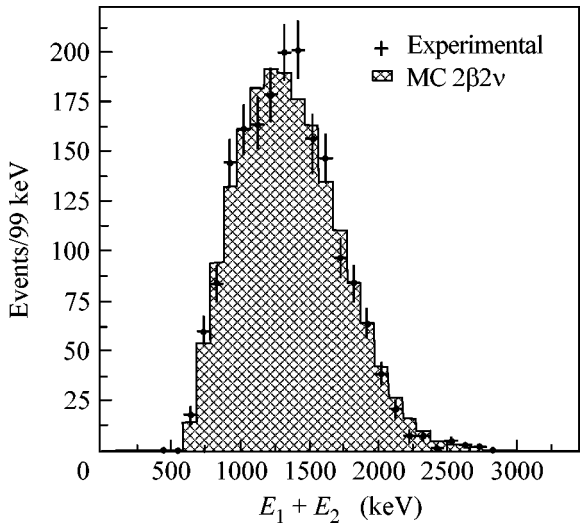

Fig. 4. 2β2ν spectrum of ^{82}Se, background subtracted.

cut on the electron energies, $|E_1 - E_2| > 800$ keV [23], allows an extra background suppression. In this case, there are only three candidate events in the 2.8–3.2 MeV window, with 2.8 (2.0 + 0.8) expected. With an efficiency of 4.2%, this gives $T_{1/2} > 1.8 \times 10^{23}$ y (90% CL) and $\langle\lambda\rangle < (1.5–2.0) \times 10^{-6}$, using the NMEs from [28].

2β0νχ-Decay

The energy interval 2.65–3.2 MeV has been studied. Introducing a threshold of 750 keV for each electron, one gets only 18 events (13.7 + 8 are expected with an efficiency of 0.49%) and the half-life limit yields $T_{1/2} > 1.4 \times 10^{22}$ y (90% CL). This value is better than the previous one ($T_{1/2} > 5.8 \times 10^{21}$ y [29]), and the corresponding limit on the Majoron-neutrino coupling constant (NMEs from [25–27]) is $\langle g_{ee}\rangle < (0.5–0.9) \times 10^{-4}$. This is one of the best limits for the majoron coupling constant.

DOUBLE BETA DECAY OF ^{82}Se

The energy spectrum of 2β2ν-events for ^{82}Se is shown in Fig. 4. A higher threshold of 300 keV was used in order to improve the signal-to-background ratio. The total number of useful events after the background subtraction is ~1800. The signal-to-background ratio is approximately 4 : 1. The detection efficiency has been calculated by MC calculations to be 6.02%. The ^{82}Se half-life value obtained is

$$T_{1/2} = [10.3 \pm 0.3(\text{stat}) \pm 0.7(\text{syst})] \times 10^{19} y.$$

This value is in agreement with our previous measurement with NEMO2 [30] and with the world average value of $(9 \pm 1) \times 10^{19}$ y [22].

2β0ν-Decay

Three events have been detected in the interval 2.65–3.2 MeV. The expected background in this energy windows is 5.3 events. Again, this background is mainly due to ^{222}Rn. An efficiency of 15.8% gives a limit for the ^{82}Se 0ν-decay of $T_{1/2} > 1.4 \times 10^{23}$ y (90% CL), which is better than the previous value by one order of magnitude ($T_{1/2} > 1.4 \times 10^{22}$ y at 90% CL [31]). The corresponding limit on the effective neutrino mass, using NMEs from [25–27], is $m_\nu < (1.5–3.1)$ eV.

For neutrinoless double beta decay caused by the right current admixture (λ term) in weak interactions, the 2.65–3.2 MeV energy window was used and a cut on the electron energy, $|E_1 - E_2| > 800$ keV [23] was applied. The number of events is zero, and the efficiency is 8.5%. This gives $T_{1/2} > 1.1 \times 10^{23}$ y (90% CL) and $\langle\lambda\rangle < (3.2–3.8) \times 10^{-6}$, using the NMEs from [32, 33].

2β0νχ-Decay

The energy interval 2.3–3.2 MeV was studied. The number of selected events is 39, while 40 is the estimated background. Using an efficiency estimated by MC calculations (4.2%), the following limit was obtained, $T_{1/2} > 1.2 \times 10^{22}$ y (90% CL). This is better than the previous best limit ($T_{1/2} > 2.4 \times 10^{21}$ y [30]). Using this result and NMEs from [25–27], one gets the corresponding limit for the Majoron-neutrino coupling constant $\langle g_{ee}\rangle < (0.7–1.6) \times 10^{-4}$.

At present, the NEMO3 tracking detector is continuing to collect data. At the same time, work is in progress to improve the detector's performance, background conditions and data analysis techniques. In particular, a radon barrier tent has been installed, and a radon-trapping factory will be in operation in the autumn of 2004, which will help reduce the ^{222}Rn background by a factor of 10–100. It is believed that the sensitivity of the experiment can be increased significantly in the near future.

ACKNOWLEDGMENTS

The authors would like to thank the Modane Underground Laboratory staff for their technical assistance in running the experiment. Portions of this work were supported by a grant from INTAS (no. 03051-3431) and a NATO grant (PST.CLG.980022).

REFERENCES

1. H. Sobel *et al.*, Nucl. Phys. B, Proc. Suppl. **91**, 127 (2001).
2. B. T. Cleveland, T. Daily, R. Davis, *et al.*, Astrophys. J. **496**, 505 (1998).
3. S. Fukuda, Y. Fukuda, M. Ishitsuka, *et al.*, Phys. Rev. Lett. **86**, 5651 (2001); Phys. Rev. Lett. **86**, 5656 (2001).

4. V. N. Gavrin *et al.*, Nucl. Phys. B, Proc. Suppl. **91**, 36 (2001).
5. M. Altman, M. Balata, P. Belli, *et al.*, Phys. Lett. B **490**, 16 (2000).
6. Q. R. Ahmad, R. C. Allen, T. C. Anderson, *et al.*, Phys. Rev. Lett. **89**, 011301 (2002); Phys. Rev. Lett. **89**, 011302 (2002).
7. P. C. de Holanda and A. Yu. Smirnov, Phys. Rev. D **66**, 113005 (2002).
8. J. N. Bahcall, M. C. Gonzalez-Garcia, and C. Pena-Garay, J. High Energy Phys. **0207**, 054 (2002); hep-ph/0204314.
9. M. Maltoni, T. Schwetz, M. A. Tortola, and J. W. F. Valle, Phys. Rev. D **67**, 013011 (2003); hep-ph/0207227.
10. K. Eguchi, S. Enomoto, K. Furuno, *et al.*, Phys. Rev. Lett. **90**, 021802 (2003).
11. S. N. Ahmed, A. E. Anthony, E. W. Beier, *et al.*, Phys. Rev. Lett. **92**, 181301 (2004).
12. S. M. Bilenky, hep-ph/0403245.
13. S. Pascoli, S. T. Petcov, and W. Rodejohann, Phys. Lett. B **558**, 141 (2003).
14. S. Pascoli and S. T. Petcov, Phys. Lett. B **580**, 280 (2004).
15. NEMO3 Proposal, Preprint 94-29 (LAL Orsay, 1994).
16. H. V. Klapdor-Kleingrothaus, A. Dietz, L. Baudis, *et al.*, Eur. Phys. J. A **12**, 147 (2001).
17. C. E. Aalseth, F. T. Avignone, R. L. Brodzinski, *et al.*, Phys. Rev. D **65**, 092007 (2002).
18. R. Arnold, C. Augier, J. Baker, *et al.*, Preprint LAL 04-05 (2004); hep-ph/0402115.
19. F. Simkovic, P. Domin, and S. Semenov, J. Phys. G **27**, 2233 (2001).
20. J. Abad, A. Morales, R. Nunez-Lagos, and A. F. Pacheco, J. Phys. (Paris) **45**, 147 (1984); An. Fis., Ser. A **80**, 9 (1984).
21. V. D. Ashitkov, A. S. Barabash, S. G. Belogurov, *et al.*, JETP Lett. **74**, 529 (2001).
22. A. S. Barabash, Czech. J. Phys. **52**, 567 (2002).
23. R. Arnold, C. Augier, J. Baker, *et al.*, Nucl. Instrum. Methods Phys. Res. A **503**, 649 (2003).
24. H. Ejiri, K. Fushimi, K. Hayashi, *et al.*, Phys. Rev. C **63**, 065501 (2001).
25. F. Simkovic, G. Panis, J. D. Vergados, and A. Faessler, Phys. Rev. C **60**, 055502 (1999).
26. S. Stoica and H. V. Klapdor-Kleingrothaus, Nucl. Phys. A **694**, 269 (2001).
27. O. Civitarese and J. Suhonen, Nucl. Phys. A **729**, 867 (2003).
28. J. Suhonen and O. Civitarese, Phys. Rev. C **49**, 3055 (1994).
29. H. Ejiri *et al.*, Phys. Lett. B **531**, 190 (2002).
30. R. Arnold, C. Augier, J. Baker, *et al.*, Nucl. Phys. A **636**, 209 (1998).
31. S. R. Elliott, A. A. Hahn, M. K. Moe, *et al.*, Phys. Rev. C **46**, 1535 (1992).
32. T. Tomoda, Rep. Prog. Phys. **54**, 53 (1991).
33. J. Suhonen, S. B. Khadkikar, and A. Faessler, Nucl. Phys. A **535**, 509 (1991).

JETP Letters, Vol. 80, No. 6, 2004, pp. 382–385. Translated from Pis'ma v Zhurnal Éksperimental'noĭ i Teoreticheskoĭ Fiziki, Vol. 80, No. 6, 2004, pp. 434–438.

On e^+e^- Pair Production by Colliding Electromagnetic Pulses

N. B. Narozhny[1], S. S. Bulanov[2], V. D. Mur[1], and V. S. Popov[2]

[1] *Moscow Engineering Physics Institute (State University), Kashirskoe sh. 31, Moscow, 115409 Russia*
e-mail: narozhny@theor.mephi.ru

[2] *Institute of Theoretical and Experimental Physics, ul. Bol'shaya Cheremushkinskaya 25, Moscow, 117259 Russia*
e-mail: bulanov@heron.itep.ru

Received August 4, 2004

Electron–positron pair production from vacuum in an electromagnetic field created by two counterpropagating focused laser pulses interacting with each other is analyzed. The dependence of the number of produced pairs on the intensity of a laser pulse and the focusing parameter is studied with a realistic three-dimensional model of the electromagnetic field of the focused wave, which is an exact solution of the Maxwell equations. It has been shown that e^+e^- pair production can be experimentally observed when the intensity of each beam is $I \sim 10^{26}$ W/cm^2, which is two orders of magnitude lower than that for a single pulse. © *2004 MAIK "Nauka/Interperiodica".*

PACS numbers: 12.20.Ds

Electron–positron pair production from vacuum in a strong constant electric field has long been predicted [1, 2]. The imaginary part of the electromagnetic-field Lagrangian, $\mathrm{Im}\mathcal{L}$, that is associated with the interaction of the field with the vacuum of charged particles with spins 0 and 1/2 was obtained in an explicit form in [3]. A similar formula for the case of vector bosons was derived in [4]. For electric field strengths much lower than the critical value, the exact expressions for $\mathrm{Im}\mathcal{L}$ [3, 4] reduce to the formulas obtained in [1, 2]. Such a process of e^+e^- pair production was referred to as the Schwinger effect.

The probability of producing e^+e^- pairs from vacuum is determined by the critical electric field $\mathcal{E}_{\mathrm{cr}} = m^2c^3/e\hbar = 1.32 \times 10^{16}$ V/cm characteristic for QED. For such fields, an electron–positron pair gains an energy of about mc^2 at a distance of the Compton electron wavelength. However, such a strong constant field cannot be obtained experimentally. Therefore, many researchers focused on theoretical analysis of pair production in alternating electric fields [5–13], which can be obtained by means of lasers [14].

Due to recent advances in laser technology, laser intensities have increased by many orders of magnitude and reached ~10^{22} W/cm^2, which is still far from the critical intensity $I_{\mathrm{cr}} = \dfrac{c}{4\pi}\mathcal{E}_{\mathrm{cr}}^2 = 4.6 \times 10^{29}$ W/cm^2. Several ways of reaching $I \sim I_{\mathrm{cr}}$ have recently been proposed. One of them was demonstrated in the SLAC experiment devoted to investigation of nonlinear QED processes accompanying the interaction of high-energy electrons and photons with laser pulses. First, experiments on the nonlinear Compton scattering of 46.6 GeV electrons by a laser pulse with an intensity of 10^{18} W/cm^2 were carried out [15]. Then, the same group observed e^+e^- pair production when laser photons that were backscattered up to several GeVs by a 46.6-GeV electron beam interacted with a pulse of the second laser [16]. This experiment is the first laboratory evidence of inelastic light-by-light scattering involving only real photons. Another possibility of creating superstrong electromagnetic fields was indicated in [17]. In the scheme proposed there, strength $\mathcal{E}_{\mathrm{cr}}$ is reached due to nonlinear interaction between electromagnetic and Langmuir waves in a plasma. In this case, the pulse is squeezed, its frequency increases, and it is focused by the breaking Langmuir wave. Thus, detailed analysis of the Schwinger effect in time-dependent electromagnetic fields, including the field of focused pulses, becomes urgent for experiments.

As is known [3], a plane electromagnetic wave of arbitrary intensity and spectral composition does not create e^+e^- pairs from vacuum, because both invariants of the electromagnetic field, $\mathcal{F} = (\mathbf{E}^2 - \mathbf{H}^2)/2$ and $\mathcal{G} = (\mathbf{E} \cdot \mathbf{H})$, are equal to zero. In [18], the Schwinger effect was studied for a focused pulse described by a realistic three-dimensional field model proposed in [19]. In contrast to a spatially uniform, time-dependent electric field [5–13], this model is based on the exact solution of the Maxwell equations. In this work, we consider the Schwinger effect in the field of two coherent, counterpropagating, focused laser pulses, each of which is described by the model developed in [19]. The use of a superposition of two focused pulses enables one to detect e^+e^- pair production for intensities much lower than those for a single pulse [18]. We compare our results with the previous results obtained in [5–13] for

the model of a uniform field $\mathscr{E}(t)$ and determine the accuracy of this approximation.[1]

We use the method based on the fact that the characteristic length of the process is determined by the Compton wavelength $\lambda\!\!\!^{-}_c = \hbar/mc$, which is much smaller than the laser-radiation wavelength, i.e., $\lambda\!\!\!^{-}_c \ll \lambda$. In this case, the number of pairs produced at an arbitrary point per unit volume per unit time can be calculated by formulas from [1–3] for a constant uniform field. Then, the total number of produced particles is obtained as an integral over volume V and pulse duration τ:

$$N = \frac{e^2\mathscr{E}_{cr}^2}{4\pi^2\hbar^2 c}\int_V dV\int_0^\tau dt\epsilon\eta\coth\frac{\pi\eta}{\epsilon}\exp\left(-\frac{\pi}{\epsilon}\right). \quad (1)$$

Here, $\epsilon = \mathscr{E}/\mathscr{E}_{cr}$ and $\eta = \mathscr{H}/\mathscr{E}_{cr}$ are the reduced fields, where the invariants $\mathscr{E}$ and $\mathscr{H}$ are equal to the electric and magnetic field strengths, respectively, in the reference frame where they are parallel to each other:

$$\mathscr{E} = \sqrt{(\mathscr{F}^2+\mathscr{G}^2)^{1/2}+\mathscr{F}}, \quad \mathscr{H} = \sqrt{(\mathscr{F}^2+\mathscr{G}^2)^{1/2}-\mathscr{F}}. \quad (2)$$

It is well known that the electromagnetic field of a focused light beam is not transverse and, therefore, cannot be assigned a certain polarization type. However, the focused-beam field is always representable as a superposition of electromagnetic fields with a transverse, only electric or magnetic, vector [20], and polarization for the transverse vector can be defined for each of these fields. Such fields are called *e* and *h* polarized, respectively. In this work, we consider only *e*-type fields.

As was shown in [19], there is an exact solution of Maxwell equations in vacuum that describes a wave propagating along the *z* axis:

$$\mathbf{E}^e = iE_0e^{-i\varphi}\{F_1(\mathbf{e}_x \pm i\mathbf{e}_y) - F_2e^{\pm 2i\phi}(\mathbf{e}_x \mp i\mathbf{e}_y)\}, \quad (3)$$

$$\mathbf{H}^e = \pm E_0e^{-i\varphi}\left\{\left(1 - i\Delta^2\frac{\partial}{\partial\chi}\right)[F_1(\mathbf{e}_x \pm i\mathbf{e}_y) + F_2e^{\pm 2i\phi}(\mathbf{e}_x \mp i\mathbf{e}_y)] + 2i\Delta e^{\pm i\phi}\frac{\partial F_1}{\partial\xi}\mathbf{e}_z\right\}. \quad (4)$$

Here, ω is the frequency; *x*, *y*, and *z* are the spatial coordinates; and

$$\varphi = \omega(t - z/c), \quad \xi = \rho/R, \quad \chi = z/L,$$
$$\rho = \sqrt{x^2+y^2}, \quad \exp(i\phi) = (x+iy)/\rho, \quad (5)$$
$$\Delta \equiv c/\omega R = \lambda/2\pi R, \quad L \equiv R/\Delta.$$

[1] Such a field is approximately realized near the antinodes of a standing light wave arising as a superposition of two laser beams.

Fields (3) and (4) describe a focused laser beam [19], where *R* can be treated as the radius of the focal spot, *L* is the diffraction length, and Δ is the focusing parameter. It is worth noting that $\Delta \sim 0.1$ even if the laser beam is focused such that $R \sim \lambda$ (diffraction limit). For this reason, we assume that $\Delta \ll 1$. Under this condition, a solution describing Gaussian beams has the form

$$F_1 = (1+2i\chi)^{-2}\left(1 - \frac{\xi^2}{1+2i\chi}\right)\exp\left(-\frac{\xi^2}{1+2i\chi}\right),$$
$$F_2 = -\xi^2(1+2i\chi)^{-3}\exp\left(-\frac{\xi^2}{1+2i\chi}\right). \quad (6)$$

To describe a laser pulse of finite duration τ, it is necessary to introduce the time envelope $g(\varphi/\omega\tau)$ by the following change in Eqs. (3) and (4):

$$\exp(-i\varphi) \longrightarrow if'(\varphi), \quad \exp(-i\varphi)\Delta \longrightarrow f(\varphi)\Delta, \quad (7)$$

where $f(\varphi) = g(\varphi/\omega\tau)\exp(-i\varphi)$ [19]. It is assumed that $g(0) = 1$ and g decreases exponentially at the periphery of the pulse for $|\varphi| \gg \omega\tau$. Then, according to [19], we take $g(t/\tau) = \exp(-4t^2/\tau^2)$ in the focal plane $z = 0$ and set $\tau = 10$ fs. In this case, the electric and magnetic fields of this model are an approximate solution of the Maxwell equations up to the second-order terms in the parameters Δ and $1/\omega\tau$.

To obtain expressions describing the electric and magnetic fields of a pulse propagating in the negative *z* direction, it is necessary to change $z \longrightarrow -z$ and $H \longrightarrow -H$ in Eqs. (3) and (4). For functions F_1 and F_2, this means a change to the complex conjugated functions F_1^* and F_2^*. The electromagnetic field arising as a superposition of the fields of two counterpropagating pulses is described by the expressions

$$\mathbf{E} = 2iE_0e^{-i\omega t}[\mathrm{Re}(F_1e^{i\omega z/c})(\mathbf{e}_x \pm i\mathbf{e}_y) - \mathrm{Re}(F_2e^{\pm 2i\phi}e^{i\omega z/c})(\mathbf{e}_x \mp i\mathbf{e}_y)], \quad (8)$$

$$\mathbf{H} = \pm 2iE_0e^{-i\omega t} \times\left[\mathrm{Im}(F_1e^{i\omega z/c})(\mathbf{e}_x \pm i\mathbf{e}_y) + \mathrm{Im}(F_2e^{\pm 2i\phi}e^{i\omega z/c}) \times(\mathbf{e}_x \mp i\mathbf{e}_y) + 2\Delta\mathrm{Re}\left(e^{\pm i\phi}e^{i\omega z/c}\frac{\partial F_1}{\partial\xi}\right)\mathbf{e}_z\right]. \quad (9)$$

Formulas for the invariants $\mathscr{F}$ and $\mathscr{G}$ of the electromagnetic field are very unwieldy and are not presented. We only emphasize that (in contrast to the case of a single focused pulse) the invariants $\mathscr{F}$ and $\mathscr{G}$ are not proportional to the focusing parameter Δ and do not vanish when $\Delta \longrightarrow 0$.

We present calculations by formulas (1)–(9). Figure 1 shows the field $\mathscr{E}$ in the $z = 0$ plane for $t = 0$ for (a) a single wave and (b) superposition of two such waves.

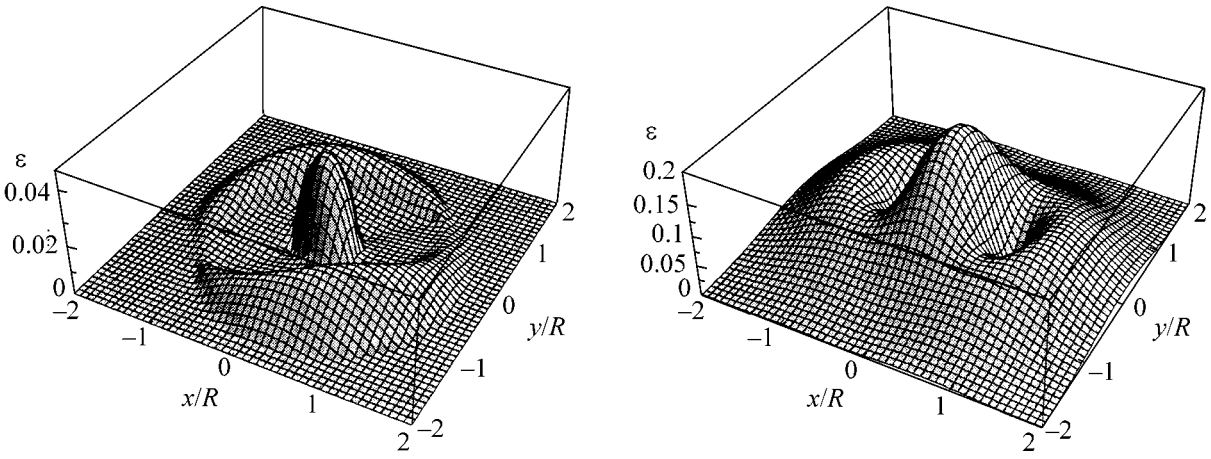

Fig. 1. Reduced field $\varepsilon = \mathscr{E}/\mathscr{E}_{cr}$ as a function of the spatial coordinates x and y at $t = 0$ for (a) a single e polarized wave and (b) counterpropagating beams. The parameters are $E_0 = 0.1\mathscr{E}_{cr}$, $z = 0$, and $\Delta = 0.1$.

The number of produced pairs as a function of the intensity of counterpropagating pulses for various Δ values is shown in Fig. 2a. It is seen that the number of pairs increases only slightly when Δ decreases, in contrast to the case of pair production by a single focused pulse [18]. This behavior is associated with the fact that the parameter Δ enters into the definition of the focused-pulse volume $V = \pi R^2 L \sim R^3/\Delta$. Therefore, a decrease in Δ leads to an increase in volume where pairs are produced. Figure 2b shows the number of produced pairs as a function of the parameter Δ for fixed beam intensity $I \sim 10^{26}$ W/cm^2.

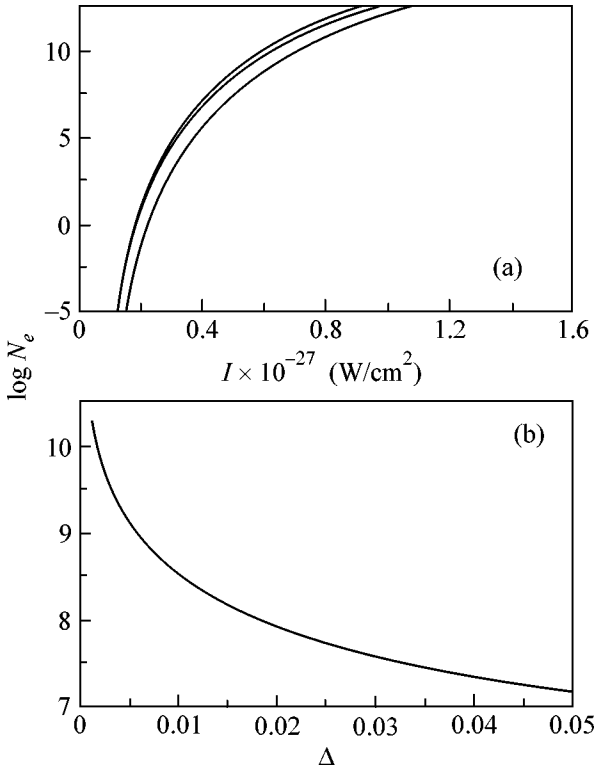

Fig. 2. Number N of e^+e^- pairs vs. the (a) intensity I of the counterpropagating beams for the focusing parameters $\Delta =$ (from bottom to top) 0.1, 0.075, and 0.05 and (b) parameter Δ for $I = 10^{26}$ W/cm^2. Calculations for pulse duration $\tau =$ 10 fs.

Thus, the effect of the pulse focusing degree on the pair production process is much weaker than that for a single focused pulse, where the number of pairs decreases rapidly when Δ decreases for fixed intensity [18]. Electron–positron pairs are produced primarily by the electric field arising in the antinodes of the standing wave. This makes it possible to compare our results with the results for the problem of pair production by a spatially uniform, time-dependent electric field [5–13].

Let us assume that the total magnetic field is equal to zero over the entire focusing region, i.e., $\mathbf{H} = 0$. Using the results of [5–13] at each space point, we obtain the number of particles as an integral over volume V and pulse duration τ. As was shown in [13, 21], the dynamic effects, i.e., the dependence of N on frequency ω, are manifested for wavelengths $\lambda < 10^{-8}$ cm, which are far from the region of available and designed laser systems. Therefore, disregarding the time dependence of the electric field, we obtain

$$N = \int_V dV \int_0^\tau d\tau \frac{c}{4\pi^2 l_c^4} \varepsilon^2 \exp\left[-\frac{\pi}{\varepsilon}\right], \qquad (10)$$

which differs from Eq. (1) only in the absence of the magnetic field. Figure 3 shows the number of pairs calculated as a function of the intensity by formulas (1), (10), and for the spatially uniform field according to [5–13]. In these calculations, the electric field is assumed to have strength $2E_0$ over the entire focusing volume. This strength corresponds to the peak strength of the field arising as a superposition of two counterpropagat-

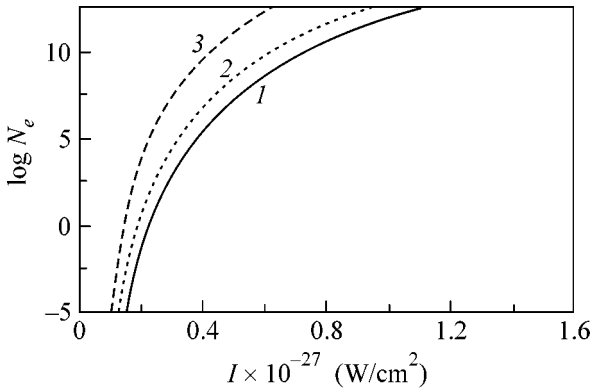

Fig. 3. Number N of pairs as a function of the intensity I for $\Delta = 0.1$. Lines *1*, *2*, and *3* correspond to formulas (1), (10), and uniform-field approximation, respectively.

ing beams. Thus, the approximation of a spatially uniform electric field provides an upper bound for the number of e^+e^- pairs. Making allowance for spatial inhomogeneity, i.e., the field structure near the focus (see Fig. 1), reduces the number of pairs. The magnetic field leads to a further decrease in the number of pairs, because it twists the subbarrier trajectory and increases the imaginary part of the action function. Thus, it is important to take into account both the spatial field structure and magnetic field effect in analysis of e^+e^- pair production by the electromagnetic field arising as a superposition of two counterpropagating laser pulses. The production of pairs can be detected for radiation intensity 10^{26} W/cm^2, which is two orders of magnitude less than that for a single focused pulse. We emphasize that the number of pairs increases only slightly when the parameter Δ decreases, and this behavior differs substantially from that obtained in [18].

This work was supported by the Russian Foundation for Basic Research (project nos. 03-02-17348 and 04-02-17157), the Ministry of Industry, Science, and Technology of the Russian Federation (Federal Program, project no. 40.052.1.1.1112), and the Ministry of Education of the Russian Federation (project no. 1618).

REFERENCES

1. F. Sauter, Z. Phys. **69**, 742 (1931); Z. Phys. **73**, 547 (1931).
2. W. Heisenberg and H. Euler, Z. Phys. **98**, 714 (1936).
3. J. Schwinger, Phys. Rev. **82**, 664 (1951).
4. V. S. Vanyashin and M. V. Terent'ev, Zh. Éksp. Teor. Fiz. **48**, 565 (1965) [Sov. Phys. JETP **21**, 375 (1965)].
5. E. Brezin and C. Itzykson, Phys. Rev. D **2**, 1191 (1970).
6. S. Popov, JETP Lett. **13**, 185 (1971); Sov. Phys. JETP **34**, 709 (1972).
7. V. S. Popov, JETP Lett. **18**, 255 (1973); Sov. J. Nucl. Phys. **19**, 584 (1974).
8. N. B. Narozhny and A. I. Nikishov, Sov. Phys. JETP **38**, 427 (1974).
9. V. M. Mostepanenko and V. M. Frolov, Sov. J. Nucl. Phys. **19**, 451 (1974).
10. M. S. Marinov and V. S. Popov, Fortschr. Phys. **25**, 373 (1977).
11. A. A. Grib, S. G. Mamaev, and V. M. Mostepanenko, *Vacuum Quantum Effects in Strong Fields* (Énergoatomizdat, Moscow, 1988) [in Russian].
12. A. Ringwald, Phys. Lett. B **510**, 107 (2001); hep-ph/0112254; hep-ph/0304139.
13. V. S. Popov, JETP Lett. **74**, 133 (2001); Phys. Lett. A **298**, 83 (2002); JETP **94**, 1057 (2002).
14. T. Tajima and G. Mourou, Phys. Rev. ST Accel. Beams **5**, 031301 (2002).
15. C. Bula, C. Bamber, D. L. Burke, *et al.*, Phys. Rev. Lett. **76**, 3116 (1996).
16. D. L. Burke, S. C. Berridge, C. Bula, *et al.*, Phys. Rev. Lett. **79**, 1626 (1997).
17. S. V. Bulanov, T. Zh. Esirkepov, and T. Tajima, Phys. Rev. Lett. **91**, 085001 (2003).
18. S. S. Bulanov, N. B. Narozhny, V. D. Mur, and V. S. Popov, Phys. Lett. A **330**, 1 (2004).
19. N. B. Narozhny and M. S. Fofanov, Zh. Éksp. Teor. Fiz. **117**, 867 (2000) [JETP **90**, 753 (2000)]; Phys. Lett. A **295**, 87 (2002).
20. M. Born and E. Wolf, *Principles of Optics*, 2nd ed. (Pergamon, New York, 1964; Nauka, Moscow, 1973).
21. S. S. Bulanov, Phys. Rev. E **69**, 036408 (2004).

Translated by R. Tyapaev

JETP Letters, Vol. 80, No. 6, 2004, pp. 386–388. From Pis'ma v Zhurnal Éksperimental'noĭ i Teoreticheskoĭ Fiziki, Vol. 80, No. 6, 2004, pp. 439–441.

Pentaquark Decay Is Suppressed by Chirality Conservation¶

B. L. Ioffe and A. G. Oganesian

Institute of Theoretical and Experimental Physics, Moscow, 117218 Russia

Received August 19, 2004

It is shown that, if the pentaquark $\Theta^+ = uudd\bar{s}$ baryon can be represented by the local quark current η_Θ, its decay $\Theta^+ \longrightarrow nK^+(pK^0)$ is forbidden in the limit of chirality conservation. The Θ^+ decay width Γ is proportional to $\alpha_s^2 \langle 0|\bar{q}q|0\rangle^2$, where $\langle 0|\bar{q}q|0\rangle$, $q = u, d, s$, is quark condensate, and, therefore, is strongly suppressed. The polarization operator of the pentaquark current is calculated using the operator product expansion. The Θ^+ mass found by the QCD sum rules method is in reasonable agreement with experiment. © *2004 MAIK "Nauka/Interperiodica".*

PACS numbers: 12.38.-t; 12.39.-x

Last year, the exotic baryon resonance Θ^+ with quark content $\Theta^+ = uudd\bar{s}$ and mass 1.54 GeV [1, 2] was discovered. Later, the existence of this resonance was confirmed by many groups, although some attempts to find it were unsuccessful (see [3] for a review). The Θ^+ baryon was predicted in 1997 by Diakonov, Petrov, and Polyakov [4] in the chiral soliton model as a member of an antidecouplet with hypercharge $Y = 2$. Recent theoretical reviews are given in [5, 6]. Θ^+ was observed as a resonance in the systems nK^+ and pK^0. No enhancement was found in pK^+ mass distributions, which indicates an isospin $T = 0$ of Θ^+, in accord with theoretical predictions [4].

One of the most interesting features of Θ^+ is its very narrow width. Experimentally, only an upper limit was found, and the stringer bound was presented in [2]: $\Gamma <$ 9 MeV. The phase analysis of *KN* scattering results in an even stronger limit on Γ [7], $\Gamma < 1$ MeV. A limitation close to the latter was found in [8] from the analysis of the $Kd \longrightarrow ppK$ reaction and in [9] from K + Xe collision data [2]. The chiral quark soliton model gives an estimation [4] of $\Gamma_{\mathrm{CQSM}} \lesssim 15$ MeV (Jaffe [10] claims that this estimation has a numerical error and, in fact, $\Gamma_{\mathrm{CQSM}} \lesssim 30$ MeV; see, however, [11]). In any case, the estimation [4] for Γ_{CQSM} follows from the cancellation of large and uncertain numbers and is not quite reliable. Therefore, until now, the narrow Θ^+ width has been a theoretical puzzle.

Here, we suggest a qualitative explanation for it. Suppose that Θ^+ may be represented by the local five-quark current η_Θ. An example of such a current is

$$\eta_\Theta(x) = [\varepsilon^{abc}(d^a C\sigma_{\mu\nu} d^b)\gamma_\nu u^c \bar{s}\gamma_\mu\gamma_5 u - (u \longleftrightarrow d)]/\sqrt{2}, \quad (1)$$

where a, b, and c are color indices; C is the charge conjugation matrix; and u, d, and s are quark fields. Suppose also that the amplitude of $\Theta^+ \longrightarrow nK^+$ decay is proportional to the vacuum average,

$$\mathcal{M} = \langle 0|T\{\eta_n(x), j_5^\lambda(y), \bar{\eta}_\Theta(0)\}|0\rangle \quad (2)$$

where $\eta_n(x)$ is the neutron quark current [12],

$$\eta_n = \varepsilon^{abc}(d^a C\gamma_\mu d^b)\gamma_5\gamma_\mu u^c \quad (3)$$

and $j_{\mu 5} = \bar{s}\gamma_\mu\gamma_5 u$ is the strange axial current. Let us neglect quark masses and perform the chiral transformation $q \longrightarrow \gamma_5 q$. It is evident that η_n and $j_{\mu 5}$ are even under such a transformation, while η_Θ is odd. Therefore, matrix element (2) vanishes in the limit of chiral symmetry. It is easy to see that this statement is valid for any form of pentaquark and nucleon quark currents (spinless and with no derivatives). In the real world, chiral symmetry is spontaneously broken. The lowest-dimension operator, corresponding to violation of chiral symmetry, is $\bar{q}q$. Thus, matrix element (2) is proportional to quark condensate $\langle 0|\bar{q}q|0\rangle$. Moreover, if Θ^+ is a genuine five-quark state (not, say, the *NK* bound state), then, in (2), hard gluon exchange is necessary, which leads to an additional factor of α_s. The necessity of having gluonic exchange in order to get a nonvanishing value of $\mathcal{M}$ is confirmed by direct calculation of $\mathcal{M}$ for any η_Θ by the QCD sum rules method for a three-point function suggested in [13]. We come to the conclusion that $\Gamma_\Theta \sim \alpha_s^2 \langle 0|\bar{q}q|0\rangle^2$, i.e., Γ_Θ is strongly suppressed. This conclusion takes place for any genuine five-quark states—the states formed from five current quarks at small separation—but not for potentially bounded *NK*-resonances, corresponding to large relative distances. There is no such suppression for the latter. In order to be confident that Θ^+ is described by the

¶ This article was submitted by the authors in English.

local five-quark current η_Θ (1), calculate in QCD the polarization operator,

$$\Pi(p) = i\int d^4x e^{ipx}\langle 0|T\eta_\Theta(x), \bar{\eta}_\Theta(0)|0\rangle \qquad (4)$$

and demonstrate that it may be represented by the contribution of Θ^+ and exited states (continuum). Consider $p^2 < 0$ and $|p^2|$ to be large enough, and use the operator product expansion (OPE) and QCD sum rule method for baryons [12]. The Lorenz structure of $\Pi(p)$ has the form

$$\Pi(p) = \hat{p}\Pi_1(p^2) + \Pi_2(p^2), \qquad (5)$$

$\Pi_1(p^2)$ is calculated with the account of operators up to dimension 12, and $\Pi_2(p^2)$ up to dimension 13. The masses of *u* and *d* quarks are neglected, and the *s*-quark mass m_s is accounted for in the first order. A factorization hypothesis is assumed for operators of higher dimensions, and operators of anomalous dimensions are neglected, as well as α_s corrections. On the other side, represent $\Pi(p)$ in terms of physical state contributions, Θ^+ and continuum, starting from some $(p^2)_0 \equiv s_0$. After Borel transformation, the sum rules are given by

$$\frac{3M^{12}}{560}\left\{\frac{7}{6}E_5 + \left(\frac{7}{18}b - \frac{28}{3}m_s a\right)\frac{E_3}{M^4} - \frac{35}{18}\left[(5+8\gamma)a^2 - \frac{31}{4}m_s m_0^2 a\right]\frac{E_2}{M^6} + \frac{35}{6}\left(\frac{5}{2}+\frac{13}{3}\gamma\right)m_0^2 a^2\frac{E_1}{M^8} + \left[\frac{560}{9}m_s a^3 - \frac{175}{48}(1+2\gamma)m_0^4 a^2 - \frac{35}{54}\left(19\gamma - \frac{3}{8}\right)ba^2\right]\times\frac{E_0}{M^{10}} + \frac{700}{27}(1.6\gamma - 0.2)\frac{a^4}{M^{12}}\right\} = \bar{\lambda}^2 e^{-m^2/M^2},$$

$$\frac{M^{10}}{32}a\left\{\frac{m_s}{10}M^2E_5 - \frac{1}{5}(8-\gamma)E_4 + \frac{1}{12}(29-3\gamma)m_0^2\frac{E_3}{M^2} - \left[\left(\frac{9}{4}-\frac{17}{36}\gamma\right)b - 4m_s a\right]\frac{E_2}{M^4} + \left[8\left(\frac{4}{3}+\frac{1}{2}\gamma\right)a^2 - \frac{41}{6}m_s m_0^2 a\right]\frac{E_1}{M^6} - \left(14+\frac{13}{3}\gamma\right)m_0^2 a^2\frac{E_0}{M^8} + \left[\left(3+\frac{131}{288}+\frac{37}{54}\gamma\right)m_0^4 a^2 - \frac{112}{9}m_s a^3\right]\frac{1}{M^{10}}\right\} = \bar{\lambda}^2 m e^{-m^2/M^2}, \qquad (6)$$

$$(7)$$

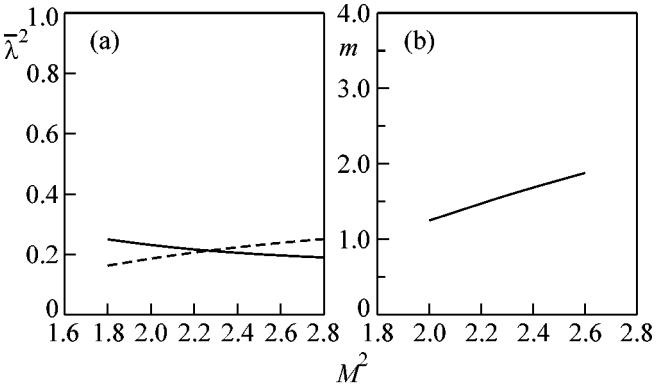

Fig. 1. The M^2 dependence of sum rules (6), (7): (a) $\bar{\lambda}^2$ from Eq. (6) (solid line), $\bar{\lambda}^2$ from Eq. (7) (dashed line); (b) *m* obtained as a ratio of (7) to (6).

where *m* is the Θ^+-mass, *M* is the Borel parameter (*q* = *u*, *d*),

$$a = -(2\pi)^2\langle 0|\bar{q}q|0\rangle, \quad \gamma = \langle 0|\bar{s}s|0\rangle/\langle 0|\bar{q}q|0\rangle,$$

$$b = (2\pi)^2\langle 0|\frac{\alpha_s}{\pi}G^2|0\rangle, \qquad (8)$$

$$g\langle 0|\bar{q}\sigma_{\mu\nu}(\lambda^n/2)G^n_{\mu\nu}q|0\rangle \equiv m_0^2\langle 0|\bar{q}q|0\rangle,$$

and the sign of *g* is defined by the form of the covariant derivative $\nabla_\mu = \partial_\mu - ig(\lambda^n/2)A^n_\mu$. $\bar{\lambda}$ is given by the matrix element

$$\langle 0|\eta_\Theta|\Theta^+\rangle = \lambda\upsilon_\Theta, \qquad (9)$$

where υ_Θ is Θ^+ spinor, and $\bar{\lambda}^2 = (2\pi)^8\lambda^2$. Continuum contributions are transferred to the left-hand side of the sum rules, resulting in the appearance of the factors

$$E_n\left(\frac{s_0}{M^2}\right) = \frac{1}{n!}\int_0^{s_0/M^2} dz z^n e^{-z}. \qquad (10)$$

The values of $\bar{\lambda}$, determined from Eqs. (6) and (7), are plotted in Fig. 1 (Fig. 1a; for *m*, the experimental value of $m_\Theta = 1.54$ GeV was put in), and the value of *m* obtained as a ratio of (7) to (6). The parameters were taken in accord with the recent determination of QCD condensates [14, 15] at the normalization point $\mu^2 = 2$ GeV^2: $a = 0.63$ GeV^3, $b = 0.24$ GeV^4, $m_0^2 = 1$ GeV^2, $m_s = 0.15$ GeV, and $\gamma = 0.8$. It was chosen that $s_0 = 4.5$ GeV^2. As is seen from Fig. 1a, the values of $\bar{\lambda}^2$ obtained from (6) and (7) weakly depend on M^2 and coincide with one another in the interval $2.0 < M^2 < 2.6$ GeV^2. The value of m_Θ may be estimated as $m_\Theta = 1.6 \pm 0.2$ GeV. The positivity of the left-hand side of (7)

clearly shows that the parity of Θ^+ is positive. The result only slightly varies at the variation of s_0 within 10–15%.

A few remarks are in order. The first term in (1) contains two left $d_L d_L$ or two right $d_R d_R$ quark components, while neutron current η_n (3) is proportional to $d_L d_R$ (see [12], Eq. (61)). Therefore, in the chiral limit, two-hadron reducible contributions [16] are absent in the case of the η_Θ current (1). The same conclusion follows from the opposite chiralities of currents η_Θ and η_n. The inspection of the sum rules shows that the main contributions arise from operators of high dimensions ($d = 6$, 8 in (6) and $d = 5$, 9, 11 in (7)), unlike in the case of normal hadrons, where low-dimension operators are dominant. This means that pentaquark indeed differs very much from usual hadrons. There is a remarkable cancellation in (6) and (7) among the contributions of various operators. Therefore, the results are sensitive to unaccounted corrections (violation of factorization, α_s corrections, etc.). Thus, a less-than-perfect fulfillment of the sum rules is not surprising.

The QCD sum rule calculations of pentaquark masses with local η_Θ were performed in [17–19]. Unfortunately, unsuitable chirally nonvariant five-quark currents were chosen, and the results change drastically after subtraction of two-hadron reducible contributions [16]. Moreover, in [17], only one structure was considered and important terms of OPE were omitted.

The consideration of $\eta_\Theta^{T=1}$ current, corresponding to isospin $T = 1$, shows that sum rule (7) is essentially smaller than (6). Thus, in case of $T = 1$, there is no resonance structure at masses of 1.5–2.0 GeV, only a background more-or-less equally populated by the states of positive and negative parities (at the total angular momentum $j = 1/2$).

One of the authors (A. Oganesian) is indebted to K. Goeke and to M. Polyakov for their hospitality and for useful discussions.

This work was supported in part by INTAS (grant no. 2000-587), by the Russian Foundation for Basic Research (grant no. 03-02-16209), and by funds given by the EC to the project “Study of Strongly Interacting Matter” (under contract 2004 no. R113-CT-2004-506078).

REFERENCES

1. T. Nakano, D. S. Ahn, J. K. Ahn, *et al.*, Phys. Rev. Lett. **91**, 012002 (2003).
2. V. V. Barmin, V. S. Borisov, A. G. Dolgolenko, *et al.*, Yad. Fiz. **66**, 1763 (2003) [Phys. At. Nucl. **66**, 1715 (2003)].
3. K. Hicks, hep-ph/0408001.
4. D. Diakonov, V. Petrov, and M. Polyakov, Z. Phys. A **359**, 305 (1997).
5. D. Diakonov, hep-ph/0406043.
6. V. B. Kopeliovich, Usp. Fiz. Nauk **174**, 323 (2004) [Phys. Usp. **47**, 309 (2004)].
7. R. A. Arndt, I. I. Strakovsky, and R. L. Workman, nucl-th/0311030.
8. A. Sibirtsev, J. Heidenbauer, S. Krewald, and Ulf-G. Meissner, hep-ph/0405099.
9. A. Sibirtsev, J. Heidenbauer, S. Krewald, and Ulf-G. Meissner, nucl-th/0407011.
10. R. Jaffe, hep-ph/0401187; hep-ph/0405268.
11. D. Diakonov, V. Petrov, and M. Polyakov, hep-ph/0404212.
12. B. L. Ioffe, Nucl. Phys. B **188**, 317 (1981).
13. B. L. Ioffe and A. V. Smilga, Nucl. Phys. B **216**, 373 (1983).
14. B. L. Ioffe and K. N. Zyablyuk, Nucl. Phys. A **687**, 437 (2001).
15. B. V. Geshkenbein, B. L. Ioffe, and K. N. Zyablyuk, Phys. Rev. D **64**, 093009 (2001).
16. Y. Kondo, O. Marimatsu, and T. Nishikawa, hep-ph/0404285.
17. Shi-Lin Zhu, Phys. Rev. Lett. **91**, 232 002 (2003).
18. R. D. Matheus, F. S. Navarra, M. Nielsen, *et al.*, Phys. Lett. B **578**, 323 (2004).
19. J. J. Sugiyama, T. Doi, and M. Oka, Phys. Lett. B **581**, 167 (2004).

JETP Letters, Vol. 80, No. 6, 2004, pp. 389–392. Translated from Pis'ma v Zhurnal Éksperimental'noĭ i Teoreticheskoĭ Fiziki, Vol. 80, No. 6, 2004, pp. 442–446.

Reduced Quantum Noise in Waveguide Coherent Raman Scattering Spectroscopy

A. M. Zheltikov

Physics Department, International Laser Center, Moscow State University, Vorob'evy gory, Moscow, 119992 Russia

e-mail: zheltikov@top.phys.msu.su

Received August 3, 2004

Waveguide regimes of nonlinear-optical interactions allow a reduction of quantum noise in spectra of coherent Raman scattering (CRS). We will find the optimal waveguide length providing the maximum quantum limit for the signal-to-noise ratio in waveguide CRS and assess this ratio for laser intensities right below the optical breakdown threshold. This analysis shows that the quantum-limit signal-to-noise ratio of coherent femtosecond CRS spectroscopy of the gas phase can be increased in the waveguide regime by more than four orders of magnitude relative to the regime of tight focusing. © *2004 MAIK "Nauka/Interperiodica".*

PACS numbers: 42.65.Dr; 61.46.+w

Coherent Raman scattering (CRS) [1, 2] is one of the most efficient and informative methods of nonlinear spectroscopy. This technique provides a high spatial, temporal, and spectral resolution [3, 4], offering a powerful tool for studying excited gas media, plasmas, flames, and combustion [5, 6]. Methods of CRS are also widely employed for the investigation of femtosecond dynamics and control of vibrational wave packets in molecular systems [7], as well as coherent microscopy of biological objects [8]. Recent years have witnessed a rapid growth of new applications of femtosecond CRS, such as three-dimensional microscopy of coherent anti-Stokes Raman scattering (CARS) [8] and coherence-controlled CARS [9].

Waveguide CRS regimes [10–14] suggest the ways to radically improve the sensitivity and expand the applicability area of CRS spectroscopy. In particular, CRS spectroscopy in planar film waveguides can provide a level of sensitivity sufficient for measuring CARS spectra from molecular monolayers [11, 12]. The sensitivity of CARS spectroscopy in the gas phase has been improved by using hollow waveguides [13, 15, 16], including hollow photonic-crystal fibers [17].

Quantum and classical noise sources set fundamental limitations on the sensitivity of CRS spectroscopy [1, 2]. In this work, we will show that waveguide regimes of nonlinear-optical interactions allow a reduction of quantum noise in CRS spectra. It will be demonstrated that the quantum limit for the signal-to-noise ratio of coherent femtosecond CRS spectroscopy of the gas phase can be increased in the waveguide regime by more than four orders of magnitude with respect to the regime of tight focusing.

Noise in CRS spectra can be induced by classical and quantum mechanisms. Fluctuation of pump field intensities is the main source of classical noise in CRS spectroscopy. The classical limit of the signal-to-noise ratio is controlled under these conditions by root-mean-square deviations of pump powers and the ratio of the resonant and nonresonant parts of the relevant nonlinear-optical susceptibility. The root-mean-square deviation of the photodetector current due to pump power fluctuations is written as [1, 2]

$$\langle \delta_c^2 \rangle = \varepsilon i_d^2 \rangle, \tag{1}$$

where the angular brackets stand for averaging in time, ε is the total root-mean-square deviation of the pump powers (in two-color CRS $\omega_{CRS} = 2\omega_1 - \omega_2$ with pump field frequencies ω_1 and ω_2, we have $\varepsilon = 4\varepsilon_1 + \varepsilon_2$, where ε_1 and ε_2 are the root-mean-square power deviations of the pump fields with the frequencies ω_1 and ω_2, respectively), and

$$i_d = \frac{\eta e}{\hbar \omega_{CRS}} P_{CRS} \tag{2}$$

is the photodetector current induced by a CRS signal with power P_{CRS} and frequency ω_{CRS} (η is the quantum efficiency of the photodetector, and e is the electron charge).

Shot noise of a photodetector is usually the most significant source of quantum noise. The shot-noise-induced root-mean-square deviation of the photocurrent from the detector used to register a CRS signal is given by [1, 2]

$$\langle \delta_q^2 \rangle = 2e\Delta\nu i_d, \tag{3}$$

where $\Delta\nu$ is the detection bandwidth, related to the time constant T of the photodetector by the expression $\Delta\nu = 1/T$.

The CRS spectroscopic signal includes both a resonant component, related to a Raman-active mode of the medium under study, and a nonresonant background:

$$P_{\mathrm{CRS}} = (P_r^2 + 4P_rP_{nr})^{1/2}, \quad (4)$$

where P_r is the power of the resonant part of the signal and P_{nr} is the power of the nonresonant background. The total signal on the photodetector is given by

$$P = P_{nr} + (P_r^2 + 4P_rP_{nr})^{1/2}. \quad (5)$$

Combining Eqs. (1)–(5), we represent the signal-to-noise ratio in CRS spectroscopy as

$$\frac{S}{N} = \left(\frac{\langle i_d^2\rangle}{\langle \delta_c^2\rangle + \langle \delta_q^2\rangle}\right)^{1/2} = \left(\frac{P_r^2 + 4P_rP_{nr}}{\varepsilon P^2 + 2\hbar\omega_{\mathrm{CRS}}\Delta\nu P/\eta}\right)^{1/2}. \quad (6)$$

In the case of an intense nonresonant background, we arrive at the following classical limit for the signal-to-noise ratio:

$$\frac{S}{N} \approx 2\left(\frac{P_r}{\varepsilon P_{nr}}\right)^{1/2}. \quad (7)$$

The coherent nonresonant background can be efficiently suppressed with the use of the polarization technique [1], by introducing a time delay between laser pulses [4], or by applying methods of coherent control [9]. With a suppressed coherent background, Eq. (6) yields the following expression for the classical limit of the signal-to-noise ratio in CRS spectroscopy:

$$\left(\frac{S}{N}\right) \approx \frac{1}{\varepsilon^{1/2}}. \quad (8)$$

The quantum limit of S/N under these conditions is given by

$$\left(\frac{S}{N}\right) \approx \left(\frac{\eta P_{\mathrm{CRS}}}{2\hbar\omega_{\mathrm{CRS}}\Delta\nu}\right)^{1/2}. \quad (9)$$

We now demonstrate that the quantum limit of the signal-to-noise ratio in waveguide CRS can be substantially reduced relative to the regime of tightly focused pump fields. We use for this purpose the following generic expression for the intensity of phase-matched two-color CRS [1, 2]:

$$I_{\mathrm{CRS}} \propto |\chi^{(3)}|^2 I_1^2 I_2 l^2, \quad (10)$$

where I_1 and I_2 are the intensities of the pump fields, $\chi^{(3)}$ is the nonlinear-optical susceptibility responsible for the CRS process, and l is the effective length of nonlinear-optical interaction. For focused pump fields, the effective length of nonlinear-optical interaction is controlled by the confocal parameter. In the case of focused Gaussian beams, this length is

$$l_t \simeq \pi a^2/\lambda, \quad (11)$$

where a is the waist radius of the focused beam and λ is the radiation wavelength. A waveguide with a core radius a would thus provide a CRS power enhancement in the phase-matching regime by a factor of

$$\xi = \frac{(P_{\mathrm{CRS}})_w}{(P_{\mathrm{CRS}})_t} \approx \frac{\lambda^2 l^2}{\pi^2 a^4}, \quad (12)$$

where $(P_{\mathrm{CRS}})_w$ and $(P_{\mathrm{CRS}})_t$ are the CRS powers in the waveguide regime and the regime of tight focusing, respectively, for the same powers of the pump pulses.

According to Eqs. (9) and (12), the figure of merit for the quantum-limit signal-to-noise ratio in phase-matched waveguide CRS relative to the regime of tight focusing is proportional to the effective nonlinear interaction length l and inversely proportional to the fiber core radius a squared:

$$\mu = \frac{(S/N)_{q,w}}{(S/N)_{q,t}} \approx \frac{\lambda l}{\pi a^2} \quad (13)$$

where $(S/N)_{q,w}$ and $(S/N)_{q,t}$ are the quantum limits for the CRS signal-to-noise ratio in the waveguide and in the regime of tight focusing, respectively, for equal powers of the pump pulses.

Radiation loss is the key factor limiting the figure of merit for the CRS signal-to-noise ratio in the waveguide regime. Radiation losses and the phase mismatch of guided modes enter into the expression for the CRS intensity through the factor [1, 2]

$$M = \exp[-(\Delta\alpha + \alpha_{\mathrm{CRS}})l] \times \frac{\sinh^2(\Delta\alpha l/2) + \sin^2(\Delta\beta l/2)}{(\Delta\alpha l/2)^2 + (\Delta\beta l/2)^2} l^2, \quad (14)$$

where $\Delta\alpha = (2\alpha_1 + \alpha_2 - \alpha_{\mathrm{CRS}})/2$; α_1, α_2, and α_{CRS} are the radiation losses at the wavelengths ω_1, ω_2, and ω_{CRS}, respectively; and $\Delta\beta$ is the mismatch of the propagation constants of the waveguide modes involved in the nonlinear-optical interaction.

Phase matching for waveguide CRS, controlled by the parameter $\Delta\beta$, can be achieved for a given set of guided modes through the cancellation of the material and waveguide dispersion components [16]. Figure 1 illustrates this possibility for the CRS process $\omega_{\mathrm{CRS}} = 2\omega_1 - \omega_2$ (ω_1 and ω_2 are the frequencies of the pump fields) in a hollow fiber filled with atmospheric-pressure air. The fundamental guided modes of the pump fields with the wavelengths $\lambda_1 = 2\pi c/\omega_1 = 532$ nm and $\lambda_2 = 2\pi c/\omega_2 = 660$ nm generate in this case the CRS signal in the fundamental waveguide mode. The phase-matching condition $\Delta\beta = 0$ is achieved for the considered process with a fiber core radius a of about 32 μm. Within a broad range of a values, starting with approximately 25 μm, the coherence length $l_c = \pi/2|\Delta\beta|$ for waveguide CRS (curve *1* in the inset to Fig. 1) is larger than the coherence length for the same process in free

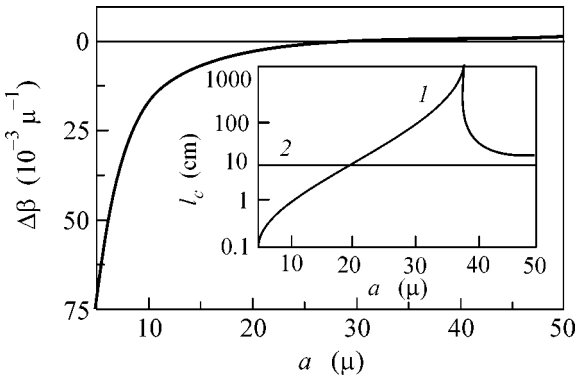

Fig. 1. Mismatch of the propagation constants for the modes of an atmospheric-air-filled hollow fiber involved in the CRS process $\omega_{CRS} = 2\omega_1 - \omega_2$ (ω_1 and ω_2 are the frequencies of the pump fields) as a function of the fiber core radius a. The fundamental waveguide modes of the pump fields with wavelengths $\lambda_1 = 2\pi c/\omega_1 = 532$ nm and $\lambda_2 = 2\pi c/\omega_2 = 660$ nm generate the CRS signal in the fundamental waveguide mode. The material dispersion of atmospheric air is included. The horizontal line shows the phase-matching condition, $\Delta\beta = 0$. The inset displays the coherence length $l_c = \pi/2|\Delta\beta|$ for the considered CRS process in an air-filled hollow fiber (*1*) and in the atmospheric air with no waveguide (*2*) as a function of the fiber core radius.

atmospheric-pressure air with no waveguide (curve *2* in the inset to Fig. 1).

Analysis of Eq. (14) reveals the existence of an optimal waveguide length in the regime of phase matching, $\Delta\beta l \ll 1$, providing the maximum figure of merit for the quantum-limit CRS signal-to-noise ratio (Fig. 2):

$$l_{opt} = \frac{1}{\Delta\alpha}\ln\left(\frac{2\alpha_1 + \alpha_2}{\alpha_{CRS}}\right). \qquad (15)$$

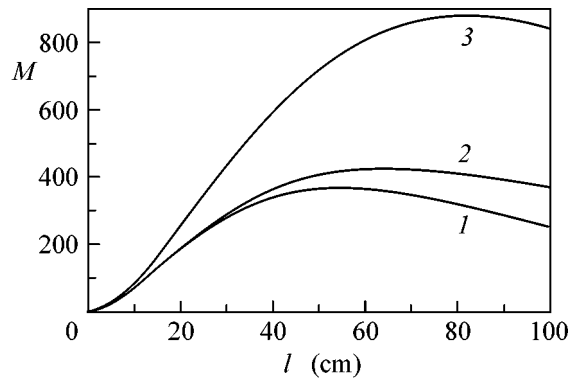

Fig. 2. The factor M [Eq. (14)], describing the influence of radiation losses and phase mismatch of guided modes on the efficiency of CRS, as a function of the nonlinear-optical interaction length l: (*1*) $\alpha_1 = 0.03$ cm^{-1} and $\alpha_2 = \alpha_{CRS} = 0.01$ cm^{-1}, (*2*) $\alpha_1 = \alpha_2 = \alpha_{CRS} = 0.02$ cm^{-1}, and (*3*) $\alpha_1 = \alpha_2 = 0.01$ cm^{-1} and $\alpha_{CRS} = 0.02$ cm^{-1}.

For hollow fibers with a core radius on the order of $a \approx 5$ μm, the quantum limit for the CRS signal-to-noise ratio in the waveguide regime, as can be seen from the results presented in Fig. 3, can be increased by roughly four orders of magnitude. For high-intensity laser pulses, decrease in the fiber core radius is limited by optical breakdown. Introducing I_b to denote the intensity corresponding to the critical laser fluence at the threshold of optical breakdown, we derive the following expression for the minimum fiber core radius: $a_{min}^2 = P/\pi I_b$, where P is the power of the pump pulse.

In view of Eqs. (13) and (15), the maximum figure of merit for the quantum-limit CRS signal-to-noise ratio is

$$\mu_{max} = \frac{\lambda I_b}{\Delta\alpha P}\ln\left(\frac{2\alpha_1 + \alpha_2}{\alpha_{CRS}}\right). \qquad (16)$$

Now, we use Eqs. (7), (13), and (16) to analyze the ways to improve the signal-to-noise ratio for the waveguide CRS spectroscopy of the gas phase. Classical noise can be reduced in this case by using power-stabilized femtosecond pump pulses. Methods for suppressing the nonresonant background in femtosecond CRS include the use of time-delayed pump–probe laser pulses [1, 4] and coherent-control strategies [9].

Hollow fibers are at the heart of waveguide-enhanced gas-phase CRS spectroscopy. For standard hollow fibers, a decrease in the fiber core radius leads to a rapid growth of radiation losses, which scale as λ^2/a^3. This circumstance imposes a limitation on the minimum core radius of hollow fibers. Core diameters for hollow fibers used in experiments typically range from 100 up to 500 μm. Such waveguides are essentially multimode. The difference in phase and group velocities of guided modes simultaneously excited in such waveguides gives rise to uncertainties in time-

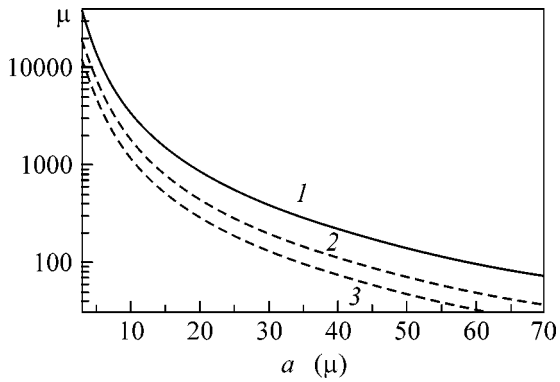

Fig. 3. Figure of merit for the quantum-limit signal-to-noise ratio in waveguide CRS spectroscopy relative to the regime of tight focusing as a function of the core radius a of a hollow fiber for $\lambda = 1$ μm; $l = l_{opt}$; and $\alpha_1 = \alpha_2 = \alpha_{CRS} =$ (*1*) 0.01, (*2*) 0.02, and (*3*) 0.03 cm^{-1}.

resolved measurements and complicates accurate calibration of the nonlinear signal as a function of the gas pressure [15]. Radiation losses of hollow-core-guided modes can be radically reduced in the case of hollow fibers with periodic (photonic-crystal) cladding [18–22]. Such fibers can support isolated guided modes confined to the hollow core, allowing a radical enhancement of nonlinear-optical processes [23–26].

Radiation intensities on the order of $I_b \sim 10^{14}$ W/cm^2, typically leading to an optical breakdown of atmospheric-pressure gases, can be achieved by coupling 75-MW laser pulses into a hollow photonic-crystal fiber (PCF) with a core radius of about 5 μm. Femtosecond pulses of such a power level are produced by standard solid-state mode-locked laser systems with regenerative amplification. Transmission of such femtosecond pulses through hollow PCFs has been demonstrated by experiments [27] (see also [22]). Expression (16) with $l_{opt} \approx 100$ cm gives the following estimate on the maximum figure of merit for the quantum-limit signal-to-noise ratio of femtosecond CRS spectroscopy with such pump pulses (Fig. 3): $\mu_{max} \sim 1.3 \times 10^4$.

The analysis performed in this work shows that waveguide regimes of nonlinear-optical interactions allow a reduction of the level of quantum noise in CRS spectra. The expressions derived in this paper for the optimal length of the waveguide providing the maximum quantum-limit CRS signal-to-noise ratio and the maximum figure of merit for this ratio in the quantum limit at the threshold of optical breakdown suggest the possibility of a substantial lowering of quantum noise in the CRS spectroscopy of the gas phase based on the use of high-power femtosecond laser pulses.

This work was supported in part by the President of the Russian Federation (grant MD-42.2003.02), the Russian Foundation for Basic Research (project nos. 02-02-17098, 03-02-16929), INTAS (project nos. 03-51-5037, 03-51-5288), the Civilian Research and Development Foundation (CRDF, project no. RP2-2558), and the European Research Office of the US Army (contract no. 62558-03-M-0033).

REFERENCES

1. S. A. Akhmanov and N. I. Koroteev, *Methods of Nonlinear Optics in Light Scattering Spectroscopy* (Nauka, Moscow, 1981) [in Russian].
2. G. L. Eesley, *Coherent Raman Spectroscopy* (Pergamon, Oxford, 1981).
3. A. M. Zheltikov and N. I. Koroteev, Usp. Fiz. Nauk **170**, 1203 (1999) [Phys. Usp. **43**, 1125 (1999)].
4. A. M. Zheltikov, *Introduction to Nonlinear Raman Spectrometry*, in *Handbook of Vibrational Spectroscopy* (Wiley, Chichester, 2002), Vol. 1, p. 572.
5. *Nonlinear Raman Spectroscopy*, Ed. by P. Radi and A. M. Zheltikov, Special Issue of J. Raman Spectrosc. **33** (11/12) (2002).
6. *Nonlinear Raman Spectroscopy*, Ed. by P. Radi and A. M. Zheltikov, Special Issue of J. Raman Spectrosc. **34** (12) (2003).
7. *Femtosecond Coherent Raman Spectroscopy*, Ed. by W. Kiefer, Special Issue of J. Raman Spectrosc. **31** (1/2) (2000).
8. A. Zumbusch, G. R. Holtom, and X. Sunney Xie, Phys. Rev. Lett. **82**, 4142 (1999).
9. N. Dudovich, D. Oron, and Y. Silberberg, Nature **418**, 512 (2002).
10. G. I. Stegeman, R. Fortenberry, C. Karaguleff, *et al.*, Opt. Lett. **8**, 295 (1983).
11. W. P. de Boeij, J. S. Kanger, G. W. Lucassen, *et al.*, Appl. Spectrosc. **47**, 723 (1993).
12. J. S. Kanger, C. Otto, and J. Greve, Appl. Spectrosc. **49**, 1326 (1995).
13. R. B. Miles, G. Laufer, and G. C. Bjorklund, Appl. Phys. Lett. **30**, 417 (1977).
14. S. O. Konorov, D. A. Akimov, A. N. Naumov, *et al.*, JETP Lett. **75**, 66 (2002).
15. A. B. Fedotov, F. Giammanco, A. N. Naumov, *et al.*, Appl. Phys. B **72**, 575 (2001).
16. A. M. Zheltikov, Usp. Fiz. Nauk **172**, 743 (2002) [Phys. Usp. **45**, 687 (2002)].
17. A. B. Fedotov, S. O. Konorov, V. P. Mitrokhin, *et al.*, Phys. Rev. A (in press).
18. R. F. Cregan, B. J. Mangan, J. C. Knight, *et al.*, Science **285**, 1537 (1999).
19. S. O. Konorov, A. B. Fedotov, O. A. Kolevatova, *et al.*, JETP Lett. **76**, 341 (2002).
20. P. St. J. Russell, Science **299**, 358 (2003).
21. C. M. Smith, N. Venkataraman, M. T. Gallagher, *et al.*, Nature **424**, 657 (2003).
22. A. M. Zheltikov, *Optics of Microstructure Fibers* (Nauka, Moscow, 2004) [in Russian].
23. F. Benabid, J. C. Knight, G. Antonopoulos, and P. St. J. Russell, Science **298**, 399 (2002).
24. S. O. Konorov, A. B. Fedotov, and A. M. Zheltikov, Opt. Lett. **28**, 1448 (2003).
25. D. G. Ouzounov, F. R. Ahmad, D. Muller, *et al.*, Science **301**, 1702 (2003).
26. S. O. Konorov, D. A. Sidorov-Biryukov, I. Bugar, *et al.*, Phys. Rev. A (in press).
27. S. O. Konorov, A. M. Zheltikov, Ping Zhou, *et al.*, Opt. Lett. **29**, 1521 (2004).

Translated by A. Zheltikov

JETP Letters, Vol. 80, No. 6, 2004, pp. 393–397. Translated from Pis'ma v Zhurnal Éksperimental'noĭ i Teoreticheskoĭ Fiziki, Vol. 80, No. 6, 2004, pp. 447–451.

Experimental Observation of Parametric X-Ray Radiation Directed Along the Propagation Velocity of Relativistic Electrons in a Tungsten Crystal

A. N. Aleinik[1], A. N. Baldin[2], E. A. Bogomazova[1], I. E. Vnukov[2, *], B. N. Kalinin[1], A. S. Kubankin[2], N. N. Nasonov[1], G. A. Naumenko[1], A. P. Potylitsyn[1], and A. F. Sharafutdinov[1]

[1] *Research Institute of Nuclear Physics, Tomsk Polytechnical University, Tomsk, 634050 Russia*

[2] *Laboratory of Radiation Physics, Belgorod State University, Belgorod, 308007 Russia*

* *e-mail: vnukov@bsu.edu.ru*

Received June 29, 2004

Parametric X-ray radiation (PXR) due to dynamic diffraction of relativistic electrons is experimentally observed at small angles to the propagation velocity of electrons in a tungsten crystal. The specific features of the experimental method are described, and forward PXR reflections from two crystallographic planes of tungsten are reliably measured. © *2004 MAIK "Nauka/Interperiodica".*

PACS numbers: 78.70.-g; 79.90.+t

Diffraction of the Coulomb field of a fast charged particle propagating in a crystal gives rise to parametric X-ray radiation (PXR) [1–3]. The theory predicts the existence of PXR reflections propagating both along the direction of Bragg scattering and along the emitting particle velocity. However, while the first of the reflections has been studied in detail theoretically and experimentally (see, for example, [4, 5] and references therein), PXR along the particle velocity, or forward PXR, has not been observed so far, although relevant attempts have been made over more than thirty years [6–8].

The forward PXR attracts interest for two reasons. First of all, the observation of such radiation would prove the existence of dynamic diffraction in the case of PXR, because the forward PXR is a purely dynamic effect [4]. In addition, the forward PXR can be interpreted as Cerenkov radiation, which appears due to a change in the refractive index of a crystal upon dynamic diffraction of the electromagnetic field of a fast particle (the effective refractive index becomes greater than unity, which opens up the channel of Cerenkov energy losses of the particle) [9]. Therefore, the observation of forward PXR would confirm the existence of a new type of Cerenkov radiation in the X-ray range.

Experimental observation of the forward PXR is mainly complicated by a small width of the PXR spectrum compared to typical energy resolution of X-ray detectors ($\Delta\omega \geq 150$ eV), which leads to the efficient averaging of the forward PXR against the background of broadband bremsstrahlung and transient radiation. This problem can be solved only by using a crystal grating spectrometer. Note that, in all experiments devoted to the search for forward PXR, targets made of light elements were used. Therefore, the width of the sought-for radiation spectrum did not exceed a few electron-volts [10], and for this reason these experiments have failed.

The observation of forward PXR produced by 855-MeV electrons on the (111) plane of a 56-μm thick silicon crystal and detected with a crystal grating spectrometer was recently reported in [11]. However, the method of suppression of the transient-radiation background in the vicinity of the Bragg frequency, where the forward PXR spectrum is located, used in this experiment is incorrect. The method is based on the use of the negative interference of transient-radiation waves appearing on the input and output surfaces of the target. As shown in [12], it is in the vicinity of the Bragg frequency, where transient radiation should be completely suppressed due to interference, that a narrow radiation peak caused by dynamic effects appears. The contribution of this mechanism to the intensity of detected radiation was not analyzed [11], and, therefore, the nature of the narrow radiation peak observed in this paper remains open.

Our paper is devoted to the experimental search for forward PXR reflection. According to the results of theoretical analysis [10], we use a crystal target made of a heavy element–tungsten. This target offers three important advantages: (i) a substantial increase (up to a few tens of eV) in the width of the forward PXR reflection, which results in a drastic improvement of the signal-to-noise ratio; (ii) an increase in the working (Bragg) frequency, which reduces absorption of photons in air with increasing the distance between the crystal and a detector and allows the use of the advantages of the measurement method [13] for analyzing radiation characteris-

0021-3640/04/8006-0393$26.00 © 2004 MAIK "Nauka/Interperiodica"

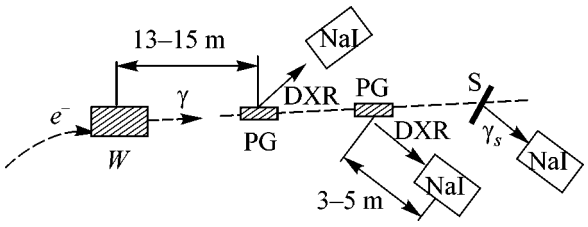

Fig. 1. Scheme of the experiment: W: tungsten crystal; PG: pyrolytic graphite crystal; NaI: NaI(Tl) spectrometers; S: scatterer.

tics; and (iii) a complete exclusion of dynamic effects, caused by diffraction of transient radiation in the crystal, due to strong absorption of detected photons in the crystal. On the other hand, as the target thickness increases, the effect of multiple scattering of electrons and the contribution of bremsstrahlung drastically increase. As shown experimentally and confirmed by a special analysis, the latter can even change the sign of the effect observed.

Measurements were performed using an inner electron beam of the Tomsk synchrotron. Figure 1 shows the scheme of the experiment. Electrons accelerated to the final energy E_0 = 500 MeV were incident on a single-crystal target placed in a goniometer. The radiation under study propagated through a collimator, "purified" by a magnet, and was directed to an experimental hall, where the detecting equipment was installed. The crystal was oriented with respect to the electron-beam direction according to the readings of a NaI(Tl) detector in the Compton mounting, which detected photons upon channeling and bremsstrahlung with energy $\omega >$ 0.5 MeV scattered in a converter. The parameters of the electron beam and experimental instruments and the method of orientation are considered in [14, 15].

The X-ray component of radiation was detected using two crystal grating spectrometers based on pyrolytic graphite crystals mounted in goniometers at a distance of 13–15 m from the target, where radiation was generated, and NaI(Tl) detectors of size $\varnothing 40 \times 1$ mm, which were located at a distance of 3–5 m from graphite crystals. Under these conditions, the energy resolution of spectrometers weakly depends on the mosaic structure of crystals but is determined by their angular aperture ($\Delta\theta_x \sim \pm 0.1$ mrad, $\Delta\theta_y = \pm 0.6$ mrad) and the collimation angle of diffracted radiation [13]. The collimation angle in the diffraction plane (horizontal) $\Delta\Theta_x \sim 0.7$ mrad provided the resolution of spectrometers $\Delta\omega/\omega \sim 1\%$. The background level for photons of energy $\omega \geq 40$ keV did not exceed 2–5%. Because of strong absorption of photons with lower energies in the air and target, the background level increased up to 20–30% for ω = 28.3-keV photons (see below). The characteristics of the spectrometers and measuring methods are described in detail in [13].

As shown in [8, 10], the optimal method for searching for forward PXR is measurement of the dependence of the number of photons in a narrow spectral range on the crystal orientation. For photons with energies above 20–25 keV, the Bragg condition can be satisfied only for several low-index planes and quite specific crystal orientations. A criterion for the observation of the effect is the coincidence of Bragg energies for the orientation angles at which the peak of the photon yield is observed with the energies to which diffractometers are tuned. According to the theory [9, 10], the forward PXR intensity in a tungsten crystal becomes comparable with the transient radiation intensity only for photons with energies $\omega \leq \gamma\omega_p \sim 80$ keV, where γ is the Lorentz factor and ω_p is the plasma frequency of the medium. Therefore, we detected simultaneously the yield of photons with $\omega < \gamma\omega_p$ (67, 40, and 29 keV) and $\omega > \gamma\omega_p$ (95 and 97 keV). To control the absence of radiation during plane channeling, we measured the yield of ≥0.5-MeV photons by means of a Compton NaI(Tl) detector. This detector was also used to make the electron-beam direction coincident with the crystal axis, from which the reorientation angles of crystal planes were measured.

Measurements were performed for a tungsten single crystal of size 8.5×0.41 mm, with the $\langle 111 \rangle$ orientation and the surface mosaic structure $\sigma < 0.2$ mrad. In tungsten crystals grown by the same method, anomalous propagation of X-rays was observed [16]. The crystal was mounted in the goniometer so that the $(11\bar{2})$ plane was almost vertical. This allowed us to study dynamic effects in radiation both for the $(11\bar{2})$ plane and two (110) planes turned by 30° with respect to this plane. The measurements of orientation dependences of the yield of scattering photons in the case of plane channeling (Fig. 2a, curve *1*) showed that the $(11\bar{2})$ plane is turned by the angle $\beta = 3.5° \pm 0.2°$ with respect to the vertical plane. Therefore, dynamic effects in radiation should be observed for each of the crystal planes at different orientation angles Θ (see Fig. 2b).

One can see from the orientation dependence of the yield of 67-keV photons (curve *2*) that the X-ray radiation intensity depends substantially on the orientation of crystal planes with respect to the electron-beam direction. Therefore, as in experiment [8], measurements were performed for the case of the intersection of the $\langle 111 \rangle$ axis, when the plane channeling effect was absent.

Our measurements showed that no forward PXR peaks were observed for relatively hard photons with $\omega \geq \gamma\omega_p$ (67, 95, and 97 keV). The presence of the crystal structure manifested in the decrease in the number of photons detected by spectrometers when the Bragg energy for the given orientation of the crystal coincided

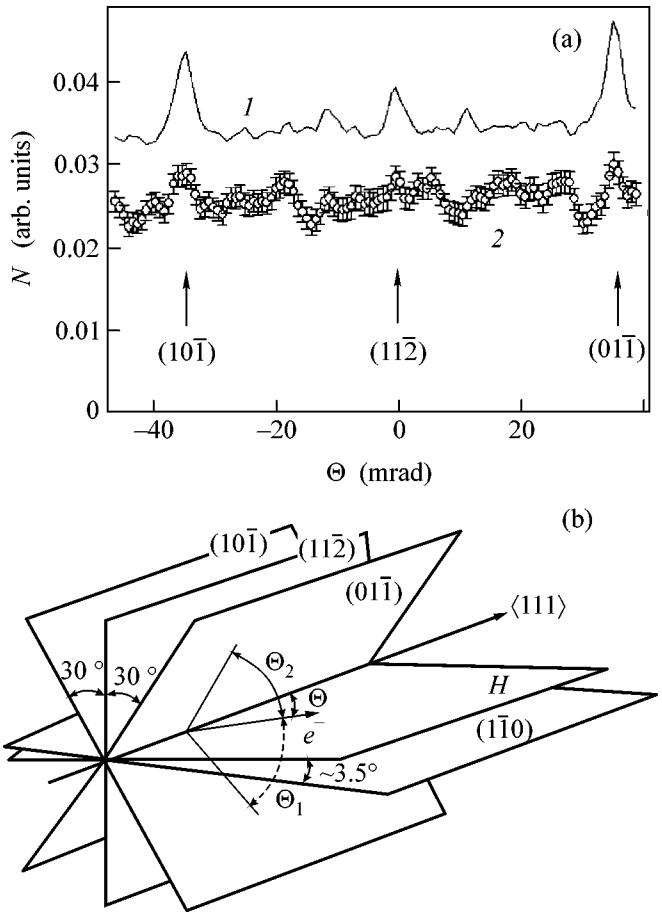

Fig. 2. (a) Orientation dependences of radiation yield. Curve *1*: signal of the detector of Compton photons with $\omega \geq 0.5$ MeV; *2*: $\omega = 67$ keV; (b) scheme of the arrangement of crystal planes: *H* is the horizontal plane (vertical plane is not shown); Θ is the angle between the ⟨111⟩ axis and the electron-beam direction in the horizontal plane; $\Theta_{2(1)} = \Theta\cos(30° \pm \beta)$ are angles between the propagation direction of electrons and planes (10$\bar{1}$) and (01$\bar{1}$).

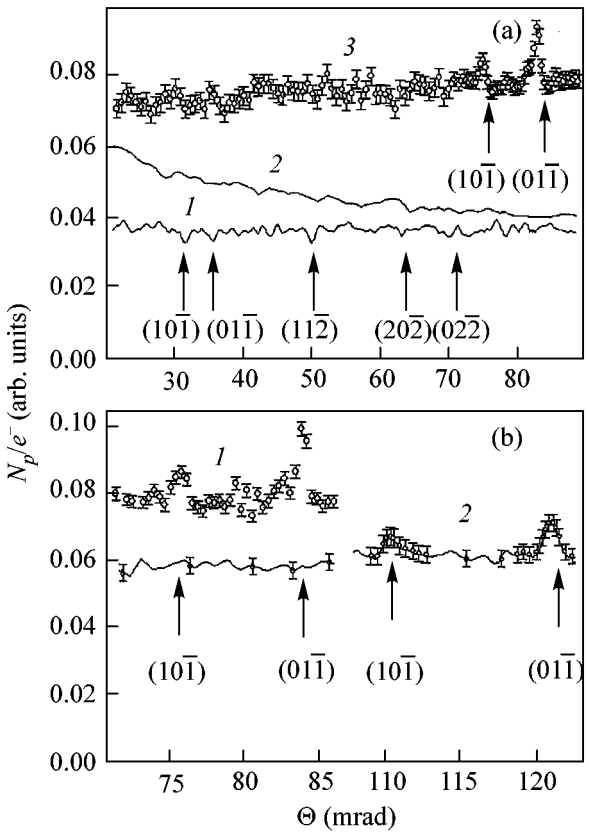

Fig. 3. Orientation dependences of soft radiation yield: (a) $\omega = 95$ keV (curve *1*); $\omega = 40$ keV (curve *2*); $\omega \geq 0.5$ MeV (curve *3*); (b) $\omega = 40$ keV (curve *1*); $\omega = 28.3$ keV (curve *3*).

with the photon energy (see Fig. 3a, curve *1*). The positions of minima of the orientation dependence correspond to the kinematic conditions for diffraction of photons directed along the electron beam with an error no worse than 1%. For example, for $\omega = 67$ keV, the calculated positions of minima for the (10$\bar{1}$), (01$\bar{1}$), and (11$\bar{2}$) reflections are 46.6, 49.9, and 72.2 mrad, whereas the measured values are 46.3, 49.5, and 71.9 mrad. The depth of minima changes from 12–15% for $\omega = 67$ keV to ~10% for $\omega > 90$ keV. The typical value of the full width of the minimum is $\Delta\Theta \sim 1.5$–2.5 mrad. The experimental curve differs from the theoretical curve (a narrow minimum with a width of the order of the Darvin table width $\Delta\Theta \leq 0.1$ mrad and depth ~0.5 from the substrate level), because graphite crystals are not parallel to the plane on which diffraction occurs and spectrometers have a finite angular aperture and a limited resolution.

The calculation of the orientation dependence of the forward PXR yield [10], taking into account multiple scattering of electrons and diffraction of bremsstrahlung in a crystal, confirmed that, for the photon energy $\omega \sim \gamma\omega_p$ and zero observation angle (the detected radiation is emitted along the electron-beam direction), diffraction of bremsstrahlung inside the crystal masks the sought-for effect. The forward PXR becomes dominant only for the photon energy $\omega \leq 0.5\gamma\omega_p$ (see Fig. 4).

The orientation dependences measured for photon energies 40 and 28.3 keV exhibit distinct maxima, whose positions, as minima for hard photons, agree with the Bragg law (see Fig. 3). These maxima are not related to radiation with a continuous spectrum or to experimental errors. This is confirmed by their absence in the yield of ≥0.5-MeV photons (Fig. 3a, curve *1*) and their different positions in the orientation dependences of the yield of photons with different energies (Fig. 3b). The position and shape of the maxima were reliably reproduced in repeated measurements.

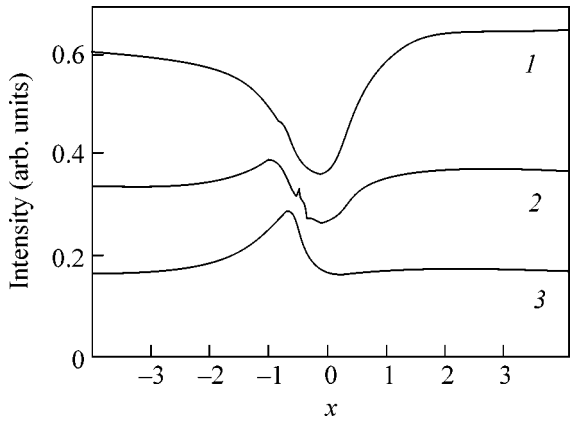

Fig. 4. Orientation dependences of the X-ray radiation yield in the (110) plane in the region of Bragg angles $x = (g^2/2\omega_g^2)(\omega - \omega_B/\omega_B)$ (see [10]). Curve *1*: ω = 65 keV; *2*: ω = 40 keV; *3*: ω = 26 keV.

Measurements of the spectra of diffracted radiation at the peak for ω = 40 keV – $\Theta_{01\bar{1}}^{\exp}$ = 83.9 mrad and at the neighboring points (Θ = 81.3 and 79.3 mrad) showed that the radiation intensity increases only for the first reflection order. The radiation intensity in the higher reflection orders coincides for all the spectra. The crystal thickness $t = 0.41$ mm substantially exceeds the lengths $l_a \sim 42$ and 19 μm at which photons are absorbed, i.e., the peaks observed in the orientation dependences of the yield of photons with $\omega < \gamma\omega_p$ are caused by radiation excited inside the crystal. The only known mechanism of radiation of electrons in crystals with such properties is parametric (quasi-Cerenkov) X-ray radiation along the electron propagation velocity in a crystal [9].

The peak positions $\Theta_{10\bar{1}}^{\exp}$ = 76.6 (110.2) mrad and $\Theta_{01\bar{1}}^{\exp}$ = 83.9 (120.9) mrad measured in experiments for photons with energy 40 (28.3) keV differ somewhat from the estimated values $\Theta_{10\bar{1}}^{\text{est}}$ = 77.9 (110.2) mrad and $\Theta_{01\bar{1}}^{\text{est}}$ = 83.6 (118.2) mrad. The distance between the peaks is larger by 1.5 and 2 mrad than follows from the Bragg law. For both photon energies, the width of the peak for the $(01\bar{1})$ plane is almost twice as large as that for the $(10\bar{1})$ plane. For ω = 40 keV, this peak quite distinctly divides into two peaks (Fig. 3b).

According to the theory, the forward PXR energy is determined by the angle $\theta_\parallel$ of escape of a photon in the direction perpendicular to the plane at which reflection occurs. The reflection intensity along the electron propagation direction is zero, while the maximum of the angular distribution corresponds to the angle $\theta_\parallel^{FPXR} = \frac{1}{\sqrt{3}}\sqrt{\gamma^{-2} + (\omega_0/\omega)^2}$. We detected photons caused by electrons moving at the angle θ^{FPXR} to the electron-beam direction. Radiation was generated on the planes of the tungsten crystal turned by the angle ~30° with respect to the reflecting plane of the diffractometers. Along with a finite angular aperture and limited resolution of the spectrometers, this should inevitably result in the broadening of experimental curves and in the decrease in the amplitude of the peaks compared to the theoretical predictions. We plan to take experimental factors into account and compare quantitatively the results of measurements with the theory in the next paper.

The results of the study can be summarized as follows:

(i) We have observed quasi-Cerenkov X-ray radiation of fast charge particles in a material with a medium refractive index $n < 1$.

(ii) Diffraction suppression of bremsstrahlung of relativistic electrons in a crystal has been reliably observed, and the competition between quasi-Cerenkov radiation and diffraction suppression of bremsstrahlung has been demonstrated.

We thank Prof. V.V. Boiko and Prof. E.P. Naiden for placing a tungsten crystal at our disposal, the study of the target quality, and determining the geometrical position of planes on the target surface. This work was partially supported by the Russian Foundation for Basic Research (grant nos. 01-02-17471 and 03-02-16587), the program "Universities of Russia" (grant nos. UR 02.01.021 and UR 02.01.002), the "Regional Scientific and Technical Program" (grant FRP no. 09-03), and the "Internal Grant Program" of Belgorod State University (grant VKG no. 008-04).

REFERENCES

1. M. L. Ter-Mikaelian, *High Energy Electromagnetic Processes in Condensed Media* (Akad. Nauk Arm. SSR, Yerevan, 1969; Wiley, New York, 1972).
2. G. M. Garibyan and Yan Shi, Zh. Éksp. Teor. Fiz. **61**, 930 (1971) [Sov. Phys. JETP **34**, 1756 (1971)].
3. V. G. Baryshevskiĭ and I. D. Feranchuk, Zh. Éksp. Teor. Fiz. **61**, 944 (1971) [Sov. Phys. JETP **34**, 1778 (1971)].
4. V. G. Baryshevskiĭ and I. Ya. Dubovskaya, Itogi Nauki Tekh., Ser.: Puchki Zaryazh. Chastits Tverd. Telo **4**, 129 (1991).
5. K.-H. Brenzinger, C. Herberg, B. Limburg, *et al.*, Z. Phys. A **358**, 107 (1997).
6. A. I. Alikhanyan, G. M. Garibyan, M. P. Lorikyan, and K. K. Shikhlarov, Pis'ma Zh. Éksp. Teor. Fiz. **13**, 201 (1971) [JETP Lett. **13**, 142 (1971)].
7. L. C. L. Yuan, P. W. Alley, A. Bamberger, *et al.*, Nucl. Instrum. Methods Phys. Res. A **234**, 426 (1985).
8. B. N. Kalinin, G. A. Naumenko, D. V. Padalko, *et al.*, Nucl. Instrum. Methods Phys. Res. B **173**, 255 (2001).

9. V. G. Baryshevsky, Nucl. Instrum. Methods Phys. Res. B **122**, 13 (1997).

10. A. Kubankin, N. Nasonov, V. Sergienko, and I. Vnukov, Nucl. Instrum. Methods Phys. Res. B **201**, 97 (2003).

11. H. Backe, C. Ay, N. Clawiter, *et al.*, in *Proceedings of the International Symposium on Channeling-Bent Crystals–Radiation Processes*, Ed. by W. Greiner, A. V. Solov'yov, and S. Misicu (Frankfurt am Main, Germany, 2003), p. 41.

12. N. Imanishi, N. Nasonov, and K. Yajima, Nucl. Instrum. Methods Phys. Res. B **173**, 227 (2001).

13. I. E. Vnukov, B. N. Kalinin, G. A. Naumenko, *et al.*, Izv. Vyssh. Uchebn. Zaved., Fiz. **44** (3), 71 (2001).

14. Yu. N. Adishchev, S. A. Vorob'ev, V. N. Zabaev, *et al.*, Yad. Fiz. **35** (1), 108 (1982) [Sov. J. Nucl. Phys. **35**, 63 (1982)].

15. B. N. Kalinin, E. I. Konovalova, G. A. Pleshkov, *et al.*, Prib. Tekh. Éksp., No. 3, 31 (1985).

16. I. K. Bdikin, S. I. Bozhko, V. N. Semenov, *et al.*, Pis'ma Zh. Tekh. Fiz. **25** (23), 16 (1999) [Tech. Phys. Lett. **25**, 933 (1999)].

Translated by M. Sapozhnikov

JETP Letters, Vol. 80, No. 6, 2004, pp. 398–404. Translated from Pis'ma v Zhurnal Éksperimental'noĭ i Teoreticheskoĭ Fiziki, Vol. 80, No. 6, 2004, pp. 452–458.

Experimental Measurements of the Compressibility, Temperature, and Light Absorption in Dense Shock-Compressed Gaseous Deuterium

S. K. Grishechkin[1], S. K. Gruzdev[1], V. K. Gryaznov[2, **], M. V. Zhernokletov[1, *], R. I. Il'kaev[1], I. L. Iosilevskii[3], G. N. Kashintseva[1], S. I. Kirshanov[1], S. F. Manachkin[1], V. B. Mintsev[2], A. L. Mikhaĭlov[1], A. B. Mezhevov[1], M. A. Mochalov[1], V. E. Fortov[2], V. V. Khrustalev[1], A. N. Shuĭkin[1], and A. A. Yukhimchuk[1]

[1] *Russian Federal Nuclear Center, All-Russia Research Institute of Experimental Physics, Sarov, Nizhni Novgorod region, 607190 Russia*

**e-mail: root@gdd.vniief.ru*

[2] *Institute of Problems of Chemical Physics, Chernogolovka Branch, Russian Academy of Sciences, Chernogolovka, Moscow region, 142432 Russia*

***e-mail: grvk@ficp.ac.ru*

[3] *Moscow Institute of Physics and Technology, Institutskiĭ per. 9, Dolgoprudnyĭ, Moscow region, 141700 Russia*

Received August 5, 2004

Experimental data on the shock compression, temperature, and absorptivity of gaseous deuterium with an initial density close to its value in the liquid state were obtained on a spherical explosion shock-wave generator in a pressure range of 80–90 GPa. The obtained results are compared with the existing experimental and theoretical data. © *2004 MAIK "Nauka/Interperiodica".*

PACS numbers: 52.25.-b; 52.35.Tc

At present, advances in laser fusion and progress in the understanding of the structure and evolution of astrophysical objects have quickened interest in the study of thermodynamic and electrophysical properties of hydrogen—the simplest and most abundant element in nature—in the megabar pressure range [1, 2]. To achieve shock-compression megabar pressures, various methods of shock-wave excitation are used: intense laser radiation [3, 4], high-power pulse currents [5, 6], and spherical explosion devices [2, 7]. Although the laser data demonstrate anomalously high compressibility of deuterium plasma, this was not confirmed by the electrodynamic and explosion experiments.

In this work, gaseous deuterium with a high initial density, close to the density of liquid deuterium, was chosen as the object of investigation. The use of gaseous deuterium was dictated by the possibility of obtaining its initial parameters with a high certainty, because they are fully determined by the initial gas pressure and temperature. Besides, the temperature and light absorption coefficients were measured in this work simultaneously with the compressibility, allowing additional information to be gained on the parameters of the state and optical properties of the shock-compressed deuterium plasma.

Experimental measurements of dynamic characteristics. For the experiments with gaseous deuterium under a high initial pressure, a hemispherical capsule was devised (Fig. 1), whose geometrical sizes corresponded to a hemispherical shock-wave generator MZ-13 [8]. Capsule frame *1* and base *2* were made from a high-strength steel possessing high stability of its characteristics in a hydrogen atmosphere. To

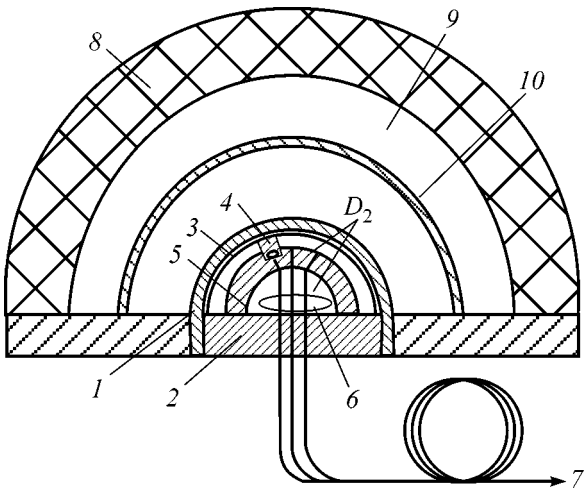

Fig. 1. Hemispherical experimental device: (*1*) frame; (*2*) base; (*3*) screen (aluminum AD-1); (*4*) aluminum (AD-1) sample; (*5*) housing; (*6*) optical sensors; (*7*) measuring line; (*8*) explosive; (*9*) air gap; (*10*) impactor (steel *3*).

enhance the shock-compression pressure in deuterium, hemispherical 1.5-mm-thick aluminum (AD-1) screen *3* was placed under steel frame *1*.

At a fixed distance (determined by the height of aluminum samples *4*) from the aluminum screen, hemispherical brass housing *5* was mounted, inside which eight optical sensors *6* for measuring shock velocity in deuterium were symmetrically arranged on a circle with radius $R = 5$ mm. Similar sensors were also placed beneath the samples to measure shock velocity in them and use this velocity for determining the shock-compression parameters in the aluminum screen. The sensors were fabricated from 200-μm o.d. silica fibers with several-micron-thick aluminum jackets along the whole length to eliminate spurious illumination. The fibers were glued in base *2* and brass hemisphere *5*; their polished top ends were mounted flush with the outer surface of the hemisphere. The bottom (in the scheme) ends terminated in the optical connector (not shown in the figure) for joining the optical sensors to external fiber lines *7*, through which the shock-front radiation was transmitted to detectors. The central fiber, with a diameter of 600 μm, served also for measuring the shock velocity in gas and the shock-front temperature.

After the initiation of potent explosive *8*, steel hemispherical impactor *10* was accelerated through gap *9* by the explosion products to form, upon the collision with hemispherical frame *1*, a shock wave in it, that was then sequentially transmitted to the aluminum housing of sensors *6* and to the gaseous deuterium. The latter was compressed and irreversibly heated. To eliminate the influence of the shock wave on the experimental results, air from the space between frame *1* and impactor *10* was pumped out to a residual pressure of no higher than 10 torr.

The capsule was filled with gaseous deuterium from a metal-hydride source of high-pressure vanadium-based hydrogen isotopes. To achieve a pressure of 250 MPa using the vanadium-deuteride source, it suffices to heat it to a temperature of ~450 K [9].

Before the experiments, the capsules were tested for strength and tightness. The tests showed that the capsules withstood up to a gas pressure of ~220 MPa without destruction and noticeable residual deformations of the construction. During the course of testing, deformation of hemisphere floors was detected, and it was subsequently taken into account in the processing of the experimental results.

Two experiments, with the initial gas parameters $P_0 \approx 203$ MPa (2000 atm) and $T_0 = 273$ K in the first experiment and $P_0 \approx 157$ MPa (1550 atm) and $T_0 = 278$ K in the second, were performed using shock-wave generators of the same type. The gas temperature was assumed to be equal to the temperature measured by a thermocouple at the hemispherical capsule surface. Under these conditions, the initial gas densities calculated according to [10] were $\rho_0 = 0.153$ g/cm^3 and $\rho_0 = 0.1335$ g/cm^3, respectively, which is close to the density of liquid deuterium ($\rho_0 = 0.171$ g/cm^3).

The shock-front glow was detected in the visible region by optical transducers based on photodiodes with a signal rise time no worse than 2 ns and photomultipliers with an anode-pulse rise time of 1.2 ns. The shock-wave passage time was measured from the instant of glow appearance to the instant of glow decay due to the damage of the fiber end by the shock wave. The typical oscillograms of the shock-front glow in gaseous deuterium are shown in Fig. 2. The brightness temperature of shock-compressed deuterium was determined from the glow amplitude (Fig. 2b) in the saturation region.

The measurements of the average shock velocities in dense gaseous deuterium gave $D_{exp} = (29.14 \pm 0.56)$ km/s at $P_0 > 203$ MPa (2000 atm) and $D_{exp} = (29.29 \pm 0.36)$ km/s at $P_0 \approx 157$ MPa (1550 atm). The measurement error was determined using Student statistics with a fiducial probability of 90%. The experimental values of the average shock velocity corresponded to the middle of the gauge length, and, to reduce them to the shock-decay boundary at the deuterium–aluminum interface (Fig. 1), corrections were introduced. To this end, one-dimensional calculations of the shock motion in the elements of the experimental hemispherical device were performed using the gas-dynamic program developed at the Russian Federal Nuclear Center, All-Russia Research Institute of Experimental Physics. For the deuterium calculations, the equation of state was borrowed from [11], and the equations of state for the remaining materials were those used at the Institute. To assess the correctness of the equations of state used in the program for the materials of the device, an independent test of the computational scheme was carried out. In the test calculations, the shock velocities in 4-mm-thick iron and aluminum screens were estimated and the results were compared with the experimental data for MZ-13 in [8]. The testing showed that shock velocities calculated for iron and aluminum agree, to within 1%, with the experimental data $D_{Fe} = 17.35$ km/s and $D_{Al} = 20.9$ km/s [8].

The transition from the measured shock velocities to their instant values corresponding to the shock-decay boundary at the aluminum–deuterium interface was done as follows. The results of gas-dynamic computations were used to calculate the average shock velocities $\bar{D}$ in deuterium and the velocities D_b at the screen–deuterium boundary. Since the shock wave in a hemispherical generator is nonstationary, the average velocity on the measurement radius exceeds the velocity D_b at the inner boundary of the screen. With allowance made for the relative difference between the values $\delta D = (\bar{D} - D_b)\bar{D}$ obtained from the computational results, the corrections $\Delta D = \delta D D_{exp}$ to the experimentally measured shock velocity were calculated. The resulting shock velocities in gaseous deuterium became

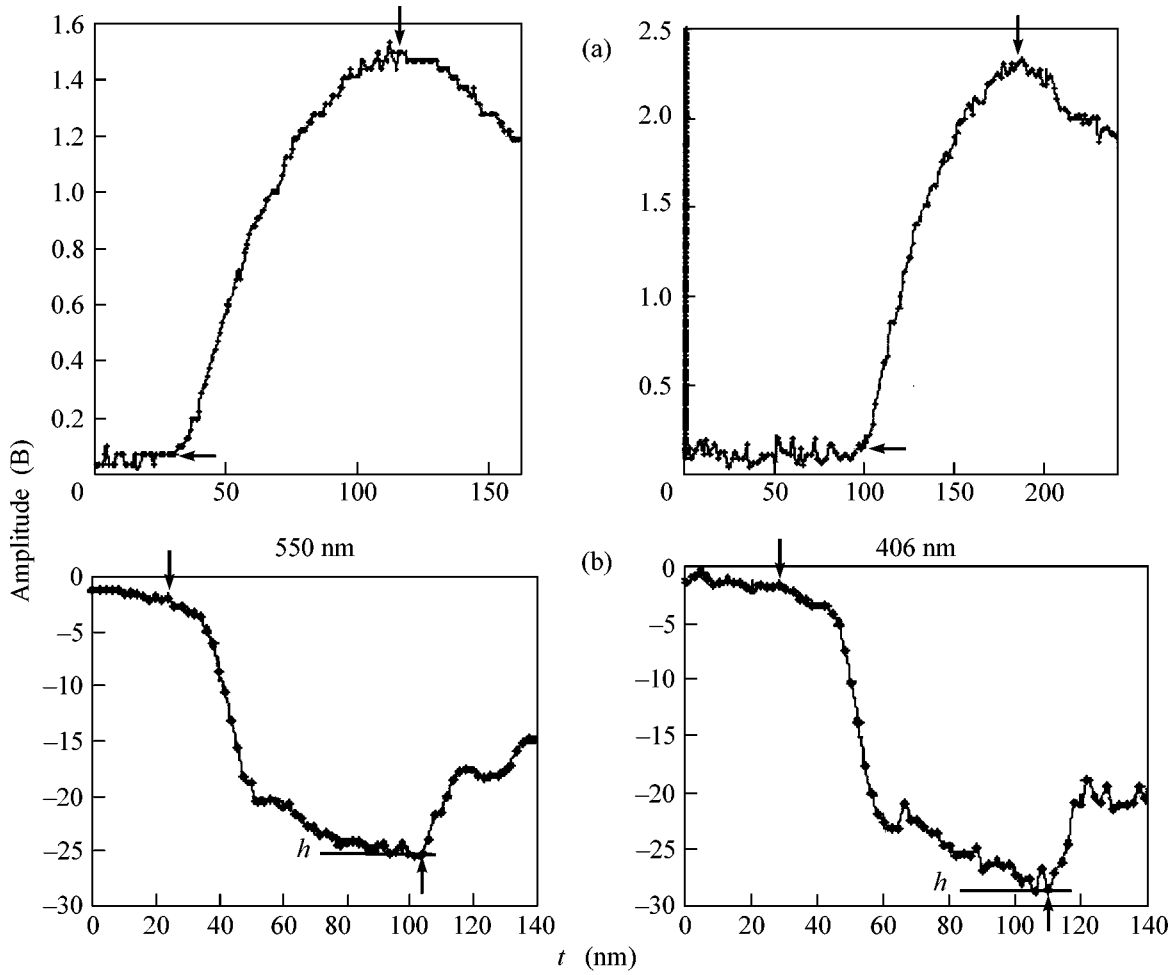

Fig. 2. Shock-front radiation oscillograms for gaseous deuterium. Detectors: (a) photodiode sensors and (b) photomultipliers. Arrows show the points at which the time of shock-wave motion was measured.

reduced to its boundary with aluminum: D_b = 27.95 km/s in the first experiment and D_b = 28.02 km/s in the second.

The correction to the average shock velocity D_{exp} = 21.17 km/s measured in the experiments with reference aluminum samples was done in a similar way. The corrected shock velocity in aluminum at the boundary with deuterium was found to be D_b(Al) = 20.4 km/s.

The solution to the problem of shock decay at the deuterium–aluminum boundary with the indicated velocities and the use of the law of conservation of mass bring about the following shock-compression parameters for gaseous deuterium: D = 27.95 km/s (shock velocity), U = 21.84 km/s (mass velocity), P = 93.4 GPa, and $\rho = (0.70 \pm 0.06)$ g/cm^3 in the first experiment and D = 28.02 km/s, U = 22.2 km/s, P = 83 GPa, and $\rho = (0.64 \pm 0.04)$ g/cm^3 in the second. To solve the problem, an aluminum unloading isentrope was constructed using the equation of state given in [12]. The initial state on the Hugoniot curve had parameters U = 12.04 km/s and P = 665.4 GPa that were obtained from the shock-velocity measurements in aluminum (D_b(Al) = 20.4 km/s).

Measurements of the optical characteristics of shock-compressed deuterium. The temperature of shock-compressed deuterium was measured using a high-speed four-channel optical pyrometer [13]. The radiation of the shock front in deuterium was recorded via the fiber line at wavelengths of 450, 498, 550, and 600 nm. To separate the corresponding spectral intervals, a set of interference light filters with a transmission bandwidth at half maximum $\Delta\lambda \approx 10$ nm was used. Prior to the experiments, the optical line for measuring temperature was calibrated against a reference light source. The thermal radiation flux from a heated body with the radiating capacity R is given by the Planck's formula,

$$N(\lambda) = RC_1\lambda^{-5}[\exp(C_2/\lambda T) - 1]^{-1} = C_1\lambda^{-5}[\exp(C_2/\lambda T_b) - 1]^{-1}. \quad (1)$$

Table

Experiment				Calculations (chemical model [1, 23])							Experiment
ρ_0, g/cm^3	P, GPa	ρ, g/cm^3	T, 10^3 K	T, 10^3 K	n_e, 10^{22}/cm	n_D, 10^{22}/cm	n_{D2}, 10^{22}/cm	Γ_D	$n_e\lambda_e^3$	$\pi(\Sigma n_j g_d^3)/6$	
0.134	83	0.64	22.9	23.2	2.3	5.1	5.6	15	2.7	0.42	This work
0.153	93.4	0.70	24.1	22.5	2.5	5.0	6.6	16	3.0	0.47	This work
0.171	107	0.77	–	23.0	2.8	5.3	7.1	17	3.4	0.50	[25]
0.199	121	0.85	–	21.9	3.0	4.9	8.5	18	3.8	0.57	[7]

Here, R is the radiating capacity of the body, λ is the wavelength, T is the actual temperature, T_b is the brightness temperature, and the constants are $C_1 = 1.19 \times 10^{-16}$ (W m^2)/sr and $C_2 = 0.0144$ mK. The temperature of the shock-compressed gaseous deuterium was determined from the four measured spectral temperatures by the nonlinear least-squares method for two parameters T and R, followed by iterations to obtain exact estimates for the quantities of interest.

At the spectral temperatures experimentally measured for the shock-compression pressure $P = 93.4$ GPa in the range 450–600 nm, the best fit to the Planck's function is achieved, in the grey-body approximation, at the temperature $T = 24100 \pm 2200$ K and a radiating capacity of 0.485 ± 0.075.

Analysis of the oscillograms obtained in the experiment with pressure $P = 83$ GPa (Fig. 2b) indicates that the saturation of the shock-front radiation corresponding to the optical thickness (close to unity) of shock-compressed gaseous deuterium is not achieved in the blue spectral region ($\lambda = 406$ nm). Since this does not allow the use of the least-squares method for estimating the actual temperature and radiating capacity, only the average value $T = 22900 \pm 2000$ K of the brightness temperature was presented for this experiment.

As in [14, 15], the rise of the shock-front glow after the wave enters gaseous deuterium can be due to the increase in the thickness of the shock-compressed layer and to its transparency. Neglecting the reflection and using the Bouguer–Lambert–Beer formula for transmittance,

$$\tau = \exp(-\alpha l), \tag{2}$$

where α is the absorption coefficient of a layer of thickness l, one can write the rise of radiation intensity in the normal direction as

$$\begin{aligned} I &= I_0[1 - \exp(-\alpha l)] \\ &= I_0[1 - \exp(-\alpha\{D - U\}t)], \end{aligned} \tag{3}$$

where I_0 is the radiation intensity of an optically dense layer, $l = (D - U)t$ is the thickness of a shock-compressed substance, and t is the shock-wave passage time in the substance. Then, with the known kinematic parameters D and U, one can use the experimental oscillogram to determine the light absorption coefficient α in the shock-compressed deuterium:

$$\alpha = -I_0[1/(D - U)t]\ln(1 - I/I_0). \tag{4}$$

The average value of this coefficient obtained for the compressed gaseous deuterium after processing the experimental oscillograms was found to be $\alpha \approx 69$ cm^{-1} in the wavelength range 450–600 nm for a shock compression of 93 GPa.

The estimates made for the absorption coefficient within the framework of the classical approach using the calculated parameters and the Kramers–Unsold formula give $\alpha \approx 4 \times 10^4$ cm^{-1}, which is three orders of magnitude larger than the measured values. Such a discrepancy is evidence that the ionization and dissociation processes at the shock front likely bypass the rise of the plasma-bunch radiation.

Comparison with the results of theoretical calculations. Our experiments differ from the majority of previous experiments in that the dynamic compression characteristics fixing the position of the Hugoniot curve in the P–V plane are measured simultaneously with the temperature of the shock-compressed deuterium, which is highly important for the construction of a complete thermodynamic map for the system.

The experimental results are presented in the table and Fig. 3 in the pressure–density coordinates and, in the temperature–pressure coordinates, in the same table and Fig. 4, together with the available experimental data and the results of theoretical calculations in two variants.

In the first variant, the calculations were carried out using the equation of state constructed for hydrogen within the relatively simple compressible covolume model (CCM) [11]. A mixture of five sorts of particles was considered: molecules, atoms, positive molecular ions, protons, and electrons. The thermal equation of state for the particle of the ith sort has the form $V_i(P, T) = V_{C,i}(P) = R_m T/P$, where V is the molar volume and R_m is the molar gas constant. The covolumes $V_{C,i}$ were assumed to depend only on pressure and be additive. For molecules, the covolume was constructed using the experimental data on the static compression of solid hydrogen up to a pressure of 2.5 GPa [16] and quasi-adiabatic compression of gaseous hydrogen in

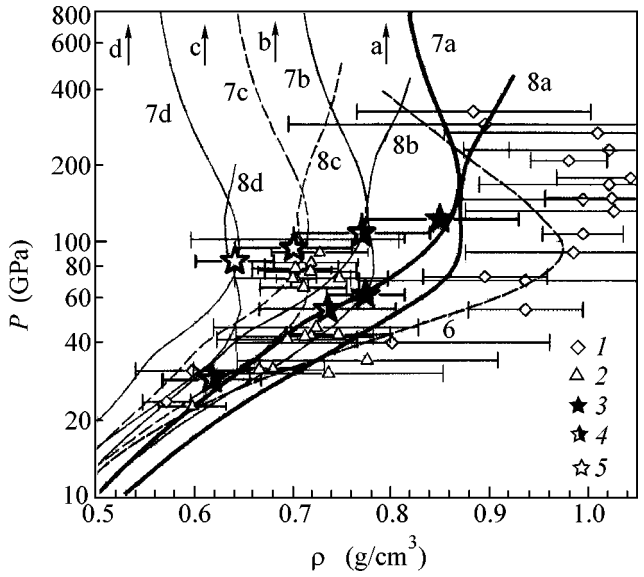

Fig. 3. Deuterium Hugoniot adiabates. Experiment: (*1*) [3], (*2*) [6], (*3*) [2, 7], (*4*) [25], and (*5*) this work. Calculations: (*6*) [27], (*7*) SAHA-IV [1, 23], (*8*) CCM [11], solid thick line for $\rho_0 = 0.199$ g/cm^3, solid thin line for $\rho_0 = 0.171$ g/cm^3, dash-and-dot line for $\rho_0 = 0.153$ g/cm^3, and the dotted line for $\rho_0 = 0.1335$ g/cm^3. Arrows indicate the "limiting" compressions ($\rho/\rho_0 = 4$) for each of the four Hugoniot curves.

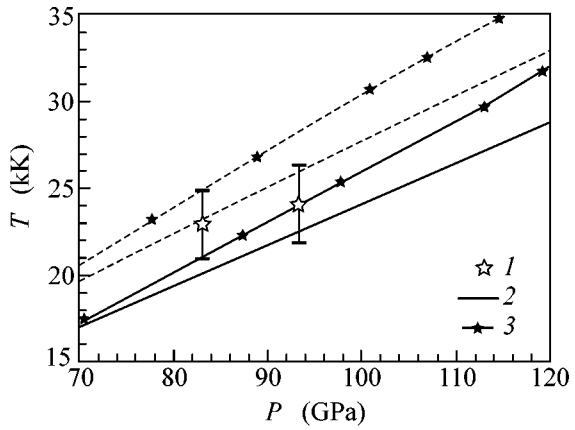

Fig. 4. Pressure dependence of the temperature of shock-compressed gaseous deuterium: (*1*) experiment; calculation: (*2*) SAHA-IV model [1, 23], (*3*) CCM model [11]; solid lines are for $\rho_0 = 0.153$ g/cm^3 and dashes are for $\rho_0 = 0.1335$ g/cm^3.

the pressure range 40–800 GPa [17, 18]. For atoms, the covolume was constructed using simple theoretical estimates and experimental results for $P > 300$ GPa [17, 18]. For molecular ions and protons, they were taken to be formally equal to the covolumes of, respectively, molecules and atoms (for electrons, $V_{C,e}(P) \equiv 0$). The caloric equation of state was obtained from the thermal equation using the second law of thermodynamics. The contribution from the vibrational and rotational degrees of freedom of molecules and molecular ions in the partition functions was taken into account in the "rigid rotator–harmonic oscillator" approximation, without rovibrational cutoff at the level of dissociation energy, while the contribution from the excited electronic states was disregarded. The equations for the equilibrium concentrations of the components have the form of the usual Saha equations, in which the equilibrium constant is additionally multiplied by the factor $\exp(-\Delta G_{C,r}(P)/RT)$, where $\Delta G_{C,r}$ is a change in the covolume chemical potential in the rth reaction. As a result, the energy of molecular dissociation into two atoms formally decreases by $\Delta G_{C,\mathrm{dis}}(P) = 2G_{G,D}(P) - G_{C,D2}(P)$ with the pressure buildup, whereas the ionization potentials of molecules and atoms do not change by virtue of the definition adopted above for the covolumes of charged particles. For the states achieved in our experiments, the CCM calculations predict a noticeable degree, $n_D/n_{D2} \sim 3$, of deuterium dissociation and a relatively low degree, $n_{D+}/n_D \sim 10^{-2}$, of temperature ionization. The CCM-calculated Hugoniot curves show two density maxima: the lower corresponds to the molecular dissociation, and the upper corresponds to the particle ionization. The position of the second maximum can be affected by many factors. In particular, the rovibrational cutoff at the level of dissociation energy of molecular ions leads to a decrease in the concentration of this component in the mixture at high temperatures and pressures and, as a result, to a noticeable decrease in the density and pressure at the upper maximum and to a steeper asymptotic form of the Hugoniot adiabate $\rho_{\mathrm{Hug}} \longrightarrow 4\rho_0$.

In the second variant, the calculations were performed using a modified plasma chemical model [19] with the universal SAHA-IV code [20]. In this model, hydrogen (deuterium) was calculated as a strongly nonideal mixture of ions, electrons, atoms, molecules, and D^- and D^{2+} ions. When calculating the equilibrium plasma composition and its thermodynamic properties, the partial degeneracy of the electronic component and the interactions between all sorts of particles were taken into account. To describe the coulombic nonideality, an improved modification of the pseudopotential approach suggested in [21] was used. With this modification, the effective electron–ion interaction was described by the short-range-corrected Coulomb potential (Glauberman–Yukhnovskiĭ potential). The effective depth of this potential was taken as equal to the interaction energy of an electron–ion pair at the average distance between heavy particles (ions, atoms, and molecules). This corresponds to the cutoff energy adopted in this model for separating the free and bound (intraatomic) states in the calculation of atomic partition functions. Apart from the contribution from the Coulomb interaction between charged particles, the strong repulsion of heavy particles at close distances [20] was

taken into account. This was accomplished using the approximate equation of state for "soft spheres" [22], modified to a mixture of particles with different diameters. The degree of softness of the intermolecular repulsion potential was chosen from the requirement of the best description of the experimentally measured equation of state for condensed hydrogen at room temperature. The calculations in this approximation [1, 23] showed not only the dominant role of the D_2–D_2 interaction but also that the position of the deuterium Hugoniot adiabate and the temperature dependences on the adiabate are highly sensitive to the choice of the D–D and, notably, D–D_2 repulsion parameters. In our calculations (part of them are summarized in the table), the parameters of the intermolecular and interatomic repulsions were chosen according to the *ab initio* atom–atom approximation [24]. In terms of the model of soft spheres, this leads to a relatively high ratio of the effective diameter of deuterium atom to the diameter $D_2\{d(D)/d(D_2) \sim 0.8\}$. An important consequence of this choice is that the "self" volumes of the reaction products show no appreciable change during the deuterium dissociation process and, correspondingly, there is no mechanism that would stimulate the pressure-induced dissociation in a strongly compressed equilibrium system of molecules and atoms at the expense of the gain in self-volume.

Calculations in the modified plasma chemical model [1, 19, 23] show that the states arising behind the shock-wave front in this work and in the experiments with maximal pressure [2, 7] correspond to a dense strongly nonideal ($\Gamma_D \approx 1$), partially ionized ($n_e/n_D \sim 1$), partially degenerate ($n_e\lambda_e^3 \sim 3$), and practically isothermic ($T \approx 22$–24 kK) deuterium plasma with parameters given in the table.

An analysis of the data presented in the table shows that the physical conditions realized in the shock experiments at the Institute of Experimental Physics are distinguished by a combination of strong coulombic nonideality ($\Gamma_d \gg 1$), electron-component degeneracy ($n_e\lambda_e^3 \sim 1$), and strong influence of the short-range repulsion that manifests itself in the high values of the so-called packing parameter $\pi n_i d_i 3/6 \sim 1$ (d_i is the self-size of a heavy particle of the ith sort (atom, molecule, etc.)).

One can see in Fig. 3 that the experimental data obtained in this work agree well with the data calculated on the basis of the CCM and SAHA-IV models. It is worthy of note that these theoretical models *agree simultaneously* both with the results of our experiments on the shock compression of a preliminarily compressed gaseous deuterium and with the results of the shock compression of liquid and solid deuterium [2, 7, 25]. This suggests that the results of all shock-wave experiments conducted at the Institute of Experimental Physics are mutually consistent. Nevertheless, the fact that, although the Hugoniot adiabates in both theoretical models tend to the ideal-gas asymptotic compression limit $\rho_{Hug}/\rho_0 \longrightarrow 4$ [26] at the high-pressure and high-temperature limits, the character of this tendency is different for both models. This renders the necessity of obtaining new experimental data in the pressure range ~0.2–1.0 TPa topical and necessitates the use of *ab initio* calculations for determining the thermodynamic functions of dense hydrogen (deuterium) plasma.

From the comparison (Fig. 4) of the experimentally determined and calculated temperatures, it follows that, as earlier, the experimental results obtained in this agree satisfactorily with the results of both CCM and SAHA-IV calculations. It should be noted that the coincidence of the theory and experiment for the caloric and thermal equations of states indicates, first, that the theoretical models are adequate and, on the other hand, that the experimental data obtained in this work are self-consistent.

This work was supported in part by the complex program "Thermal Physics and Mechanics of Intense Pulsed Actions," a Presidential Grant (no. (NSh-1938.2003.2), and a State Contract of the Ministry of Education and Science of the Russian Federation (no. 40.009.1.1.1192).

REFERENCES

1. V. E. Fortov, V. Ya. Ternovoĭ, M. V. Zhernokletov, *et al.*, Zh. Éksp. Teor. Fiz. **124**, 288 (2003) [JETP **97**, 259 (2003)].
2. S. I. Belov, G. V. Boriskov, A. I. Bykov, *et al.*, Pis'ma Zh. Éksp. Teor. Fiz. **76**, 508 (2002) [JETP Lett. **76**, 433 (2002)].
3. L. D. Da Silva, P. Gelliers, G. W. Collins, *et al.*, Phys. Rev. Lett. **78**, 483 (1997).
4. A. N. Mostovych, Y. Chan, T. Lehecha, *et al.*, Phys. Rev. Lett. **85**, 3870 (2000).
5. D. L. Hanson, J. R. Asay, C. A. Hall, *et al.*, in *Shock Compression of Condensed Matter*, Ed. by M. D. Furnish, L. C. Chhabildas, and R. S. Hixson (Am. Inst. of Physics, Melville, N.Y., 1999), p. 1175.
6. M. D. Knudson, D. L. Hanson, J. E. Bailey, *et al.*, Phys. Rev. Lett. **87**, 225501 (2001); Phys. Rev. Lett. **90**, 035505 (2003); Phys. Rev. B **69**, 144 209 (2004).
7. G. V. Boriskov, A. I. Bykov, R. I. Il'kaev, *et al.*, Dokl. Akad. Nauk **392**, 755 (2003) [Dokl. Phys. **48**, 553 (2003)].
8. L. V. Al'tshuler, R. F. Trunin, K. K. Krupnikov, and N. V. Panov, Usp. Fiz. Nauk **166**, 575 (1996) [Phys. Usp. **39**, 539 (1996)].
9. A. N. Golubkov and A. A. Yukhimchuk, Hyperfine Interact. **138**, 403 (2001).
10. A. Michels, W. de Graff, T. Wassenaar, *et al.*, Physica (Amsterdam) **25**, 25 (1959).
11. V. P. Kopyshev and V. V. Khrustalev, Prikl. Mekh. Tekh. Fiz., No. 1, 122 (1980).

12. B. L. Glushak, L. F. Gudarenko, Yu. M. Styazhkin, and V. A. Zherebtsov, Vopr. At. Nauki Tekh., Ser.: Mat. Model. Fiz. Protsessov, No. 1, 32 (1991).
13. M. A. Mochalov, T. S. Lebedeva, A. B. Medvedev, *et al.*, in *Proceedings of 12th APS Topical Group Meeting on Shock Compression of Condensed Matter*, Ed. by Donna M. Baudrau (CMP, Atlanta, Georgia, 2001); Bull. Am. Phys. Soc. **46** (4), 60 (2001).
14. S. B. Kormer, Usp. Fiz. Nauk **94**, 641 (1968) [Sov. Phys. Usp. **11**, 229 (1968)].
15. V. D. Glukhodedov, S. I. Kirshanov, T. S. Lebedeva, and M. A. Mochalov, Zh. Éksp. Teor. Fiz. **116**, 551 (1999) [JETP **89**, 292 (1999)].
16. M. S. Anderson and C. A. Swenson, Phys. Rev. B **10**, 5184 (1974).
17. F. V. Grigor'ev, S. B. Kormer, O. L. Mikhaĭlova, *et al.*, Pis'ma Zh. Éksp. Teor. Fiz. **16**, 286 (1972) [JETP Lett. **16**, 201 (1972)].
18. F. V. Grigor'ev, S. B. Kormer, O. L. Mikhaĭlova, *et al.*, Zh. Éksp. Teor. Fiz. **69**, 743 (1975) [Sov. Phys. JETP **42**, 378 (1975)].
19. *Thermal Properties of Working Media of Gas-Phase Nuclear Reactor*, Ed. by V. M. Ievlev (Atomizdat, Moscow, 1980) [in Russian].
20. V. K. Gryaznov, I. L. Iosilevskiĭ, and V. E. Fortov, in *Shock Waves and Extreme States of Matter*, Ed. by V. E. Fortov, L. V. Al'tshuler, R. F. Trunin, and A. I. Funtikov (Nauka, Moscow, 2000; Springer, New York, 2004).
21. I. L. Iosilevskiĭ, Teplofiz. Vys. Temp. **18**, 355 (1980).
22. D. Young, *Soft Spheres Model for Equation of State*, LLNL Report (Univ. of California, 1977), UCRL-52352.
23. V. K. Gryaznov, I. L. Iosilevskiĭ, and V. E. Fortov, in *Physics of Extreme States of Substance-2001*, Ed. by V. E. Fortov (IKhPF, Chernogolovka, 2001), p. 114 [in Russian].
24. E. S. Yakub, Teplofiz. Vys. Temp. **28**, 664 (1990); Physica B (Amsterdam) **265**, 31 (1999).
25. G. V. Boriskov, A. I. Bykov, R. I. Il'kaev, *et al.*, Phys. Rev. B (in press).
26. Ya. B. Zel'dovich and Yu. P. Raĭzer, *Physics of Shock Waves and High-Temperature Hydrodynamic Phenomena*, 2nd ed. (Nauka, Moscow, 1966; Academic, New York, 1967).
27. M. Ross, Phys. Rev. B **58**, 669 (1998).

Translatedrho by V. Sakun

JETP Letters, Vol. 80, No. 6, 2004, pp. 405–409. Translated from Pis'ma v Zhurnal Éksperimental'noĭ i Teoreticheskoĭ Fiziki, Vol. 80, No. 6, 2004, pp. 459–463.

Thermoelectric Properties of High-Pressure Silicon Phases

S. V. Ovsyannikov[1], V. V. Shchennikov[1, *], and A. Misiuk[2]

[1] *Institute of Metal Physics, Ural Division, Russian Academy of Sciences, Yekaterinburg, Russia*

[2] *Institute of Electron Technology, PL-02-668 Warsaw, Poland*

* *e-mail: vladimir.v@imp.uran.ru*

Received June 3, 2004; in final form, July 12, 2004

The thermo emf in Czochralski-grown silicon single crystals (Cz-Si) was experimentally studied in a range of pressures up to 20 GPa. The pressure dependences revealed phase transitions in the metallic phase of silicon, which passed from tetragonal to orthorhombic and then to hexagonal lattice. The high-pressure silicon phases, as well as the metallic high-pressure phases in A_NB_{8-N} semiconductors, possess conductivity of the hole type. As the pressure decreases, the emf behavior reveals transitions to the metastable phases Si-XII and Si-III. Preliminary thermobaric treatment of the samples at a pressure of up to 1.5 GPa and a temperature of T = 450–650°C influences the thermoelectric properties of Cz-Si at high pressures. © *2004 MAIK "Nauka/Interperiodica".*

PACS numbers: 72.20.Pa

The advantages of high-pressure measurements, offering an effective tool for studying semiconductor materials, were demonstrated half a century ago by the results of investigation of the electrical properties of silicon and germanium [1]. Theoretical and experimental investigations of the properties of silicon at high pressures P are still of considerable importance for elucidating the laws governing transformations of the electron structure depending on the interatomic distances in the entire class of semiconductor materials of the A_NB_{8-N} type (which is most important for practical applications) [2–5]. In addition, the interest in studying the behavior of silicon at high pressures is related to the wide use of silicon-based structures in tensometric devices and, in recent years, in micro- and nanoelectromechanical and -optoelectromechanical (MEMS, NEMS, MOEMS) systems [2].

In a range of pressures up to 20 GPa, silicon forms (besides the initial diamondlike structure) three structural modifications, including body-centered tetragonal (β-Sn type), orthorhombic (*Imma*), and simple hexagonal (*sh*) [3]. The study of the structure of silicon at high pressures (up to ~20 GPa) was performed by means of diffraction of X-ray and synchrotron radiation [3], Raman scattering [4], optical transmission and absorption spectroscopy [5], electric resistance measurements [6, 7], and superconducting transition temperature determination [8, 9]. Some of these methods were more sensitive to certain phase transitions and much less effective in the study of other transformations. For example, the transition from tetragonal (β-Sn) to orthorhombic (*Imm*) modification, according to the structural data [3], is accompanied by a very small change in the volume (~0.2%) as compared to that observed for the subsequent phase transition onto the hexagonal *sh* phase (~0.5%). However, the former transition, being much stronger, affects the superconducting transition temperature [9]. The scatter of pressures corresponding to the phase transitions in silicon observed in the published data [3–9] is also related to the fact that structure-sensitive techniques reflect termination of the phase transformation [3], whereas monitoring of the electron properties allows the onset of the transition to be detected [6, 7].

A highly effective method for the investigation of phase transitions in crystals under pressure is based on the measurement of thermo emf [10, 11], especially in cases where such transitions are accompanied by significant changes in the electron structure (in particular, by inversion of the sign of majority carriers). The original investigations of the thermoelectric properties of silicon at high pressures [12–14] revealed a semiconductor–metal phase transition related to the structure transformation from a diamondlike to tetragonal β-Sn lattice, which is actually accompanied by inversion of the sign of thermo emf [13, 14]. It is interesting to note that the results of thermoelectric measurements in silicon under pressure [12] were also useful for explaining a decrease in thermo emf observed in the experiments with silicon point contacts [15] performed within the framework of investigations of the electron-phonon interactions and the phonon density of states [15]. However, the phase transitions under pressure in the metallic phase of silicon were not studied by the thermoelectric method.

In this context, the aim of this study was to trace the phase transitions in silicon under pressure of up to ~20 GPa by means of thermo emf measurements.

The experiments were performed on silicon crystals grown by the Czochraski technique. Czochralski-grown

The main parameters of silicon samples (Cz-Si)

No.	Wafer	Annealing conditions			Concentration (cm^{-3})	
		Temperature (°C)	Pressure (GPa)	Time (h)	Residual oxygen	Carrier (type)
I	Si W18		Initial		11×10^{17}	1.86×10^{15} (*p*)
D1	Si W18	450	0.0001	10	10.3×10^{17}	3.1×10^{15} (*n*)
D2	Si W18	450	0.1	10	8.9×10^{17}	3.7×10^{15} (*n*)
D3	Si W18	450	0.6	10	8.7×10^{17}	5×10^{15} (*n*)
D4	Si W18	450	1.4–1.45	10	7.7×10^{17}	1.48×10^{16} (*n*)
B1	Si W18	600	0.0001	10	10.7×10^{17}	1.86×10^{15} (*p*)
B2	Si W18	600	0.1	10	9.9×10^{17}	9.3×10^{14} (*p*)
B3	Si W18	600	0.6	10	10.2×10^{17}	5.1×10^{14} (*p*)
B4	Si W18	600	1.4–1.45	10	10.2×10^{17}	9.6×10^{14} (*p*)
C1	Si W19	650	0.0001	10	9.1×10^{17}	2.04×10^{15} (*p*)
C2	Si W19	650	1.5	10	8.2×10^{17}	1.12×10^{15} (*p*)

silicon (Cz-Si) wafers contain residual oxygen atoms occupying predominantly interstitial lattice sites [16–18]. Under the action of pressure and temperature (annealing), a certain fraction of interstitial oxygen atoms forms (depending on the treatment conditions) electrically active clusters (thermodonors), while other atoms form coarse, electrically inactive precipitates. This may change both mechanical and electrical properties of Cz-Si [16–18]. Our samples were cut from two Cz-Si wafers (W18 and W19) with a high content of interstitial oxygen. In order to vary the charge carrier density, the samples were annealed (at 450, 600, or 650°C) under high pressure (~1.5 GPa) in the gas phase (helium or argon) [19]. The treatment conditions are listed in Table 1. The crystal structure of Cz-Si samples before and after treatment at various pressures up to ~20 GPa was monitored by ultrasoft X-ray spectroscopy using $L_{2,3}$ emission lines [14].

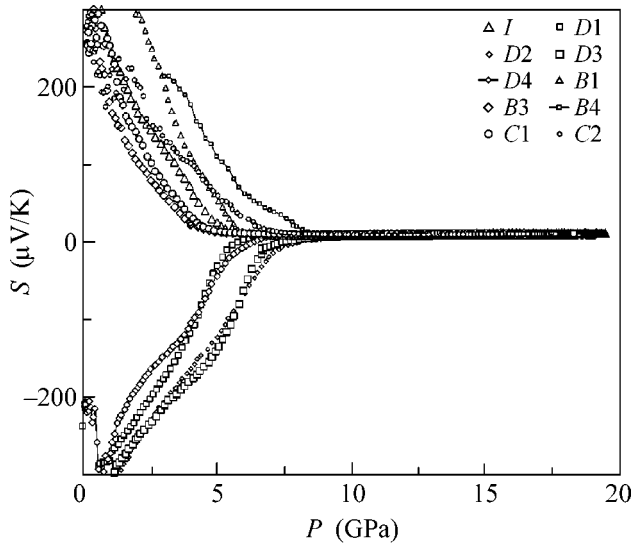

Fig. 1. Plots of the thermo emf *S* vs. pressure *P* for Cz-Si samples measured at $T = 295$ K in the vicinity of the semiconductor–metal transition (measurements in the pressure increase mode).

In this study, the values of thermo emf $S(P)$ and electric resistance $R(P)$ of Cz-Si samples with dimensions ~$0.2 \times 0.2 \times 0.05$ mm were measured in high-pressure chambers made of conducting diamond anvils [10]. Alternative techniques using a chamber with a compressed capsule [20] or transparent diamond anvils with implanted contacts [21] restrict the pressure interval of thermo emf measurements to 12 GPa. The pressure in a compressed spacer made of a lithographic stone was determined using calibration plots preliminarily constructed by monitoring phase transitions in a series of reference substances (ZnSe, CdTe, etc.) with an error of ~10% [10, 12]. The temperature gradient was created by heating one of the anvils; the temperature was monitored with the aid of thermocouples fastened at various points on the anvils [22, 23]. The values of $S(P)$ and $R(P)$ were measured as described in [10, 12] on an automated setup capable of monitoring and storing data on the pressure (force), temperature difference, sample response signals, anvil displacement (compressive strain of the sample), and some other parameters [22, 23]. The errors of determining *S* and *R* amounted to ~20 and 5%, respectively. The accuracy of thermo emf determination was checked by measuring a sample of lead (special purity grade), the thermo emf of which is close to zero ($S \approx -1.27$ μV/K) [24, 25].

Preliminary thermobaric (P–T) treatment of the samples led to a change in the density and type of charge carriers (as a result of the formation of thermodonors [26, 27]; see table) and, accordingly, to modification of the $S(P)$ curve (Fig. 1). However, in the region corresponding to the metallic phase of silicon (i.e., above the point of the semiconductor-metal phase tran-

sition, $P \geq 7$ GPa), the plots of thermo emf versus pressure for Cz-Si samples of both *p* and *n* types were similar (Fig. 2). The samples with positive thermo emf exhibited a minimum of *S* at $P \sim 7$–11 GPa, followed by a growth of *S* with *P* up to ~13–14 GPa and by subsequent decrease of *S* at pressures above 15–16 GPa (Fig. 2). The last two features were also observed in the *S*(*P*) curves of most samples with the *n* type of conductivity (Fig. 2). The values of thermo emf in the metallic phases of all samples were close ($S \approx 8 \pm 3$ μV/K), but these values exhibited significant variations with pressure. For example, the baric coefficient of thermo emf for samples of the *p* type doubly changed sign in the pressure range studied (*P* up to 20 GPa) (see Fig. 2).

It is natural to attribute sharp changes in the baric coefficient of thermo emf, *dS*/*dP* (Fig. 2), to phase transitions in the metallic phase of silicon, where β-Sn, *Imma*, and *sh* lattices are sequentially formed as the pressure increases from ~10 to 16 GPa [3]. In contrast to thermo emf, the values of electric resistance *R* and its baric coefficient changed rather insignificantly in the pressure range studied (these data are not presented here). The high-pressure phases of silicon are characterized by high values of the optical reflection coefficients in the visible spectral range [5], which gives evidence of a high density of charge carriers and agrees with the low values of thermo emf observed for these phases (Fig. 2). Indeed, the optical properties of the *sh* phase of silicon correspond to the model of a polyvalent metal (such as aluminum) with almost free charge carriers [5]. However, in contrast to trivalent aluminum characterized by the negative thermo emf [25], the high-pressure phases of silicon (as well as most of the metallic high-pressure phases of $A_N B_{8-N}$ semiconductors [11]) exhibit positive thermo emf (Fig. 2).

The results of the electron structure calculations for the β-Sn silicon phase [28] showed that this phase represents a metal with strongly overlapped bands. Reduction of the crystal symmetry from cubic to tetragonal, with the corresponding increase in the coordination number from 4 to 6, alters the arrangement of electron energy levels. As a result, the *d* orbitals begin to participate in the formation of two new bonds. In the metallic β-Sn silicon phase, the *d*-orbitals are strongly coupled with the occupied valence *s* and *p* states, especially in the vicinity of the Fermi level [28]. An expression for the thermo emf of a metal with *s* and *d* electrons playing the role of charge carriers is as follows [24]:

$$S \approx -(\pi^2/3)(k_0/e)(k_0T)[3/(2E_F) - (1/N_d(E))(dN_d(E)/dE)]_{E=E_F},$$

where E_F is the Fermi energy, k_0 is the Boltzmann constant, *e* is the electron charge, *T* is the absolute temperature, *E* is the electron energy, and N_d is the density of states in the *d* band. A contribution due to the scattering of *s* electrons by carriers in the *d* band (the second term in square brackets] usually significantly influences the value and sign of thermo emf [24]. According to the above formula, the difference in thermo emf between various metallic high-pressure silicon phases observed in this study can be explained by variations of the *s*–*d* scattering as a result of crystal lattice reconstruction and the corresponding transformation of the electron structure.

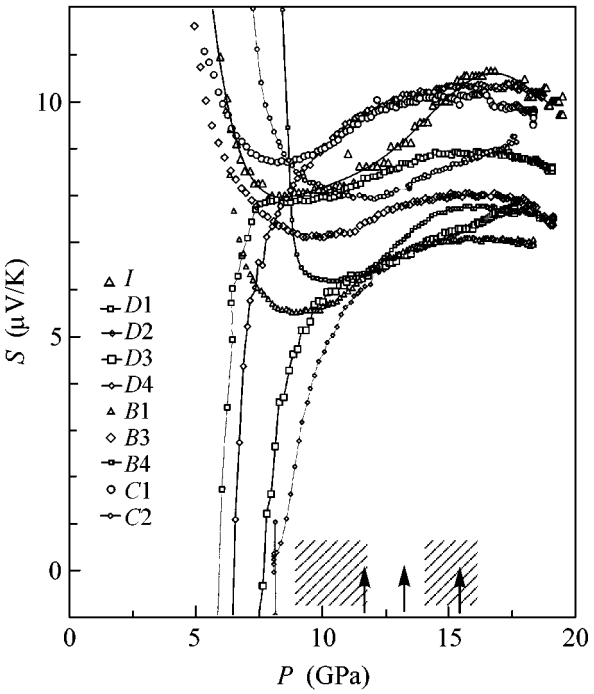

Fig. 2. Fragments of the *S*(*P*) curves in the region of phase transitions in the metallic silicon phase. Arrows indicate the boundaries of transitions to the body-centered tetragonal (β-Sn type), orthorhombic (*Imma*), and simple hexagonal (*sh*) according to [3]. Cross-hatched regions show the scatter of phase transition pressures according to the data reported in [4–9].

When the pressure applied to a sample decreases, silicon exhibits reverse phase transitions to the rhombohedral Si-XII (*r*8) phase (at ~9.4 GPa) and the body-centered cubic Si-III (*bc*8) phase (~2 GPa) [3, 29]. These transitions are clearly manifested by changes in the baric coefficient of thermo emf observed below the indicated *P* values (Fig. 3). The fact that thermo emf values of the Si-III phase ($S \approx +15 \pm 5$ μV/K) are higher than those of the metallic high-pressure silicon phases is consistent with the results of measurements of the Hall effect [29], according to which Si-III is a *p*-type semimetal with indirect (~0.3 eV) band overlap and a hole density of $n_p = (5 \pm 2) \times 10^{20}$ cm^{-3}.

The X-ray emission spectra of the samples measured upon pressure release were rather close to the spectra of amorphous silicon [14]. Detailed analysis of these spectra will be presented in a special publication.

Thus, we have monitored a sequence of phase transitions in silicon (β-Sn ⟶ *Imma* ⟶ *sh*) by measuring changes in thermo emf in the course of increasing

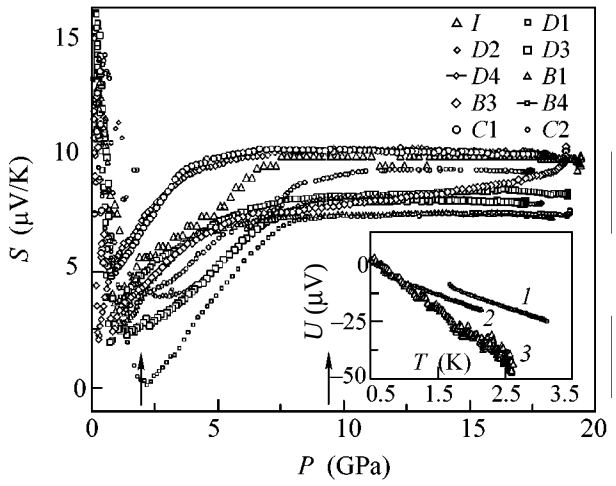

Fig. 3. Plots of the thermo emf S vs. pressure P for Cz-Si samples at T = 295 K (measurements in the pressure decrease mode). Arrows indicate the boundaries of transitions to the rhombohedral Si-XII (*r*8) phase and the body-centered cubic Si-III (*bc*8) phase according to [3]. The inset shows the typical plots of thermoelectric response vs. temperature difference for (*1*) sample *D*2 at 18 GPa and (*2*, *3*) sample *I* at 19.5 GPa and upon pressure release, respectively.

pressure applied to the sample; measurements in the pressure decrease mode revealed transitions to the Si-XII and Si-III phases. The observed high-pressure silicon phases, as well as the metallic high-pressure phases in A_NB_{8-N} semiconductors [11], possess conductivity of the hole type. Because of a very small difference in the total energy of the crystal lattice, the structural transitions between metallic silicon phases accompanied by insignificant volumetric changes [3]. These phase transitions are also rather weakly manifested in the electric resistance (as shown in [6, 7] and confirmed in this study) and in the optical spectra [5], but they are reliably revealed by changes in the baric coefficient of thermo emf. There is a certain similarity in the pressure-induced variations in the thermo emf S observed in this study and in the superconducting transition temperature T_c [9], whereby the maximum changes are observed for the phase transition with the minimum volumetric effect (β-Sn $\longrightarrow$ *Imma* [3]).

The pressure dependences of thermo emf in Cz-Si have proved to be sensitive to the oxygen defect structure of samples modified using preliminary *P*–*T* treatments (Fig. 2). In particular, the maximum pressure of the semiconductor–metal phase transition was observed for the sample (*D*2) with an oxygen concentration of about 9×10^{17} cm^{-3} (see the inset in Fig. 2 and data in the table), which also showed the minimum value of thermo emf in the metallic high-pressure phases (Fig. 2). Since the structural defects modify not only the elastic properties, but the electron structure as well (by changing the occupancy of electron energy bands and the character of carrier scattering), they may actually account for an additional contribution to thermo emf [24, 25]. For this reason, thermoelectric measurements at high pressures can be used for rapid diagnostics of the microsamples taken from commercial single crystal silicon ingots (grown for the most part by the Czochralski technique) [16–18].

ACKNOWLEDGMENTS

The authors are grateful to S.N. Shamin for his help in conducting X-ray emission measurements.

This study was supported by the Russian Foundation for Basic Research (project no. 04-02-16178) and by the INTAS Foundation (grant no. 03-55-629).

REFERENCES

1. P. W. Bridgman, Proc. Am. Acad. Arts Sci. **81**, 167 (1952).
2. W. P. Eaton and J. H. Smith, Smart Mater. Struct. **6**, 530 (1997).
3. A. Mujica, A. Rubio, A. Munoz, and R. J. Needs, Rev. Mod. Phys. **75**, 863 (2003).
4. H. Olijnyk, Phys. Rev. Lett. **68**, 2232 (1992).
5. A. R. Goni and K. Syassen, Semicond. Semimet. **54**, 247 (1998).
6. S. Minomura and H. G. Drickamer, J. Phys. Chem. Solids **23**, 451 (1962).
7. O. Shimomura, S. Minomura, N. Sakai, *et al.*, Philos. Mag. **29**, 547 (1974).
8. M. A. Il'ina and E. S. Itskevich, Fiz. Tverd. Tela (Leningrad) **22**, 3139 (1980) [Sov. Phys. Solid State **22**, 1833 (1980)].
9. J. M. Mignot, G. Chouteau, and G. Martinez, Physica B (Amsterdam) **135**, 235 (1985).
10. I. M. Tsidil'kovskiĭ, V. V. Shchennikov, and N. G. Gluzman, Fiz. Tekh. Poluprovodn. (Leningrad) **17**, 958 (1983) [Sov. Phys. Semicond. **17**, 604 (1983)].
11. S. V. Ovsyannikov and V. V. Shchennikov, Physica B (Amsterdam) **344**, 190 (2004).
12. V. V. Shchennikov, Fiz. Met. Metalloved. **67**, 93 (1989).
13. V. V. Shchennikov, S. V. Popova, and A. Misiuk, Pis'ma Zh. Tekh. Fiz. **29** (14), 57 (2003) [Tech. Phys. Lett. **29**, 598 (2003)].
14. V. V. Shchennikov, S. V. Gudina, A. Misiuk, and S. N. Shamin, Physica B (Amsterdam) **340–342**, 1026 (2003).
15. L. Weber, M. Lehr, and E. Gmelin, Phys. Rev. B **46**, 9511 (1992).
16. I. V. Antonova, A. Misiuk, V. P. Popov, *et al.*, Physica B (Amsterdam) **225**, 251 (1996).
17. I. V. Antonova, A. Misiuk, V. P. Popov, *et al.*, Physica B (Amsterdam) **253**, 131 (1998).
18. V. V. Emtsev, G. A. Oganesyan, and K. Schmalz, Fiz. Tekh. Poluprovodn. (St. Petersburg) **27**, 1549 (1993) [Semiconductors **27**, 1111 (1993)].
19. A. Misiuk, Mater. Phys. Mech. **1**, 119 (2000).

20. L. G. Khvostantsev, L. F. Vereshchagin, and N. M. Uliyanitskaya, High Temp.–High. Press. **5**, 261 (1973).
21. D. A. Polvani, J. F. Meng, M. Hasegawa, *et al.*, Rev. Sci. Instrum. **70**, 3586 (1999).
22. V. V. Shchennikov and A. V. Bazhenov, Rev. High Pressure Sci. Technol. **6**, 657 (1997).
23. V. V. Shchennikov, A. Yu. Derevskov, and V. A. Smirnov, in *High Pressure Chemical Engineering*, Ed. by R. V. Rohr and Ch. Trepp (Elsevier, Amsterdam, 1996), pp. 667–672.
24. R. D. Barnard, *Thermoelectricity in Metals and Alloys* (Taylor and Francis, London, 1972).
25. F. J. Blatt, P. A. Schroeder, C. L. Foiles, and D. Greig, *Thermoelectric Power of Metals* (Plenum, New York, 1976; Metallurgiya, Moscow, 1980).
26. A. Misiuk, W. Jung, B. Surma, *et al.*, Solid State Phenom. **57–58**, 393 (1997).
27. A. Misiuk, Proc. SPIE **4412**, 85 (2001).
28. R. Biswas and M. Kertesz, Phys. Rev. B **29**, 1791 (1984).
29. J. M. Besson, E. H. Mokhtari, J. Gonzales, and G. Weill, Phys. Rev. Lett. **59**, 473 (1987).

Translated by P. Pozdeev

JETP Letters, Vol. 80, No. 6, 2004, pp. 410–412. Translated from Pis'ma v Zhurnal Éksperimental'noĭ i Teoreticheskoĭ Fiziki, Vol. 80, No. 6, 2004, pp. 464–467.

Impurity Transport in Percolation Media

A. M. Dykhne, P. S. Kondratenko*, and L. V. Matveev

Nuclear Safety Institute, Russian Academy of Sciences, Moscow, 113191 Russia

**e-mail: kondrat@ibrae.ac.ru*

Received July 30, 2004

An equation describing the impurity transport in a percolation medium is obtained and the inferences drawn from this equation are analyzed based on the scale invariance concept. A determining part in this analysis is allowance for the sinks inherent in such media. At distances shorter than the correlation length, the particles are transferred in the regime of subdiffusion; at large distances, the concentration asymptotics exhibits a characteristic "tail" shape. In the medium occurring in the state above the percolation threshold, the impurity transport over time periods longer than the characteristic time related to the correlation length is well described by the classical equation with a renormalized diffusion coefficient. In this case, the concentration tail has a Gaussian shape at moderate distances and tends to subdiffusion asymptotics at very long distances. A relation is established between the factor determining renormalization of the diffusion coefficient and the factor determining a decrease in the number of active impurity particles at large times. © *2004 MAIK "Nauka/Interperiodica".*

PACS numbers: 05.40.-a; 05.45.Df; 05.60.Cd

A considerable number of practically important problems involving the migration of impurities in strongly disordered media reduce to the problem of impurity transport in a percolation medium [1–3]. The results obtained so far refer predominantly to evaluations of the mean square displacements of particles $R(t)$ for large times. However, in many cases, it is also important to know more detailed characteristics of the impurity distribution, in particular, for the distances $r \gg R(t)$ representing the so-called concentration "tails." In order to determine these characteristics, it is necessary to derive an equation describing evolution of the particle concentration with time. In our opinion, the equations reported in the literature are not satisfactory, being either based on the formalism of fractional derivatives not involving profound physical content [4] or obtained by generalization of the classical diffusion equation with a coordinate-dependent diffusion coefficient [3]. The latter circumstance is in obvious discrepancy with the fact that the impurity concentration of interest is a characteristic averaged over an ensemble of realizations of the strongly disordered medium studied.

The aim of this study was to obtain an equation describing the impurity transport in a percolation medium and to derive and analyze the inferences from this equation.

First, let us briefly formulate the properties of a medium that are substantial for the subsequent analysis [1]. The main specific feature of percolation media is that they consist of nonoverlapping regions (clusters) such that the transport inside each cluster is possible whereas the passage of particles between clusters is impossible. Since only finite clusters exist in such a medium occurring in the state below the percolation threshold, the transport of particles over large distances in this state is hindered. Finite clusters possess fractal properties. Above the percolation threshold, the medium contains an infinite cluster and the transport of particles is not limited with respect to the range. A key characteristic of such a medium is the correlation length ξ. Below the percolation threshold, the distribution of clusters with respect to size l falls in the region $l < \xi$ (the number of clusters with dimensions $l \gg \xi$ is exponentially small). On approaching the percolation threshold, the correlation length exhibits unlimited growth: $\xi \longrightarrow \infty$. Above the percolation threshold, this parameter becomes finite again and the distribution of finite clusters exhibits the same properties as those below the threshold. As for the infinite cluster, it possesses (like the finite clusters) fractal properties and is scale invariant on the spatial scale $L < \xi$, while being statistically homogeneous on the scale $L \gg \xi$. An important topological feature of any cluster is that it can be subdivided into two regions, backbone (*bb*) and a set of dead ends (*de*), so that *bb* connects remote parts of the cluster and all *de* are linked to *bb*, each at a single site, while being isolated from each other. It is important to note that the fractal dimension of *de* is greater than that of *bb*. In what follows, the particles of impurity occurring within *bb* will be called "active." The total number of active particles decreases with time, since they are lost in *de* and localized in small clusters.

Taking into account the above considerations, the equation describing the concentration of active parti-

cles averaged over an ensemble of realizations of the medium can be written as follows:

$$\frac{\partial c(\mathbf{r}, t)}{\partial t} + Q + \operatorname{div}\mathbf{j} = 0, \quad (1)$$

where $\mathbf{j}(\mathbf{r}, t)$ is the density of the particle flux related to the transport over *bb*. In comparison to the usual transport equation reflecting the law of conservation of the total number of articles $N(t) = \int d^3 r c(\mathbf{r}, t)$, Eq. (1) contains the additional term Q describing the sinks of particles lost in *de* and localized in small clusters:

$$Q = \int_{-\infty}^{t} dt' \varphi(t - t') c(\mathbf{r}, t'). \quad (2)$$

The flux density $\mathbf{j}(\mathbf{r}, t)$ is determined by the physical mechanism of particle transport. We will assume that the transport proceeds by walks with a limited step size. The particle flux and concentration are related by Fick's law: $\mathbf{j} = -D\nabla c$. Accordingly, transport equation (1) can be rewritten with allowance for expression (2) as

$$\frac{\partial c(\mathbf{r}, t)}{\partial t} + \int_{-\infty}^{t} dt' \varphi(t - t') c(\mathbf{r}, t') = D\Delta c. \quad (3)$$

Let us analyze the structure of the integrand kernel $\varphi(t)$. Possessing fractal properties, the percolation medium is scale invariant in the spatial interval $\xi_0 \ll l \ll \xi$, where ξ_0 determines the short-range correlation radius. This implies that there exists a time interval $\tau_0 \ll t \ll \tau$ in which the function $\varphi(t)$ is self-similar and can be written in the following form:

$$\varphi(t) \sim -\frac{1}{\tau_0^2}\left(\frac{\tau_0}{t}\right)^{1+\alpha} \quad (4)$$

(the minus sign is explained below). The exponent α is confined within the interval $0 < \alpha < 1$, where the left boundary is determined by the condition of convergence of the integral of $\varphi(t)$ for large times and the right boundary by the condition that the contribution of sink in Eq. (3) at $\tau_0 \ll t \ll \tau$ will predominate over the derivative with respect to time. A comparison between various terms in Eq. (3) shows that $\varphi(\tau_0)\tau_0 \sim D/\xi_0^2$ and $\varphi(\tau)\tau \sim D/\xi^2$, from which it follows that

$$\tau_0 \sim \xi_0^2/D, \quad \tau \sim \tau_0(\xi/\xi_0)^{2/\alpha}.$$

Beyond the fractal interval and at large times, $t \gg \tau$, the function $\varphi(t)$ (similar to the spatial correlations for $r \gg \xi$) decreases quite rapidly, so that all power moments in time exist. At short times, $t < \tau_0$, the contribution of the second term in Eq. (3) does not exceed the first term, which implies that

$$\varphi(t) \sim 1/\tau_0^2, \quad t \lesssim \tau_0.$$

It should be emphasized that Eq. (3), obtained by averaging over an ensemble of realizations of the medium, is valid for the spatial scales greater than ξ_0.

Proceeding from the established properties of the function $\varphi(t)$, let us find the corresponding Laplace's transform of φ_s. In the interval $\tau^{-1} \ll s \ll \tau_0^{-1}$ of Laplace's variable, we have

$$\varphi_s \cong \frac{1}{\tau_0}(s\tau_0)^{\alpha}. \quad (5)$$

For $s < \tau^{-1}$, the function φ_s can be expanded into series in integer powers of $s\tau$. This property of φ_s, together with formula (5), implies that the function φ_s possesses a branching point at $s_1 = -\tau^{-1}$ (this can be considered as the definition of τ) in the complex plane of the variable s and that the values of φ_s at $s = 0$ and $s = s_1$ are of the same order of magnitude (in the absence of other special conditions). These values can be estimated as

$$\varphi_0, \varphi_{s_1} \sim \frac{1}{\tau_0}\left(\frac{\tau_0}{\tau}\right)^{\alpha}. \quad (6)$$

Now, let us study the properties of solutions of Eq. (3). For definiteness, we will consider a problem with the initial condition, assuming that all particles at $t = 0$ are concentrated at the origin (in view of the translational invariance of the problem, selection of the origin is arbitrary), $c(\mathbf{r}, 0) = N_0\delta(\mathbf{r})$. Then, the solution of Eq. (3) has the following form:

$$c(\mathbf{r}, t) = \frac{N_0}{4\pi D r}\int_{a-i\infty}^{a+i\infty}\frac{ds}{2\pi i}\exp\left(-\left(\frac{\varphi_s + s}{D}\right)^{1/2} r + st\right), \quad (7)$$
$$\operatorname{Im} a = 0, \quad a > 0.$$

Let us analyze inferences from this expression. For the times $t \ll \tau_0$, solving Eq. (3) reduces to finding a solution of the classical diffusion equation with $Q = 0$ and, accordingly, $\varphi = 0$.

In the interval $\tau_0 \ll t \ll \tau$, integration of solution (7) over the entire space gives the total number of active particles as a function of time:

$$\frac{N(t)}{N(0)} = \Gamma^{-1}(\alpha)\left(\frac{\tau_0}{t}\right)^{1-\alpha}, \quad (8)$$

where $\Gamma(x)$ is the Euler gamma function. Note that the plus sign in the right-hand side of formula (8) is due to the minus sign selected in formula (4), which is evidence of the correct choice of sign in the latter expression.

Using solution (7), we obtain an expression for the concentration of active impurity particles at the origin in the time interval $\tau_0 \ll t \ll \tau$:

$$c(0, t) \cong \frac{N_0}{(4\pi D t)^{3/2}}\left(\frac{\tau_0}{t}\right)^{-(1-\alpha)/2}\frac{2}{\sqrt{\pi}}\Gamma\left(1 + \frac{\alpha}{2}\right)\sin\frac{\alpha\pi}{2}. \quad (9)$$

In accordance with (7), the general expression for the concentration of active particles at $\tau_0 \ll t \ll \tau$ and $\xi_0 \ll r \ll \xi$ has the following structure:

$$c(\mathbf{r}, t) = c(0, t)F(\eta), \quad \eta = \frac{r^2}{4Dt}\left(\frac{t}{\tau_0}\right)^{1-\alpha}, \quad (10)$$

where the function $F(\eta)$ rapidly decreases for $\eta > 1$. According to this, the size of the main concentration cloud at time t can be estimated as

$$R(t) \sim \sqrt{4Dt}(t/\tau_0)^{(1-\alpha)/2}. \quad (11)$$

This estimate shows that the impurity transport in the model under consideration (with allowance for $0 < \alpha < 1$) corresponds to the regime of subdiffusion.[1] With allowance for relations (8) and (11), expression (9) obeys the obvious relation $c(0, t) \sim N(t)/R^3(t)$.

The concentration of active particles at large distances (i.e., in the "tail") is given by the formula

$$c(\mathbf{r}, t) \cong \frac{N_0}{(4\pi Dt)^{3/2}}\left(\frac{\tau_0}{t}\right)^{-(1-\alpha)/2}\frac{\alpha^{1/(2-\alpha)}}{\sqrt{2-\alpha}}\eta^{-(1-\alpha)/2(2-\alpha)} \times \exp\left\{-\frac{2-\alpha}{\alpha}(\alpha^2\eta)^{1/(2-\alpha)}\right\}. \quad (12)$$

This expression describes the behavior of the concentration at distances up to $r \sim \xi_0 t/\tau_0$. In order to determine the asymptotic behavior of the concentration for $r \gg \xi_0 t/\tau_0$, it is necessary to go out of the framework of the applicability of Eq. (3). Proceeding from the model adopted, it is only possible to indicate a majorant criterion:

$$c(\mathbf{r}, t) < \frac{N_0}{(4\pi Dt)^{3/2}}\frac{\alpha}{\sqrt{2-\alpha}}\exp\left\{-\frac{2-\alpha}{\alpha}\frac{t}{\tau_0}\right\}, \quad r \gg \xi_0 t/\tau_0. \quad (13)$$

The behavior of the particle concentration at $t \gg \tau$ depends on whether the medium occurs in the state below or above the percolation threshold. Below this threshold, we obtain an estimate:

$$c(\mathbf{r}, t) \sim \frac{N_0}{\xi_0^3}\left(\frac{\xi_0}{\xi}\right)^{(2+\alpha)/\alpha}\left(\frac{\tau}{t}\right)^{1+\alpha}\exp\left(-\frac{r}{\xi}-\frac{t}{\tau}\right).$$

In order to describe the transport in a medium above the percolation threshold, let us divide the concentration of active particles into two parts, $c(\mathbf{r}, t) = c_f(\mathbf{r}, t) + c_\infty(\mathbf{r}, t)$, where the first part includes the particles belonging to the system of finite clusters and the second refers to particles occurring in the infinite cluster. The initial conditions are set as $c_f(\mathbf{r}, 0) = c(\mathbf{r}, 0)(1 - P_\infty)$ and $c_\infty(\mathbf{r}, 0) = c(\mathbf{r}, 0)P_\infty$, where P_∞ is the probability for a particle to fall within the infinite cluster. The behavior of $c_f(\mathbf{r}, t)$ is analogous to that considered for the subthreshold states. The same laws are valid for the behavior of $c_\infty(\mathbf{r}, t)$ at $t < \tau$, except that the exponent α in relation (6) differs from the previous value [6, 7] (although it still falls within the interval $0 < \alpha < 1$).

The cardinal difference in the transport for $t > \tau$ is related to the fact that the infinite cluster obeys the condition $\varphi_0 = 0$. This condition follows from the property of statistical homogeneity at $r \gg \xi$, whereby the number of active particles in the infinite cluster at $t \longrightarrow \infty$ tends to a finite limit. Indeed, Eq. (3) implies that

$$\frac{\partial N_\infty}{\partial t} + \int_0^t dt\varphi(t-t')N_\infty(t') = 0.$$

From this, we infer (since $N_\infty(\infty) \neq 0$ and $\partial N_\infty(\infty)/\partial t = 0$), that $\int_0^\infty dt\varphi(t) \equiv \varphi_0 = 0$. Hence, for $s \ll \tau^{-1}$, the function φ_s has the form $\varphi_s \cong As$, where $A \sim (\tau/\tau_0)^{1-\alpha} \gg 1$. This implies that, for $t \gg \tau$, the concentration of particles $c(\mathbf{r}, t) \cong c_\infty(\mathbf{r}, t)$ obeys the classical diffusion equation with renormalized diffusion coefficient $\tilde{D}$. The renormalization factors for the diffusion coefficient and the total number of particles obey the equality

$$\frac{\tilde{D}}{D} = \frac{N_\infty(\infty)}{N_\infty(0)} = A^{-1}. \quad (14)$$

The behavior of the particle concentration at the tail of the distribution for the times $t \gg \tau$ has the following character. First, at distances in the interval, $\sqrt{4\tilde{D}t} \ll r \ll \xi(t/\tau)$, the concentration tail has a Gaussian shape corresponding to a renormalized diffusion coefficient $\tilde{D}$ and the total number of particles $N_\infty(\infty)$. Then, at $r \gg \xi(t/\tau)$, a subdiffusion asymptotics of type (12) is followed with the limitations indicated above.

The authors are grateful to S.A. Rybak for fruitful discussions.

[1] It should be noted that both the physical formulation of the problem and the results of analysis are, on the whole, different from those for the model [5] based on the equation with a fractional derivative with respect to time.

REFERENCES

1. M. B. Isichenko, Rev. Mod. Phys. **64**, 961 (1992).
2. M. Sahimi, Rev. Mod. Phys. **65**, 1393 (1993).
3. V. Mendez, D. Campos, and J. Fort, Phys. Rev. E **69**, 016613 (2004).
4. A. Compte, Phys. Rev. E **53**, 4191 (1996).
5. K. V. Chukbar, Zh. Éksp. Teor. Fiz. **108**, 1875 (1995) [JETP **81**, 1025 (1995)].
6. Y. Gefen and A. Aharony, Phys. Rev. Lett. **50**, 77 (1983).
7. A. Harris, Y. Meir, and A. Aharony, Phys. Rev. B **36**, 8752 (1987).

Translated by P. Pozdeev

JETP Letters, Vol. 80, No. 6, 2004, pp. 413–416. Translated from Pis'ma v Zhurnal Éksperimental'noĭ i Teoreticheskoĭ Fiziki, Vol. 80, No. 6, 2004, pp. 468–471.

On the Bistable Behavior of a Low-Frequency Raman-Active Phonon Line in Superconducting Oxide $Ba_{1-x}K_xBiO_3$

A. P. Saiko* and S. A. Markevich

Institute of Solid-State and Semiconductor Physics, National Academy of Sciences of Belarus, Minsk, 220072 Belarus

**e-mail: saiko@ifttp.bas-net.by*

Received August 2, 2004

The two-loop temperature hysteresis of integrated intensity of Raman scattering of light is explained theoretically for a line of frequency 50 cm^{-1} in a superconducting oxide $Ba_{1-x}K_xBiO_3$ single crystal. © *2004 MAIK "Nauka/Interperiodica".*

PACS numbers: 74.25.Kc; 74.25.Gz

The cuprate-free superconductor $Ba_{1-x}K_xBiO_3$ (BKBO) with the superconducting transition temperature $T_c \cong 32$ K (for samples with $x \cong 0.37$) occupies a special place among high-temperature oxide superconductors. Superconducting BKBO compounds crystallize into a cubic perovskite structure, do not contain an analog of the CuO_2 layers inherent in cuprates, are diamagnetic, and do not possess a static magnetic order. Although the considerable isotopic effect and the superconducting gap width match the results of the standard BCS model, other mechanisms of the formation of the superconducting state (in addition to the phonon mechanism) should be employed for explaining high values of T_c and low densities of states of charge carriers.

It has been generally accepted [1] that the unique properties of these compounds are determined to a considerable extent by the dynamics and the electron structure of BiO_6 octahedra. The vibrational spectrum of BKBO strongly depends on the dopant (potassium) concentration x; however, all samples with different values of x exhibit a phonon vibration at a frequency of 50 cm^{-1}. This line appears in the Raman spectra for the *XX* polarization owing to the *R* type rotational distortion [2]. The line intensity is maximal for metallic samples with $x \approx 0.33$ and exhibits an intriguing feature, i.e., two-loop hysteretic behavior as a function of temperature in the range 10–200 K [2]. It is interesting to note that latticed instability with a strong softening of elastic moduli, as well as hysteretic temperature behavior for samples with $x \approx 0.37$ (which was discovered with the help of ultrasonic measurements [3]), is observed in the same temperature range.

It will be shown below that the existence of the 50-cm^{-1} line in the Raman spectra and that its bistable behavior can be explained using existing concepts of the dynamics of building blocks of the BKBO crystal lattice, i.e., BiO_6 octahedra, as well as their electronic structure.

It was found [4] that there exist two types of BiO_6 octahedra with two different lengths of the Bi–O bond and rigidities. The crystal structure of the parent compound $BaBiO_3$ is formed by alteration of expanded (soft) and compressed (hard) BiO_6 octahedra. The electronic structures of soft and hard octahedra are also different. In a soft BiO_6 octahedron, 2 antibonding orbitals are completely filled with 20 electrons, while such orbitals in a hard $Bi\underline{L}^2O_6$ octahedron are filled with 18 electrons and a free energy level (hole pair $\underline{L}^2$) is present in the upper antibonding orbital. Doping of $BaBiO_3$ with potassium is equivalent to addition of holes and leads to partial replacement of large soft octahedra by small hard ones. This results in a decrease in the number of static breather and rotational distortions and their gradual disappearance. According to neutron diffraction data [5], the structure of the compound ultimately becomes, on average, cubic for a doping level of $x \geq 0.37$. However, the EXAFS analysis of the four nearest spheres in the bismuth surroundings for samples with $x \geq 0.37$ indicates local rotations of octahedra through 4°–5° [6], while Raman spectra indicate that the symmetry becomes lower as compared to simple cubic symmetry [7]. Moreover, it was found [1, 8] that oxygen ions belonging simultaneously to BiO_6 and $Bi\underline{L}^2O_6$ octahedra vibrate in a two-well asymmetric potential, while oxygen ions belonging to identical $Bi\underline{L}^2O_6$ octahedra vibrate in a simple harmonic potential. The two-well shape of the potential is due to different fillings of the upper antibonding orbital in BiO_6 and $Bi\underline{L}^2O_6$ octahedra. During tunneling of an oxygen ion from one well to the other, an electron pair simulta-

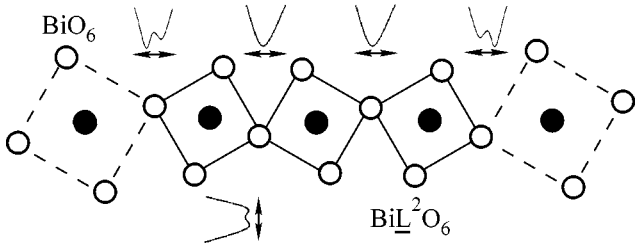

Fig. 1. Schematic representation of a cooperated complex of octahedra in the BiO_2 plane in the [100] direction (see text); dark circles correspond to Bi and light circles, to O.

neously passes from a BiO_6 octahedron to a BiL^2O_6 octahedron; accordingly, these octahedra exchange their roles (i.e., the dynamic exchange $BiO_6 \longleftrightarrow BiL^2O_6$ takes place). In [1], superconductivity in bismuth-containing compounds is regarded as movement of local electron pairs of this type.

With increasing doping level, the number of BiL^2O_6 octahedra increases and, for $x \geq 0.33$, the lattice acquires three-dimensional complexes, i.e., spatially overlapping BiL^2O_6 octahedra. The free energy level in these complexes expands to form the conduction band, and metal-type conductivity is formed when the energy of localization of electron pairs becomes equal to zero [1]. As a result, all octahedra in a complex can perform coherent rotational vibrations (e.g., around the [001] axis). Figure 1 shows such a complex schematically in the BiO_2 plane of octahedra along the [100] direction. The dynamic exchange by the roles of octahedra $BiO_6 \longleftrightarrow BiL^2O_6$, which is realized due to the escape of an oxygen ion from the global minimum of the asymmetric two-well potential and the transfer of an electron pair to a BiL^2O_6 octahedron, is complicated in this case since it would require mismatching of the cooperative movement of the entire complex of BiL^2O_6 octahedra. Cooperativity first leads to suppression of fluctuation-induced jumps of an oxygen ion from the global minimum to a local one upon heating of the system to a certain temperature. Second, matched rotational vibrations of the octahedra in the complex, which locally distort the cubic perovskite structure, may become Raman-active (this is actually observed for vibrations at a frequency of 50 cm^{-1}). The emergence of local distortions of cubic structure due to correlated rotational vibrations of octahedra in the entire complex of this type can be treated as a locally realized phase transition of displacement type (the symmetric potential with two shallow minima in the [010] direction in Fig. 1 confirms this statement).

We will consider the emergence of local distortions and lattice instability in rotational distortions of octahedra about the [001] axis by using the Hamiltonian

$$H = \sum_l \left(\frac{P_l^2}{2M} + \frac{M\nu_o^2}{2} Q_l^2 + \frac{B}{4} Q_l^4 \right) - \frac{1}{2} \sum_{l \neq l'} v_{ll'} Q_l Q_{l'}, \quad (1)$$

where ν_o is the local frequency of small oscillations in the absence of interactions ($\nu_o = 50$ cm^{-1} in our case), Q_l is the generalized coordinate describing the rotation of octahedra, B is the anharmonicity constant, $v_{ll'}$ are the interaction constants, and M is the mass. We choose the asymmetric two-well potential for describing the motion of oxygen ion belonging to BiO_6 and BiL^2O_6 octahedra in the form

$$V = \frac{\alpha}{2} q^2 - \frac{\beta}{3} q^3 + \frac{\gamma}{4} q^4, \quad (2)$$

where α, β, and γ (>0) are constants and q is the generalized coordinate of the ion. Vibrations of octahedra depend on the position of oxygen ions in the two-well potential. This can be accounted for by introducing the cubic and quartet terms of the interaction,

$$H_{\text{int}}^{(3)} = q^2 \sum_k \lambda_k^{(3)} Q_k, \quad H_{\text{int}}^{(4)} = q^2 \sum_{k,k'} \lambda_{k,k'}^{(4)} Q_k Q_{k'}, \quad (3)$$

where Q_k are the Fourier components of coordinates Q_l and $\lambda_k^{(3)}$ and $\lambda_{k,k'}^{(4)}$ are the coupling coefficients. We can represent the renormalization of the initial frequency ($\nu_o \longrightarrow \nu_r$) in the self-consistent phonon approximation in the fourth-order interaction in Hamiltonian (1) and in the first and second approximations in perturbation theory in $H_{\text{int}}^{(4)}$ and $H_{\text{int}}^{(3)}$, respectively, in the form

$$\nu_r^2 = \nu_o^2 + \frac{3B}{M_{\text{eff}}} (\langle Q \rangle^2 + \langle \delta Q^2 \rangle) + \frac{2\lambda_{k,k'}^{(4)}}{M_{\text{eff}}} (\langle q \rangle^2 + \langle \delta q^2 \rangle) - \frac{(\lambda_k^{(3)})^2}{m M_{\text{eff}} \Omega^2} (4\langle q \rangle^2 + \langle \delta q^2 \rangle). \quad (4)$$

(see also [9]). Here, $\langle Q \rangle$ and $\langle \delta Q^2 \rangle = \langle (Q - \langle Q \rangle)^2 \rangle$ are the mean statistical values of the coordinate and its variance ($\langle q \rangle$ and $\langle \delta q^2 \rangle$ have an analogous meaning), M_{eff} is the effective mass of the complex of octahedra generating local distortion $\langle Q \rangle$ (a complex may have a linear size of four to six octahedra), and $\Omega^2 = \frac{1}{m} [\alpha - 2\beta \langle q \rangle + 3\gamma (\langle q \rangle^2 + \langle \delta q^2 \rangle)]$ is the oxygen ion frequency in the two-well potential. The mean values $\langle q \rangle$ and $\langle \delta q^2 \rangle$ can be determined self-consistently from the equations

$$\langle \delta q^2 \rangle = \frac{1}{2m\Omega} \coth \frac{\Omega}{2\theta}, \quad (\beta - 3\gamma \langle q \rangle) \langle \delta q^2 \rangle = \alpha \langle q \rangle - \beta \langle q \rangle^2 + \gamma \langle q \rangle^3, \quad (5)$$

while $\langle Q\rangle$ and $\langle \delta Q^2\rangle$ can be determined from the equations

$$\langle \delta Q^2\rangle = \frac{\theta}{M_{\text{eff}}\nu_r^2},$$
$$M_{\text{eff}}\nu_o^2 + 3B\langle \delta Q^2\rangle + B\langle Q\rangle^2 - \nu = 0, \quad (6)$$

where $\nu = \sum_{l'} \nu_{ll'}$, m is the mass of an oxygen ion, and $\theta = k_B T$. In deriving Eq. (4), we took into account the fact that the vibrational frequency of octahedra is much smaller than the frequency of oxygen ions. For the temperature range we are mainly interested in, we have $k_B T \gg \nu_o$; for this reason, for simplicity, variance $\langle \delta Q^2\rangle$ is represented by the classical formula in relations (6). The value of M_{eff} can be determined by comparing the local phase transition temperature T_o, estimated by formula $k_B T_o \approx M_{\text{eff}}\nu_o^2\langle Q\rangle_{\max}^2$, with the experimentally measured value T_o^{exp}. Since $\langle Q\rangle_{\max} \approx 0.15$ Å for rotation of octahedra through 5° for a lattice constant $\mathbf{a} \approx 4.3$ Å and $T_o^{\text{exp}} \approx 300$ K [2], we obtain an estimate of $M_{\text{eff}} \approx 800m$; i.e., the complex consists of 200 octahedra and occupies a region of approximately $25 \times 25 \times 25$ Å^3. Parameters α, β, and γ of potential (2) can be estimated on the basis of EXAFS data, i.e., from a potential barrier height of ~0.026 eV and the local maximum and local minimum coordinates ~0.075 and ~0.15 Å, respectively [8].

For crystals with a perovskite cubic structure, principal-order terms in the power expansion of polarizability in Raman-active modes are absent in view of the symmetry and the main contribution to the Raman scattering tensor comes from second-order terms. For this reason, we can express the integrated intensity of light scattering in the form

$$I \sim \langle Q\rangle^2\langle \delta Q^2\rangle = \langle Q\rangle^2 \frac{\theta}{M_{\text{eff}}\nu_r^2} \quad (7)$$

or, taking into account the second equation in (6), we can write the reduced intensity in the form

$$\frac{I}{\theta} \sim \frac{\langle Q\rangle^2}{2B\langle Q\rangle^2 + \nu}. \quad (8)$$

At temperatures higher than the critical temperature T_o of a local phase transition of the displacement type, we have $\langle Q\rangle = 0$ and, in accordance with formula (8), intensity $I = 0$. After the emergence of local distortions $\langle Q\rangle^2 \sim T_o - T$, intensity in the temperature range $T < T_o$ differs from zero and increases upon cooling. The temperature dependence of reduced intensity I/θ calculated using formulas (8) and (4)–(6) is in qualitative agreement with the experimental curve (Fig. 2). Obviously, the temperature hysteresis in the form of a two-loop curve is due to temperature renormalization of frequency ν_o because of interactions $H_{\text{int}}^{(3)}$ and $H_{\text{int}}^{(4)}$ (see Fig. 3). It should be recalled that these interactions represent the nonlinear relations between rotational vibrations of octahedra with the breather-type vibrations of oxygen ions in a two-well potential in the [100] direction. The inclusion of the contribution from $H_{\text{int}}^{(3)}$ or from $H_{\text{int}}^{(4)}$ alone leads to a simple (one-loop) hysteresis: the intensity of scattered light in the bistability region is lower for sample cooling and higher for sample heating

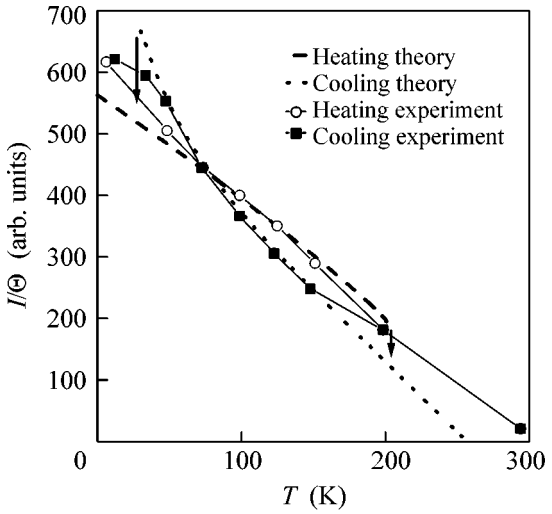

Fig. 2. Hysteretic behavior of the reduced integrated intensity of Raman scattering for a line at frequency 50 cm^{-1} in a single crystal of $Ba_{0.67}K_{0.33}BiO_3$; $B = 4.6$ eV Å^{-4}, $\nu = 3.11$ eV Å^{-2}, $\lambda_k^{(3)} = 1.65$ eV Å^{-3}, $\lambda_{kk}^{(4)} = 1.24$ eV Å^{-4}, $\alpha = 3.69 \times 10^1$ eV Å^{-2}, $\beta = 7.5 \times 10^2$ eV Å^{-3}, $\gamma = 3.3 \times 10^3$ eV Å^{-4}, and $M_{\text{eff}} = 800m$, where m is the mass of an oxygen atom.

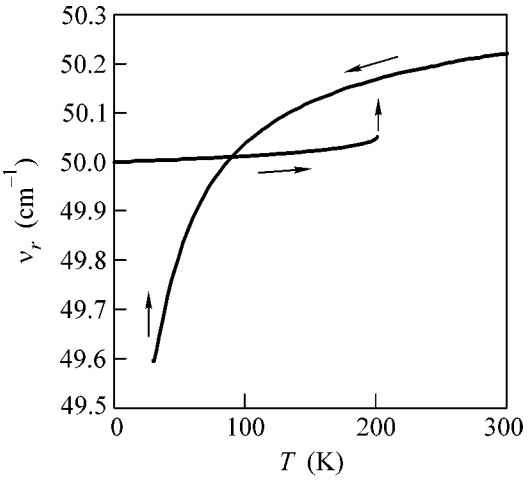

Fig. 3. Temperature dependence of renormalized frequency ν_r plotted in accordance with formula (4).

if $H_{\text{int}}^{(3)}$ is taken into account. If only $H_{\text{int}}^{(4)}$ is taken into consideration, the circumvention of the hysteresis curve is inverted (i.e., the cooling curve lies above the heating curve). The competition of the contributions from $H_{\text{int}}^{(3)}$ (with a minus sign, since this contribution differs from zero in the second order of perturbation theory) and from $H_{\text{int}}^{(4)}$ (with the plus sign if $\lambda_{kk}^{(4)} > 0$) forms the hysteresis curve of the two-loop type.

Thus, the presence of a phonon line of frequency 50 cm^{-1} in the Raman spectrum of a single crystal of superconducting oxide $Ba_{1-x}K_xBiO_3$ and the bistable temperature dependence of its integrated intensity reflect a number of features of the local lattice and electronic structures of this compound. First, this line emerges due to rotation of soft and hard BiO_6 octahedra. Rotational distortions are realized in the form of a local phase transition of the displacement type in the cooperated complex of hard octahedra, which may exchange their roles with soft octahedra owing to breather-type vibrations of oxygen ions in a two-well potential. Second, the integrated intensity of Raman scattering for this line decreases upon sample heating and vanishes at the critical temperature T_o of a local phase transition of the displacement type (i.e., in the case when cooperated coherent vibrations of the complex of octahedra are disrupted and local distortions in the cubic perovskite structure disappear). Third, the temperature hysteresis of the integrated intensity is due to the asymmetric nature of the dependence of rotational vibrations of octahedra with renormalized frequency ν_r on two nonequivalent positions of the oxygen ion transferring an electron pair from a soft to a hard octahedron. The bistable behavior of this ion in the two-well potential is ensured by the cooperative behavior of the complex of octahedra; in addition, the competition of the contributions from interactions $H_{\text{int}}^{(3)}$ and $H_{\text{int}}^{(4)}$ to ν_r forms a hysteretic curve of the two-loop type for the temperature dependence of the intensity.

REFERENCES

1. A. P. Menushenkov, K. V. Klementev, A. V. Kuznetsov, and M. Yu. Kagan, Zh. Éksp. Teor. Fiz. **120**, 700 (2001) [JETP **93**, 615 (2001)].
2. Yu. G. Pashkevich, V. P. Gnezdilov, A. V. Eremenko, *et al.*, Int. J. Mod. Phys. **14**, 3637 (2000).
3. S. Zherlitsyn, B. Lüthi, V. Guzakov, *et al.*, Eur. Phys. J. **16**, 59 (2000).
4. D. E. Cox and A. W. Sleight, Acta Crystallogr. **35**, 1 (1989).
5. Shiyou Pei, J. D. Jorgensen, B. Dabrowski, *et al.*, Phys. Rev. B **41**, 4126 (1990).
6. Y. Yacoby, S. M. Heald, and E. A. Stern, Solid State Commun. **101**, 801 (1997).
7. M. Braden, W. Reichardt, W. Schmidbauer, *et al.*, J. Supercond. **8**, 595 (1995).
8. A. P. Menushenkov, K. V. Klement'ev, P. V. Konarev, and A. A. Meshkov, Pis'ma Zh. Éksp. Teor. Fiz. **67**, 977 (1998) [JETP Lett. **67**, 1034 (1998)].
9. A. P. Saĭko and V. E. Gusakov, Zh. Éksp. Teor. Fiz. **116**, 168 (1999) [JETP **89**, 92 (1999)]; Zh. Éksp. Teor. Fiz. **108**, 757 (1995) [JETP **81**, 413 (1995)].

Translated by N. Wadhwa

JETP Letters, Vol. 80, No. 6, 2004, pp. 417–420. Translated from Pis'ma v Zhurnal Éksperimental'noĭ i Teoreticheskoĭ Fiziki, Vol. 80, No. 6, 2004, pp. 472–476.

Disk-Shaped Electronic Bubbles in Gaseous Helium

V. B. Shikin

Institute of Solid-State Physics, Russian Academy of Sciences, Chernogolovka, Moscow region, 142432 Russia
e-mail: shikin@issp.ac.ru

Received August 5, 2004

The structure of 2D anions placed on a hydrogen substrate in the presence of gaseous helium is discussed. It is shown that these structures, shaped like quasi-two-dimensional disks, are created in a threshold-like manner in the vicinity of critical density $n_c \sim 10^{20}$ cm^{-3}, which is appreciably lower than the critical density for the appearance of spherical electronic bubbles in gas and linearly depends on temperature. Experiment confirms the existence of such autolocalized states. © *2004 MAIK "Nauka/Interperiodica".*

PACS numbers: 67.55.Ig

Electronic bubbles in helium are beautiful autolocalized formations. After they had been first discovered and identified in liquid [1, 2], they were studied in detail in gaseous helium with the aim of determining the critical conditions for their appearance [3]. It turned out that the creation of bubbles has a threshold character, the gas density in the center of the bubble is (exponentially) close to zero, and the critical density n_k is sensitive to temperature:

$$n_k \propto T^{2/3}. \quad (1)$$

Almost at the same time, the idea became popular of the possible change in the critical conditions for the formation of bubbles in the presence of external forces that localize electron free motion in one or two spatial directions, irrespective of autolocalization mechanism. This effect was described in detail for an electron in a strong magnetic field, in which its motion in the plane normal to the magnetic field is restricted by the cyclotron orbit with radius r_c. It was shown [4, 5] that the free electron motion in this case along the magnetic axis is also limited. A thresholdless one-dimensional autolocalization arises with the characteristic coupling length

$$l_H = \frac{2mT}{\pi\hbar^2 n_g}\left(\frac{r_c}{a_o}\right)^2, \quad l_H \gg r_c, \quad (2)$$

and gas density weakly perturbed in a cigar-like region. Here, T is the temperature, m is the free-electron mass, $a_o > 0$ is the zero-point scattering amplitude for an individual gas atom, and n_g is the unperturbed gas density.

A disk-shaped autolocalization was also briefly pointed out when an electron is placed near a insulator free boundary and its vertical degree of freedom is quantized by the image force. In this case, gaseous helium autolocalizes electron free motion in the insulator plane in the threshold-like fashion with the localization radius R [6],

$$R^{-2} \propto (1 - n_c/n_g), \quad n_g > n_c, \quad (3)$$

where the critical value n_c is given below by Eq. (13). As in the case of Eq. (2), the gas density inside the bubble is weakly perturbed at the initial stage, allowing one to speak about a weak autolocalization regime.

To date, results (2) and (3) and other predictions of the theory of weak autolocalization were thought to be speculative. However, it has become clear that the autolocalization occurs in other experiments, namely, in the works of Adams *et al.* [7–12] mainly devoted to the study of the influence of weak localization on the conductivity of 2D electrons over solid hydrogen in the presence of gaseous helium. It turned out that, apart from "weak coherent localization," the data [7–12] give evidence of another interesting phenomenon, called by those authors "fluctuative localization" (in my opinion, corresponding to a weak 2D electron autolocalization in the gas phase). The commonly accepted term *weak localization* is complemented by the term *coherent* to emphasize the difference between two types of weak localization: coherent and autolocalization. In the first case, one implies a contribution to the scattering cross section for the closed electron trajectories appearing with a certain probability upon multiple electron scattering by defects (e.g., gas atoms). In this case, the gas density is not perturbed. In the second case [7–12], 2D electrons are autolocalized on the deep gas-density fluctuations. The "depth" of gas holes is maintained by the electrons localized in them. Nevertheless, particular details of this model are not clear (see below). Weak (as in [6]) autolocalization is a possible alternative. It is physically clearer, and the computational details for conditions [7–12] are close to the experimental data. It is the purpose of this work to consider the problem of disk-shaped electron localization in gaseous helium.

1. Let us consider the functional F determining the degree of electron localization over a flat dielectric substrate in the presence of gaseous helium with concentration n_g. Its density $\tilde{F}$ has the form

$$\tilde{F} = \tilde{F}_e + \tilde{F}_{\text{int}} + \tilde{F}_{\text{gas}} + \tilde{F}_{\nabla g}, \quad (4)$$

$$\tilde{F}_e = \frac{\hbar^2}{2m}|\nabla\varphi(z,r)|^2, \quad \tilde{F}_{\text{int}} = \frac{2\pi\hbar^2 a_o}{m}n(z,r)|\varphi(z,r)|^2,$$

$$\tilde{F}_{\text{gas}} = nT\ln[nf(T))], \quad \tilde{F}_{\nabla g} = \frac{\hbar^2}{2m_g}|\nabla n(z,r)|^2, \quad (5)$$

$$\int|\varphi(z,r)|^2 dz d^2r = 1, \quad \int n(r,z)dz d^2r = \text{const}.$$

Here, m and m_g are the electron mass and the mass of a gas atom, respectively; $n(z, r)$ is the local gas density; $\varphi(z, r)$ is the electron wave function; and $f(T)$ is the known function of temperature T. As in the case of the electronic bubble in liquid helium, the main energy gain leading to electron localization comes as a result of a decrease in gas density in the bubble zone ($\tilde{F}_{\text{int}}$ in Eq. (4)); the energy of zero-point vibrations ($\tilde{F}_e$ in Eq. (4)) prevents the decrease in the anion size. In contrast, the terms $\tilde{F}_{\text{gas}}$ and $\tilde{F}_{\nabla g}$ restrict the anion size from above. With an increase in the gas density, the term $\tilde{F}_{\nabla g}$ transforms into the well-known contribution from surface tension. However, at the initial stage of weak localization, this term is insignificant and will be considered below as perturbation. For stages (4) and (5), this assumption is confirmed by the experimental data on the sensitivity of critical conditions (1) and (3) to temperature. This is possible if the first term in the sum $\tilde{F}_{\text{gas}} + \tilde{F}_{\nabla g}$ is dominant (T scenario). In the regime of strong localization, the situation may change (∇ scenario).

In the T scenario, the variation of F with respect to n leads to the well-known relation between $n(z, r)$ and $\varphi|(z, r)|^2$ [3]:

$$n(z,r) = n_g\exp(-\psi(z,r)/T),$$
$$\psi(z,r) = \frac{2\pi\hbar^2 a_o}{m}|\varphi(z,r)|^2. \quad (6)$$

In this variation, the total number of helium atoms must be conserved (requirement (5) for gas density), and the corresponding Lagrange factor should be introduced in the Euler equation for $n(z, r)$.

Using Eq. (6), one can rewrite the functional F as

$$F = \int dz d^2r\left[\frac{\hbar}{2m}|\nabla\varphi(z,r)|^2 - n_g T\ln(n_g f(T))\right.$$
$$\left.\times[1-\exp(-\psi(z,r)/T)] + n_g T\ln(n_g f(T)\right), \quad (7)$$
$$\ln(n_o f(T)) < 0.$$

By varying Eq. (7) with respect to φ and using Eq. (5), one can write the nonlinear equation for this function. However, it cannot be analytically solved in the general case. Because of this, to reveal the details of electron autolocalization, one should apply the variational method to functional (7).

The form F in Eq. (7) also applies in the three-dimensional case. By taking the wave function in the form

$$\varphi(r) = \pi^{-1/2}k^{3/2}\exp(-kr) \quad (8)$$

(r is the three-dimensional radius, and k is the variable parameter) and determining the expression for F from Eqs. (7) and (8), one finds that a well-defined minimum for F as function of k may exist, with the extremal value $k_{\min}$ belonging to the parameters corresponding to the inequality

$$\kappa = \psi_{\min}(0)/T \gg 1, \quad \psi_{\min}(0) = \psi(r=0, k=k_{\min}),$$
$$\tilde{k}_{\min} = k_{\min}/k_o \simeq 1.5, \quad k_o^3 = \frac{mT}{2\hbar^2 a_o}. \quad (9)$$

In other words, a three-dimensional electron in gaseous helium may be autolocalized (small-radius anion), and the localization region is virtually free of helium vapor even at the initial moment (see [4] for details). In liquid helium, this formation assumes the form of an electronic bubble with a characteristic radius on the order of 20 A. Among other important statements about the 3D bubble in gas, we note the possibility of making F in Eq. (7) dimensionless after the introduction

$$\tilde{k} = k/k_o, \quad \tilde{n} = n/n^*, \quad n^* = \frac{1}{2\pi a_o}\left(\frac{mT}{2\hbar^2 a_o}\right)^{2/3}. \quad (10)$$

It follows, in particular, that the critical density for the formation of a 3D bubble should depend on temperature as in Eq. (1).

For the electronic states at the insulator surface, the conditions for electron autolocalization should be sorted. This assumption is in accordance with the general positions of quantum mechanics and is confirmed by the subsequent calculations.

Setting

$$\varphi(r,z) = 2\gamma^{3/2}\exp(-\gamma z)\sqrt{2/\pi}q\exp(-q^2r^2), \quad q = R^{-1},$$
$$\gamma = \frac{me^2(\epsilon-1)}{4\hbar^2(\epsilon+1)}, \quad \int dz d^2r|\psi^2(r,z)| = 1 \quad (11)$$

for quasi-2D electron (ϵ is the dielectric constant of solid hydrogen, r is the two-dimensional radius, and q is the variable reciprocal localization radius) and minimizing F (7) with $\varphi(r, z)$ from Eq. (11) with respect to q, one finds for $q_{\min}$:

$$\frac{\hbar^2 q_{\min}^2}{m} = \frac{27}{160}\left(\frac{3}{2}\right)^4\frac{T}{\gamma a_o}\left[1-\frac{n_c}{n_o}\right], \quad (12)$$

$$n_c = \frac{4mT}{3\pi\hbar^2 a_o^2 \gamma |\ln(n_o f(T)|}, \quad (13)$$

with γ from Eq. (11). Result (12), (13) has structure (3) and was obtained with some numerical remarks in [6].

The quantity $q_{\min}$ is positive by definition. This means that weak localization in the form (11), (12) is possible only if

$$n_c < n_g, \quad (14)$$

i.e., if appears in the threshold-like fashion.

Using Eqs. (11)–(13), expression (7) for F can be written in the form

$$F = -c\frac{a_o n_g \hbar^2}{m}\left(1 - \frac{n_c}{n_g}\right)^2, \quad c = \frac{\pi}{20}(3/2)^9 \simeq 1.92. \quad (15)$$

Note that Eqs. (11)–(14) are obtained on the assumption that

$$\kappa \ll 1,$$

where κ is from Eq. (9) One can readily see that this parameter has an additional multiplier,

$$\gamma a_o / z \ll 1,$$

compared to F/T. In other words, the parameter κ can be relatively small when the relative localization energy F/T already exceeds unity. This fact should be taken into account in the analysis of Eq. (15).

2. Let us dwell upon the localization mechanism in [11]. Here, it is assumed that the localization energy E_c is the sum of two terms,

$$E_c = E_c^- + E_c^+. \quad (16)$$

The gain E_c^- is due to a decrease in the gas density in the vicinity of localized electron, and the loss E_c^+ corresponds, as above, to the electron zero-point vibrations.

To determine E_c^-, one uses the probability of equilibrium particle-number fluctuation in an ideal gas [16]:

$$(\delta N)^2 = N. \quad (17)$$

Next, taking into account that

$$N = n_g V, \quad \delta N = \delta n_g V, \quad V = \langle z \rangle R^2$$

(R and $\langle z \rangle$ are the electron-localization lengths in the horizontal and vertical directions, respectively), one obtains from Eq. (17),

$$\delta n_g^2 = n_g / V. \quad (18)$$

Finally, the expression for δn_g should be substituted with a plus sign into definition (4) for $\tilde{F}_{\text{int}}$, which is a version of E_c^-:

$$E_c^- = \frac{2\pi\hbar^2 a_o}{m}\delta n_g = \frac{2\pi\hbar^2 a_o n_g^{1/2}}{m V^{1/2}}. \quad (19)$$

The quantity E_c^- (19) depends on R, and the general expression E_c in Eq. (16) has an extremum as a function of R. The resulting extremal expression for the energy of electron capture by the fluctuative hole has the form

$$E_c^* = \gamma_* n_g, \quad \gamma_* = \frac{2\pi\hbar^2 a_o^2}{m\langle z \rangle}. \quad (20)$$

Note that the use of formula (17) in scenario (16)–(20) is not necessary. To make sure of that, let us introduce Eq. (17) (the authors of [7–12] assume that this expression is universal for the description of any polaron formation) into the problem of a bubble in liquid helium. In this case, formula (17) or its analog (18) gives again

$$\delta n_l^2 = n_l / V, \quad V = 4\pi R^3/3, \quad R \gg a. \quad (21)$$

Here R is the bubble radius, a is the interatomic distance, and n_l is the liquid density.

Then, one has for the bubble $\delta n_l = n_l$, so that estimate δn_l (21) takes the form

$$\delta n_l = 1/V. \quad (21a)$$

This estimate is invalid, because the electronic bubble is empty in liquid and, hence, δn_l should be estimated as

$$\delta n_l = 1/a^3. \quad (21b)$$

Although model (16)–(20) is qualitatively inconsistent, one may take it into account sometimes, because the data in [11] were processed using this model. By comparing Eqs. (15) and (20), one can readily verify that, in the region linear with respect to n_g (i.e., where $n_g \gg n_c$), they differ by the factor $a_o/\langle z \rangle$:

$$\left.\frac{E_c^*}{F}\right|_{n_g > n_c} \simeq a_o / \langle z \rangle. \quad (22)$$

This fact should be taken into account when discussing the experimental data.

3. Experimental. The authors of [7–12] assumed that an electron can be autolocalized over solid hydrogen in the presence of gaseous helium on the basis of the data on 2D conductivity, which demonstrates activation behavior in a certain range of parameters (in the vicinity of density n_c much lower than the 3D threshold in Eq. (9)). The corresponding activation energy increases linearly with gas density. The authors of [7–12] assumed that their localization model is consistent and that the linear increase in the activation energy as a function of n_g is the most important detail. They repre-

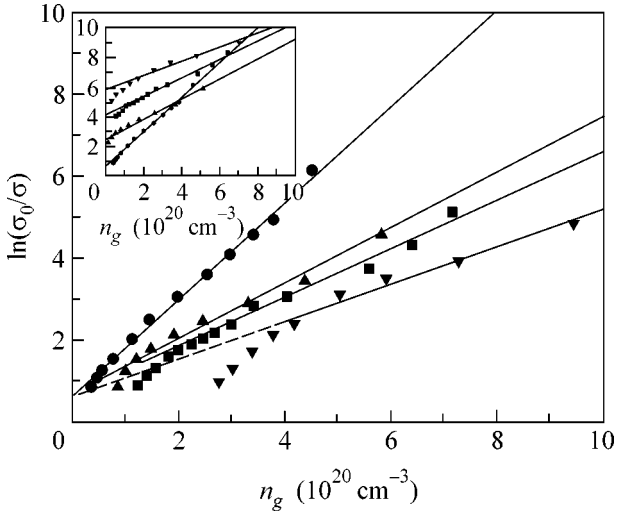

Inset: data from [11] on $\ln\sigma_o/\sigma(n_g, T)$ as a function of n_g at various temperatures: T = (circles) 1.8 K; (triangles) 4 K; (squares) 5.1 K; and (inverted triangles) 7.7 K. The figure contains the same data shifted with the retention of the slopes and satisfying the two requirement: all lines must converge at the point $n_g = 0$ (this requirement corresponds to definition (20)), and the threshold for the appearance of activation behavior of conductivity should be the same for different temperatures shown in the figure. For comments, see text.

sented the data on the activation energy in the form (inset in the figure) that demonstrates this linearity most clearly. For the unknown reason some portions of the $\ln\sigma_o/\sigma(n_g, T)$ curves were shifted relative to each other (see comment to Fig. 4 in [11]). This linearity is clearly seen from the normal positions of these lines. The constant γ_* obtained from the graphs in Fig. 4 in [11] well coincides with (20). This fact counts in favor of model (16)–(20) and not model (11)–(15). However, nothing was said in [11] about the correction to gas density over the hydrogen surface. The van der Waals forces make gaseous helium denser over hydrogen, just as this occurs over liquid helium, where the surface sealing brings about the additional terms of gas origin in the temperature dependence of surface tension (see [17]). As a result, the local gas density is higher in the anion-localization region than in the volume. For this reason, the agreement between the experiment and predictions (20) with respect to the correctness of estimating γ_* (using Eq. (22)) signifies that the experiment is closer to formula (15) than to (20).

Let us discuss the initial portions of all $\ln\sigma_o/\sigma(n_g, T)$ curves (figure). They show noticeable (increasing with T) departure from linearity. This effect is absent in model (16)–(20) and present in description (11)–(15). For clarity, the data from [11] are reconstructed on the basis of two considerations: first, all curves for the $\ln\sigma_o/\sigma(n_g, T)$ dependences as functions of density n_g must converge, by definition, at the zero point for different T. Second, the relative threshold for creating local states should demonstrate approximately the same sensitivity for different temperatures. The results of such reconstruction are presented in the figure. The threshold character of the appearance of 2D anions is clearly seen, as well as a shift of critical point in the desired direction upon an increase in T and smooth transitions to the linear dependences at $n_g > n_c$.

Thus, information on the disk-shaped electronic bubbles at the hydrogen surface in the presence of gaseous helium has been collected in this work. The formalism determining the parameters of such a formation has the same origin as in [3–5]. It allows one to work with both three-dimensional bubbles and their analogs in the presence of external localizing fields. The conclusions of the theory have been compared with conclusions following from the model suggested in [11] for electron localization in deep gas-density fluctuations. The experiments [11] evidencing the presence of disk-shaped autolocalized electron states at solid hydrogen + gaseous helium have been discussed.

This work was supported in part by the Russian Foundation for Basic Research, project no. 03-02-16121.

REFERENCES

1. R. Ferrel, Phys. Rev. **108**, 167 (1957).
2. G. Carrery, V. Fazoli, and F. Gaeta, Nuovo Cimento **15**, 774 (1960).
3. J. Levin and T. Sanders, Phys. Rev. **154**, 138 (1967).
4. L. Kukushkin and V. Shikin, Zh. Éksp. Teor. Fiz. **63**, 1830 (1972) [Sov. Phys. JETP **36**, 969 (1973)].
5. V. Shikin, Usp. Fiz. Nauk **121**, 457 (1977) [Sov. Phys. Usp. **20**, 226 (1977)].
6. V. B. Shikin and Yu. P. Monarkha, Zh. Éksp. Teor. Fiz. **65**, 751 (1973) [Sov. Phys. JETP **38**, 373 (1974)].
7. P. Adams and M. Paalanen, Phys. Rev. Lett. **58**, 2106 (1987).
8. P. Adams and M. Paalanen, Phys. Rev. Lett. **61**, 451 (1988).
9. P. Adams and M. Paalanen, Surf. Sci. **196**, 150 (1987).
10. P. Adams, Surf. Sci. **263**, 663 (1991).
11. P. Adams, Phys. Rev. Lett. **65**, 3333 (1990).
12. P. Adams, D. Brown, and M. Paalanen, Phys. Rev. B **45**, 8837 (1992).
13. E. Abrahamson, P. Anderson, D. Licciadello, and T. Ramakrishnan, Phys. Rev. Lett. **42**, 673 (1979).
14. B. Al'tshuler, D. Khmelnizkii, A. Larkin, and P. Lee, Phys. Rev. B **22**, 5142 (1980).
15. B. Al'tshuler, A. Aronov, A. Larkin, and D. Khmel'nitskiĭ, Zh. Éksp. Teor. Fiz. **81**, 768 (1981) [Sov. Phys. JETP **54**, 411 (1981)].
16. L. D. Landau and E. M. Lifshitz, *Course of Theoretical Physics*, Vol. 5: *Statistical Physics*, 4th ed. (Nauka, Moscow, 1995; Butterworth, London, 1999).
17. A. Dyugaev and P. Grigor'ev, Pis'ma Zh. Éksp. Teor. Fiz. **78**, 935 (2003) [JETP Lett. **78**, 466 (2003)].

Translated by V. Sakun

JETP Letters, Vol. 80, No. 6, 2004, pp. 421–425. Translated from Pis'ma v Zhurnal Éksperimental'noĭ i Teoreticheskoĭ Fiziki, Vol. 80, No. 6, 2004, pp. 477–481.

Inductive Current in a Quantum Ring

L. I. Magarill* and M. V. Éntin

Institute of Semiconductor Physics, Siberian Division, Russian Academy of Sciences, pr. Akademika Lavrent'eva 13, Novosibirsk, 630090 Russia

**e-mail: levm@isp.nsc.ru*

Received June 29, 2004; in final form, August 11, 2004

The induction current in a single-channel quantum ring placed in a quasi-stationary magnetic field is calculated taking into account the scattering of electrons by phonons. © *2004 MAIK "Nauka/Interperiodica".*

PACS numbers: 71.70.Ej; 73.50.Jt; 73.63.Hs

Apparently, Bloch was the first to consider a quantum nonsuperconducting ring in an alternating magnetic field [1]. He proposed this model as a simple illustration of the Josephson effect. Later, quantum rings in alternating fields were studied, in particular, in view of the problems of quantum pumps (beginning with [2]) and as applied to Aharonov–Bohm oscillations in the mesoscopic regime [3]. Despite the fact that it is rather difficult to study experimentally the effect of an alternating magnetic field on quantum objects, these problems have attracted the attention of researchers. The problem is still of interest, which is evidenced by the studies published from time to time [4–9]. However, the effect of the inelastic scattering of electrons on the electric response of a quantum ring has not been investigated.

In this study, we consider a single-channel quantum ring in an adiabatically changing magnetic field. In such a field, along with a persistent current, an inductive current is induced in the ring, which is proportional to the vortex electric field. In contrast to the persistent current, the inductive current is determined by the electron kinetics. We will consider the problem, taking into account the scattering of electrons by phonons. It is assumed that a magnetic field varies slowly, which makes it possible to expand the response of the circular current in terms of the vortex electric field, i.e., the derivative of the magnetic flux with respect to time. The response to the vortex field can be considered the conductance of a contactless quantum ring. In contrast to the conventional statement of the problem, it is proposed to perform contactless measurements of the ring conductance, in particular, by absorption of a high-frequency electromagnetic field. Note that the steady-state potential of impurities in the ring does not lead to real scattering, since, due to the conservation of coherence, the steady states of electrons in a magnetic field are Bloch states with conservation of the azimuthal current (which is zero in the absence of a magnetic field). That is why we restrict our consideration to an ideal ring interacting with phonons. At low temperatures, the scattering by phonons is relatively weak; therefore, the ring conductance can reach a large value (significantly exceeding the conductance quantum). This is the difference of a single-channel ring from a single-channel microcontact, the conductance of which is restricted from above by the conductance quantum due to the inevitable relaxation of electrons in reservoirs.

STATEMENT OF THE PROBLEM

Let us consider an ideal quantum ring of radius R made of an n-type semiconductor with a quadratic electron spectrum. The ring is placed in slowly varying magnetic field $H(t)$ directed along the ring axis. The effect sought is a correction to the persistent current $J_0(\Phi)$:

$$J(\Phi) = J_0(\Phi) + G(\Phi)\mathscr{E}. \quad (1)$$

Here, $\mathscr{E} = -\dot{\Phi}(t)/c$ is the voltage induced in the ring by the alternating magnetic field, $\Phi(t) = H(t)\pi R^2$ is the magnetic flux, and G is the ring conductance. The conductance of the ring depends on its size and the magnetic flux. Obviously, in the large-radius limit, ring conductance G must pass into the conductance of a one-dimensional (1D) system and cease to depend on magnetic flux Φ. We will expand all expressions in $\dot{\Phi}$.

The electronic states in the absence of scattering can be described by adiabatic (instantaneous) terms ϵ_ν. In particular, in the absence of spin–orbit interaction, states of electrons ν are characterized by the projection of angular momentum m on the ring axis z and spin number $\sigma = \pm 1$ and described by the adiabatic terms $\epsilon_\nu = (m + \phi)^2/2m_eR^2 + \sigma g\mu_B H/2$, $\phi = \Phi/\Phi_0$ (hereinafter, the flux is measured in quantum-flux units $\Phi_0 = 2\pi c/e$, and m_e is the electron mass), μ_B is the Bohr magneton, and g is the Landé g factor. Hereinafter, $\hbar = 1$. The levels with the same values of σ intersect each other at the points $\phi = 0$ and 1/2.

0021-3640/04/8006-0421$26.00

The angular-velocity operator contains the value of magnetic flux. Thus, when the flux varies, the current of electrons in the above states varies synchronously with the flux [9]. With an increase in the flux, acceleration of electrons (similar to the betatron acceleration) occurs. For example, if the flux changes linearly with time, the current also increases linearly. At the same time, it is obvious that the vortex electric field is constant in this case. Taking into account the relaxation should lead to a constant current superimposed on the alternating as a function of flux persistent current. Thus, the effect of relaxation radically changes the final result.

KINETIC EQUATION

The relaxation of electrons will be taken into account in terms of the quantum kinetic equation. Simplifying this equation, we will use the fact that the magnetic flux varies slowly. This makes it possible to neglect the effect of the time dependence of the flux on the scattering. In addition, the scattering is considered in the lowest order of the perturbation theory. Technically, we used the form of the kinetic equation from [10, 11].

As the relaxation mechanism, we consider the scattering of electrons by acoustic phonons. For simplicity, we assume that the spectrum of phonons is isotropic and their interaction with electrons is not violated by the existence of the object boundaries (in particular, for a quantum ring buried in the bulk of a material with similar properties). In this case, the Hamiltonian describing the interaction of one electron with phonons has the form

$$\mathcal{H}_{e-ph} = \sum_{\mathbf{q}} C_{\mathbf{q}}(e^{i\mathbf{qr}}b_{\mathbf{q}} + \text{h.c.}). \quad (2)$$

Here, $b_{\mathbf{q}}$ is the operator of annihilation of a phonon in state $\mathbf{q}$. The interaction with phonons is described by the quantity $|C_q|^2 = (B_D q + B_P/q)/V$ [12], which includes the deformation ($B_D q$) and piezoelectric (approximated by the isotropic ratio B_P/q) contributions (V is the volume of the system). The quantities B_D and B_P are related to the momentum-relaxation times in the initial three-dimensional crystal with respect to the deformation and piezoelectric interactions (τ_{DA} and τ_{PA}, respectively) for the temperature and the energy of an electron corresponding to the energy of optical phonon ω_0:

$$B_D = \frac{\pi s}{\tau_{DA}(2m_e\omega_0)^{3/2}}, \quad B_P = \frac{2\pi s}{\tau_{PA}(2m_e\omega_0)^{1/2}}. \quad (3)$$

Here, s is the speed of sound.

In the representation of the $m\sigma$ states, Hamiltonian (2) proves to be diagonal with respect to quantum number σ:

$$(e^{i\mathbf{qr}})_{m,\sigma;m',\sigma'} = J_{m-m'}(q_\perp R)\delta_{\sigma\sigma'}. \quad (4)$$

Here, $q_\perp = \sqrt{q_x^2 + q_y^2}$ and $J_n(x)$ is a Bessel function.

The density matrix is also diagonal with respect to σ and (in view of the axial symmetry of the ring) m. As a result, the kinetic equation can be written for the diagonal elements of the density matrix $\rho_{\nu\nu} \equiv \rho_\nu$:

$$\dot{\rho}_\nu = \sum_{\nu'}(w_{\nu'\nu}\rho_{\nu'}(1-\rho_\nu) - w_{\nu\nu'}\rho_\nu(1-\rho_{\nu'})). \quad (5)$$

The probability of a phonon-induced transition is given by the expression

$$w_{\nu'\nu} = \delta_{\sigma\sigma'}\frac{B_D}{4\pi^2}\int d^3\mathbf{q}\left(q + \frac{\gamma}{q}\right)J^2_{m-m'}(q_\perp R) \times [N(\omega_q)\delta(\epsilon_{\nu'\nu} + \omega_q) + (N(\omega_q)+1)\delta(\epsilon_{\nu'\nu} - \omega_q)], \quad (6)$$

where $N(\omega_q) = (\exp(\omega_q/T) - 1)^{-1}$ is the equilibrium phonon distribution function, $\epsilon_{\nu'\nu} = \epsilon_{\nu'} - \epsilon_\nu$, and $\gamma = B_P/B_D$.

Note that $w_{\nu'\nu} = w_{\nu\nu'}\exp(\epsilon_{\nu'\nu}/T)$.

Let us represent the density matrix as an expansion in the nonadiabaticity: $\rho_\nu = f(\epsilon_\nu - \mu) + \rho_\nu^{(1)} + \ldots$. The first term is the quasi-equilibrium density matrix, which coincides with the Fermi function $f(x) = (\exp(x/T) + 1)^{-1}$. The latter depends on the instantaneous values of levels and the corresponding values of the chemical potential μ. The chemical potential is determined from the condition of constant average number of electrons N in the ring:

$$\sum_\nu f(\epsilon_\nu - \mu) = N, \quad \sum_\nu \rho^{(1)} = 0. \quad (7)$$

This approach is valid in the absence of spin splitting. When spin splitting is taken into account, due to the difference in the energy levels with different values of σ, one has also to consider the conservation of the number of electrons with given σ, introducing different Fermi levels μ_σ for spin sublevels:

$$\sum_m f(\epsilon_\nu - \mu_\sigma) = N_\sigma, \quad (8)$$

$$\sum_m \rho_\nu^{(1)} = 0. \quad (9)$$

The quasi-equilibrium density matrix makes the right-hand side of Eq. (5) vanish. Let us linearize Eq. (5) with respect to the additional term in the density matrix, assuming the flux to be slowly varying. The derivatives of $f_\nu \equiv f(\epsilon_\nu - \mu_\sigma)$ with respect to time give the left-hand part of the quantum kinetic equation:

$$D_\nu = \dot{\phi}\left[\frac{\partial f_\nu}{\partial\mu}\sum_{m'}V_{\nu'}\frac{\partial f_{\nu'}}{\partial\mu}\Big/\sum_{m'}\frac{\partial f_{\nu'}}{\partial\mu} - V_\nu\frac{\partial f_\nu}{\partial\mu}\right], \quad (10)$$

where the angular velocity of an electron in the state ν is $V_\nu = \partial\epsilon_\nu/\partial\phi$ and, after the linearization, the chemical potentials can be considered identical. The condition of conservation of the number of particles (8) is ensured by the equality $\sum_m D_\nu = 0$. In fact, expression (10) includes only the "orbital" part of the velocity $(m + \phi)/m_e R$, since the spin contribution vanishes.

The resulting quantum kinetic equation has the form of a steady-state equation,

$$\sum_{\nu'} W_{\nu'\nu}\rho_{\nu'}^{(1)} - W_{\nu\nu'}\rho_\nu^{(1)} = D_\nu, \tag{11}$$

where $W_{\nu'\nu} = w_{\nu',\nu}(1 - f_\nu) + w_{\nu\nu'}f_\nu$. In this equation, time serves a parameter entering the instantaneous values of the chemical potential and the spectrum via the flux. System (11) has a degenerate kernel: the additional term in the quasi-equilibrium distribution function related only to the variation in the Fermi level $((\partial f_\nu/\partial\mu)\Delta\mu)$ makes the left-hand side vanish; the unambiguous solution to the system is fixed by the additional condition (9).

After integration, we find:

$$W_{\nu'\nu} = \delta_{\sigma\sigma'}\frac{B_D}{2\pi s^4}$$
$$\times(|\epsilon_{\nu'\nu}|^3 + \gamma s^2|\epsilon_{\nu'\nu}|)S_{m'-m}(|\epsilon_{\nu'\nu}|R/s) \tag{12}$$
$$\times[\theta(\epsilon_{\nu'\nu})(N(\epsilon_{\nu'\nu}) + 1 - f_\nu) + \theta(\epsilon_{\nu\nu'})(N(\epsilon_{\nu\nu'}) + f_\nu)],$$

$$S_m(y) = \int_0^1 \frac{xdx}{\sqrt{1-x^2}}J_m^2(xy).$$

When the condition $\epsilon_{\nu\nu'}R/s \gg 1$ is satisfied, the function $S_m(y)$ can be replaced by its asymptotic form at large values of the argument: $S_m(y) \approx 1/2y$.

The conductance is determined by the equation

$$G\dot{\phi} = \frac{e^2}{2\pi}\sum_\nu V_\nu\rho_\nu^{(1)} \equiv \frac{e^2}{2\pi m_e R}\sum_\nu (m + \phi)\rho_\nu^{(1)}. \tag{13}$$

CALCULATION OF THE CONDUCTANCE IN THE ABSENCE OF SPIN SPLITTING

In the absence of spin splitting ($g = 0$), the energy spectrum of electrons satisfies the following conditions:

$$\epsilon_m(\phi) = \epsilon_{-m}(-\phi), \tag{14}$$

$$\epsilon_m(\phi + 1) = \epsilon_{m+1}(\phi). \tag{15}$$

It follows from the first condition that $W_{m,m'}(-\phi) = W_{-m,-m'}(\phi)$, $\rho_m^{(1)}(-\phi) = -\rho_{-m}^{(1)}(\phi)$, and $G(-\phi) = G(\phi)$. The second condition yields $G(\phi + 1) = G(\phi)$.

These properties of the electron spectrum make it possible to solve analytically system of equations (12) at $\phi = 0$ or 1/2. It can be easily seen that the income term in kinetic equation (11) becomes zero at these values of ϕ. As a result, we have, for these values of the flux:

$$G(\phi) = \frac{e^2}{\pi}\frac{1}{(m_e R^2)^2}$$
$$\times\sum_m \tau_m(\phi)(m + \phi)^2\frac{\partial f_m}{\partial\mu}, \quad \phi = 0, 1/2, \tag{16}$$

with the inverse relaxation time

$$\tau_m^{-1}(\phi) = \sum_{m'} W_{mm'}(\phi). \tag{17}$$

At $\phi \neq 0, 1/2$, formula (16) can be considered a naive solution in the relaxation-time approximation. The exact result can be found by numerical solution of system of algebraic equations (11). At sufficiently low temperatures, the main contribution to the conductance is determined by the pair levels (for example, *a* and *b*) that are closest to the Fermi level and located at opposite sides of it. In this case,

$$G = \frac{e^2}{\pi}\frac{(V_a - V_b)^2}{W_{ab} + W_{ba}}\frac{\partial f_a}{\partial\mu}\frac{\partial f_b}{\partial\mu}\left(\frac{\partial f_a}{\partial\mu} + \frac{\partial f_b}{\partial\mu}\right)^{-1}. \tag{18}$$

It can be seen from (18) and (12) that the conductance exponentially increases when the levels *a* and *b* approach each other.

This behavior is affected by a factor related to C_q. If the emitted energy is low, the piezoelectric interaction is dominant; otherwise, the deformation interaction prevails. In both limits, the transition probability increases. The other factor, $S_{mm'}(|\epsilon_{mm'}|R/s)$, also affects the behavior of the conductance. In particular, the conductance oscillates at a large product of the wave vector of an emitted phonon by the ring radius.

Figure 1 shows the numerically calculated dependence of the conductance of a ring with a radius of 10^{-6} cm with one electron on magnetic flux at different temperatures. Parameters of GaAs were used: $\tau_{PA} = 4$ ps, $\tau_{DA} = 8$ ps, $s = 5 \times 10^5$ cm/s, and $\omega_0 = 421$ K. With these parameters, electrons from lower levels ($m = 0, -1$) are involved in the conduction and the deformation mechanism of scattering is dominant. For comparison, the dependence of the conductance on flux calculated in the τ approximation (dotted line) for $T = 0.3/2m_eR^2$ is also shown in Fig. 2. This curve coincides with the dependence obtained by numerical solution of the kinetic equation at $\phi = 0$ and 0.5 and significantly differs from it at other points. The strong peak at $\phi = 0.5$ is due to the intersection of levels. The same peak at $\phi = 0$ is suppressed because the velocity of an electron in the state with $m = 0$ is zero. The oscillations are due to the commensurability of the wavelengths of emitted

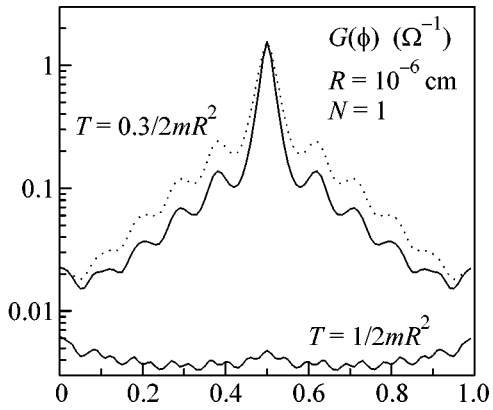

Fig. 1. Dependences of the conductance (on logarithmic scale) on magnetic flux for a quantum ring with a radius of 10^{-6} cm containing one electron at different temperatures. The dotted line is the calculation in the τ approximation. The parameters of GaAs were used.

phonons and the ring radius. Note the presence of a discontinuity in the derivative $G(\phi)$ at the points $\phi = 0$ and 1/2, which is caused by the nonanalyticity of the transition probability as a function of $\epsilon_{\nu\nu'}$ at $\epsilon_{\nu\nu'} = 0$.

Figures 2a and 2b show the results of calculation of the conductance for many-electron quantum rings with radii $R = 10^{-6}$ and 10^{-5} cm and a fixed integer number of electrons N. At low temperatures, at the points $\phi = 0$ and 1/2, the chemical potential lies between the nearest levels for $N = 4n + 2$ and coincides with one of the levels for $N \neq 4n + 2$. When $\phi \neq 0, 1/2$, the Fermi level coincides with one of the ring levels at an odd N and lies between ring levels at an even N. This circumstance determines the difference in the behavior of the conductance for different N. In the ring with a radius of 10^{-6} cm, the main mechanism is scattering by the deformation potential, while in the ring with a radius of 10^{-5} cm the scattering by the piezoelectric potential plays a key role. Oscillations mainly manifest themselves in the ring with a small radius, where the energies of phonons are higher and their wavelengths are shorter. In this case, since only longitudinal phonons are involved in the scattering, the spread of oscillations due to the difference in the frequencies of phonons of different type is insignificant. Hence, it was neglected.

ACCOUNT OF THE SPIN SPLITTING

Since the Hamiltonian is diagonal with respect to the spin indices, the contributions of different spin projections on the z axis to the current are additive. Therefore, the conductance regarded as a function of the chemical potential and flux, taking into account the

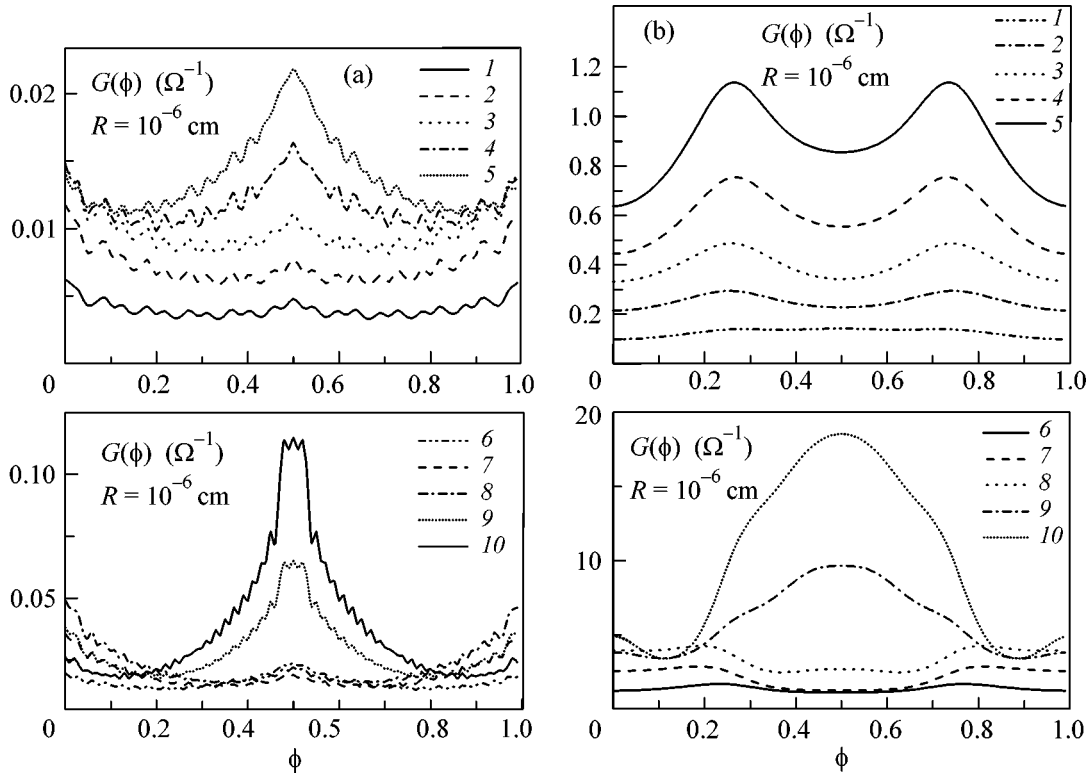

Fig. 2. Dependences of the conductance of a GaAs quantum ring with an integer number of electrons (indicated for the corresponding curves) in the absence of spin splitting at $T = 1/2m_eR^2$ and R = (a) 10^{-6} and (b) 10^{-5} cm on a magnetic field.

splitting, G^s is the sum of the conductances of the spin components. Each spin component is determined by the same expressions as in the absence of splitting with a shift of μ by a half of the spin splitting $\mu \longrightarrow \mu \pm g\mu_B H/2$:

$$G^s = \frac{1}{2}\left(G\left(\mu - \frac{1}{2}g\mu_B H, \phi\right) + G\left(\mu + \frac{1}{2}g\mu_B H, \phi\right)\right). \quad (19)$$

At a given integer number of electrons, the chemical potential should be determined according to formula (7). Formula (19) can also be used for an oblique magnetic field, taking into account that the total magnetic field enters the expression for the spin splitting, whereas only the vertical component of the field enters the expression for the flux. Note that the periodicity with respect to the flux (taking into account the spin splitting) occurs only when ϕ and H are regarded as independent arguments.

DISCUSSION

In view of the fact that, at low temperatures, we obtained a very large change in the conductance with changing the magnetic field, the question arises whether this result is the consequence of the approximations used here or not. Let us note the limitations related to these approximations and begin with the adiabatic approximation. It was assumed that the field varies slowly, so that $\dot{\phi} \ll \delta\epsilon$. This condition is violated when levels intersect each other. However, the rate of variation in the magnetic field is generally very low and, therefore, this effect can manifest itself only in a very narrow range near the point of intersection of the levels.

It was also assumed that energy equilibrium is established in the absence of exchange in particles between the ring and reservoir. This condition can be easily satisfied using sufficiently thick barriers. In addition, taking into account the energy of the ring charging leads to the occurrence of a finite energy barrier between different charge states and to the quantization of the average charge of the ring at low temperatures (below the charging energy).

In our opinion, the most significant limitation is the assumption about the ideality of the ring. The asymmetry caused by the fluctuation potential inevitably results in the level splitting. When this potential is low, it manifests itself only near the point of intersection of the levels $\phi = 0$ and 1/2, due to which the electron velocity becomes zero at these points; as a result, the contribution of the levels that are closest to the Fermi level to the conductance vanishes and the conductance peaks in the low-temperature range sharply decrease. When the level splitting induced by the magnetic field exceeds the asymmetry-induced splitting, the result should pass to the above-considered limit of an ideal ring. When the fluctuation potential is rather high in a ring of large radius, the allowed bands become exponentially narrow due to the localization; as a result, with an increase in the length of the ring circumference, the average electron velocity and the conductance exponentially decrease.

To conclude, we should note that, with an increase in the magnetic field, the scattering mechanism studied here limits the current in an ideal ring. The resulting current is determined by the dissipative conductance. The conductance of an isolated ring may reach significant values, greatly exceeding the conductance quantum. At low temperatures, the interlevel transitions are suppressed, whereas only these transitions lead to scattering. A variation in the spacing between the levels with varying the magnetic field strongly (exponentially) affects the conductance that leads to the sharp maxima in the dependence of the conductance on the magnetic field. Thus, the conductance of a 1D ring, in contrast to a 1D conductor, depends on the magnetic field even in the absence of spin splitting. In weak magnetic fields, the magnetoconductance $G(\phi) - G(0)$ can be either negative or positive. In addition, in the model with scattering by the deformation potential, a linear dependence of the conductance on magnetic field can be observed.

This study was supported by the Russian Foundation for Basic Research (project nos. 00-02-16377 and 02-02-16398), the program "Leading Scientific Schools" (project no. NSh-593.2003.2), and INTAS (grant no. 03-51-6453).

REFERENCES

1. F. Bloch, Phys. Rev. Lett. **21**, 1241 (1968).
2. D. J. Thouless, Phys. Rev. B **27**, 6083 (1983).
3. B. L. Altshuler, A. G. Aronov, D. E. Khmelnitskii, and A. I. Larkin, in *Quantum Theory of Solids*, Ed. by I. M. Lifshits (Mir, Moscow, 1982).
4. K. B. Efetov, Phys. Rev. Lett. **66**, 2794 (1991).
5. V. E. Kravtsov and V. I. Yudson, Phys. Rev. Lett. **70**, 210 (1993).
6. M. Moskalets and M. Büttiker, Phys. Rev. B **66**, 245321 (2002).
7. L. Arrachea, Phys. Rev. B **66**, 045315 (2002).
8. V. Gudmundsson, Chi-Shung Tang, and A. Manolesku, Phys. Rev. B **67**, 161301(R) (2003).
9. A. V. Chaplik and L. I. Magarill, Laser Phys. **14** (3), 412 (2004).
10. F. T. Vas'ko, Fiz. Tverd. Tela (Leningrad) **17**, 2288 (1975) [Sov. Phys. Solid State **17**, 1514 (1975)].
11. I. B. Levinson, Zh. Éksp. Teor. Fiz. **57**, 660 (1969) [Sov. Phys. JETP **30**, 363 (1969)].
12. V. F. Gantmakher and Y. B. Levinson, *Carrier Scattering in Metals and Semiconductors* (Nauka, Moscow, 1984; North-Holland, Amsterdam, 1987), Chap. 4.

Translated by Yu. Sin'kov

JETP Letters, Vol. 80, No. 6, 2004, pp. 426–432. Translated from Pis'ma v Zhurnal Éksperimental'noĭ i Teoreticheskoĭ Fiziki, Vol. 80, No. 6, 2004, pp. 482–488.

Structural and Electronic Transitions in Gadolinium Iron Borate $GdFe_3(BO_3)_4$ at High Pressures

A. G. Gavriliuk[1, 2], S. A. Kharlamova[3], I. S. Lyubutin[2, *], I. A. Troyan[1], S. G. Ovchinnikov[3], A. M. Potseluiko[3], M. I. Eremets[4], and R. Boehler[4]

[1]*Institute of High-Pressure Physics, Russian Academy of Sciences, Troitsk, Moscow region, 142092 Russia*
[2]*Institute of Crystallography, Russian Academy of Sciences, Moscow, 119333 Russia*
[3]*Kirensky Physics Institute, Siberian Division, Russian Academy of Sciences, Krasnoyarsk, 660036 Russia*
[4]*Max-Planck Institut für Chemie, 55020 Mainz, Germany*
**e-mail: lyubutin@ns.crys.ras.ru*
Received July 30, 2004

The optical properties and structure of gadolinium iron borate $GdFe_3(BO_3)_4$ crystals are studied at high pressures produced in diamond-anvil cells. X-ray diffraction data obtained at a pressure of 25.6 GPa reveal a first-order phase transition retaining the trigonal symmetry and increasing the unit cell volume by 8%. The equation of state is obtained and the compressibility of the crystal is estimated before and after the phase transition. The optical spectra reveal two electronic transitions at pressures ~26 GPa and ~43 GPa. Upon the first transition, the optical gap decreases jumpwise from 3.1 to ~2.25 eV. Upon the second transition at $P = 43$ GPa, the optical gap deceases down to ~0.7 eV, demonstrating a dielectric–semiconductor transition. By using the theoretical model developed for a $FeBO_3$ crystal and taking into account some structural analogs of these materials, the anomalies of the high-pressure optical spectra are explained. © *2004 MAIK "Nauka/Interperiodica".*

PACS numbers: 61.50.Ks; 71.27.+a; 71.30.+h; 81.40.Tv

1. INTRODUCTION

A $GdFe_3(BO_3)_4$ crystal belongs to the family of rare-earth borates $RM_3(BO_3)_4$ (R is a rare-earth element, M = Al, Ga, Fe, Sc), which are isostructural to a natural mineral huntite $CaMg_3(CO_3)_4$ [1] and have trigonal symmetry with the space group R32 (D_{3h}^7) [2, 3]. Recently, the nonlinear optical and laser properties of these materials were found [4–6], which attracted great attention from researchers.

The structure of rare-earth iron borates $RFe_3(BO_3)_4$ can be represented in the form of layers perpendicular to the *c*-axis (C_3) and consisting of trigonal RO_6 prisms and lower-size FeO_6 octahedra [2, 3]. The FeO_6 octahedra are connected by their faces and form helical one-dimensional weakly coupled chains elongated along the *c*-axis. Boron atoms form isolated triangles with oxygen atoms, producing BO_3^{3-} groups of two types. Triangles of the type $B(1)O_3$ are connected by their vertices only with the FeO_6 polyhedra, while triangles of the type $B(2)O_3$ are connected by two vertices with different chains of the FeO_6 octahedra and by the third vortex with the RO_6 prism.

The physical properties of rare-earth iron borates are poorly studied, which is mainly explained by the difficulty of growing high-quality crystals, especially for optical studies. The recent measurements [7, 8] of the magnetic susceptibility, magnetization, and heat capacity showed that a $GdFe_3(BO_3)_4$ borate crystal is a compensated antiferromagnetic with the Néel temperature $T_N = 38$ K, and the spin-flop transition occurs in the crystal at a temperature about 10 K. It is assumed that magnetic ordering below T_N concerns only iron ions, whereas the Gd^{3+} ions remain paramagnetic at least down to liquid helium temperature [7]. In addition, quite recently the structural phase transition was also discovered in this crystal at $T = 156$ K [9].

In this paper, we studied the optical properties and change in the structure of a $GdFe_3(BO_3)_4$ crystal at high pressures produced in diamond-anvil cells. We found two phase transitions at pressures ~26 and ~43 GPa accompanied by the jumpwise narrowing of the optical gap and the dielectric–semiconductor transition.

2. EXPERIMENTAL

High-quality transparent, dark green $GdFe_3(BO_3)_4$ crystals were grown from solution in a melt [10]. The crystal lattice parameters at normal pressure are $a = 9.5491(6)$ and $c = 7.5741(5)$ Å.

X-ray diffraction studies at pressures up to 40 GPa were performed with a polycrystalline sample obtained by single-crystal crushing. The sample was studied at room temperature in a diamond-anvil cell in a specialized laboratory setup at the Max-Planck Institut für

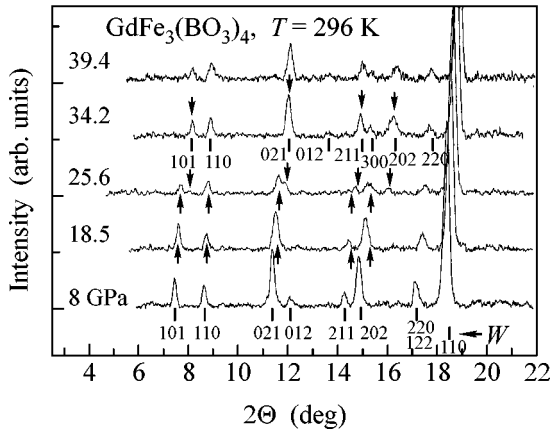

Fig. 1. X-ray diffraction patterns of the $GdFe_3(BO_3)_4$ polycrystal at room temperature at some pressures below and above the phase transition. *W* denotes the position of a reflection from a tungsten gasket.

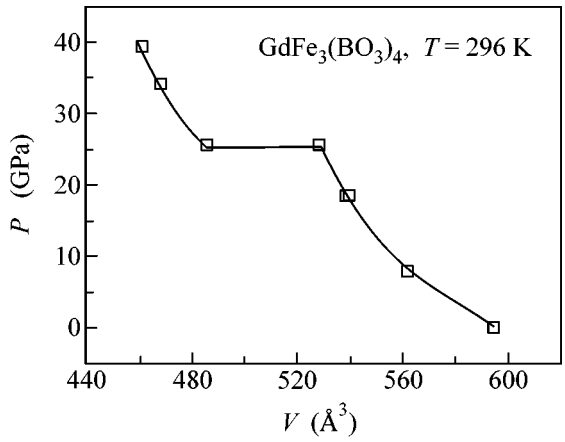

Fig. 2. Baric dependence of the unit cell volume of the $GdFe_3(BO_3)_4$ crystal at room temperature.

Chemie (Mainz, Germany). X-rays were generated by a rotating Mo anode (0.7093 Å) with a special focusing system. Spectra were recorded in the transmission geometry using an Image Plate detector. The high-pressure cell allowed the recording of the spectra in the 30° range of angles 2Θ. The diameter of the diamond anvils was 300 μm, and the diameter of a hole in a tungsten gasket, where a sample was placed, was about 100 μm. Pressure was transmitted to a sample through a PES-5 polyethylsilaxane liquid. To provide quasi-hydrostatic conditions, the working volume of the cell was filled by 1/3 with a sample and by 2/3 with the PES-5 liquid. Pressure was measured by a standard method by the shift of the fluorescence line of ruby.

The optical absorption spectra were measured for a $GdFe_3(BO_3)_4$ crystal at pressures up to 60 GPa at room temperature in the diamond-anvil cell. Diamond anvils of diameter ~400 μm were used. The hole at the center of a rhenium gasket had a diameter of ~120 μm. Measurements were performed for a thin plate of size ~50 × 40 × 15 μm punctured from a massive $GdFe_3(BO_3)_4$ crystal. The light beam was directed perpendicular to the basis plane of the crystal. Pressure was imparted to a sample through a PES-5 liquid providing quasi-hydrostatic compression. A single crystal remained undamaged after the pressure removal. The optical setup for the study of absorption spectra allows one to perform measurements in the visible and near-IR ranges from 0.3 to 5 μm. An FEU-100 photomultiplier was used as a detector in the visible region, while in the near-IR region a germanium diode cooled in liquid nitrogen was used. The light-spot diameter on a sample was ~20 μ. The absorption spectrum was calculated from the expression $I = I_0\exp(-\alpha d)$, where d is the sample thickness, I_0 is the reference signal intensity outside the sample, and α is the absorption coefficient.

3. EXPERIMENTAL RESULTS

3.1. High-pressure X-Ray Studies

The dependence of the X-ray diffraction pattern of a $GdFe_3(BO_3)_4$ crystal on pressure is shown in Fig. 1. As pressure increases, peaks in the diffraction pattern shift in the direction of larger angles, and new peaks appear at $P > 25$ GPa, indicating the transformation of the crystal structure. For $P = 25.6$ GPa, reflections from two coexisting low- and high-pressure phases are observed. This can be caused by incompletely hydrostatic conditions and the presence of a pressure gradient in the cell or by a peculiarity of the first-order phase transition. One can see from Fig. 1 that the main peaks for a new high-pressure phase are identical to those for the low-pressure phase. Therefore, the high-pressure phase was indexed assuming that the crystal symmetry is preserved after the structural phase transition (see Fig. 1). Figure 2 shows the pressure dependence of the unit cell volume for the $GdFe_3(BO_3)_4$ crystal at room temperature calculated using the data presented in Fig. 1. Experimental points for the low-pressure phase were approximated by the Berch–Murnagan equation,

$$P = \frac{3}{2}B_0\left(\frac{V}{V_0}\right)^{-5/3}\left(1-\left(\frac{V}{V_0}\right)^{-2/3}\right) \times\left[\frac{3}{4}(B'-4)\left(1-\left(\frac{V}{V_0}\right)^{-2/3}\right)-1\right]. \quad (1)$$

The approximation gave the bulk modulus $B_0 = 159.5 \pm 6.3$ GPa, its derivative $B' = 4$ (fixed), and unit cell volume at the normal pressure $V_0 = 594.69$ Å^3. After the structural transition at $P = 25.6$ GPa, experi-

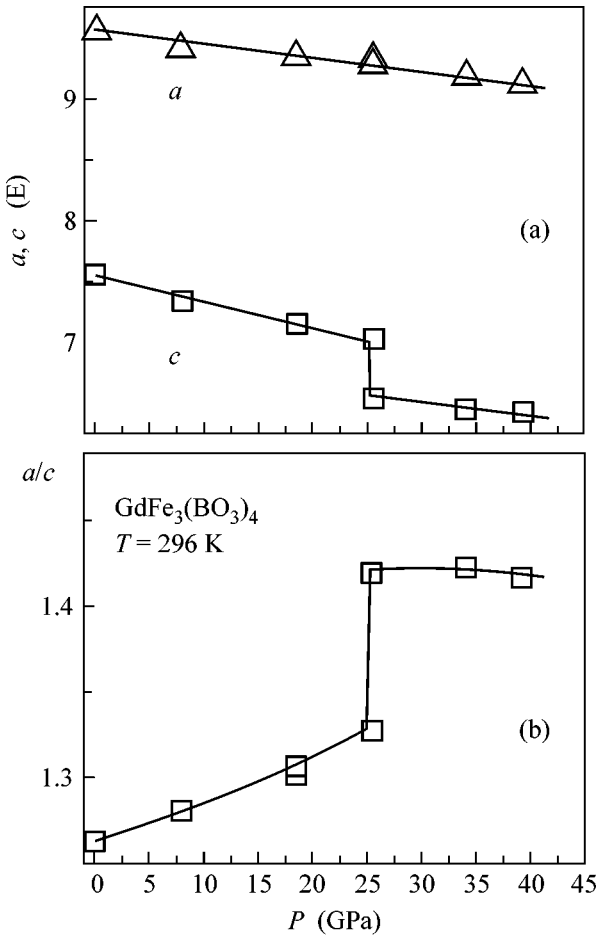

Fig. 3. Baric dependences of the unit cell parameters *a* and *c* in the $GdFe_3(BO_3)_4$ crystal at room temperature (a) and of the *a*/*c* ratio (b).

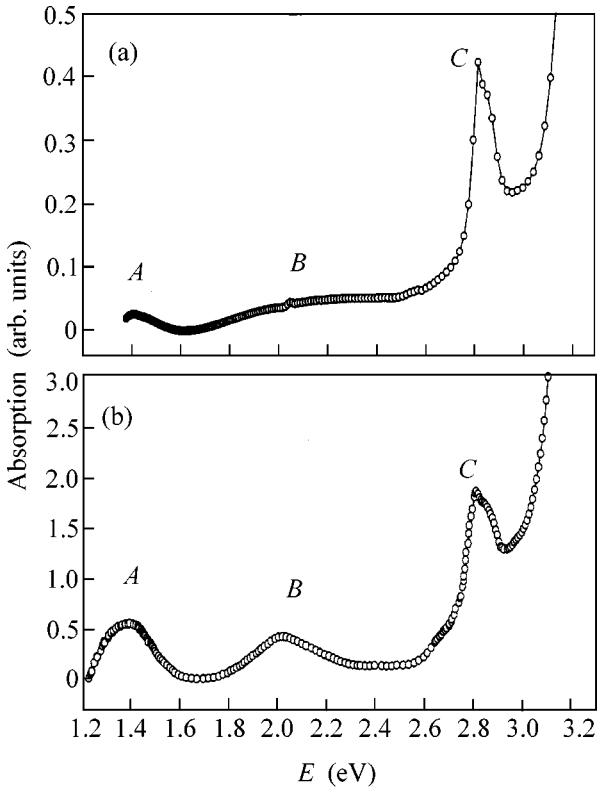

Fig. 4. Absorption spectra of (a) $GdFe_3(BO_3)_4$ and (b) $FeBO_3$ single crystals at normal pressure and room temperature.

mental points for the high-pressure phase were approximated by the modified Birch-Murnagan equation,

$$P + 25.6\ \text{GPa} = \frac{3}{2}B_{26}\left(\frac{V}{V_{26}}\right)^{-5/3}\left(1-\left(\frac{V}{V_{26}}\right)^{-2/3}\right) \times\left[\frac{3}{4}(B'_{26}-4)\left(1-\left(\frac{V}{V_{26}}\right)^{-2/3}\right)-1\right] \quad (2)$$

and we obtained $B_{26} = 219.5 \pm 6.5$ GPa, $B'_{26} = 4$ (fixed), and $V_{26} = 486.022$ Å^3.

Therefore, the structural transition in the $GdFe_3(BO_3)_4$ crystal at $P = 25.6$ GPa is the first-order symmetry-retaining transition accompanied by the ~8% jump in the unit cell volume. Note that the crystal compressibility in the high-pressure phase is higher than that in the low-pressure phase.

Figure 3a shows the pressure dependence of the crystal-lattice parameters. One can see that the structural transition is accompanied by a jumpwise decrease in the parameter *c*, whereas the parameter *a* decreases gradually. Figure 3b shows the pressure dependence of the ratio *a*/*c* of the lattice parameters.

3.2. Optical Absorption Spectra

For measurements at normal pressure, the $GdFe_3(BO_3)_4$ crystals were prepared in the form of thin plates of area ~2 mm^2 and thickness from 42 to 53 μm. The plate plane was oriented parallel or perpendicular to the threefold crystallographic axis C_3, and a light beam was directed perpendicular to the plate. Optical spectra were recorded in the spectral range from 10000 to 40000 cm^{-1} (1.24–4.96 eV) at 300 K. The spectral width of the slit of a grating monochromator was 10 cm^{-1}. The accuracy of measurement of the absorption coefficient was 3%. We found that the absorption spectra were virtually identical for both orientations.

Figure 4 shows the absorption spectrum of the $GdFe_3(BO_3)_4$ crystal at normal pressure at room temperature. For comparison, the absorption spectrum of the well-studied iron borate $FeBO_3$ obtained by us earlier [11] is also presented. We found that the energies of absorption bands of the $GdFe_3(BO_3)_4$ and $FeBO_3$ crystals coincide with an accuracy to tenths of electronvolts. Three groups of absorption bands at 1.4, 2.0, and 2.8 eV were observed. The energy gap determining the

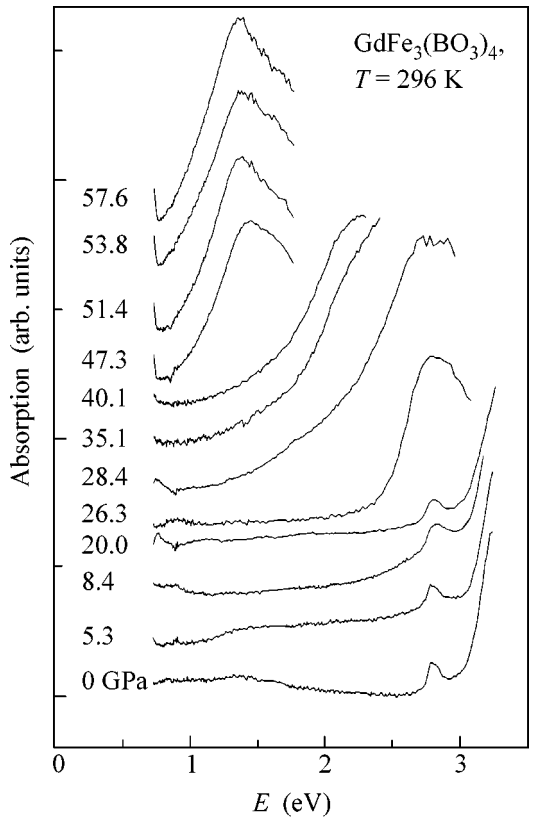

Fig. 5. Absorption spectra of the $GdFe_3(BO_3)_4$ crystal at different pressures at room temperature.

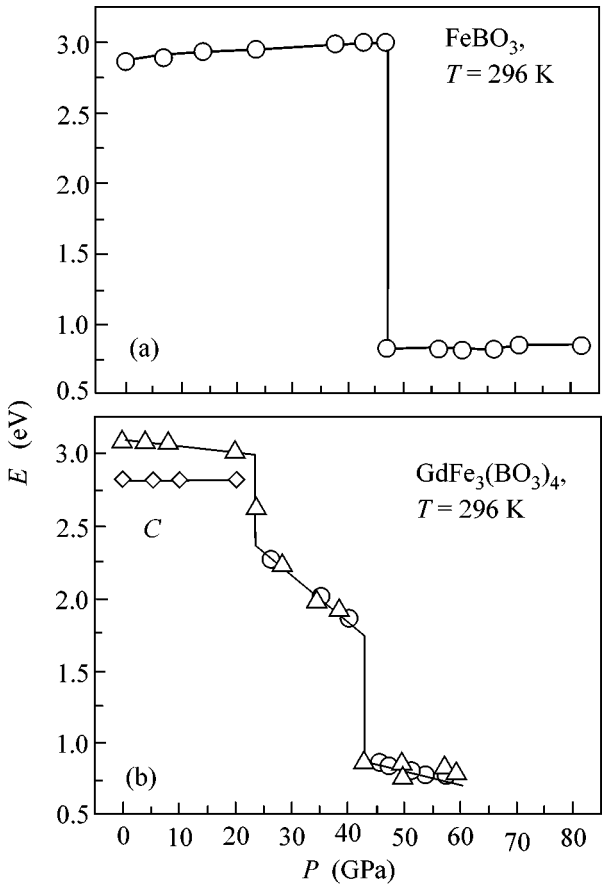

Fig. 6. Baric dependences of the absorption edge in (a) $FeBO_3$ and (b) $GdFe_3(BO_3)_4$ single crystals at room temperature. The triangles and circles for $GdFe_3(BO_3)_4$ correspond to different measurement series; *C* is the absorption band.

fundamental absorption edge in the $GdFe_3(BO_3)_4$ crystal is E_g = 3.1 eV, which is somewhat greater than in $FeBO_3$ (2.9 eV).

The similarity of the absorption bands suggests that the optical properties of $FeBO_3$ and $GdFe_3(BO_3)_4$ coincide in the energy range 1–3 eV, and the three groups of bands *A*, *B*, and *C* (Fig. 4) are caused by the ${}^6A_{1g}({}^6S) \longrightarrow {}^4T_{1g}({}^4G)$, ${}^6A_{1g}({}^6S) \longrightarrow {}^4T_{2g}({}^4G)$, and ${}^6A_{1g}({}^6S) \longrightarrow {}^4A_{1g,\,{}^4E_g}({}^4G)$ *d*–*d* transitions, respectively [11].

To determine the possible contributions from rare-earth ions, we recorded the transmission spectra of the $GdFe_3(BO_3)_4$ crystal of thickness 1.58 mm at 300 K using the InSb and Si detectors [12]. We found that the Gd^{3+} ion has no absorption bands in a broad spectral region up to 32500 cm^{-1} (4 eV). Therefore, the *A*, *B*, and *C* bands in the spectra of $GdFe_3(BO_3)_4$ (Fig. 4) should be assigned to the *d*–*d* transitions in Fe^{3+}, i.e., to the transition from the 5/2 ground state to the 3/2 excited state.

The pressure dependence of the absorption spectrum of the $GdFe_3(BO_3)_4$ crystal is shown in Fig. 5. Before the phase transition at $P \approx 26$ GPa, the position of the *C* band can be distinctly observed. One can see that the energy of this band is virtually independent of pressure in this pressure range, being equal to ~2.8 eV (Fig. 6).

In the critical region near P_{c1} = 26 GPa, the spectrum changes noticeably due to the phase transition described above. In this case, the optical gap decreases jumpwise from ~3 to ~2.25 eV (Fig. 6). In a new phase, the optical gap strongly decreases down to ~1.7 eV with increasing pressure from 26 to 43 GPa (Fig. 6) and then sharply decreases down to ~0.7 eV at the pressure P_{c2} = (43 ± 2) GPa. Therefore, at $P_{c2} \approx 43$ GPa, the second phase transition occurs in the $GdFe_3(BO_3)_4$ crystal with changing electronic structure, and, according to the optical-gap value, this transition can be interpreted as the dielectric–semiconductor transition.

To estimate the pressure P_{met} at which the optical gap vanishes and complete metallization occurs, we approximated the baric dependence of the optical gap after the phase transition at P_{c2} = 43 GPa by the linear function

$$E = E_0\left(1 - \frac{P}{P_{met}}\right). \quad (3)$$

The B–O and Fe–O interionic distances and the optical gap E_g in $GdFe_3(BO_3)_4$ and $FeBO_3$ crystals

	B–O, Å	Fe–O, Å	E_g, eV
$FeBO_3$	1.3790	2.028	2.9
$GdFe_3(BO_3)_4$	1.3676	2.029	3.1

In the absence of additional transitions, the approximation gives $E_0 = (1.31 \pm 0.05)$ eV (E_0 is the effective optical gap in a new phase extrapolated to zero pressure) and $P_{met} = 135 \pm 11$ GPa.

Therefore, we observed two phase transitions accompanied by an optical-gap jump in the $GdFe_3(BO_3)_4$ crystal at $P_{c1} \approx 26$ GPa and $P_{c2} \approx 43$ GPa. The electronic transition at the point $P_{c1} \approx 26$ GPa coincides with the structural transition. It is quite probable that the second electronic transition at $P_{c2} \approx 43$ GPa is also accompanied by the structural transition. However, we could increase pressure only up to 40 GPa in our study and, therefore, could not achieve the second phase transition. Note that after pressure was decreased to the normal value, the single crystal remained undamaged; however, its color changed from dark green to light brown.

Figure 6 also shows the baric dependence of the optical gap in iron borate $FeBO_3$ [13]. The pressure at which the electronic phase transition occurs with a drastic change in the energy gap in $FeBO_3$ is close to the value of P_{c2} for the $GdFe_3(BO_3)_4$ crystal, which again confirms the similarity of the electronic structures of these compounds.

4. DISCUSSION OF RESULTS. COMPARISON OF THE ELECTRONIC STRUCTURE OF IRON BORATES $GdFe_3(BO_3)_4$ AND $FeBO_3$

The absorption spectra show that the electronic structure of the $GdFe_3(BO_3)_4$ crystal is close to that of $FeBO_3$ and is determined in the energy range to 4 eV in the vicinity of the Fermi level by the Fe ion and its environment. The interionic distances Fe–O and B–O in $FeBO_3$ and $GdFe_3(BO_3)_4$ are also close to each other (see table). This allows one to use some theoretical concepts developed for $FeBO_3$ [11, 13, 14] and $GdFe_3(BO_3)_4$.

The $GdFe_3(BO_3)_4$ dielectric has in the ground state the localized *d* electrons of Fe^{3+} in FeO_6 octahedra and the localized *f* electrons of Gd^{3+} in GdO_6 prisms. Inside the BO_3 group, a strong *sp* hybridization of boron and oxygen orbitals takes place. At the same time, the hybridization of the *d* electrons in Fe with the *sp* electrons in BO_3 is extremely weak (as follows from the calculations of the band structure of $FeBO_3$ [15, 16]).

In the one-electron approach based on *ab initio* calculations, the partially filled d^5 terms of Fe^{3+} and f^7 terms of Gd^{3+} would lead to partially filled bands and, hence, to the metallic state. However, due to strong electron correlations, both the *d* and *f* electrons are in the regime of the Mott-Hubbard dielectric. Therefore, the many-electron approach taking strong electron correlations into account is required to describe adequately the electronic structure and optical properties of $GdFe_3(BO_3)_4$.

A strong boron-oxygen hybridization in the BO_3 triangle determines the splitting of bonding and antibonding molecular orbitals that form the top E_v of the filled valence band and the bottom E_c of the empty conduction band. The energy gap between them for $GdFe_3(BO_3)_4$ $E_{go} = E_c - E_v = 3.1$ eV is somewhat greater than that in the $FeBO_3$ crystal (2.9 eV) because the smaller B–O distance in the first crystal leads to a stronger hybridization (see table).

The one-electron scheme of the valence band and the conduction band is overlapped by the single-particle *d* and *f* electron resonances with energies

$$\Omega_d = E(d^{n+1}) - E(d^n), \quad \Omega_f = E(f^{n+1}) - E(f^n),$$

where $E(d^n)$ and $E(f^n)$ are the energies of many-electron terms of iron and gadolinium. These energies are calculated taking into account the effects of strong electron correlations [13]. Because the hybridization for Fe–O and Gd–O is weak, the levels Ω virtually do not interact with the *sp* bands of the BO_3 group.

Because the Gd^{3+} ion does not absorb at energies $h\omega$ below 4 eV, the filled level $\Omega_{fv} = E(f^7) - E(f^6)$ lies below this energy, while the empty level $\Omega_{fc} = E(f^8) - E(f^7)$ lies above this energy. Therefore, only the *d* states of iron are located within the forbidden gap E_g, and in this sense the electronic structures of $FeBO_3$ and $GdFe_3(BO_3)_4$ are similar in this energy range. Moreover, because the Fe–O bond lengths in the FeO_6 octahedra in $FeBO_3$ and $GdFe_3(BO_3)_4$ crystals are close (see table), one can expect a similarity of the Racah parameters *A*, *B*, *C* and the cubic component of the crystal field $\Delta = \varepsilon_d(e_g) - \varepsilon_d(t_{2g})$ for the iron ion. The ground-level energies of the d^n configurations, taking strong electronic configurations into account, are expressed in terms of these parameters as [11, 17]

$$\begin{aligned} E(^5E_1, d^4) &= 4\varepsilon_d + 6A - 21B - 0.6\Delta, \\ E(^6A_1, d^5) &= 5\varepsilon_d + 10A - 35B, \\ E(^5T_2, d^6) &= 6\varepsilon_d + 15A - 21B - 0.4\Delta. \end{aligned} \qquad (4)$$

Here, ε_d is the one-electron energy of the *d* electron in an atom. For the t_{2g} and e_g orbitals in a cubic crystal field, this level splits into $\varepsilon_d(t_{2g}) = \varepsilon_d - 0.4\Delta$ and $\varepsilon_d(e_g) = \varepsilon_d + 0.6\Delta$. The Racah parameters in a crystal field depend on the number of the *d* electrons in the d^n configuration. However, this dependence is rather weak

and therefore can be neglected for simplicity. As in $FeBO_3$, the absorption spectrum of the $GdFe_3(BO_3)_4$ crystal at $\hbar\omega < E_g$ is determined by the *d–d* transitions in the Fe^{3+} ion (excitons) with the energies

$$\begin{aligned}\varepsilon_A &= E(^4T_1) - E(^6A_1),\\ \varepsilon_B &= E(^4T_2) - E(^6A_1),\\ \varepsilon_C &= E(^4E_1) - E(^6A_1) \text{ or } {}^4A_1.\end{aligned} \tag{5}$$

A comparison of the absorption spectra of $FeBO_3$ and $GdFe_3(BO_3)_4$ at normal pressure shows (Fig. 4) that the energies of these excitons coincide, which confirms that the Racah parameters and crystal-field parameters are coincident for these two crystals. These parameters are [11, 18]: $A = 3.42$ eV, $B = 0.084$ eV, $C = 0.39$ eV, and $\Delta = 1.57$ eV.

The great intensity of the absorption band *C* in the spectrum of $GdFe_3(BO_3)_4$, as in the case of $FeBO_3$, can be explained by the overlap of the charge-transfer absorption due to the $p^6d^5 \longrightarrow p^5d^6$ process. The creation of an additional electron in the $Fe^{3+} \longrightarrow Fe^{2+}$ transition requires the energy

$$\Omega_c = E(^5T_2, d^6) - E(^6A_1, d^5), \tag{6}$$

while the annihilation of an electron (creation of a hole) in the $Fe^{3+} \longrightarrow Fe^{4+}$ transition requires the energy

$$\Omega_v = E(^6A_1, d^5) - E(^5E_1, d^4). \tag{7}$$

The Ω_c and Ω_v levels have the meaning of the upper and lower Hubbard subbands and can be expressed in terms of the Racah parameters in the form

$$\begin{aligned}\Omega_c &= \varepsilon_d + 5A + 14B - 0.4\Delta,\\ \Omega_v &= \varepsilon_d + 4A - 14B + 0.6\Delta.\end{aligned} \tag{8}$$

The difference between them (or splitting) is determined by the effective Hubbard parameter,

$$\begin{aligned}U_{\text{eff}} &= \Omega_c - \Omega_n = E_0(d^4) + E_0(d^6)\\ &- 2E_0(d^5) = A + 28B - \Delta = 4.2 \text{ eV}.\end{aligned} \tag{9}$$

The analysis of behavior of the optical spectra of the $FeBO_3$ crystal at high pressures showed [13] that the crystal field increases with pressure, whereas the Hubbard subbands broaden only slightly. As the crystal field increases, the energy of high-spin terms of iron ions almost does not change, while the energy of low-spin states decreases. For $P = 47$ GPa, this leads to the crossover of the terms, which is accompanied by the magnetic collapse and a jumpwise change in electronic and transport properties [13].

The similarity of the electronic structures of the $GdFe_3(BO_3)_4$ and $FeBO_3$ crystals suggests that the electronic transition that we found in the $GdFe_3(BO_3)_4$ crystal at $P_{c2} = 43$ GPa is also related to the spin crossover and the values of critical pressures for both crystals are close (Fig. 6).

However, these crystals also reveal some differences at high pressures. First, we found the structural and optical transitions in $GdFe_3(BO_3)_4$ at 26 GPa, which were not observed in $FeBO_3$. Because the crystal structure of $GdFe_3(BO_3)_4$ is more complicated, the presence of the additional transitions in this crystal is not surprising. The theory [11, 13, 14] considered the pressure-induced variation in the electronic properties only for a specific crystal lattice, and it cannot explain the transition at 26 GPa. To do this, the total energy of the crystal should be calculated, as was done for $FeBO_3$ [19].

The second difference is related to magnetic properties. It is also caused by the more complicated crystal structure of $GdFe_3(BO_3)_4$, where the chains of oxygen-octahedral-containing iron are weakly coupled, and the exchange interaction between neighboring iron atoms involves a long chain of intermediate atoms, being therefore much weaker than in $FeBO_3$. Indeed, the Néel temperature in $GdFe_3(BO_3)_4$ $T_N = 38$ K is an order of magnitude lower than that in $FeBO_3$ ($T_N = 350$ K). The Mössbauer spectra in the $FeBO_3$ crystal at room temperature reveal a magnetically ordered state at the low-pressure phase [20], and the magnetic collapse at the transition point P_c is manifested as the disappearance of the magnetic order parameter owing to a drastic decrease of T_N at the high-pressure phase during the spin crossover. Unlike $FeBO_3$, the spin crossover in the $GdFe_3(BO_3)_4$ crystal, which is observed from optical spectra at room temperature, occurs against the background of the paramagnetic state and is not a real (magnetic) phase transition. At the crossover point, the effective magnetic moment of the Fe^{3+} ion changes, which can be observed by the jumpwise change in the slope of the temperature dependence of the inverse magnetic susceptibility and by Mössbauer spectra. We plan to perform such studies in the near future.

This work was supported by the Russian Foundation for Basic Research (project nos. 02-02-17364a, 03-02-16286a, 04-02-26679, and 04-02-16945a) and the Program of the Department of Physical Sciences, RAS, "Strongly Correlated Electrons." A.M.P. thanks the Foundation for Support of Russian Science for support.

REFERENCES

1. J. A. Campá, C. Cascales, E. Gutierrez-Puebla, *et al.*, Chem. Mater. **9**, 237 (1997).
2. N. I. Leonyuk and L. I. Leonyuk, Prog. Cryst. Growth Charact. Mater. **31**, 179 (1995).
3. N. I. Leonyuk, Prog. Cryst. Growth Charact. Mater. **31**, 279 (1995).
4. D. Jaque, J. Alloys Compd. **323–324**, 204 (2001).
5. M. Huang, Y. Chen, X. Chen, *et al.*, Opt. Commun. **208**, 163 (2002).

6. X. Chen, Z. Luo, D. Jaque, *et al.*, J. Phys.: Condens. Matter **13**, 1171 (2001).
7. A. D. Balaev, L. N. Bezmaternykh, I. A. Gudim, *et al.*, J. Magn. Magn. Mater. **258–259**, 532 (2003).
8. A. D. Balaev, L. N. Bezmaternykh, A. D. Vasil'ev, *et al.*, J. Magn. Magn. Mater. **272–276** (Suppl. 1), E359 (2004).
9. R. Z. Levitin, E. A. Popova, R. M. Chtsherbov, *et al.*, Pis'ma Zh. Éksp. Teor. Fiz. **79**, 531 (2004) [JETP Lett. **79**, 423 (2004)].
10. L. N. Bezmaternykh, S. A. Kharlamova, and V. L. Temerov, Crystallogr. Rep. **49**, 855 (2004).
11. S. G. Ovchinnikov and V. N. Zabluda, Zh. Éksp. Teor. Fiz. **125**, 150 (2004) [JETP **98**, 135 (2004)].
12. E. P. Chukalina, D. Yu. Kuritsin, M. N. Popova, *et al.*, Phys. Lett. A **322**, 239 (2004).
13. A. G. Gavrilyuk, I. A. Troyan, S. G. Ovchinnikov, *et al.*, Zh. Éksp. Teor. Fiz. **126** (3), 650 (2004) [JETP **99**, 566 (2004)].
14. S. G. Ovchinnikov, Pis'ma Zh. Éksp. Teor. Fiz. **77**, 808 (2003) [JETP Lett. **77**, 676 (2003)].
15. A. V. Postnikov, S. T. Bartkowski, M. Neumann, *et al.*, Phys. Rev. B **50**, 14 849 (1994).
16. N. B. Ivanova, V. V. Rudenko, A. D. Balaev, *et al.*, Zh. Éksp. Teor. Fiz. **121**, 354 (2002) [JETP **94**, 299 (2002)].
17. D. T. Sviridov, R. K. Sviridova, and Yu. F. Smirnov, *Optical Spectra of Transition-Metal Ions in Crystals* (Nauka, Moscow, 1976), p. 356 [in Russian].
18. I. S. Édel'man and A. V. Malakhovskiĭ, Opt. Spektrosk. **35**, 959 (1973).
19. K. Parlinski, Eur. Phys. J. B **27**, 283 (2002).
20. V. A. Sarkisyan, I. A. Troyan, I. S. Lyubutin, *et al.*, Pis'ma Zh. Éksp. Teor. Fiz. **76**, 788 (2002) [JETP Lett. **76**, 664 (2002)].

Translated by M. Sapozhnikov

JETP Letters, Vol. 80, No. 6, 2004, pp. 433–435. Translated from Pis'ma v Zhurnal Éksperimental'noĭ i Teoreticheskoĭ Fiziki, Vol. 80, No. 6, 2004, pp. 489–492.

Transition of the Near-Surface δ Layer in an Al/δ(Si)–GaAs Tunnel Structure to the Insulating State under Pressure

E. M. Dizhur[1, *], A. N. Voronovsky[1], A. V. Fedorov[1], I. N. Kotel'nikov[2], and S. E. Dizhur[2]

[1] *Institute of High-Pressure Physics, Russian Academy of Sciences, Troitsk, Moscow region, 142190 Russia*

** e-mail: dizhur@ns.hppi.troitsk.ru*

[2] *Institute of Radio Engineering and Electronics, Russian Academy of Sciences, ul. Mokhovaya 18, Moscow, 125009 Russia*

Received August 12, 2004

The tunnel and lateral conductivities of an Al/GaAs tunnel structure with a surface Si δ-doped layer are measured at liquid-helium temperatures under a hydrostatic pressure of up to 3 GPa. Transition of the δ layer to the insulating state at a pressure of about 2 GPa is revealed. During this transition, the tunnel resistance increases steadily (on a logarithmic scale) and the zero-bias anomaly in the tunnel resistance exhibits a sharp peak. These results are interpreted in terms of representations of the effect of pressure on the energy-band structure and behavior of *DX* levels. © *2004 MAIK "Nauka/Interperiodica".*

PACS numbers: 62.50.+p; 73.21.-b; 73.30.+y; 73.40.Gk

Recently, in the study of the effect of pressure on the tunnel spectrum of the Al/δ–GaAs structure [1], it was suggested that a two-dimensional (2D) electron gas formed in the near-surface δ-doped layer may undergo a transition to the insulating state. The experimental difficulties inherent in tunnel measurements of high-impedance samples were overcome by developing an improved measurement scheme [2], which makes it possible to measure a voltage drop on a δ layer and exclude the distortion of the restored tunnel spectrum caused by this drop.

In this paper, we report the results of simultaneous measurements of the conductivity of a δ layer and the tunnel spectra under pressures above 2 GPa.

We investigated an Al/δ(Si)–GaAs structure having two tunnel junctions with the initial (at $P = 0$) density of 2D-electron gas $n_{2D} \sim 1 \times 10^{12}$ cm^{-2} (sample *Z1B7*) grown by molecular-beam epitaxy at the Institute of Radio Engineering and Electronics of the Russian Academy of Sciences (IREE RAS) [3]. The distance between the Al/GaAs interface and the δ-doped layer (common for both junctions) was about 20 nm.

The tunnel spectra and the conductivity of the δ layer were measured by the four- and two-contact methods, respectively, at a temperature of 4.2 K, and, in some cases, upon evacuation at temperatures $\lesssim 2$ K under pressures of up to 3 GPa.

Hydrostatic pressures were applied at room temperature using a fixed-pressure chamber of the cylinder–piston type using polyethylene–siloxane liquid PÉS-1 as a pressure-transmitting medium. Upon loading, the pressure was monitored by a Manganin resistance sensor, and, after fixing pressure, the chamber was placed in a cryostat. The exact value of pressure at low temperatures was determined from the well-known baric dependence of the temperature of superconducting transition in tin. This technique was described in detail in [4].

Figure 1 shows typical tunnel spectra (dependences of the logarithmic derivative of the conductivity $d\ln\sigma/dV$ on bias) measured at different pressures. These curves account for the effect of pressure on both the position of quantum-confinement bands (to which wide minima correspond) and the many-body interactions—electron–electron interaction (the singularity of

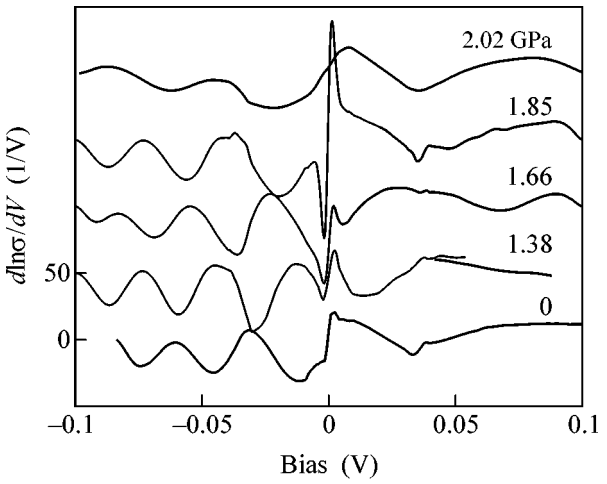

Fig. 1. Tunnel spectrum of sample *Z1B7* at $T = 4.2$ K. The curves for different pressures are shifted along the vertical axis with respect to each other by 50 V^{-1}. Pressure in GPa is indicated near each curve.

0021-3640/04/8006-0433$26.00 © 2004 MAIK "Nauka/Interperiodica"

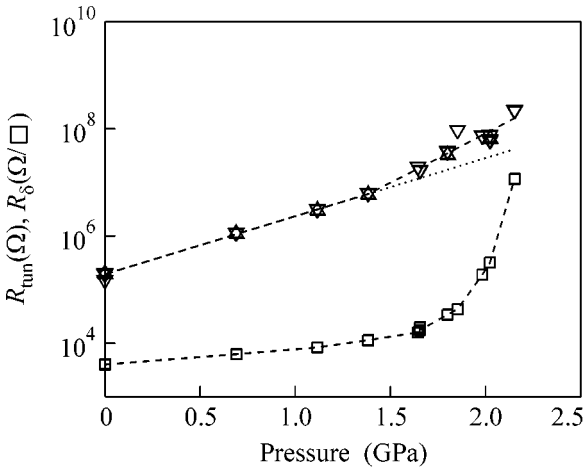

Fig. 2. Dependences of the differential tunnel resistance R_{tun} at $V_{bias} = 0$ (△ and ▽ for gates *1* and *2*, respectively) and the lateral resistance R_δ on pressure at $T = 4.2$ K.

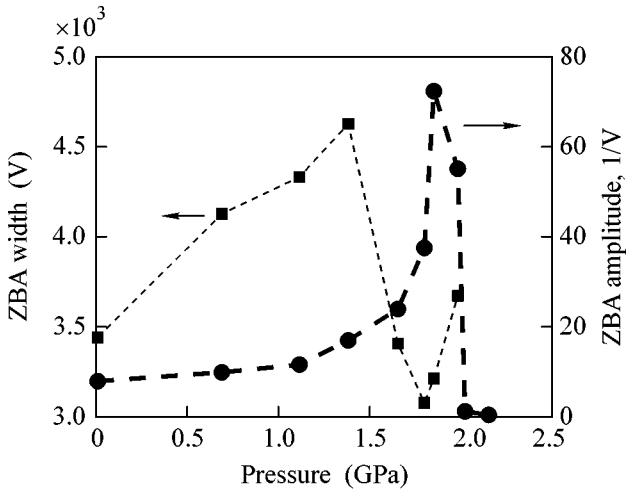

Fig. 3. Dependences of the (●) ZBA amplitude and (■) ZBA width on pressure.

the type of derivative of the dip in the conductivity at a zero bias and the so-called zero-bias anomaly (ZBA)) and electron–phonon interaction at biases corresponding to the energies of LO phonons (about ±36.5 meV).

Figure 2 shows the baric dependences of the δ-layer sheet resistance and the tunnel resistance at a zero bias (excluding the ZBA). As can be seen from Fig. 2, a sharp increase in the lateral resistance (sheet resistance of the δ layer) by about three orders of magnitude is observed at a pressure ≈1.9 GPa, which is indicative of the transition to the insulating state. Figure 3 shows that a sharp increase in the ZBA amplitude with a subsequent drop is observed in the same pressure range. Since the ZBA accounts for the properties of specifically the tunnel contact (i.e., including the properties of the δ-layer region located directly under the gate), we can assume that the properties of the δ layer change synchronously over its total area. At somewhat lower pressures, a small change in the slope of the logarithmic baric dependence of the tunnel resistance was also observed.

As additional evidence of the transition of the δ layer to the insulating state, we can note the sharp change in the thermal resistance coefficient: from $\approx -0.03 \pm 0.02$ K^{-1} in the range 0–1.8 GPa to ≈–4 K^{-1} at $P = 2$ GPa.

We believe that the transition of the δ layer to the insulating state is mainly due to the pressure-induced changes in the energy-band structure of GaAs and, in particular, to the presence of *DX* centers, which are characteristic of substitutional impurities (Sn, Si, Te) in III–V semiconductors.

Figure 4a shows the potential distribution near the interface, which determines the number, position, and filling of quantum-confinement levels. In the case under consideration, as found from the self-consistent solution of the Schrödinger and Poisson equations [1], at $P = 0$, only one level E_0 is located in the potential well below the Fermi level and the corresponding energy distances are $E_0 - E_\Gamma \sim 92$ meV and $E_F - E_0 \sim 33$ meV. According to the data of Maude *et al.* [5], at concentrations of Si close to the doping level of the δ layer in the samples studied here (4.5×10^{12} cm^{-2}), $E_{DX} - E_\Gamma \sim 270$ meV and $dE_{DX-\Gamma}/dP \sim 94$ meV/GPa.[1]

As can be seen from the energy-band diagram (Fig. 4b), the overlap of the Fermi level with the level of *DX* centers must begin at the pressure

$$P_1 = \frac{(E_{DX} - E_\Gamma) - (E_0 - E_\Gamma) - (E_F - E_0)}{|dE_{DX-\Gamma}/dP|} \approx 1.65 \text{ GPa}.$$

A further increase in the pressure leads to the Fermi-level pinning and localization of carriers at *DX* centers, due to which the effective concentration of carriers involved in the charge transport over the δ layer gradually decreases. When the Fermi level is below the mobility threshold with respect to the quantum-confinement level, transition to the insulating state occurs. The pressure range corresponding to this transition can be roughly estimated as

$$\Delta P \approx \frac{E_F - E_0}{|dE_{DX-\Gamma}/dP|} \gtrsim 0.35 \text{ GPa}.$$

These estimates are in good agreement with the experimental values.

Within these representations, the behavior of the tunnel resistance can be explained qualitatively as follows. Under pressure, the height of the tunnel barrier increases no faster than the band gap width (~100 meV/GPa); the barrier width is determined (in

[1] In another publication by the authors (Phys. Rev. Lett. **59**, 815 (1987)), the following values were reported: $E_{DX} - E_\Gamma \sim 234$ meV and $dE_{DX-\Gamma}/dR \sim -48 \pm 23$ meV/GPa.

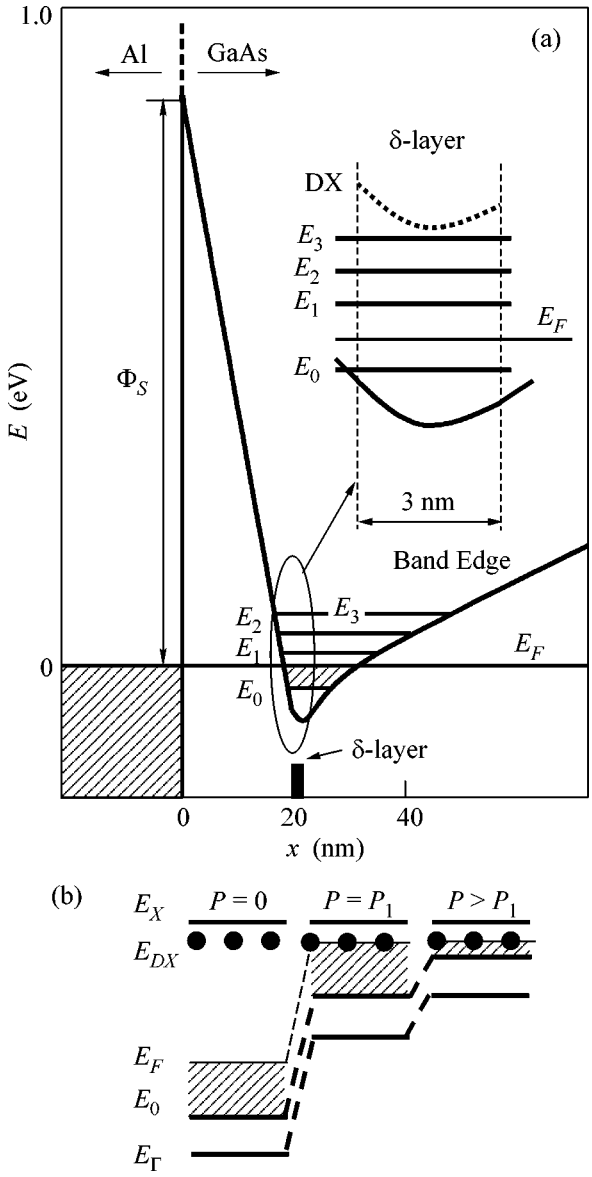

Fig. 4. (a) Distribution of the potential near the interface and the system of quantum-confinement levels and (b) change in the relative position of the characteristic energy levels under pressure. E_X is the edge of the X valley, E_{DX} is the level of DX centers, E_F is the Fermi level, E_0 is the edge of the lower quantum-confinement subband, and E_Γ is the edge of the conduction band (the Γ valley).

the first-order approximation) by the distance between the δ layer and the interface, i.e., changes insignificantly, and the density of states at the Fermi level for the 2D level changes as the effective mass, i.e., also insignificantly. Therefore, the general exponential character of the dependence of the tunnel current on bias undergoes no sharp changes at the transition to the insulating state.

Nevertheless, the above factors still have some effect and the slope of the dependence $\ln R_{tun}(P)$ begins to change as soon as some of the free electrons are localized at *DX* centers, which leads to a change in the space charge. As can be seen from Fig. 1, the dips corresponding to the quantum-confinement levels are fairly wide. This circumstance indicates a significant inhomogeneity of the δ layer (or the barrier height) over the tunnel-contact area, which manifests itself as an apparent broadening of the E_0 level. Due to this, the kink in the baric dependence of the logarithm of the tunnel resistance shifts to somewhat lower pressures as compared with the above estimate.

The behavior of the ZBA is not quite clear. On the one hand, this phenomenon was attributed to the effects of exchange-correlation interaction and an increase in the ZBA amplitude under pressure was predicted for three-dimensional systems [7]. On the other hand, the behavior of the ZBA near the transition to the insulating state of the 2D system studied here may indicate, for example, the appearance of a Coulomb gap [8] in the spectrum, which, as is known, may manifest itself in tunneling [9]. In any case, the origin of a sharp peak in the baric dependence of the ZBA near the transition to the insulating state, the significant magnitude of this effect, and the nonmonotonic dependence of the ZBA width on pressure deserve to be carefully studied.

We are grateful to A.Ya. Shul'man and V.A. Volkov for their helpful participation in discussions and V.M. Pudalov for valuable remarks. This study was supported by Russian Foundation for Basic Research and grants from the INTAS and the Division of Physical Sciences of RAS.

REFERENCES

1. E. M. Dizhur, A. N. Voronovsky, I. N. Kotelnikov, *et al.*, Phys. Status Solidi B **235**, 531 (2003).
2. E. M. Dizhur and A. V. Fedorov, cond-mat/0408206.
3. I. N. Kotel'nikov, V. A. Kokin, Yu. V. Fedorov, *et al.*, Pis'ma Zh. Éksp. Teor. Fiz. **71**, 564 (2000) [JETP Lett. **71**, 387 (2000)].
4. A. N. Voronovskiĭ, E. M. Dizhur, and E. S. Itskevich, Zh. Éksp. Teor. Fiz. **77**, 1119 (1979) [Sov. Phys. JETP **50**, 564 (1979)].
5. D. K. Maude, J. C. Portal, L. Dmowski, *et al.*, Solid State Phenom. **10**, 121 (1989).
6. A. R. Goñi, K. Syassen, and M. Cardona, Phys. Rev. B **41**, 10104 (1990).
7. A. Ya. Shul'man, I. N. Kotel'nikov, N. A. Varvanin, *et al.*, Pis'ma Zh. Éksp. Teor. Fiz. **73**, 643 (2001) [JETP Lett. **73**, 573 (2001)].
8. B. I. Shklovskiĭ and A. L. Éfros, *Electronic Properties of Doped Semiconductors* (Nauka, Moscow, 1979; Springer, New York, 1984).
9. J. G. Massey and Mark Lee, Phys. Rev. Lett. **75**, 4266 (1995); Phys. Rev. Lett. **77**, 3399 (1996).

Translated by Yu. Sin'kov

JETP Letters, Vol. 80, No. 6, 2004, pp. 436–440. From Pis'ma v Zhurnal Éksperimental'noĭ i Teoreticheskoĭ Fiziki, Vol. 80, No. 6, 2004, pp. 493–497.

Landau–Zener Problem for Energies Close to Potential Crossing Points¶

V. A. Benderskii[1, 3], E. V. Vetoshkin[1], and E. I. Kats[2, 3]

[1] *Institute of Problems of Chemical Physics, Russian Academy of Sciences, Chernogolovka, Moscow region, 142432 Russia*

[2] *Laue-Langevin Institute, F-38042, Grenoble, France*

[3] *Landau Institute for Theoretical Physics, Russian Academy of Sciences, Moscow, 117334 Russia*

Received August 16, 2004

We examine a previously overlooked aspect of the well-known Landau–Zener (LZ) problem, namely, the behavior in the intermediate, i.e., close to a crossing point, energy region, when all four LZ states are coupled and should be taken into account. We calculate the 4×4 connection matrix in this intermediate energy region, possessing the same block structure as the known connection matrices for the tunneling and in the over-barrier regions of the energy and continuously matching those in the corresponding energy regions. Applications of the results may concern various systems of physics, chemistry, or biology, ranging from molecular magnets and glasses to Bose condensed atomic gases. © *2004 MAIK "Nauka/Interperiodica".*

PACS numbers: 05.45.-a; 31.50.Gh; 72.10.-d

The standard textbook Landau–Zener (LZ) theory [1] concerns a crossing problem of two linear diabatic potentials $U^{\#} \pm FX$ ($X = 0$ is the crossing point). However, in spite of its more than half-century history, semiclassical solutions of this problem have been found only in the limits of small or large energies E (we will call these regions tunneling and over-barrier, respectively), i.e., for

$$\left|U^{\#} - E\right| \gg U_{12}; \quad \left|U^{\#} - E\right| \ll U_{12}, \tag{1}$$

where U_{12} is the interlevel interaction, which, in the LZ model, does not depend on X. For the intermediate energy region,

$$\left|U^{\#} - E\right| \leq U_{12}, \tag{2}$$

only interpolating relations between exponentially decaying solutions in the tunneling and oscillating solutions in the over-barrier energy regions are known (see e.g., [2, 3]). Analytical and numerical study of this region (2) is the objective of this paper.

Our approach is motivated by a semiclassical instanton approximation [4–6]. The idea is to construct two linearly independent continuous (with continuous first derivatives) approximate solutions to the Schrödinger equation that, in the asymptotic region, coincide with semiclassical solutions, and, in the vicinity of the turning points, coincide with the exact solutions of the so-called comparison equation (i.e., the exact solution of the Schrödinger equation for the chosen appropriately approximate near the turning points' potentials). In what follows, the Weber equation [7] will be used as the comparison equation and be valid near the second-order turning points for an anharmonic potential [3, 8, 9]. To justify this choice, it is sufficient to note that the anharmonic corrections remain semiclassically small (i.e., proportional to higher orders of the $\hbar$ series) in the region where the solutions of the comparison equation have to be matched smoothly with the semiclassical solutions. Luckily, the analogous approach is valid for treating two diabatic potential crossing points (the LZ problem), and the comparison equations for this case are two coupled Weber equations with indices and arguments determined by the solutions of the algebraic characteristic equation.

The LZ problem for crossing diabatic potentials is equivalent to the coupled Schrödinger equations, which can be transformed by the substitution

$$\Psi = \exp(\kappa X)\Phi \tag{3}$$

into a fourth-order linear differential equation with coordinate-independent coefficients at the derivatives,

$$D^4\Phi + 4\kappa D^3\Phi + (6\kappa^2 - 2\alpha\gamma^2)D^2\Phi$$

$$+ 4\left(\kappa^3 - \alpha\gamma^2\kappa - \frac{1}{2}\gamma^2 f\right)D\Phi \tag{4}$$

$$+ [\kappa^4 - 2\alpha\gamma^2\kappa^2 - 2\gamma^2 f\kappa + \gamma^4(\alpha^2 - u_{12}^2 - f^2X^2)]\Phi = 0,$$

where $D^n \equiv d^n/dX^n$ and $\gamma \gg 1$ is the dimensionless semiclassical parameter, which is determined by the ratio of the characteristic potential scale over the zero oscilla-

¶ This article was submitted by the authors in English.

tion energy, and all other dimensionless appropriately rescaled variables are

$$\alpha = 2\frac{U^{\#} - E}{\gamma\hbar\Omega}, \quad f = \frac{2a_0 F}{\gamma\hbar\Omega}, \quad u_{12} = \frac{2U_{12}}{\gamma\hbar\Omega}, \qquad (5)$$

where scale for the energy is given by $\Omega^2 = F^2/mU_{12}$ (m is a mass) and space scale is determined by the characteristic size a_0 of the potential in the vicinity of the crossing point.

Equation (4) admits semiclassical solutions by the Fedoryuk method [10–12], since the coefficients at the nth-order derivatives proportional to γ^{-n} and all the four asymptotic solutions read as

$$\Psi_j^{(sc)} = (u_{12}^2 + f^2X^2)^{-1/4}\exp\left(\int_0^X \lambda_j(x)dx\right), \qquad (6)$$
$$j = (++, +-, -+, --),$$

where we designated

$$\lambda_j = \lambda_j^0 + u_j, \quad \lambda_j^0 = \pm\sqrt{\gamma(\alpha \pm \sqrt{u_{12}^2 + f^2X^2})},$$
$$\text{and } u_j = \gamma f((\lambda_j^0)^2 - \alpha\gamma)^{-1}.$$

Equation (4), up to anharmonic terms proportional to $X^2D\Phi$, $X^3\Phi$, and $X^4\Phi$, can be formally derived by simple manipulations (two sequential differentiations and summations) from the following second-order equation:

$$D^2\Phi + (a_0 + a_1X + a_2X^2)\Phi = 0, \qquad (7)$$

where the coefficients are

$$a_0 = \kappa^2 - \alpha\gamma^2 - \frac{\gamma^2 f}{2\kappa}(1+\delta);$$
$$a_1 = \gamma^2 f\delta; \quad a_2 = -\gamma^2 f\kappa\delta, \qquad (8)$$

where the equation for κ referred to in what follows by the characteristic equation is

$$\kappa^4 - \alpha\gamma^2\kappa^2 + \frac{1}{4}\gamma^4 u_{12}^2 = -\kappa^4\delta^2(1+2\delta) + R(\kappa,\delta), \qquad (9)$$

where

$$R(\kappa,\delta) = (2\kappa^6)^{-1}(1-3\delta)(1+\delta)^{-3}(1-Q-\sqrt{1-2Q^2});$$
$$Q = 8\delta^2(1+\delta),$$

and

$$\delta = \frac{\gamma^2 f}{4\kappa^3}. \qquad (10)$$

The fundamental solutions to (7) read as

$$D_p\left[\pm\left(\frac{\gamma^4 f^2}{\kappa^2}\right)^{1/4}\left(X - \frac{1}{2\kappa}\right)\right], \qquad (11)$$

where

$$p = -\frac{1}{2} + \left(\frac{\gamma^4 f^2}{\kappa^2}\right)^{-1/2}\left(a_0 - \frac{a_1^2}{4a_2}\right). \qquad (12)$$

In the tunneling and over-barrier regions of energies, where $\delta < 1/4$, these four solutions (two solutions of (11) for the two largest modulus roots of characteristic Eq. (9)) can be separated into two independent pairs (orthogonality of the Weber functions with different indices). Thus, one can say that the crossing point is equivalent to two second-order turning points with different Stokes constants (see, e.g., [13]).

In the tunneling region, the two largest modulus roots of (9) are (two other roots are small and do not satisfy semiclassical approach)

$$\kappa = \pm\kappa_0\left(1 \pm \frac{\delta^2}{2}\frac{\kappa_0^2}{2\kappa_0^2 - \alpha\gamma^2}\right);$$
$$\kappa_0 = \frac{\gamma}{\sqrt{2}}(\alpha + \sqrt{\alpha^2 - u_{12}^2})^{1/2}, \qquad (13)$$

and the four linearly independent solutions (11) are matched to semiclassical solutions (5) in the region $\alpha > f|X| > u_{12}$, where the exponent of the wave function can be expanded over the small parameter δ:

$$\Phi \propto \exp\left(\kappa X + \delta(\kappa X)^2 - \frac{2}{3}\delta^2(\kappa X)^3 + \ldots\right). \qquad (14)$$

Since $\kappa|X| \le (4\delta)^{-1}$, expansion (13), which is convergent with alternating signs, determines the accuracy of the asymptotically smooth transformation. Putting everything together, we obtain the conclusion that the anharmonic corrections to Weber functions (11) are small (in other words, the parameter δ determines the accuracy of our approximation). The same kind of analysis can be performed in the over-barrier region, where one finds two imaginary largest modulus roots of the characteristic equation (see details in [9]).

It is a more difficult task to find solutions in the intermediate energy region, where two roots of the characteristic equation are real and two are imaginary ones having the same modulus, i.e., moving upon α variation along a circle with the radius $\gamma\sqrt{u_{12}/2}$. In this case, the semiclassical solutions can be presented as certain linear combinations of the comparison equation solutions, and the roots are

$$\kappa_{1,2} \simeq \pm\gamma\sqrt{\frac{u_{12}}{2}}\exp(i\varphi);$$
$$\kappa_{3,4} \simeq \pm i\gamma\sqrt{\frac{u_{12}}{2}}\exp(-i\varphi), \qquad (15)$$

where

$$\tan\varphi = \sqrt{\frac{u_{12}-\alpha}{u_{12}+\alpha}}. \quad (16)$$

Correspondingly to roots (16), the arguments and the indices of Weber functions (11) and (12) read as

$$z_1 = z_2 = 2\kappa_{\rm int}\sqrt{\delta_{\rm int}}\exp(-i\varphi/2)(X-(2\kappa_{\rm int})^{-1}\exp(-i\varphi)),$$
$$z_3 = z_4 \quad (17)$$
$$= 2\kappa_{\rm int}\sqrt{\delta_{\rm int}}\exp(i\varphi/2)(X-(2\kappa_{\rm int})^{-1}\exp(i\varphi)),$$

and

$$p_1 = p_2 - 1$$
$$= -1 - \frac{1}{4\delta_{\rm int}}\exp(-i\varphi)(1+2\delta_{\rm int}^2\exp(-2i\varphi)), \quad (18)$$
$$p_4 = p_3 - 1 = -1 - \frac{1}{4\delta_{\rm int}}\exp(i\varphi)(1+2\delta_{\rm int}^2\exp(2i\varphi)),$$

where

$$\kappa_{\rm int} = \gamma(u_{12}/2)^{1/2}; \quad \delta_{\rm int} = (\gamma^2 f)/(4\kappa_{\rm int}^3). \quad (19)$$

Semiclassical solutions (6) are matched asymptotically smoothly to the linear combinations of the Weber functions in the region $u_{12} > f|X|$. Since it follows from (17) and (18) that, at large $\delta_{\rm int}$, the indices of the Weber functions are also large, one can use the asymptotics of the Weber functions (known due to Oliver [14, 15]) with large arguments and indices,

$$D_p(z) \propto \exp\left[-\frac{1}{2}\int\left(z^2 - 4\left(p+\frac{1}{2}\right)\right)^{1/2}dz\right]. \quad (20)$$

At $z^2 \gg 4|p+(1/2)|$, (20) is reduced to the usual asymptotic expansion of the large argument Weber functions and, in the opposite limit (i.e., in the intermediate region), (20) corresponds to the expansion of the exponent over odd powers of z. We can also find the asymptotics to the solutions of (7),

$$\Phi_0 \propto \exp(-i\int\sqrt{a_0 + a_1X + a_2X^2}dx) \quad (21)$$

that are valid at arbitrary values of the parameters a_i (including $a_2 = 0$).

The fundamental solutions to the comparison equation are the asymptotics for the wave functions in form (3), namely,

$$\Psi_j^{\pm} = \exp(\kappa X)D_p(\pm z_j(X)), \quad (22)$$

and

$$\Psi_1^+, \Psi_4^+ \propto \exp(F_1(X)), \quad \Psi_2^-, \Psi_3^- \propto \exp(-F_1(X)),$$
$$\Psi_1^-, \Psi_3^- \propto \exp(iF_2(X)), \quad \Psi_2^+, \Psi_4^- \propto \exp(-iF_2(X)), \quad (23)$$

where

$$F_{1,2}(X) = \gamma\sqrt{u_{12}\pm\alpha}(1+\delta_{\rm int})X - \kappa_{\rm int}^2\delta_{\rm int}^2\exp(-2i\varphi)X^2$$
$$+ \frac{\gamma f^2}{12u_{12}\sqrt{u_{12}\pm\alpha}}\left(1\pm\frac{\alpha}{u_{12}} - \delta_{\rm int}\right)X^3. \quad (24)$$

Wave functions (23) asymptotically smoothly turn into semiclassical functions (6). The accuracy of this matching is determined by the anharmonic corrections, i.e., by the parameter $\delta_{\rm int}$ (19) and Olver asymptotic (20) works, even on the boundary $z^2 \simeq 4|p+(1/2)|$. The parameter $\delta_{\rm int}$ is no longer small when, simultaneously,

$$|\alpha| \le \left(\frac{f}{\gamma}\right)^{2/3} = \left(\frac{u_{12}}{2\gamma^2}\right)^{1/3}; \quad u_{12} \le \frac{2}{\gamma}. \quad (25)$$

However, asymptotic matching of the solutions should be performed at small $|X| < \gamma^{-1}$, where comparison Eq. (12) and, therefore, the characteristic Eq. (9) are valid, even though, upon increasing $\delta_{\rm int}$, the potential becomes more and more anharmonic. At $\alpha = 0$ and $u_{12} = 0$, Eq. (9) (taking into account the term $R(\kappa, \delta)$) has the doubly degenerate root $\kappa = 0$, i.e., in terms of (12), $a_1 = \pm\gamma^2 f$ and $a_2 = 0$. Thus, in this limit, (12) is equivalent to two decoupled Airy equations, corresponding to the diabatic potentials. These solutions turn smoothly into semiclassical solutions (6), and the anharmonic corrections in the matching region are small over the parameter $\gamma^{-1/2}$.

We conclude that, in the both intermediate energy subregions—large κ (i.e., $\propto\gamma$) and small κ (i.e., $\propto\sqrt{\gamma}$)—comparison Eq. (12) is reduced to two decoupled equations: Weber or Airy ones, respectively. This simple observation enables us to construct the universal connection matrix for both intermediate energy regions by using Olver asymptotic expansion (21). The four roots (15) distributed over the circle with the radius $\gamma\sqrt{u_{12}/2}$ on the complex plane determine the following combinations of the comparison equation solutions matching semiclassical solutions (6). Namely,

$$\Psi_1^+ + \Psi_4^+ \longrightarrow \Psi_{++}^{sc}; \quad \Psi_2^- + \Psi_3^- \longrightarrow \Psi_{+-}^{sc};$$
$$\Psi_1^- + \Psi_3^+ \longrightarrow \Psi_{-+}^{sc}; \quad \Psi_2^+ + \Psi_4^- \longrightarrow \Psi_{--}^{sc}, \quad (26)$$

where the superscript "sc" indicates the semiclassical solutions. Combining the asymptotic expansions for these combinations, we find that, at the crossing point, the matrix $\hat{U}_c''$ is

$$\hat{U}_c'' = \begin{bmatrix} (\sqrt{2\pi}/\Gamma(q^*))\exp(-2\chi(q^*)) & 0 \\ 0 & (\Gamma(q)/\sqrt{2\pi})\exp(2\chi(q))(1-\exp(-2\pi q_2)\cos^2(\pi q_1)) \\ 0 & \exp(-2\pi q_2)\cos(\pi q_1) \\ \exp(-2\pi q_2)\cos(\pi q_1) & 0 \end{bmatrix}$$

$$\begin{bmatrix} 0 & -\exp(-2\pi q_2)\cos(\pi q_1) \\ -\exp(-2\pi q_2)\cos(\pi q_1) & 0 \\ (\sqrt{2\pi}/\Gamma(q))\exp(2\chi(q)) & 0 \\ 0 & (\Gamma(q^*)/\sqrt{2\pi})\exp(2\chi(q^*))(1-\exp(-2\pi q_2)\cos^2(\pi q_1)) \end{bmatrix}, \quad (27)$$

where

$$q = q_1 + iq_2;\ \ q_{1,2} = \frac{\gamma u_{12}\sqrt{u_{12} \pm \alpha}}{4f};\ \ q^* = q_1 - iq_2, \quad (28)$$

and, in addition, we introduce the following abridged notations:

$$\chi = \chi_1 + i\chi_2;\quad 2\chi_1 = q_1 - \left(q_1 - \frac{1}{2}\right)\ln|q| + \varphi q_2, \quad (29)$$

and, analogously,

$$2\chi_2 = q_2 - q_2\ln|q| - \varphi\left(q_1 - \frac{1}{2}\right), \quad (30)$$

where φ is defined by (16).

Connection matrix (27) in the intermediate energy region is our main result and the motivation for this publication. This matrix generalizes the results we presented in [3]. It is ready for further applications, and, to reap the fruits of the result, we compute the LZ transition probability $|T|^2$, which is universally valid for the tunneling, over-barrier, and intermediate energy regions (solid line in the figure). It is instructive to compare our result with the perturbative Landau approach (see, e.g., [1]) valid at small coupling constants. In first-order perturbation theory, the transition amplitude $A_{LZ}^{(1)}$ reads

$$A_{LZ}^{(1)} = 2iu_{12}\sqrt{\frac{\pi}{\varepsilon}}\mathrm{Ai}(2^{2/3}\varepsilon), \quad (31)$$

where we designated $\varepsilon = -\alpha f^{-2/3}$ and Ai is the first kind Airy function. All even higher order terms equal zero, and odd terms read as

$$A_{LZ}^{(2n+1)} = (A_{LZ}^{(1)})^{2n+1}. \quad (32)$$

Therefore, the series can be easily summed up giving, the generalized Landau formula

$$A_{LZ} = A_{LZ}^{(1)}[1 + (A_{LZ})^2]^{-1}. \quad (33)$$

We show this perturbative solution by the dashed line in the figure. Note that, although Eq. (32) reproduces the oscillating energy dependence of the LZ transition amplitudes, the equation gives oscillation periods that are quite different from those we calculated by our 4×4 connection matrix (27). This difference occurs because the perturbation (say, two) method disregards the contributions from the increasing solutions to the Schrödinger equation, which are relevant in the intermediate energy region.

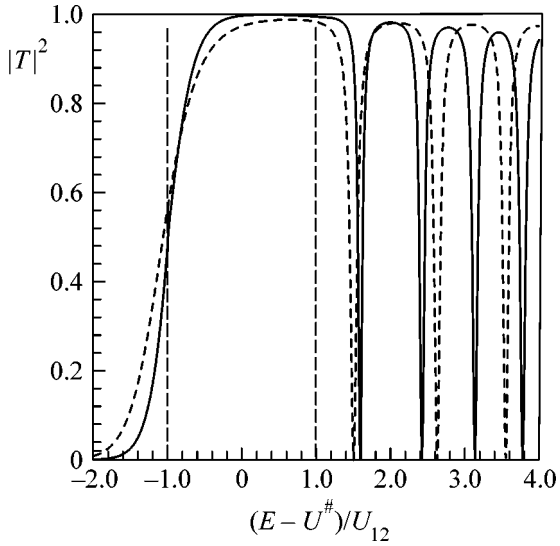

Energy dependent LZ transition probability: the solid line is the 4×4 connection matrix (27) calculations; the dashed line represents the generalized perturbative Landau formula (33).

The research described in this publication was made possible in part by RFFR grants. One of us (E.K.) is indebted to an INTAS grant (no. 01-0105) for partial support, and V.B. and E.V. are thankful to the CRDF (grant no. RU-C1-2575-MO-04).

REFERENCES

1. L. D. Landau and E. M. Lifshitz, *Course of Theoretical Physics*, Vol. 3: *Quantum Mechanics: Non-Relativistic Theory*, 2nd ed. (Nauka, Moscow, 1963; Pergamon, New York, 1965).
2. C. Zhu, Y. Teranishi, and H. Nakamura, Adv. Chem. Phys. **117**, 127 (2001).
3. V. A. Benderskii, E. V. Vetoshkin, and E. I. Kats, JETP **97**, 232 (2003).
4. A. M. Polyakov, Nucl. Phys. B **129**, 429 (1977).
5. S. Coleman, *Aspects of Symmetry* (Cambridge Univ. Press, Cambridge, 1985).
6. V. A. Benderskii, D. E. Makarov, and C. A. Wight, *Chemical Dynamics at Low Temperatures* (Wiley–Interscience, New York, 1994).
7. A. Erdelyi, W. Magnus, F. Oberhettinger, and F. G. Tricomi, *Higher Transcendental Functions* (McGraw-Hill, New York, 1953; Nauka, Moscow, 1965), Vols. 1–3.
8. V. A. Benderskii, E. V. Vetoshkin, and E. I. Kats, JETP **95**, 645 (2002).
9. V. A. Benderskii, E. V. Vetoshkin, and E. I. Kats, Phys. Rev. A **69**, 062508 (2004).
10. M. V. Fedoryuk, Proc. Russ. Acad. Sci. **158**, 540 (1964).
11. M. V. Fedoryuk, Proc. Russ. Acad. Sci. **162**, 287 (1965).
12. M. V. Fedoryuk, Russ. Math. Survey **21**, 1 (1966).
13. J. Heading, *An Introduction to Phase-Integral Methods* (Wiley–Interscience, London, 1962; Mir, Moscow, 1965).
14. F. W. J. Olver, J. Res. Natl. Bur. Stand., Sect. B **63**, 131 (1959).
15. F. W. J. Olver, *Asymptotics and Special Functions* (Academic, New York, 1974; Nauka, Moscow, 1990).

JETP Letters, Vol. 80, No. 6, 2004, pp. 441–444. Translated from Pis'ma v Zhurnal Éksperimental'noĭ i Teoreticheskoĭ Fiziki, Vol. 80, No. 6, 2004, pp. 498–502.

Effect of Anisotropy on the Entanglement of Quantum States in a Spin Chain

P. F. Kartsev and V. A. Kashurnikov*

Moscow Engineering Physics Institute (State University), Kashirskoe sh. 31, Moscow, 115409 Russia

** e-mail: kashur@rol.ru*

Received June 28, 2004; in final form, August 5, 2004

The effect of the anisotropy of the interaction of a spin chain in the *XXZ* Heisenberg model on the concurrence of the states of neighboring sites is studied. When anisotropy increases, the maximum concurrence in a magnetic field increases above the value reached in the absence of the field. The maximum magnetic field allowing entanglement is linearly related to the anisotropy parameter. © *2004 MAIK "Nauka/Interperiodica".*

PACS numbers: 03.65.Ud; 73.43.Nq; 75.10.Pq; 75.30.Gw

As is known, quantum states can exhibit a so-called entanglement that corresponds to nonlocal correlations of measurable quantities and has no classical analog. The state of a part of such quantum system can be determined by measuring (possibly destroying) the other part of the system. This property underlies quantum processing of information and is necessary for working quantum algorithms. The so-called Einstein–Podolsky–Rosen pair $|\psi\rangle = (|01\rangle - |10\rangle)/\sqrt{2}$ is a classical example of an entangled state [1].

One of the quantum-computer schemes under consideration is based on interacting electron spins in solid-state quantum dots [2]. Spin systems have an important property: the entanglement of a state is easily controlled by varying an external field [3] or the parameters of the system [4] and can be large [5]. An increase in temperature, which is usually harmful for the nanodevices under development, generally reduces entanglement. The inverse effect is, however, possible for certain external-field magnitudes; i.e., a rise in temperature increases entanglement [6].

Therefore, despite difficulties in realization, spin systems are among the promising systems for realization of quantum computations. In addition to their use in quantum informatics, investigations of entanglement are of independent importance, in particular because they provide a deeper insight into the nature of irreversibility [7].

Since spin models are simple, entanglement can be studied in the Ising model [8], *XY* model [5], isotropic and anisotropic Heisenberg models [6, 9], in longitudinal [3] and transverse [8] magnetic fields (magnetic entanglement) or in the absence of any magnetic field [10], in the ground state [11], and with an increase in temperature (thermal entanglement) [3, 6]. The asymptotic values of concurrence were found for an infinite antiferromagnetic chain and a square lattice [11].

However, the effect of interaction anisotropy on entanglement in the Heisenberg model is still poorly studied, although analytical results have been obtained for two and three qubits [6, 9]. In this work, a sufficiently large spin system (up to 16 spins) is considered. General properties are found, and the phase diagram is constructed.

The Hamiltonian of an antiferromagnetic *XXZ* chain has the form

$$\hat{H} = \sum_{i=1}^{L} (S_i^x S_{i+1}^x + S_i^y S_{i+1}^y + \Delta S_i^z S_{i+1}^z) - H\sum_{i=1}^{L} S_i^z, \quad (1)$$

where $\mathbf{S} = 1/2\boldsymbol{\sigma}$, $\sigma^{x,y,z}$ are the Pauli matrices and $\mathbf{S}_{L+1} = \mathbf{S}_1$. All quantities are measured in the exchange energy unit *J*, and interaction anisotropy is determined by the parameter Δ.

There are several parameters characterizing the entanglement of the system under consideration: von Neumann entropy [12], the entanglement of formation and distillable entanglement, and the concurrence of a pair of qubits and the fidelity of a multiqubit state to the Greenberger–Horn–Zeilinger state [13]. The last two measures are most often used to study spin systems.

In this work, we explored entangled states of spin chains by calculating the concurrence of adjacent qubits. The concurrence of two qubits in an entangled state with the environment is expressed as [14]

$$C = \max(\sqrt{\lambda_1} - \sqrt{\lambda_2} - \sqrt{\lambda_3} - \sqrt{\lambda_4}, 0). \quad (2)$$

Here, the eigenvalues λ_i of the matrix $R = \rho(\sigma^y \otimes \sigma^y)\rho^*(\sigma^y \otimes \sigma^y)$, where ρ is the reduced density matrix of these two qubits and ρ^* is obtained from ρ by time inversion, are numbered in decreasing order. Concurrence *C* determines the entanglement of formation $E(C)$ [14],

$$E(x) = -x\log_2(x) - (1-x)\log_2(1-x), \quad (3)$$

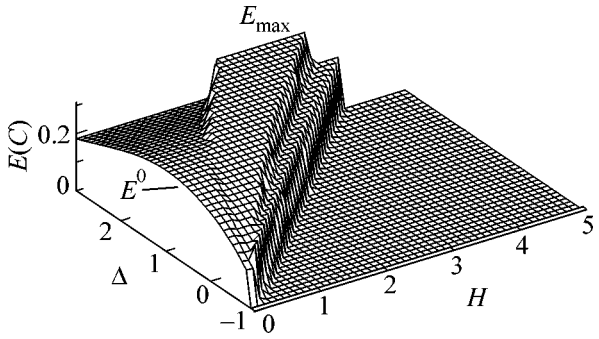

Fig. 1. Entanglement $E(C)$ of the states of adjacent spins in a six-site chain for $T = 0$ as a function of the external field H and anisotropy parameter Δ varying from –1.0 to 3.0. Entanglement is zero for $\Delta < -1.0$. With an increase in anisotropy, the maximum entanglement E_{max}, as well as the limiting field value for which states in adjacent sites are consistent ($C \neq 0$), increases. Value E^0 is entanglement in the absence of the field.

where $x = (1 + \sqrt{1 - C^2})/2$. For a pure state, x is the coefficient of the corresponding Schmidt decomposition [12].

For an anisotropic *XXZ* Heisenberg chain in the absence of a magnetic field, exact solutions were obtained by the Bethe-ansatz method [13] and method of inverse scattering problem [10]. In this work, we use the numerical method of the exact diagonalization of the Hamiltonian matrix. All energy levels and eigenstates of spin chains were determined, the total density matrix $\hat{\rho}$ was then calculated, and $\mathrm{Tr}\hat{\rho}$ over the states of sites $i = 3, 4, \ldots, L$ was calculated according to Eq. (2).

Figure 1 shows entanglement E calculated for a six-site chain as a function of the external field and anisotropy parameter Δ. First, it is worth noting that, with an increase in Δ, entanglement in the field becomes significantly different from its value E^0 in the absence of the field. Moreover, its maximum value is larger than that for the isotropic case.

Figure 2 shows entanglement E^0 for chains of various lengths. With an increase in L, this quantity tends to the known asymptotic value $E^0_\infty = E(C \simeq 0.386) \simeq 0.236$ (see [11]). Entanglement E^0 reaches a maximum for the isotropic case. The anisotropy effect is approximated by the formula $C \simeq C_0 - C_1(\Delta - 1)^2$ presented in [10] with the coefficients $C_0 \simeq 0.386$ and $C_1 \simeq 0.047$ (for the six-site chain).

Figure 3 shows the maximum entanglement E_{max} as a function of the anisotropy degree. This quantity is virtually saturated for $\Delta \geq 3.0$.

We emphasize that the range of magnetic fields for which the concurrence of the states of adjacent spins is nonzero extends when anisotropy increases. This dependence presents the general relation between

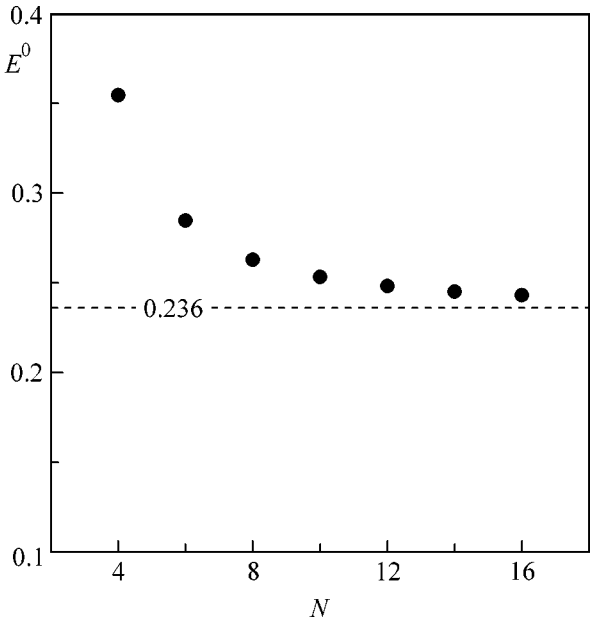

Fig. 2. Entanglement E^0 (for $H = 0$) of the states of adjacent spins in a chain consisting of $N = 4, \ldots, 16$ sites for $\Delta = 1.0$. A tendency to an asymptotic value of 0.236 [11] is seen.

entanglement and interaction. Let us explain this behavior. The boundary of the nonzero-entanglement region corresponds to a phase transition where all spins of the chain are aligned along the field (spontaneous magnetization of a ferromagnetic material). The step nearest to the transition in the entanglement plot (see Fig. 5) corresponds to the set of states $|\Psi\rangle = \frac{1}{\sqrt{N}}(|01\ldots1\rangle + e^{i\phi}|10\ldots1\rangle + \ldots + e^{i\phi(N-1)}|11\ldots0\rangle)$ with

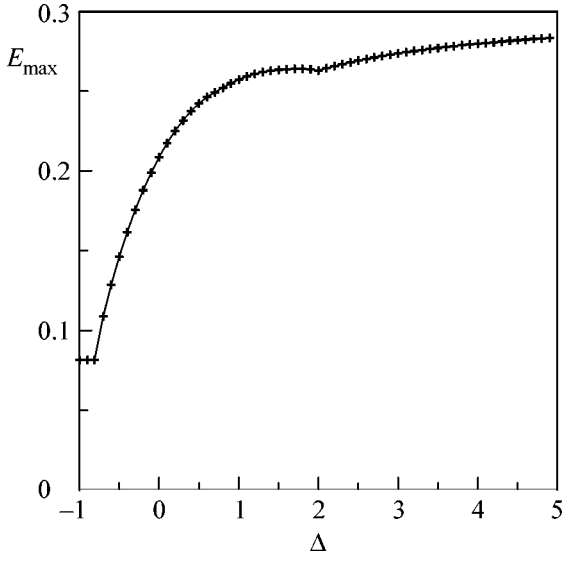

Fig. 3. Maximum achievable entanglement E^{max} of the states of adjacent spins in a ten-site chain as a function of the anisotropy degree.

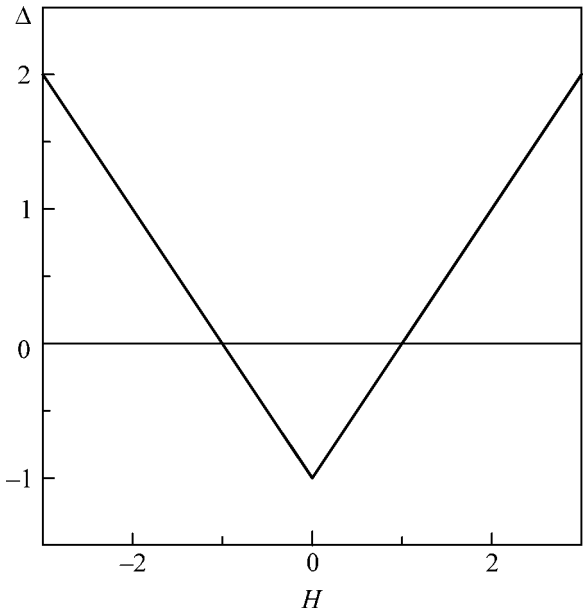

Fig. 4. Magnetic field–anisotropy phase diagram describing a domain with a nonzero concurrence of the states of adjacent spins: $C > 0$ for $|H| < 1 + \Delta$.

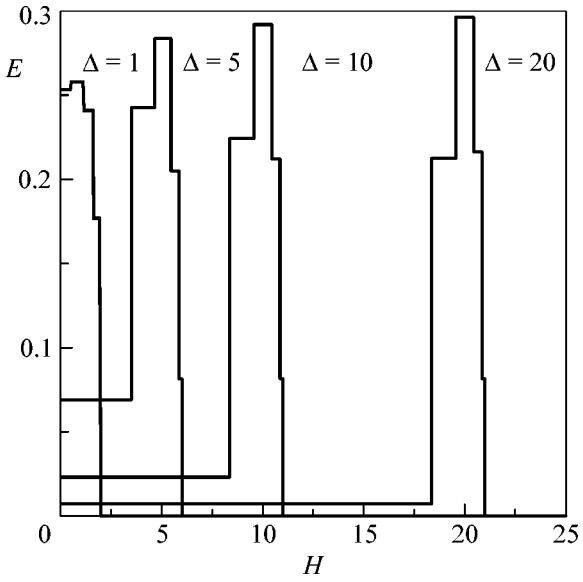

Fig. 5. Entanglement $E(C)$ of formation of adjacent spins in a ten-site chain as a function of the external field H for $T = 0$ and anisotropy parameter $\Delta = 1, \ldots, 20$. With an increase in Δ, the peak is shifted to the right (more precisely, a single peak splits into two peaks: the peak is symmetric for $H < 0$), and the maximum value of $E(C)$ increases slightly.

the total-spin projection $\sum_i S_i^z = N/2 - 1$, where ϕ is the phase parameter. It is easy to determine the corresponding entanglement. The reduced density matrix of two adjacent spins of the chain has the form

$$\rho = \frac{1}{N}\begin{pmatrix} N-2 & 0 & 0 & 0 \\ 0 & 1 & 1 & 0 \\ 0 & 1 & 1 & 0 \\ 0 & 0 & 0 & 0 \end{pmatrix}, \quad (4)$$

and Eq. (2) yields $C = 2/N$.

The minimum-energy level in this set corresponds to $\phi = \pi$:

$$E_1^{\min} = -H\left(\frac{N}{2} - 1\right) + \Delta\left(\frac{N}{4} - 1\right) - 1. \quad (5)$$

For $|H| > H^*$, where

$$H^*/J = 1 + \Delta, \quad (6)$$

state $|111\ldots1\rangle$ becomes energetically preferable and concurrence vanishes (see Figs. 1 and 4).

Similar formulas for ($d = 2$) square and ($d = 3$) cubic lattices yield $C = 2d/N$ and $|H^*|/J = d(1 + \Delta)$.

For $\Delta \longrightarrow \infty$, the model given by Eq. (1) is transformed to the Ising model whose ground state is not entangled in the absence of the transverse field [8]. In view of this circumstance, let us analyze the behavior of entanglement for large Δ values.

First, when approaching the Ising limit, entanglement decreases in a wide range of applied field magnitudes. Entanglement can be estimated in the simplest perturbation theory in the parameter $1/\Delta$. We consider a change in the ground state with zero total spin projection:

$$|\Psi\rangle \simeq a|\Psi_0\rangle + \sum_{i=1}^{L} b_i|\phi_i\rangle, \quad (7)$$

where

$$|\Psi_0\rangle = |01\ldots0_i1_{i+1}\ldots01\rangle, \quad (8)$$

$$|\phi_i\rangle = |01\ldots1_i0_{i+1}\ldots01\rangle \quad (9)$$

under the action of the transverse-interaction operator, which can be represented as

$$J/2\sum_{i=1}^{L}(\sigma_i^+\sigma_{i+1}^- + \sigma_{i+1}^+\sigma_i^-),$$

$$\sigma_i^+ = \begin{pmatrix} 0 & 0 \\ 1 & 0 \end{pmatrix}_i, \quad \sigma_i^- = \begin{pmatrix} 0 & 1 \\ 0 & 0 \end{pmatrix}_i.$$

Taking the first order of perturbation theory, we ignore states obtained from $|\Psi_0\rangle$ by applying perturbation more than once. In this case, in the truncated basis $\{|\Psi_0\rangle, |\phi_i\rangle\}$, the Hamiltonian matrix takes the form

$$\hat{H} = J\Delta\begin{pmatrix} 0 & 1/2\Delta & 1/2\Delta & \ldots & 1/2\Delta \\ 1/2\Delta & 1 & 0 & \ldots & 0 \\ \ldots & \ldots & \ldots & \ldots & \ldots \\ 1/2\Delta & 0 & 0 & \ldots & 1 \end{pmatrix}. \quad (10)$$

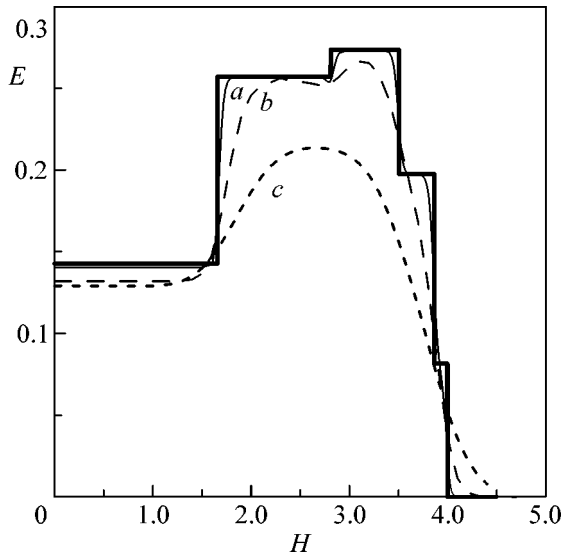

Fig. 6. Entanglement of adjacent spins in a ten-site chain as a function of the external field H for $\Delta = 3.0$ and temperature T = (thick line) 0, (*a*) 0.025, (*b*) 0.1, and (*c*) 0.25.

The ground level becomes lower by $-JL/4\Delta$, and the ratio of the coefficients of the wave-function expansion is $b_i/a = -1/2\Delta$. As a result, the concurrence of adjacent spins of the chain is approximately equal to $1/\Delta$.

However, we emphasize that the above reasoning is invalid near the transition point ($H \simeq \Delta$), where energy levels corresponding to various total-spin projections overlap each other. In this case, the transverse part of interaction cannot be treated as weak and the system is far from the Ising model. For such a field, concurrence remains large for any anisotropy parameter. Figure 5 shows a substantially nonmonotonic concurrence plot uniting these two features.

Calculations for longer chains ($L = 14$) reveal the same behavior. With an increase in the chain length, the number of steps corresponding to different total-spin projections increases and the dependence becomes smoother, but the same feature remains.

Figure 6 shows the effect of temperature on concurrence. With an increase in temperature, the entanglement plot is smeared and decreases. Entanglement decreases locally between the second and third steps, which are characterized by close $E(C)$ values (cf. the result from [3] for $L = 6$ and $\Delta = 1.0$).

Conclusions. New results for the entanglement of a spin chain have been presented for the anisotropic Heisenberg model. Since real magnetic systems usually have an anisotropy axis, these results can be used to develop and analyze quantum algorithms based on spin systems, and the phase diagram enables one to predict working parameters.

The calculations showed that interaction anisotropy considerably changes the concurrence of adjacent spins of the antiferromagnetic *XXZ* chain, increasing its maximum value in the presence of the field and extending the magnetic-field range where nonzero concurrence is possible. The limiting field is related to the anisotropy parameter by simple linear relation (6).

Thus, the available data on entanglement in various spin models make it possible to choose the external conditions or system parameters best for entanglement. Examination of inhomogeneous spin systems with impurities (as in [4]), open boundary conditions and a nonuniform external field, which correspond to realistic conditions of creating quantum dots, is one of the expected directions of further investigations in this field.

We are grateful to K.A. Valiev, A.A. Kokin, and A.A. Larionov for useful advice and discussions. This work was supported by the Russian Foundation for Basic Research, project no. 03-02-16979.

REFERENCES

1. A. Einstein, B. Podolsky, and N. Rosen, Phys. Rev. **47**, 777 (1935) [Usp. Fiz. Nauk **16**, 440 (1936)].
2. S. Bandyopadhyay, B. Das, and A. E. Miller, Nanotechnology **5**, 113 (1994).
3. M. C. Arnesen, S. Bose, and V. Vedral, Phys. Rev. Lett. **87**, 017901 (2001).
4. O. Osenda, Zhen Huang, and S. Kais, Phys. Rev. A **67**, 062321 (2003).
5. A. Osterloh, L. Amico, G. Falci, and R. Fazio, Nature **416**, 608 (2002); quant-ph/0202029v2 (2002).
6. G. Rigolin, quant-ph/0311185v1.
7. M. B. Mensky, *Quantum Measurements and Decoherence: Models and Phenomenology* (Fizmatlit, Moscow, 2001; Kluwer Academic, Dordrecht, 2000).
8. D. Gunlycke, S. Bose, V. M. Kendon, and V. Vedral, Phys. Rev. A **64**, 042302 (2001); quant-ph/0102137v2.
9. X. Wang, H. Fu, and A. I. Solomon, J. Phys. A: Math. Gen. **34**, 11307 (2001).
10. Shi-Jian Gu, Hai-Qing Lin, and You-Quan Li, Phys. Rev. A **68**, 042330 (2003); quant-ph/0307131v2.
11. X. Wang and P. Zanardi, Phys. Lett. A **301** (1–2), 1 (2002); quant-ph/0202108v1 (2002); V. Subrahmanyam, Phys. Rev. A **69**, 022311 (2004); quant-ph/0309004v2 (2003).
12. K. A. Valiev and A. A. Kokin, *Quantum Computers: Hopes and Reality* (Regul. Khaot. Din., Izhevsk, 2001), p. 42 [in Russian].
13. X. Wang, Phys. Rev. A **66**, 044305 (2002); quant-ph/0205049v3 (2002).
14. W. K. Wootters, Phys. Rev. Lett. **80**, 2245 (1998).

Translated by R. Tyapaev

JETP Letters, Vol. 80, No. 6, 2004, pp. 445–454. Translated from Pis'ma v Zhurnal Éksperimental'noĭ i Teoreticheskoĭ Fiziki, Vol. 80, No. 6, 2004, pp. 503–514.

ON THE RESULTS OF PROJECTS OF THE RUSSIAN FOUNDATION FOR BASIC RESEARCH, project no. 01-02-17771

One-Dimensionality Effects in Quasi-One-Dimensional Conductors

S. V. Zaĭtsev-Zotov

Institute of Radio Engineering and Electronics, Russian Academy of Sciences, ul. Mokhovaya 18, Moscow, 125009 Russia
e-mail: serzz@cplire.ru

Received August 3, 2004

The electrophysical properties of quasi-one-dimensional conductors with a charge-density wave change qualitatively upon a decrease in their transverse sizes. The temperature and electric-field dependences of the conductivities of thin samples are governed by the laws expected for one-dimensional electron systems. The results of studying these effects and the present-day knowledge of their origin are presented. © *2004 MAIK "Nauka/Interperiodica".*

PACS numbers: 71.45.Lr; 72.15.Nj

Introduction. At present, the physics of one-dimensional electron systems is a rapidly progressing field of solid-state physics. The physical properties of one-dimensional electron systems differ substantially from the properties of bulk systems. The distinctions arise primarily due to the electron–electron interactions, which are invariably essential in the one-dimensional electron systems and cannot be treated perturbatively. In what follows, by one-dimensional conductors are meant the structures formed by atomic chains, and by quasi-one-dimensional conductors are meant crystals comprised of a large number of such chains.

Historically, the first idea of the unusual properties of one-dimensional metals was proposed by Peierls, who pointed out that the spatially inhomogeneous state with periodic atomic displacements and electron-density modulation in crystal lattice, the so-called state with a charge-density wave (CDW), is energetically favorable [1]. Experimentally, the Peierls transition with the formation of a CDW was discovered in 1976 in a quasi-one-dimensional $NbSe_3$ conductor, i.e., more than 20 years after it had been predicted. It should be noted that the Peierls transition is accompanied by the formation of a three-dimensionally ordered CDW, while the transition is clearly seen only in sufficiently large (by today's standards) crystals of quasi-one-dimensional conductors with transverse sizes no less than several tens of nanometers. At present, the physics of quasi-one-dimensional conductors is rather well explored. Quasi-one-dimensional conductors possess a number of unusual properties associated with the presence of CDWs: the collective conduction caused by CDW sliding in the above-threshold electric fields, the generation of a narrow-band noise upon this sliding, a large low-frequency dielectric constant (up to 10^8) that arises due to the contribution of the pinned CDW, etc. [3].

The construction of the theory of low-energy excitations in a one-dimensional electron liquid was another important achievement in the physics of one-dimensional systems [4]. The excitation parameters were determined using the Luttinger model, and a broad class of one-dimensional many-particle quantum systems, for which the solution was found, has received, after Haldane [5], the name of *Luttinger liquid class*. Intensive studies of the physics of one-dimensional electron systems started in the 1900s, after it had become clear that such systems can be prepared experimentally, while the anticipated phenomena are highly unusual and interesting. The existence of collective charge and spin elementary-excitation modes, the absence of single-particle excitations (quasiparticles), the appearance of spin–charge separation (i.e., dispersion laws for the charge and spin modes are dissimilar), etc., were predicted for one-dimensional electron systems [4].

In the one-dimensional systems, impurities form energy barriers that can be overcome through tunneling [6]. The density of tunneling states in a Luttinger liquid is a power-law function of energy distance from the Fermi level, and the exponent depends on the electron–electron interaction strength and also on whether electrons tunnel to the end or middle of the one-dimensional chain. For this reason, the current–voltage characteristics (CVCs) and the temperature dependences of the conductivity of a one-dimensional chain with a Luttinger liquid and a single impurity are determined by power-law energy dependences that are specific of

0021-3640/04/8006-0445$26.00

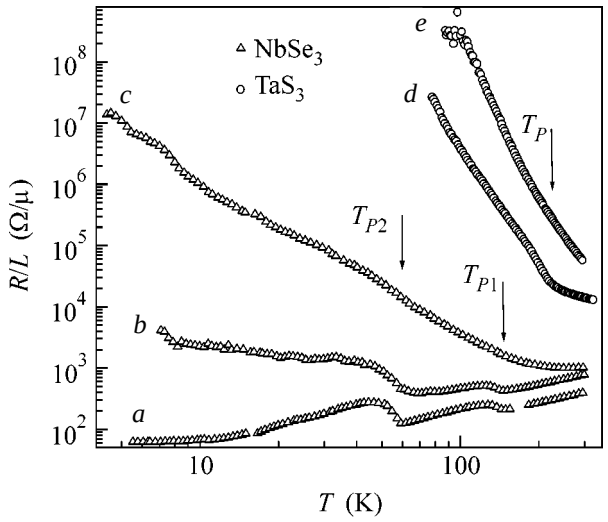

Fig. 1. Evolution of the temperature dependence of the conductivity of quasi-one-dimensional $NbSe_3$ and TaS_3 conductors upon their thinning. Arrows indicate the Peierls-transition temperatures. Data from [13].

the density of tunneling states of one-dimensional systems [6].

Experimental studies in this field are being carried out for various structures, including carbon nanotubes [7], semiconductor nanowires [8, 9], and many other objects (see, e.g., [10]).

Until recently, the physics of quasi-one-dimensional conductors and physics of one-dimensional electron systems were developed almost independently of each other. The investigations discussed in this review are devoted to phenomena that were originally observed in thin samples of quasi-one-dimensional conductors. It turns out that phenomena very similar to those expected for one-dimensional electron systems arise in these physical objects under certain conditions. The reason for such behavior remains to be clarified.

Subject of investigation. Quasi-one-dimensional conductors are suitable objects for a search for the one-dimensionality effects, because the low-dimensionality effects are inherent in these materials. They have a chain structure, allowing their use in the fabrication of thin samples by various splitting, layering, and other methods.

Below the Peierls-transition temperature, quasi-one-dimensional conductors with a CDW have several characteristic lengths that govern many physical properties of these materials. These are the CDW phase- and amplitude-correlation lengths. The phase-correlation length appears due to breaking the CDW long-range order by impurities. In pure samples, it is equal to tens of microns along the chains and is on the order of one micron in the transverse direction. In samples with sizes smaller than the CDW phase-correlation length, a multitude of size effects arises [11]. The amplitude-correlation length is determined by the parameters of the material and characterizes the distances at which the amplitude of the CDW order parameter changes. Estimates show that the amplitude-correlation length in quasi-one-dimensional conductors with a CDW is equal to 3–10 nm along the chain and is approximately an order of magnitude smaller in the transverse direction. It has been established in previous studies that, upon a decrease in the transverse sizes of the samples to the submicron level, the threshold field for the onset of nonlinear conduction increases by several orders of magnitude, the Peierls transition becomes diffuse and shifts to low temperatures, the threshold behavior smears, the breaking of the CDW metastable state accelerated, etc. [11]. These phenomena can all be considered as precursors of the CDW breaking and the transition of a quasi-one-dimensional conductor to some new state.

The assumption that the transition from quasi-one-dimensionality (bulk samples) to one-dimensionality (single chain) should inevitably occur upon a decrease in the sample sizes served as the basis for a search for the one-dimensionality effects in the quasi-one-dimensional conductors. The studies discussed below were carried out for quasi-one-dimensional conductors of the MX_3 (M = Nb, Ta; X = S, Se) family, primarily for $NbSe_3$. This material was not chosen accidentally. Despite the occurrence of two Peierls transitions at temperatures $T_{P1} = 145$ K and $T_{P2} = 59$ K in $NbSe_3$, it retains metallic properties at very low temperatures. For this reason, the one-dimensionality effects should be accompanied by a qualitative change in the character of conduction. Moreover, the charge-carrier concentration in $NbSe_3$ at $T < T_{P2}$ is exceedingly low: $n = 2 \times 10^{-18}$ cm^{-3} [12]. Thus, at $T < T_{P2}$, $NbSe_3$ is a metal with an unprecedently low electron concentration, so that the appearance of one-dimensionality effects as a consequence of the size effects can be expected even for comparatively large transverse sizes of the samples.

Electrical conductivity of thin $NbSe_3$ samples and one-dimensionality effects. *$NbSe_3$ samples prepared by plasmochemical etching.* In [13], the electrophysical properties of $NbSe_3$ samples were studied as a function of their transverse sizes. The studies were carried out with $NbSe_3$ samples obtained by splitting high-quality crystals and their additional thinning by plasmochemical etching in an SF_6 plasma, and also with TaS_3 samples prepared by splitting without any additional processing. It was found that the character of temperature dependence of the electrical conductivity qualitatively changed with a decrease in the sample transverse sizes (Fig. 1). As the thickness of $NbSe_3$ crystals decreased, the metallic behavior of $R(T)$ showing two maxima corresponding to two phase transitions with CDW formation (curve *a* in Fig. 1) graded into dielectric behavior with $dR/dT < 0$ (curve *c*). In the thinnest samples (with the resistance per unit length $R/L \sim 10^3$ Ω/μm, which corresponds to the cross-sectional

area of less than 3000 nm^2), the conductivity was described by the law $R(T) \propto T^{-\alpha}$ ($\alpha \approx 3$) over a change in R by three to four orders of magnitude. According to this law, $R(0) = \infty$ (dielectrization). Moreover, it turned out that the CVCs of the majority of thin samples also qualitatively changed, became nonlinear, and obeyed the same power law $I \propto V^{\beta}$ ($\beta \approx 3$) in the nonlinearity region (Fig. 2). The power-law temperature and electric-field dependences of this type are precisely those which are expected for the conductivity of a one-dimensional electron gas [4, 6]. However, the predicted relationship $\beta = \alpha + 1$ was not fulfilled in those experiments.

The electrophysical properties of the TaS_3 samples also changed upon a decrease in their transverse sizes, but these changes were less pronounced and observed mainly in the temperature range $T > T_P$, where metallic conduction disappeared and the dielectric behavior prevailed (Fig. 1, curves *e*, *d*).

Structures with a constriction. Analogous behavior was observed for the $NbSe_3$ structures prepared by etching with a focused ion beam. The structures studied in [14] are shown in Fig. 3. These structures were prepared using high-quality $NbSe_3$ samples placed on a substrate with the preliminary applied contacts. Thereupon, two types of structures were obtained from these samples by etching by a focused ion beam. The structure of the first type had constriction (Fig. 3a). It turns out that the size effect arises in the constriction as well: as the constriction width decreased to about 100 nm, the character of the temperature dependence of conductivity changed qualitatively and a dielectric state resembling the aforementioned state with $\alpha \approx 1$–3 and $\beta \approx 3$ appeared.

One-dimensional behavior in bulk $NbSe_3$ samples. It was also established [14] that the same power-law temperature and electric-field dependences of conductivity can arise in the structures of the other type, e.g., in bulk $NbSe_3$ samples after cutting them in the transverse direction by a focused ion beam (right side of Fig. 3b), followed by healing with platinum (left side of Fig. 3b). It was shown that, after this procedure, which supposedly results in the introduction of the Ga ions to mediate the Pt deposition, the properties of the sample changed at distances on the order of 10 μm from the cut in the direction of the highest-conductivity axis. The temperature set of CVCs for such samples is shown in Fig. 4. In the same figure, the solid lines correspond to the CVCs calculated from the equation

$$\frac{I}{T^{\alpha+1}} = C\sinh\left(\gamma\frac{eV}{kT}\right)\left|\Gamma\left(1+\frac{\beta}{2}+i\frac{\gamma}{\pi}\frac{eV}{k_BT}\right)\right|^2, \qquad (1)$$

which describes the CVC shape and its temperature evolution for a Luttinger liquid [15] with $\alpha = 6$, $\beta = 4$, and $\gamma = 0.1$. One can see that Eq. (1) fully describes the CVC shape and its temperature evolution over the entire temperature range used. It is worth noting that

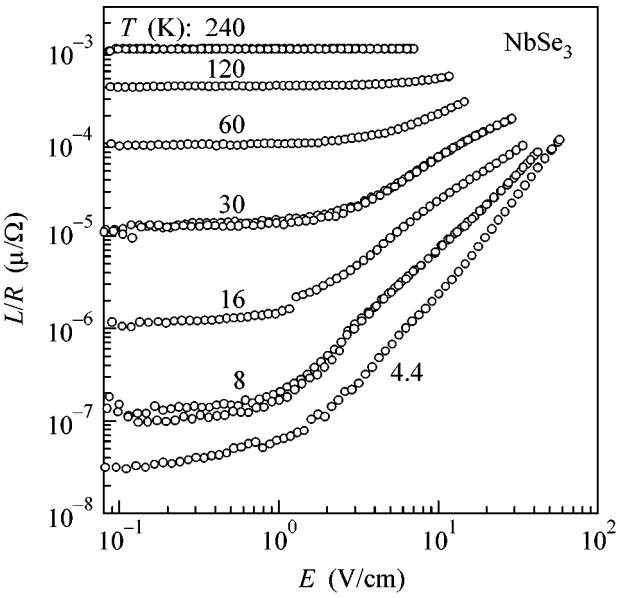

Fig. 2. Current–voltage characteristics of a thin sample of $NbSe_3$ for various temperatures. Data from [13].

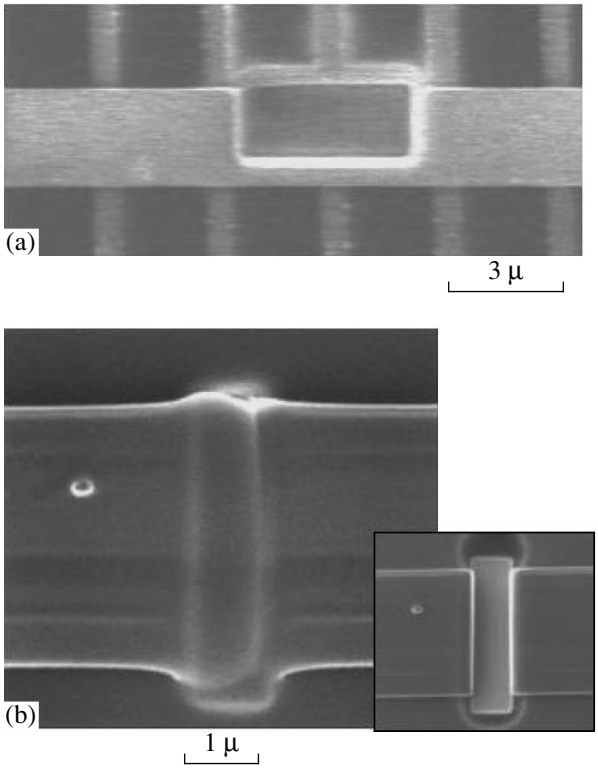

Fig. 3. Structures prepared using a focused ion beam. Data from [14].

the exponents α and β in these samples, as a rule, were appreciably larger than in thin $NbSe_3$ samples exhibiting a dielectric behavior. For instance, $2.9 \le \alpha \le 3.4$ for

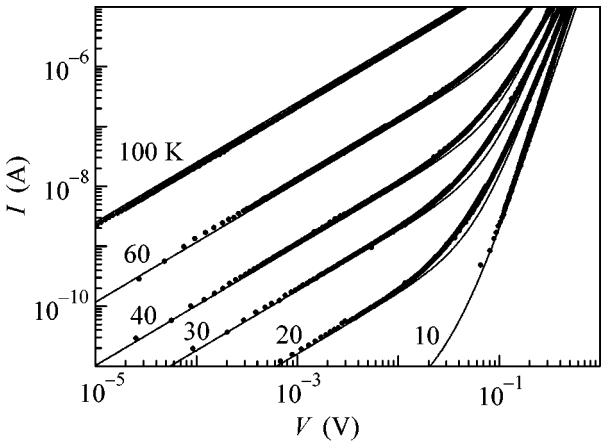

Fig. 4. Current–voltage characteristics of the $NbSe_3$ sample with a platinum-healed area (see Fig. 3b). Numerals indicate the measurement temperatures in Kelvins. Solid lines are the theoretical CVCs given by Eq. (1). Data from [14].

three of the ten studied samples, whereas, for the remaining seven samples, $5.5 \le \alpha \le 6.5$.

The results presented above gave grounds to assume that the observed unusual properties of the thin samples of quasi-one-dimensional conductors may arise as a result of the introduction of additional impurities and defects during the course of the technological procedures used for curtailing the transverse sizes. For this reason, care was taken to reduce the number of defects during the fabrication of thin samples. In particular, the ultrasonic [16] and electric-field [17] methods of splitting quasi-one-dimensional conductors were developed and subsequently used for the preparation of even thinner $NbSe_3$ samples.

Sample "aging." In some experiments [16, 18], the properties of the thinnest $NbSe_3$ samples gradually changed in time on the order of 10^3 h. In particular, it was found that holding in air led to a smooth increase in the sample resistance (aging). With time, initially thin samples with metallic conduction can undergo transition to the dielectric state. A comparison of the sample geometric sizes measured using atomic-force and electron microscopes with sizes determined from the conductivity data showed the presence of a dielectric layer with a thickness of several nanometers at the surfaces of the samples prepared by ultrasonic grinding and subsequent fabrication of the contacts by electron-beam lithography [16]. It was also shown in [16] that, at least at the initial aging stage, the changes in the conduction of the $NbSe_3$ samples are analogous to those arising upon the formation of a constriction in the sample. Since no transition to a new stable conducting state upon sample aging was observed experimentally in [16, 18], the conclusion was drawn that the aging effect mainly results in the narrowing of the conduction channel and in the chain breakup with the appearance of a contribution from the transverse conduction. It was also shown that sample heating to a temperature of 120–140°C substantially accelerates the aging process [16].

Electrophysical properties of quasi-one-dimensional conductors with nanometer transverse sizes. Further investigations [18] have shown that the conductivity of even thinner $NbSe_3$ and TaS_3 samples prepared by splitting in an electric field ($R/L \sim 2 \times 10^5$ Ω/μm, which corresponds to $s \sim 10$ nm^2) does not obey the power-law dependence. To reduce effects caused by aging, the total time of holding in air prior to the fabrication of the contacts did not exceed 1 h in these exper-

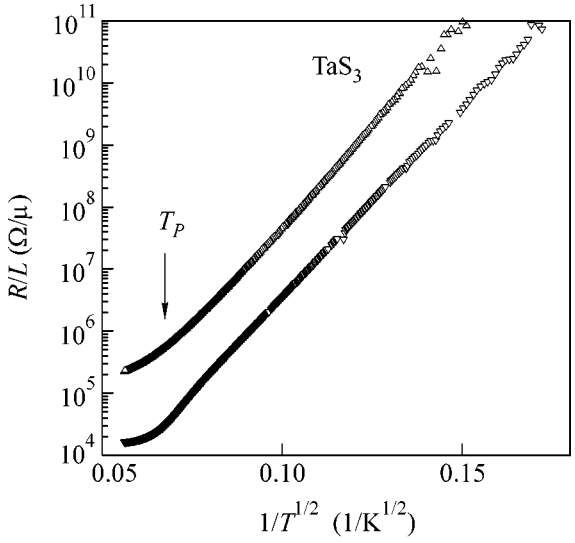

Fig. 5. Temperature dependences of the conductivity of thin TaS_3 samples. Arrows indicate the Peierls transitions in the crystals with standard sizes. Data from [18].

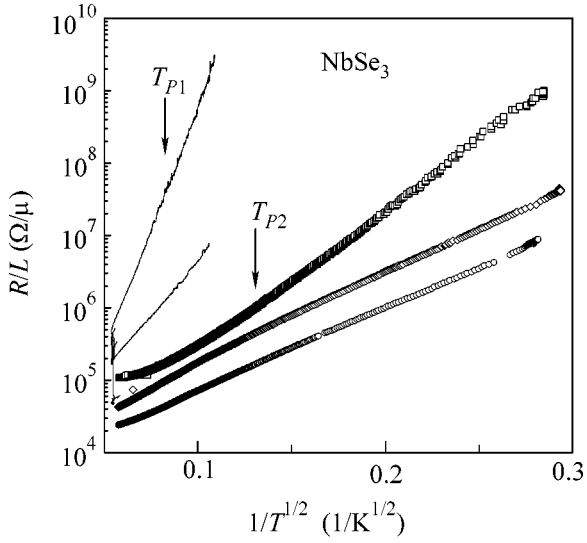

Fig. 6. Temperature dependences of the conductivity of thin $NbSe_3$ samples. Arrows indicate the Peierls transitions in the crystals with standard sizes. Data from [18].

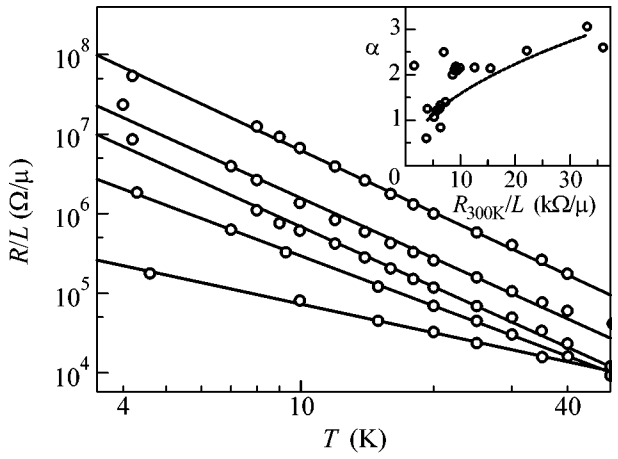

Fig. 7. Temperature dependences of the conductivity of thin $NbSe_3$ samples at temperatures below T_{P2}. In the inset, the exponent α is shown as a function of the parameter R/L. Data from [20].

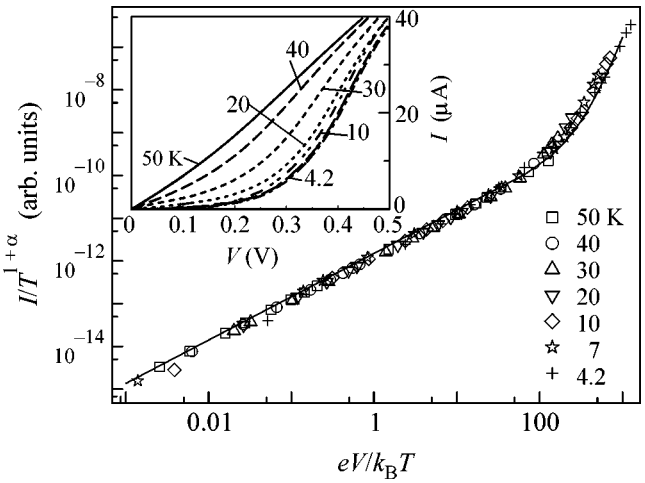

Fig. 8. Current–voltage characteristics of the $NbSe_3$ sample at various temperatures, as functions of $I/T^{\alpha+1}$ on eV/T. Solid line is the result of curve-fitting procedure using Eq. (1) with parameters $\alpha = 2.15$, $\beta = 4.2$, and $1/\gamma = 77$. The original CVCs are shown in the inset. Data from [20].

iments, while the measurements started within a day after the sample preparation. In Figs. 5 and 6, the sets of temperature dependences are shown for such samples. One can see that these dependences obey quite satisfactorily the law

$$R \propto \exp\left(-\left[\frac{T_0}{T}\right]^{\gamma}\right) \qquad (2)$$

with $\gamma = 1/2$. This equation describes the variable-range hopping conduction [19] (the Mott's law with $\gamma = 1/(1 + D)$, where D is the space dimensionality) for a one-dimensional case ($D = 1$) and hopping conduction with the Coulomb electron–electron interaction (Efros–Shklovskiĭ law) [19].

Anomalous behavior of $NbSe_3$ below T_{P2}. Recent results on the electrical conductivity of $NbSe_3$ samples prepared by ultrasonic splitting [20] proved to be quite interesting. In those experiments, the contacts were applied using electron-beam lithography. The sample surface layer was removed by short-term immersion into hydrofluoric acid, and the contacts were fabricated by evaporating gold onto a titanium thin film that is necessary for better adhesion. It turned out that the dielectrization of the electronic spectra of such samples occurs only at temperatures below $T_{P2} = 59$ K, whereas, at higher temperatures, the traces of a metallic state and the presence of both CDWs are retained in the samples. Thus, the electronic spectra of these samples undergo dielectrization on the background of both CDWs. The low-temperature dependences of the resistances of the $NbSe_3$ samples prepared by the procedure [20] are shown in Fig. 7. One can see that these dependences are satisfactorily described by the power laws $R \propto T^{-\alpha}$. The dependence of α on the parameter R/L is shown in the inset. The typical value of α equals 1–3 and increases with decreasing the sample thickness.

The set of CVCs of one of the $NbSe_3$ samples, whose electronic spectrum undergoes dielectrization only at $T < T_{P2}$, are shown in the inset in Fig. 8 [20]. Contrary to the previously studied samples, these CVCs are almost linear at temperatures above 50 K (Figs. 2, 4). Upon a decrease in temperature, the nonlinearity rapidly increases. It was found that all CVCs of these samples could be described by a single universal curve with currents and voltages scaled according to Eq. (1). The results of such scaling are shown in Fig. 8: all measured CVCs constructed on the $I/T^{\alpha+1}$ vs. eV/T scale fall on a universal curve described by Eq. (1) with parameters $\alpha = 2.15$, $\beta = 4.2$, and $1/\gamma = 77$. Note that the relation $\beta = \alpha + 1$ does not hold for these samples.

Influence of impurities on the conductivity of quasi-one-dimensional conductors. Experimental data. The results presented above require a detailed analysis of the experiments devoted to the study of the influence of impurities on the electrophysical properties of quasi-one-dimensional conductors. Most of these studies were carried out shortly after the discovery of the Peierls transition. Inasmuch as these investigations were mainly devoted to the influence of impurities on the CDW pinning, they did not analyze in detail the temperature dependence of linear conductivity. A change in the $R(T)$ dependence in $NbSe_3$ at low temperatures and the appearance of the dependence with $dR/dT < 0$ in the samples with impurities was observed in a number of works. In the $NbSe_3$ samples with the 0.1% Ti and 5% Ta contents, the resistance increased at low temperatures [21]. The most pronounced increase was observed for the Ti impurities: the resistance had a minimum at about 40 K and doubled as $T \longrightarrow 0$. The

influence of V, Mn, Cr, Gd, Pd, Fe, Co, and Ni impurities on the temperature dependence of the linear $NbSe_3$ conductivity was studied in [22]. It was found that the conductivity of the $NbSe_3$ samples containing Cr and Pd at a level of 3–5% was qualitatively different from the conductivity of pure $NbSe_3$. For instance, the introduction of 5% Cr leads to the dielectric behavior with a sharp increase in the resistance upon lowering temperature below 700 K, while the introduction of 3% Pd, on the contrary, eliminates any traces of the Peierls transitions and gives rise to the metallic conduction down to liquid helium temperature. No phenomena similar to those observed in thin $NbSe_3$ samples (transition to $dR/dT < 0$ at $T = 50$–200 K and disappearance of conduction at $T \longrightarrow 0$) have been observed so far. Note that the appearance of the temperature dependences with $dR/dT > 0$, by itself, is not indicative of the dielectrization of the electronic spectrum: similar behavior is also well known for metals, e.g., in the case of weak localization or in the presence of magnetic impurities. The clearly defined tendency to the disappearance of conduction at $T \longrightarrow 0$ in the samples studied is a basic distinction of the phenomena discussed in this review.

Impurities can also penetrate into crystal through contacts. In [23], this was demonstrated by the example of CDW pinning by indium impurities. Indium atoms were introduced into bulk $NbSe_3$ samples by the diffusion through the contacts upon heating to 120°C and diffused at macroscopic distances on the order of the sample lengths (1 mm). Since indium contacts were also used in the experiments in [13, 18], it is not improbable that the aging effect is due, in part, to the diffusion of indium atoms. Note also that in [20], where the contacts to the samples were fabricated using gold evaporated onto the titanium sublayer, the dielectrization of electronic spectrum of $NbSe_3$ was observed only below T_{P2}.

Experimental. Concluding remarks. Thus, the dielectrization of the electronic spectrum is observed in bulk crystals of quasi-one-dimensional $NbSe_3$ conductors after treating them with a Ga ion beam (dielectrization temperature 100–150 K), in thin $NbSe_3$ crystals with $R_{300}/L \gtrsim 10^3$–10^4 Ω/cm (dielectrization temperature 120–200 K), and in $NbSe_3$ crystals with the removed surface layer at $R_{300}/L \gtrsim 10^4$ Ω/cm (dielectrization temperature $\sim T_{P2}$). The corresponding temperature dependences of conductivity are divided into two main types: those obeying Eq. (1), which describes the conductivity of a broad class of one-dimensional electron systems, including Luttinger liquid, and the dependences obeying Eq. (2), which describes both the variable-range hopping conduction in the one-dimensional case (Mott's law) and the hopping conduction with the Coulomb interaction between the current carriers (Efros–Shklovskiĭ law).

Current notion of the possible reasons for the dielectrization of electronic spectrum. Thus, a great body of data indicating that the character of temperature and field dependences of conductivity can qualitatively change in quasi-one-dimensional conductors and they can undergo transition to the dielectric state under certain conditions has been accumulated to date. The properties of the corresponding dielectric state are described by the laws that are expected for one-dimensional electron systems. As now, no unified viewpoint has been drawn up on the origin of this phenomenon. In what follows, the possible reasons for the dielectrization of electronic spectrum are considered, and the possible scenarios for the one-dimensional behavior are briefly discussed.

Dielectrization of the surface layer. The dielectrization of thin samples may arise because the condition for the CDW formation near the surface is different from the conditions for its formation in the bulk. Although an assumption about the dielectrization of surface layer was conjectured in a number of experimental works [13, 24], no theoretical analysis of this question has come to our notice. When it is assumed that the surface dielectrization involves the surface unit cells and their nearest neighbors, one can estimate the area of a sample whose properties are determined by the surface dielectrization. The unit-cell area of $NbSe_3$ is 1.5 nm^2 [3]. The cross section of a typical sample has the rectangular shape with a thickness-to-width ratio on the order of five. Then, the cross-sectional area of an $NbSe_3$ sample consisting of four unit cells in the transverse direction and twenty cells in the longitudinal direction (each unit cell comprises three metallic chains) equals 120 nm^2, which corresponds to the ratio $R/L = 1.7 \times 10^4$ Ω/μm. This value is comparable to the experimentally observed values $R/L = 10^3$–10^4 Ω/μm corresponding to the onset of the dielectrization of the electronic spectrum.

Impurities in the surface layer. It is also pertinent to analyze the possible existence of an excessive impurity concentration in the near-surface layer of quasi-one-dimensional conductors. Although this assumption seems to be quite natural, it has not been experimentally justified so far. The point is that the excessive impurity concentration in the near-surface layer should give rise to surface pinning and make an additional contribution to the increase in the threshold field E_T upon a decrease in the cross-sectional area s of the samples. There has been much discussion on surface pinning in relation to the results of studying the size effect, namely, the $E_T(s)$ dependence in $NbSe_3$ [11, 24–27]. Recent investigations of the $E_T(s)$ dependence in $NbSe_3$ samples up to $R/L \approx 10^4$ Ω/μm [28] have shown that these samples demonstrate an $E_T \propto (R/L)^{2/3}$ dependence, which is fully described within the framework of the theory of weak CDW pinning by bulk impurities (one-dimensional CDW pinning) without invoking any considerations concerning the surface pinning, for which $E_T \propto (R/L)^{1/2}$.

The analysis of the pinning types [11, 24–28] should be supplemented by the case of interest to us, namely, by a weak pinning to the surface-layer impurities that additionally contribute to the impurities homogeneously distributed over the sample bulk. For a weak pinning, the threshold field is determined by the expression given by the Fukuyama–Lee–Rice model [3, 11]:

$$E_T \sim \frac{q}{e\rho_e}\left(\frac{w_i^4 n_i^2}{K^D}\right)^{1/(4-D)}, \quad (3)$$

where ρ_e, n_i, and K are, respectively, the electron and impurity concentrations and the CDW elastic modulus. If the transverse sizes of a sample are much smaller than the phase-correlation length in the transverse direction, pinning is one-dimensional; i.e., $D = 1$, $\rho_e \propto s$, $n_i \propto s$ (impurities are distributed over the sample volume), and $K \propto s$, yielding $E_T \propto s^{2/3}$ (see also [28]). However, if most impurities are distributed over the sample surface, then $n_i \propto \sqrt{s}$, giving $E_T \propto 1/s$. Therefore, the contribution ($\propto \sqrt{s}$) from the surface impurities in thin samples should inevitably exceed the contribution ($\propto s$) from the bulk concentration and give rise to the $E_T \propto 1/s$ dependence, which, however, was not observed in the experiments in [28]. For this reason, it is beyond reason to believe that the dielectrization of the electronic spectrum of thin $NbSe_3$ samples is the result of the increase in the concentration of impurities located in the near-surface layer of such samples. Note also that the maximal values of the exponent α in the samples prepared using the ion-beam treatment (Fig. 3b) are almost twice as large as in the thin samples, indicating that there are certain distinctions between the origins of the dielectrization of electronic spectrum in the thin and impurity samples.

Coulomb blockade. In [20], it was pointed out that there is a certain analogy between the properties of thin quasi-one-dimensional conductors and the properties of multilayer carbom nanotubes, where electron gas cannot be considered one-dimensional but the temperature and electric-field dependences of conductivity show a power-law behavior [29]. Such a behavior arises in a "metal–tunneling junction–nanowire" system due to the Coulomb blockade in a tunneling junction with a high resistance [29–31]. The corresponding exponent is given by the expression

$$\beta = \frac{2Z}{R_Q} + 1, \quad (4)$$

where Z is the impedance of a nanowire through which the tunneling junction is connected to an external electric circuit and $R_Q = 2\pi\hbar/e^2$ is quantum resistivity [30, 31]. Estimates made in [20] showed that, for a nanowire of width $w = 50$ nm separated from a conducting substrate by a 1-μm-thick silica layer (dielectric constant 3.9), the expected value of exponent β is 4.2, which is close to the experimental data. Moreover, this approach predicts that $\alpha \propto \sqrt{1/s}$, which correlates well with the observed behavior (inset in Fig. 7). Although this model accounts for the majority of observed features in the behavior of thin $NbSe_3$ samples, its applicability is not unconditional. First, this model was developed for a single tunneling junction, whereas the transition from the linear CVC portion to the nonlinearity increase in the conductivity occurs at $eV \approx 80k_BT$, which corresponds to the presence of 80 identical tunneling junctions. Second, it is still unclear why the dielectrization onset was locked to T_{P2} in [20] and was not in [13, 18]. Note that an equation analogous to Eq. (4) can be obtained by the generalization of the model of tunneling in one-dimensional electron gas [6] to the case of a multimode quantum wire [32].

Impurity-induced stabilization of Luttinger liquid in quasi-one-dimensional metals. A crucial question is whether the dependences observed in quasi-one-dimensional conductors are manifestations of the one-dimensionality effects or not. According to the generally accepted notion of Luttinger liquid, pure samples with more than ten chains can be regarded as bulk samples, so that the one-dimensionality effects in them should be negligible. The reason for such a behavior is that quasi-one-dimensional conductors are unstable against the transition to the three-dimensional electronic spectrum even if the probability of electron hopping between the chains is exceedingly low. From the viewpoint of the physics of quasi-one-dimensional conductors with a CDW, samples with a cross-sectional area less than 10^3 nm^2 (thousand chains) are exceedingly thin, so that the CDW fluctuations in them are so large that they destroy three–dimensional ordering. Such a fluctuation-induced CDW breaking manifests itself by smearing the phase transition, its shift to lower temperatures, spontaneous CDW-phase slip, acceleration of the metastable-state relaxation, and by other size effects [11].

The three-dimensional CDW order can be broken by the introduction of impurities with a sufficiently high concentration; of interest is the nature of the resulting state. In this context, recent theoretical work by Artemenko, who has shown that the introduction of impurities into a quasi-one-dimensional metal stabilizes Luttinger liquid is noteworthy [33]. Note that this result differs substantially from the widespread opinion that certain features of the Luttinger liquid can be observed in quasi-one-dimensional conductors only at temperatures higher than the Peierls-transition temperature, while Fermi liquid is always the ground state of a quasi-one-dimensional metal (cf., e.g., [4]). The physical mechanism suggested in [33] for the impurity-induced stabilization of Luttinger liquid in a quasi-one-dimensional system is associated with the appearance of size-quantization levels in the chain segments between impurities. Since the impurities in Luttinger liquid form barriers, the energy spectrum of the electron motion

between impurities becomes quantized. The characteristic size-quantization energy is $\omega_l \propto v_F/l$, where l is the separation between the neighboring impurities in the chain. If such one-dimensional chains compose a crystal in which the hopping integral between the chains is smaller than ω_l, then, as shown in [33], Luttinger liquid will remain the ground state of such a quasi-one-dimensional metal. According to the estimates made in [33], the conditions for the appearance of a Luttinger liquid in a quasi-one-dimensional conductor of the $NbSe_3$ type are fulfilled for the dimensionless impurity concentration $c_i \gg 10^{-2}$. In this case, the dielectrization of the electronic spectrum should arise at temperatures $T \lesssim 100$ K, in good agreement with the experimental data. Thus, calculations within the framework of the model of Luttinger liquid [33] suggest that one-dimensional behavior in quasi-one-dimensional conductors is possible.

Characteristic decay length of Friedel oscillations. Although the cause for the dielectrization of electronic spectrum in $NbSe_3$ remains to be understood, it is clear that impurities play a crucial role in this process. Electron scattering by impurities produces Friedel oscillations of electron density. One-dimensional electron systems are distinguished by the slow decease in the amplitude of Friedel oscillations. For instance, in the case of one-dimensional electron gas with long-range Coulomb potential, the electron-density correlation function contains both the component with wavenumber $2k_F$ corresponding to the CDW periodicity and the $4k_F$ component corresponding to Wigner crystal [34]:

$$\langle \rho(x)\rho(0)\rangle = A_1\cos(2k_Fx)\exp(-c\sqrt{\ln x}) + A_2\cos(4k_Fx)\exp(-4c\sqrt{\ln x}).$$

The decay of the $4k_F$ correlations is exceedingly slow.

In Luttinger liquid, the oscillation amplitudes corresponding to the wavenumbers $2k_F$ and $4k_F$ decrease with the distance x from impurity as $x^{-(1+g)/2}$ and x^{-2g}, respectively [35], where g is a dimensionless coupling constant, i.e., slightly faster than in the case of Wigner crystallization, but still appreciably slower than in a three-dimensional metal. The relation between the $2k_F$ and $4k_F$ components depends on the electron–electron interaction parameter.

Slowly decreasing Friedel oscillations are also essential in the quasi-one-dimensional case. One-dimensional relations for the decay of Friedel oscillations are retained up to lengths on the order of

$$L = \frac{2\pi}{\delta k},$$

where $\delta k \approx t_\perp/v_F$ is the amplitude of Fermi-surface corrugation caused by the interchain electronic transitions ($t_\perp$ is the hopping integral) and v_F is the electron velocity at the Fermi surface. Since $t_\perp \sim T_P$, $E_F = \hbar q v_F/4$, where $q = 2k_F$ is the CDW wavenumber, one has

$$L = 4\lambda\frac{E_F}{T_P},$$

where $\lambda = 2\pi/q$ is the CDW wavelength. By substituting the values $E_F \approx 1$ eV, $T_P \approx 100$ K, and $\lambda \approx 1$ nm characteristic of quasi-one-dimensional conductors, one obtains the value $L \approx 400$ nm that corresponds to a relatively low dimensionless impurity concentration $c_i \sim 10^{-3}$. Friedel oscillations are the efficient scatterers of electrons at the Fermi surface of a quasi-one-dimensional metal. The overlap between the Friedel oscillations related to the neighboring impurities can produce a state analogous to the CDW or Wigner crystal and provide conditions for the dielectrization of the electronic spectrum.

Wigner electronic crystallization. The dielectrization scenario for Wigner electronic crystallization below T_{P2} was discussed in [20]. As was mentioned above, the charge-carrier concentration n_e in $NbSe_3$ below the temperature T_{P2} is exceedingly low (on the order of 10^{-18} cm^{-3}) [12]. Because of this, the Fermi energy at $T < T_{P2}$ may become appreciably lower than the energy of Coulomb interaction, setting prerequisites for the Wigner crystallization. The Wigner crystal phase can adjust to the impurities to reduce the pinning energy, much as happens in quasi-one-dimensional crystals with a CDW. If the localization length is greater than the average distance between impurities, the tunnel density of states of such a system obeys the power law [36]. The corresponding exponent β depends on the localization length and can vary from three to six, which is close to the observed values.

Influence of impurities on the conduction in one- and quasi-one-dimensional electron systems. In the one-dimensional case, a single impurity gives rise to the power-law dependences of the conductivity on temperature and electric field [6, 37]. In the presence of many impurities, one can expect electron localization [38] and the dependences described by Eq. (2) with $D = 1$ [39, 40]. On the whole, as was mentioned above, the observed dependences of conductivity on temperature and electric field correspond to the dependences expected for one-dimensional electron systems.

The linear conductivity of quasi-one-dimensional conductors with a CDW is due to the quasiparticle (electron and hole) thermal excitation through the Peierls gap, rendering these conductors akin to standard semiconductors. The introduction of impurities into a quasi-one-dimensional conductor gives rise to pinning centers and distorts the CDW. In turn, the CDW distortion results in a shift of chemical potential, i.e., in the appearance of a potential relief for the quasiparticle motion. The scale of potential relief is given by the product $E_TL_\parallel$, where E_T is the threshold field for nonlinear conduction and $L_\parallel$ is the CDW-phase correlation

length. Due to the size effects, this product increases as $(n_i/s)^{1/3}$ with an increase in the impurity concentration and decrease in the sample transverse sizes [11]. Whereas the value of $E_T L_\parallel$ is on the order of 1 meV at $T = 120$ K for the rated pure TaS_3 samples with $s \sim 1\ \mu m^2$, this value increases by an order of magnitude and becomes comparable to kT for samples with $s = 10^{-3}\ \mu m$. For even smaller s values, the spatial inhomogeneity of the potential must be taken into account in the entire temperature range at $T < T_P = 220$ K. This approach can explain the appearance of hopping conduction at $T < T_P$, but it fails to explain the dielectrization in TaS_3 at $T > T_P$ and in $NbSe_3$. Note that hopping conduction in the bulk crystals of quasi-one-dimensional conductors with CDW was observed in the region of linear conduction of $Fe_{0.25}Nb_{0.75}Se_3$ [41] ($T < 140$ K) and in the regions of linear [42] and nonlinear [43] conduction of rhombic TaS_3 with a high impurity concentration (threshold field ~10 V/cm). However, in all these cases, $\gamma = 1/4$, whereas $\gamma = 1/2$ in thin films (Figs. 5, 6). The power-law dependences of the conductivity on temperature and electric field were not predicted for quasi-one-dimensional conductors with CDW.

Interaction between impurities. The models of one- and quasi-one-dimensional systems described above presume a random impurity distribution. However, impurities in quasi-one-dimensional conductors interact with each other and can form superstructures. In [22], atomic-force microscopic study of the surface of doped $NbSe_3$ revealed a concentration-dependent impurity ordering. The period and symmetry of this ordering depended on the impurity concentration. In particular, the period of this structure could attain ten lattice parameters. The inter-impurity interaction effects caused by slowly decaying Friedel oscillations in a quasi-one-dimensional metal were considered theoretically in [44]. It was shown that, depending on the impurity concentration and valency, various types of ordered impurity arrangement can arise in a quasi-one-dimensional metal. In the presence of impurity superstructures, the influence of Friedel oscillations can be more pronounced and they can have an appreciable effect on the conductivity of a quasi-one-dimensional conductor.

Outlook for lines of investigation. Up to now, the size effects have been the main object of experimental studies. The analysis presented in this review shows that there is a need for a more detailed study of the impurity effect on the conductivity of samples of quasi-one-dimensional conductors with standard sizes, including quasi-one-dimensional $TaSe_3$ metal, which has the chain structure but does not undergo the Peierls transition [45]. Preliminary results [46] suggest that thin samples of this material can behave like $NbSe_3$. Inasmuch as the one-dimensional transition implies the disappearance of quasiparticles and appearance of a pseudogap, of interest is the problem of the conduction type (collective or single-particle) and the lifetimes of quasiparticles and metastable CDW states in samples of different sizes and different impurity contents. The result of these studies will be helpful in elucidating the nature of the observed dielectrization of the electronic spectrum in quasi-one-dimensional conductors.

Conclusions. Thus, quasi-one-dimensional conductors with nanometer transverse sizes possess properties that are predicted for one-dimensional electron systems. Such behavior cannot be explained on the basis of the laws known for three-dimensional electron systems. At the same time, the observed phenomena can be described by a number of alternative methods using different models of electron systems. There are grounds to believe that the dielectrization is associated with the one-dimensionality effects arising as a result of the impurity-induced stabilization of Luttinger liquid [33]. If this is so, we will obtain an object that is highly suitable for experimental studies of the physics of one-dimensional structures.

I am grateful to S.N. Artemenko for discussion and to H.S.J. van der Zant and E. Slot for assistance. This work was supported by the Russian Foundation for Basic Research (project no. 04-02-16509), INTAS (grant no. 01-0474), CDRF (grant no. 2563), and the Presidium of the Russian Academy of Sciences.

REFERENCES

1. R. E. Peierls, *Quantum Theory of Solids* (Clarendon Press, Oxford, 1955; Inostrannaya Literatura, Moscow, 1956).
2. P. Monceau, N. P. Ong, A. M. Portis, *et al.*, Phys. Rev. Lett. **37**, 602 (1976); N. P. Ong and P. Monceau, Phys. Rev. B **16**, 3443 (1977).
3. P. Monceau, in *Electronic Properties of Quasi-One-Dimensional Materials* (Reidel, Dordrecht, 1985), Part 2, p. 139; G. Grüner, *Density Waves in Solids* (Addison-Wesley, New York, 1994); Rev. Mod. Phys. **60**, 1129 (1988).
4. J. Voit, Rep. Prog. Phys. **58**, 977 (1995).
5. F. D. M. Haldane, J. Phys. C: Solid State Phys. **14**, 2585 (1981).
6. C. L. Kane and M. P. A. Fisher, Phys. Rev. Lett. **68**, 1220 (1992); Phys. Rev. B **46**, 15 233 (1992).
7. M. Bockrath, D. H. Cobden, J. Lu, *et al.*, Nature **397**, 598 (1999).
8. S. Tarucha, T. Honda, and T. Saku, Solid State Commun. **94**, 413 (1995); F. P. Millken, C. P. Umbach, and R. A. Webb, Solid State Commun. **97**, 309 (1996).
9. S. V. Zaitsev-Zotov, Yu. A. Kumzerov, Yu. A. Firsov, and P. Monceau, J. Phys.: Condens. Matter **12**, L303 (2000).
10. D. Natelson, cond-mat/0307600.
11. S. V. Zaĭtsev-Zotov, Usp. Fiz. Nauk **174**, 585 (2004) [Phys. Usp. **47**, 533 (2004)].
12. N. P. Ong, Phys. Rev. B **18**, 5272 (1978).

13. S. V. Zaĭtsev-Zotov, V. Ya. Pokrovskiĭ, and P. Monceau, Pis'ma Zh. Éksp. Teor. Fiz. **73**, 29 (2001) [JETP Lett. **73**, 25 (2001)].
14. V. Zaitsev-Zotov, M. S. H. Go, E. Slot, and H. S. J. van der Zant, Phys. Low-Dimens. Semicond. Struct. **1–2**, 79 (2002); cond-mat/0110629.
15. L. Balents, cond-mat/9906032.
16. S. V. Zaitsev-Zotov, E. Slot, and H. S. J. van der Zant, J. Phys. IV **12**, Pr9-115 (2002).
17. S. V. Zaitsev-Zotov (unpublished).
18. S. V. Zaitsev-Zotov, Microelectron. Eng. **69**, 549 (2003).
19. V. F. Gantmakher, *Electrons in Disordered Media* (Fizmatlit, Moscow, 2003) [in Russian].
20. E. Slot, M. A. Holst, H. S. J. van der Zant, and S. V. Zaitsev-Zotov, Phys. Rev. Lett. **93**, 176602 (2004).
21. J. W. Brill, N. P. Ong, J. C. Eckert, *et al.*, Phys. Rev. B **23**, 1517 (1981).
22. Y. Gong, Q. Xue, D. L. Drake, *et al.*, Phys. Rev. B **51**, 12975 (1995).
23. J. C. Gill, Phys. Rev. B **53**, 15586 (1996).
24. P. J. Yetman and J. C. Gill, Solid State Commun. **62**, 201 (1987).
25. J. McCarten, D. A. DiCarlo, M. P. Maher, *et al.*, Phys. Rev. B **46**, 4456 (1992).
26. J. C. Gill, Phys. Rev. Lett. **65**, 271 (1990).
27. R. E. Thorne and J. McCarten, Phys. Rev. Lett. **65**, 272 (1990).
28. E. Slot, H. S. J. van der Zant, K. O'Neill, and R. E. Thorne, Phys. Rev. B **69**, 073105 (2004).
29. A. Bachtold, M. de Jonge, K. Grove-Rasmussen, *et al.*, Phys. Rev. Lett. **87**, 166 801 (2001).
30. M. H. Devoret, D. Esteve, H. Grabert, *et al.*, Phys. Rev. Lett. **64**, 1824 (1990).
31. S. M. Girvin, L. I. Glazman, M. Jonson, *et al.*, Phys. Rev. Lett. **64**, 3183 (1990).
32. K. A. Matveev and L. I. Glazman, Phys. Rev. Lett. **70**, 990 (1993).
33. S. N. Artemenko, Pis'ma Zh. Éksp. Teor. Fiz. **73**, 335 (2001) [JETP Lett. **73**, 277 (2001)].
34. H. J. Schulz, Phys. Rev. Lett. **71**, 1864 (1993).
35. R. Egger and H. Grabert, Phys. Rev. Lett. **75**, 3505 (1995).
36. H. C. Lee, Phys. Rev. B **66**, 052202 (2002).
37. K. A. Matveev, D. Yue, and L. I. Glazman, Phys. Rev. Lett. **71**, 3351 (1993).
38. A. Furusaki and N. Nagaosa, Phys. Rev. B **47**, 4631 (1993).
39. T. Nattermann, T. Giamarchi, and P. Le Doussal, Phys. Rev. Lett. **91**, 056603 (2003).
40. M. M. Fogler, S. Teber, and B. I. Shklovskii, Phys. Rev. B **69**, 035413 (2004).
41. S. J. Hillenius, R. V. Coleman, R. M. Fleming, and R. J. Cava, Phys. Rev. B **23**, 1567 (1981).
42. S. K. Zhilinskiĭ, M. E. Itkis, I. Yu. Kal'nova, *et al.*, Zh. Éksp. Teor. Fiz. **85**, 362 (1983) [Sov. Phys. JETP **58**, 211 (1983)].
43. S. V. Zaitsev-Zotov, G. Remenyi, and P. Monceau, Phys. Rev. B **56**, 6388 (1997).
44. S. Turgut and L. M. Falicov, Phys. Rev. B **49**, 14043 (1994).
45. B. Fisher and M. Fibich, Phys. Rev. B **37**, 2820 (1988).
46. A. V. Zavalko, Thesis (Moscow Inst. of Engineering Physics, Moscow, 2004).

Translated by V. Sakun

JETP Letters, Vol. 80, No. 6, 2004, p. 455.

Erratum: "Search for the Emission of π^0 Mesons from the Neutron-Induced Fission of ^{235}U Nuclei" [JETP Lett. 80, 149 (2004)]

V. A. Varlachev, G. N. Dudkin, Yu. F. Krechetov, V. N. Padalko, and E. N. Shuvalov

PACS numbers: 25.85.Ec; 99.10.Cd

In the article "Search for the Emission of π^0 Mesons from the Neutron-Induced Fission of ^{235}U Nuclei" there is misprint:

P. 172, left column, 9th line from the top: ^{239}Pu should be reads instead ^{252}Cf.

0021-3640/04/8006-0455$26.00